Fall 2013

Enamel coated steel reinforcement for improved durability and life-cycle performance of concrete structures: microstructure, corrosion, and deterioration

Fujian Tang

ENAMEL COATED STEEL REINFORCEMENT FOR IMPROVED DURABILITY AND LIFE-CYCLE PERFORMANCE OF CONCRETE STRUCTURES: MICROSTRUCTURE, CORROSION, AND DETERIORATION

by

FUJIAN TANG

A DISSERTATION

Presented to the Faculty of the Graduate School of the

MISSOURI UNIVERSITY OF SCIENCE AND TECHNOLOGY

In Partial Fulfillment of the Requirements for the Degree

DOCTOR OF PHILOSOPHY

in

CIVIL ENGINEERING

2013

Approved by

Dr. Genda Chen, Advisor
Dr. Richard K. Brow
Dr. Jeffery S. Volz
Dr. Matthew J. O'Keefe
Dr. Lesley H. Sneed

ABSTRACT

This study is aimed (a) to statistically characterize the corrosion-induced deterioration process of reinforced concrete structures (concrete cracking, steel mass loss, and rebar-concrete bond degradation), and (b) to develop and apply three types of enamel-coated steel bars for improved corrosion resistance of the structures. Commercially available pure enamel, mixed enamel with 50% calcium silicate, and double enamel with an inner layer of pure enamel and an outer layer of mixed enamel were considered as various steel coatings. Electrochemical tests were respectively conducted on steel plates, smooth bars embedded in concrete, and deformed bars with/without concrete cover in 3.5 wt.% NaCl or saturated $Ca(OH)_2$ solution. The effects of enamel microstructure, coating thickness variation, potential damage, mortar protection, and corrosion environment on corrosion resistance of the steel members were investigated. Extensive test results indicated that corrosion-induced concrete cracking can be divided into four stages that gradually become less correlated with corrosion process over time. The coefficient of variation of crack width increases with the increasing level of corrosion. Corrosion changed the cross section area instead of mechanical properties of steel bars. The bond-slip behavior between the corroded bars and concrete depends on the corrosion level and distribution of corrosion pits. Although it can improve the chemical bond with concrete and steel, the mixed enamel coating is the least corrosion resistant. The double enamel coating provides the most consistent corrosion performance and is thus recommended to coat reinforcing steel bars for concrete structures applied in corrosive environments. Corrosion pits in enamel-coated bars are limited around damage locations.

ACKNOWLEDGMENTS

First and foremost, I would like to express my sincere gratitude to Dr. Genda Chen, for providing continuing support, encouragement and invaluable advice during my study at Missouri University of Science and Technology. I would also like to thank Drs. Richard K. Brow, Jeffery S. Volz, Matthew J. O'Keefe, and Lesley H. Sneed for their time and effort as Ph.D. committee members in reviewing this dissertation and providing constructive review comments.

Financial support for this study was provided in part by the U.S. National Science Foundation under Award No. CMMI-0900159, by the Missouri Department of Transportation under Award No. 28015485-09R000587, and by the Center for Transportation Infrastructure and Safety at Missouri University of Science and Technology under Award No. DTRT06-G-0014. Special thanks are due to Michael L. Koenigstein for coating enamels on steel specimens that are vital to the completion of this study.

I would like to thank the Center for Infrastructure Engineering Studies laboratory technicians Jason Cox and John Bullock, and civil engineering department laboratory technicians Gary Abbott, Scott Parker, and Brian Swift for their assistance during the fabrication and test preparation of various specimens.

Thanks are extended to the Materials Science and Engineering laboratory technicians Eric Bohannan and Clarissa Wisner for their assistance during the characterization of enamel coating using XRD and SEM.

I also appreciate the assistance from my fellow students and friends during various laboratory tests, including Xing Tao, Ying Huang, Xiaoming Cheng, Charles Robert Werner, Zhibin Lin, John A. Cain, Hongya Qu, Yi Bao, Yizheng Chen, and Yan Tang.

Last but not the least, I wishes to express my special and sincere gratitude to my parents, sister, and brother-in-law for their continuous love, understanding and encouragement throughout the Ph.D. study. And I would like to express my sincere gratitude to my aunt Josephine Chain for her care and encouragement during my study in the U.S.

TABLE OF CONTENTS

LIST OF ILLUSTRATIONS

LIST OF TABLES

1. INTRODUCTION

1.1 BACKGROUND, PROBLEM AND JUSTIFICATION

Corrosion has resulted in a significant financial burden to the U.S. Department of Transportation. According to the 2002 study by Federal Highway Administration [1], the total cost to combat corrosion had been approximately $276 billion annually or 3.1% of the nation's Gross Domestic Product (GDP). Over the following 10 years, the direct corrosion cost for highway bridges was estimated to be $8.3 billion per year, including $3.8 billion for replacement of deficient bridges, $2 billion for maintenance and capital cost of concrete bridge decks, $2 billion for maintenance and capital cost of concrete substructures, and $0.5 billion for maintenance painting of steel bridges. The indirect cost such as traffic delay and lost productivity was estimated to be as high as 10 times the direct cost. According to the 2009 American Society of Civil Engineers Report Card for America's Infrastructure, more than 26% of the nation's bridges are either structurally deficient or functionally obsolete, and a $17 billion annual investment is needed to substantially improve the current bridge conditions [2]. By 2012, the total cost for corrosion-induced maintenance and replacement has exceeded $ 1 trillion in the U.S., and the annual cost to the U.S. Department of Defense (DOD) has been estimated to be $ 20.9 billion [3].

Corrosion in transportation infrastructure is not only the main reason for substantial financial costs, but also a matter of public safety and commuter inconvenience when not assessed and mitigated in time. As an example, the I-35W Bridge over the Mississippi River in Minneapolis collapsed on August 1, 2007, killing 13 people. The National Transportation Safety Board discovered that cracks occurred along corroded gusset plates on the failed bridge. Although the root cause for the bridge collapse was due to the under designed gusset plate [4], corrosion was also observed on the approximately 50-years old bridge. On October 22, 2010, the City of Minneapolis closed another bridge (Plymouth Avenue Bridge) over the Mississippi River because serious corrosion was observed in at least five of the post-tensioned tendons in the bridge's center span. Closure

of bridges for corrosion-induced inspection and maintenance forces vehicles to detour, increasing commuting time and thus gas consumption and greenhouse gas emission.

Porcelain enamel is typically a silicate-based material that is deposited from slurries and fused at high temperature. It has many advantages as follows. First, enamel has very stable chemical properties in harsh environments such as high temperature, acid and alkaline. Therefore, it can protect reinforced concrete (RC) structures located in any environment. Second, the properties of enamel are flexible and can be tailored for various applications by regulating the chemical composition of enamel and/or pre-treating the metal substrate to be coated. For example, replacing B_2O_3 with SiO_2/TiO_2 can increase the corrosion resistance of enamel in acidic environments; adding ZrO_2 can improve the performance of enamel in alkaline environments. Third, an enamel coating can establish a physical barrier between steel rebar and its surrounding concrete, delaying the penetration of aggressive chloride ions and thus prolonging the service life of RC structures. Lastly, enamel with cement additives is fused on a steel substrate at high temperature to establish a chemical bond with the steel and concrete when applied to RC structures, which is important for the long-term performance of structures. The main disadvantage of enamel coating is its brittleness and can potentially damage during shipping and transportation, though its impact in applications can be minimized through precast constructions. Overall, enamel coating can be an alternative method to protect steel from corrosion.

1.2 LITERATURE REVIEW ON STATE-OF-THE-ART DEVELOPMENT

1.2.1 Electrochemical Corrosion Test Techniques. A number of test methods and techniques to detect and measure reinforcement steel corrosion have been developed in the past [5]. They can be divided into two groups: electrochemical and non-destructive. For example, the electrochemical methods include the open-circuit potential measurement, linear polarization resistance (LPR) measurement, galvanostatic pulse transient response, and electrochemical impedance spectroscopy (EIS). The non-destructive techniques include the concrete cover thickness measurement, ultrasonic pulse velocity measurement, and x-ray and Gamma radiography measurements. Following is a detail review of the four frequently-used electrochemical techniques.

1.2.1.1 Open-circuit potential. The open-circuit potential (also referred to as half-cell potential) measurement has been widely used to assess reinforcement steel corrosion in concrete due to its simplicity and cost effectiveness. This method often provides the probability of corrosion activity through a measurement of potential differences among a standard portable reference electrode, a copper/copper sulphate electrode (CSE), and a reinforcing steel electrode. ASTM standard C876 [6] provides the general guidelines for the corrosion evaluation of RC structures based on the potential thresholds as summarized in Table 1.1.

Table 1.1 Corrosion condition related with half-cell potential measurement [6]

Corrosion potential vs. CSE	Corrosion activity
Less negative than -0.2 V	90% probability of no corrosion
Between -0.2 and -0.35 V	Corrosion activity is uncertain
More negative than -0.35 V	90% probability of corrosion

However, the above potential measurement method has some drawbacks. The potential mapping on existing structures require careful interpretation because many factors can affect the corrosion potential measurement [7], such as oxygen and chloride concentration, concrete resistivity [8], use of corrosion inhibitors, epoxy-coated or galvanized reinforcing steel, presence of stray currents [9], carbonated concrete [10], and presence of concrete cracks [11]. Therefore, evaluation on the reinforcement steel corrosion based on the half-cell potential measurement alone may mislead engineers and cause errors in their judgment if these factors are not taken into account. It must be stressed that this method just evaluates the probability of corrosion activity at a given location and time, long-term monitoring of the half-cell potential in combination with other techniques is more meaningful.

1.2.1.2 Linear polarization resistance. The most extensively used method to evaluate rebar corrosion rates in concrete is the LPR measurement. This technique is rapid and non-destructive; it only requires a connection to the reinforcing steel under investigation. The data provides a valuable insight into the instantaneous corrosion rate of

steel reinforcement, thus giving more detailed information than the hall-cell potential measurement. For each LPR measurement, the reinforcing steel is perturbed by a small electrical signal from its equilibrium potential. This can be accomplished potentiostatically by changing the potential applied to the reinforcing steel by a fixed amount ΔV and then monitoring the current decay, ΔI, after a given time or vice versa. In either case, the test conditions are selected such that the variation in potential, ΔV, falls within the linear Stern-Geary range of 10-30 mV. The polarization resistance representing the slope of a polarization curve, R_p, can be calculated by:

$$R_p = \Delta V / \Delta I \tag{1.1}$$

where ΔV and ΔI represent the potential and current increments, respectively, in the linear portion of a polarization curve at I=0. LPR measurements were used to calculate the corrosion current density by the Stern-Geary equation [12]:

$$i_{corr} = \beta_a \beta_c / [2.303(\beta_a + \beta_c) R_p] = B / R_p \tag{1.2}$$

where i_{corr} is the corrosion current density, β_a is the anodic Tafel slope, β_c is the cathodic Tafel slope, and B is a constant related to β_a and β_c.

However, there are still some difficulties associated with this technique. It is often difficult to determine the Tafel slopes when the steel surface is in passive state. As a result, the B value estimated from Eq. (1.2) is likely inaccurate or very sensitive to the change in steel surface condition. Furthermore, some requirements must be met during each test. For example, the electrochemical current at the fixed potential should remain constant during the entire polarization period and uniform along the length of a steel bar. The effect of the high electrical resistance of concrete should be properly taken into account.

In order to meet the above two requirements, an outer auxiliary guard ring electrode has been placed around the inner auxiliary electrode. The outer guard ring electrode maintains a confinement current during each LPR measurement. The

confinement current prevents the perturbation current in the inner auxiliary electrode from spreading beyond a known area. To select an approximate level of the confinement current, two sensor electrodes are placed between the inner and outer auxiliary electrodes. The potential difference between the two sensor electrodes is monitored and maintained throughout the LPR measurement by selecting a proper confinement current. The LPR measurement is affected by a few factors such as temperature and humidity. Therefore, special attention should be paid to the interpretation of measured data. Table 1.2 gives the general criteria for the extent of corrosion based on the corrosion rate measured with and without guard ring.

Table 1.2 Corrosion rate vs. condition of reinforcement steel [13]

Extent of corrosion	I_{corr} applied to device with guard ring ($\mu A/cm^2$)	I_{corr} applied to device without guard ring($\mu A/cm^2$)
Passive	$i_{corr}<0.1$	$i_{corr}<0.22$
Low to moderate	$0.1<i_{corr}<0.5$	$0.22<i_{corr}<1.08$
Moderate to high	$0.5<i_{corr}<1$	$1.08<i_{corr}<10.8$
high	$i_{corr}>1$	$i_{corr}>10.8$

1.2.1.3 Transient technique. Transient techniques such as galvanostatic pulse or coulostatic methods in time domain recently became more receptive in the study of steel and concrete composite structures [14-18]. These techniques recognize the fact that corrosion is a relatively slow electrochemical response/process at steel-concrete interfaces, which makes data collection more preferably done in time domain than in frequency domain. In time domain, they can directly provide the measurement of both polarization resistance and double layer capacitance per unit surface area, independent of the size or total steel area of a test specimen. Such a measurement makes the transient techniques advantageous for in situ monitoring over others that require the prior knowledge of the cross sectional area of the test system.

For transient measurements, a counter electrode is placed on the surface of concrete, a small current perturbation (pulse effect) is applied to a reinforcing steel bar embedded in the concrete, and the transient potential in the reinforcing steel is recorded

with respect to the reference electrode. The analysis of the transient response allows the determination of corrosion rate in steel. Figure 1.1 shows a typical potential response for a corroding reinforcement bar. Under a galvanostatic pulse, the electrochemical system can be approximately simulated by a simple Randles circuit due to the current pulse *I* and its potential response can be expressed into:

$$V_t = IR_S + IR_p[1 - \exp(-\frac{t}{C_{dl}R_p})] \tag{1.3}$$

where V_t is the total potential change in the steel working electrode, IR_s is the ohmic drop in the concrete between the counter electrode and the working electrode, IR_p is the effective polarization potential during a charging or discharging period, R_p is the polarization resistance of the rebar, C_{dl} is the double layer capacitance of the steel-concrete interface, and $C_{dl}R_p$ represents the time constant for the corrosion process.

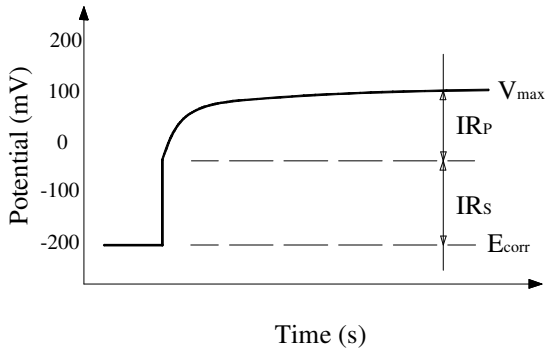

Figure 1.1 Typical potential-time curve as response to a galvanostatic pulse.

As shown in Figure 1.1, each measurement with the galvanostatic pulse transient technique may take a long period of time since the response to the pulse must be stabilized before V_{max} can be determined accurately. Curtailing the response measurement before V_{max} has been reached may lead to an erroneous evaluation of R_p and C_{dl}.

1.2.1.4 Electrochemical impedance spectroscopy. Electrochemical impedance spectroscopy (EIS) has been widely used in fundamental and applied electrochemistry research for a long time. This technique has also been used extensively for the

investigation of corrosion mechanisms in laboratory and for the determination of the corrosion rate of reinforcing steel in concrete. For each measurement, a harmonic potential signal (10 to 20 mV in amplitude) around the open-circuit potential is usually applied to the system or specimen under test, and the current signal is recorded as a function of the excitation frequency. By analyzing the test data in various frequency ranges, EIS can be used to study the corrosion kinetics and insights into the corrosion mechanism of a test specimen in a short time, and investigate the evolution of corrosion over a relatively long time.

The interpretation of EIS test data is usually done in combination with simulations of the electrochemical system under investigation by an equivalent electrical circuit. As shown in Figure 1.2(a-1), the simplified Randles circuit consists of a solution resistance in series with a parallel set of polarization resistance and capacitor. In order to extract the non-homogeneity and diffusion phenomenon, Sagues et al. [14, 15] and Feliu et al. [19-20] modified the simplified circuit by replacing the capacitor with a constant phase element (CPE) and adding a diffusion impedance, as shown in Figure 1.2(a-2). In an EIS measurement, multiple semi-circles are often observed because various materials have different characteristic frequencies [21-23]. The semi-circles can be represented either by a series of parallel pairs of capacitor (or CPE) and resistor as shown in Figure 1.2(b-1) or a series of mixed pairs of resistor and capacitor (or CPE) as shown in Figure 1.2(c-1), each pair representing a certain material behavior. The diffusion behavior is generally combined into a particular pair that represents the steel-concrete interface, as shown in Figures 1.2(b-2, c-2). More advanced circuit representations of the steel-concrete systems were also introduced as shown in Figures 1.2(e, f) [18, 24]. The fact that diverse electrical circuits have been used to reasonably represent a steel-concrete system warrants further study on the equivalent circuit representation of steel-concrete systems.

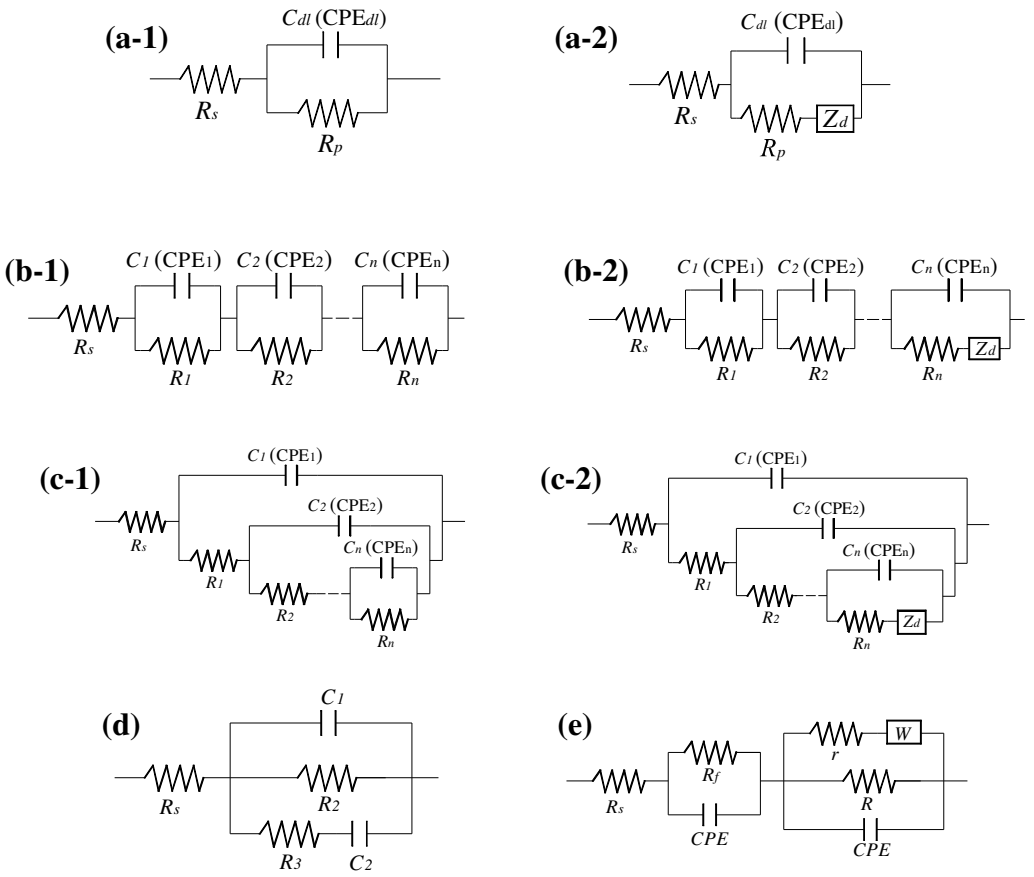

Figure 1.2 Various electrical circuits for steel-concrete systems: (a-1) Randle's circuit, (a-2) modified Randle's circuit, (b-1) resistor-capacitor in series, (b-2) modified resistor-capacitor with diffusion in series, (c-1) resistor-capacitor in mixed mode, (c-2) modified resistor-capacitor with diffusion in mixed mode, (d) and (e) other models.

The use of EIS as a monitoring technique provides substantial information on the corrosion characteristics of a steel-concrete system. However, it is a time-consuming task and sometimes a challenge to interpret the EIS test data. Nevertheless, EIS is a powerful tool that has recently gained increasing acceptance for the understanding of corrosion behavior in various steel-concrete systems.

1.2.2 Corrosion Prevention Methods. A number of measures can be taken to protect reinforcement steel from corrosion. They can be divided into four categories [25]: (1) alternative reinforcement, (2) barrier to chloride ingress, (3) corrosion inhibitors, and (4) cathodic protection.

1.2.2.1 Alternative reinforcement. To improve the corrosion resistance of RC structures, reinforcing bars with various materials can be used as an alternative to the widely used low carbon steel bars in civil engineering, including stainless steel rebar, stainless steel clad rebar, nickel clad rebar, copper clad rebar, and fiber reinforced polymer (FRP) rebar.

Stainless steel bars are produced by adding a minimum of 12% chromium into the low carbon steel so that an invisible film can be formed on the surface of the stainless steel bars and thus protect the steel from oxidation. It offers many advantages including high corrosion resistance, high strength, good ductility, and good weldability. Castro et al. [26] mechanically characterized two types of austenitic stainless steel bars, 304 LN and 316 LN grades, and found that the cold-rolled rib shaping significantly increased their strength and hardness but maintained their high toughness when compared with carbon steel bars. In a chloride-containing aqueous solution, the cold-rolled 304 LN bars were prone to pitting corrosion while the cold-rolled 316LN bars revealed excellent corrosion behavior. Garcia-Alonso et al. [27] studied the corrosion behavior of three low-cost and low Ni-content stainless steels embedded in mortar contaminated with chloride ions, and they concluded that the new stainless steel remained in the passive state in mortar specimens with both 2% and 5% chloride contents. Moser et al. [28] evaluated the corrosion resistance of austenitic, duplex, and precipitation-hardened martensitic high strength stainless steels and a pearlitic high-C prestressing steel bar in simulated alkaline and carbonated concrete pore solutions and found that all types of the steel materials showed high corrosion resistance at chloride concentrations from zero to 0.25M.

However, the high cost of stainless steel bars may prevent them from wide applications in construction. Therefore, stainless steel clad bars were studied as a lower cost corrosion resistance reinforcement option. It was produced by spraying 304 stainless steel on the surface of a portion of a billet and then rolling the steel in a traditional fashion. Darwin et al. [29] compared the performances of stainless steel clad bars and uncoated black steel bars. They found that the stainless steel clad bars corroded at a rate about two orders of magnitude lower than that of the black steel bars.

Nickel clad bars are produced by applying a heavy layer of nickel to a billet before it is hot rolled, resulting in a continuous coating of wrought nickel on the surface

of the steel bars. In 1980, copper clad bars were tested in concrete, leveraging with an FHWA study [30]. The copper clad reinforcing bars were compared with the black steel bars with and without calcium nitrite corrosion inhibitors and compared with epoxy–coated bars. The copper clad bars were not discussed in the FHWA report, but their results were published in 1996 by McDonald et al. [31]. The test results indicated that the copper clad bars with a coating thickness of approximately 0.5 mm exhibited a much higher corrosion resistance than the other types of reinforcement including the black steel with calcium nitrite corrosion inhibitors. Tests up to that time have shown excellent corrosion behaviors of copper clad reinforcing bars in concrete. Copper clad bars could also prove to be cost effective.

Fiber reinforced polymers (FRP) bars is another non-corroding reinforcement option for RC structures. It is made by three elements: fibers for strength, resinous synthetic polymers for binding with the fibers, and finishing or coupling agents for enhanced adhesion between the fibers and the polymers. Although carbon FRP strands exhibit superior fatigue behavior, high tensile elastic modulus and low relaxation, they typically have a low tensile strain at failure [32]. Another problem with glass composites is that they are made of silica, which can combine with calcium hydroxide in concrete and result in a loss of reinforcement over time.

1.2.2.2 Barrier to chloride ingress. Steel reinforcement can be protected from corrosion by establishing a barrier layer between it and its aggressive environment. It can be achieved by using high quality concrete (low permeability and thick cover), or protective coating on reinforcement steel. Two of the most widely used barriers for reinforcement steel are fusion-bonded epoxy (FBE) coating and hot-dipped galvanized (HDG) zinc coating.

Epoxy-coated reinforcing bars were developed in the early 1970s. They are made by first cleansing black steel bars, heating them to around 230 °C, and passing them through an electrostatic spray that applies charged, dry epoxy powders to the steel surface. In this process, epoxy materials melt, flow and cure on steel bars, which are finally quenched with usually a water spray bath [33]. Epoxy coating functions in two ways, first by acting as a barrier and keeping oxygen and chloride ions from reaching the

surface of steel bars, and second by increasing the electrical resistance between adjacent steel bars in practical applications.

Epoxy-coated steel bars were widely used for bridge construction in the 1960s and 1970s because they are sufficiently flexible to bend in application and can be produced at high speed [33]. However, in 1986, the substructure of the Long Key Bridge with epoxy-coated steel rebar began to show signs of corrosion only five to seven years after construction [34]. In the following several years, corrosion was observed in other bridges [35]. After several studies, corrosion in epoxy-coated rebar was mainly attributed to the damage induced during transportation and handling. Equally if not more important, corrosion at one location of the damaged epoxy coating was widely spread underneath the coating due to relatively weak physical bond between the epoxy and its steel substrate. In addition, use of epoxy-coated steel rebar reduced the bond strength between rebar and concrete [36].

Metallic coatings have been used successfully to prevent corrosion of steel in other applications, and were recently expected to protect reinforcement steel from corrosion in RC structures. One of the most popular metallic coatings for reinforcement steel is the application of hot-dip galvanic (HDG) zinc on steel bars. Zinc-coated or galvanized bars are produced by a hot-dip process in which the steel bars are first cleansed by pickling, and then immersed in molten zinc. Like steel, zinc can generate corrosion products that occupy more space than the zinc itself, and can consequently cause concrete to cracking. An advantage of galvanized reinforcement is that, as zinc corrodes sacrificially, a hydrated oxide is formed on the rebar surface that acts as an electrical insulator. The insulator is thought to form a barrier at active corrosion sites that will prevent further corrosion from occurring [37].

Galvanized steel rebar have at least two main concerns in engineering applications. First, the zinc coating corrodes vigorously due to the high alkaline environment in fresh concrete, likely leaving an insufficient galvanic protection for the underlying steel in long term. Second, the hydrogen produced in the corresponding cathodic half-cell reaction would increase the porosity of adjacent cement pastes and thus reduce the bond strength between the rebar and the concrete [38].

1.2.2.3 Corrosion inhibitors. Corrosion inhibitors may be a good alternative to other protection methods due to their lower cost and easy application. They can be added into fresh concrete as an admixture and repair mortar for existing RC structures, or directly applied on hardened concrete surfaces and rebar surfaces before concrete casting. There are three mechanisms of protection from inhibitors [39]: anodic, cathodic, and mixed. Anodic inhibitors act on the dissolution of steel and reduce the corrosion rate by increasing the corrosion potential of the steel. Cathodic inhibitors act on the oxygen reaction on the steel surface and reduce the corrosion rate by decreasing the corrosion potential. Mixed inhibitors act on both anodic and cathodic sites and reduce the corrosion rate without significantly changing the corrosion potential, generally by surface absorption of the steel in contact with the inhibitors and consequently forming a thin protective layer.

The most commonly-used anodic inhibitors are calcium nitrite ($Ca(NO_2)_2$ and sodium nitrite; sodium benzoate and sodium chromate are the next [40, 41]. The most commonly-used cathodic inhibitors are sodium hydroxide and sodium carbonate, which are supposed to increase the pH near steel and reduce the oxygen transportation by covering the steel surface; phosphates, silicate and polyphosphates are the next [42]. Mixed type inhibitors include materials with hydrophobic groups such as N, S, and OH are effective. Organic polymer compounds such as amine and aminoalcohol (AMA) are also used [42].

1.2.2.4 Cathodic protection. Cathodic protection is an electrochemical technique for corrosion control by connecting the metal to be protected to a more easily corroded metal so that the protected metal and the "sacrificial" metal act as the cathode and anode of an electrochemical cell, respectively. It has been widely adopted to control the corrosion of reinforcing steel embedded in concrete [43-45]. The goal of cathodic protection is to shift the potential of the protected steel to the least probable range for corrosion. Cathodic protection has been determined by Federal Highway Administration to be the only rehabilitation technique that can prevent further corrosion in RC structures regardless of the salt content in concrete [46].

Sacrificial anode methods have such an advantage as no auxiliary power supply requirement. They can be used in prestressed or post-tensioned concrete with no risk of

increasing potential shifts and thus no hydrogen embrittlement of the steel. In addition, since the anode is directly connected to the protected steel, electrical shorting is of no concern. Anode materials made of arc sprayed zinc, aluminum alloys containing Zn, and magnesium alloy have been studied extensively in laboratory and field conditions [47, 48].

1.2.3 Corrosion-induced Structural Deterioration. Corrosion of reinforcing steel bars in concrete may impair the capacity of RC structures in the form of concrete cracking, steel reduction, and loss of the bond between the steel reinforcement and concrete. Following is a presentation of a detailed review on the three effects.

1.2.3.1 Concrete cover cracking. Corrosion-induced cracking in concrete cover is an important criterion for the analysis and evaluation of the service life of a RC structure. Cracks in concrete cover provide paths for a rapid ingress of aggressive chemicals to the reinforcing steel bars, and accelerate structural deterioration. Therefore, the appearance of the first crack is a key indication for the end-of-service-life of structural concrete. Indeed, concrete cover cracking induced by corrosion has been identified as the serviceability limit state of RC structures [49, 50].

Both laboratory and field tests have been conducted extensively to investigate the corrosion-induced cracking in concrete cover. These studies can be classified into three main categories: empirical (experimental), analytical, and numerical modeling [51]. The empirical models are primarily based on a regression analysis of experimental data and observations. Andrade et al. [52] conducted accelerated corrosion tests and observed that regardless of corrosion rate, cracking occurred at a structurally negligible steel loss of approximately 20 um in diameter. Webster [53] conducted a regression analysis of 50 sets of experimental data obtained by other researchers and proposed a very simple model for a rough estimation of critical attack penetration, which initiates concrete cover cracking. The analytical models are based primarily on the fundamental of solid mechanics under some assumptions. Bazant [54] used a comprehensive mathematical formulation for corrosion rate and proposed a predictive model for crack width using the principles of linear elastic solid mechanics. Finite element model (FEM) has also been applied to study concrete cracking. Yokozeki et al. [55] simulated the internal pressure by

imposing strains to the corrosion front. Using a regression analysis of the results from multiple FEMs, an empirical equation for the prediction of cracking time was proposed.

Although the above models shed insight on steel corrosion and concrete cracking, their predictions are often deviated from respective observations. The possible sources of discrepancy between the theory and observations are [56]: (1) lack of an accurate model for corrosion rate, (2) neglecting the residual strength of cover concrete after its tensile capacity is exceeded, and (3) lack of full understanding of the composition and mechanical properties of corrosion products. Corrosion products can migrate away from the bar surface through open cracks and concrete pores toward the free surface.

1.2.3.2 Mechanical degradation of corroded rebar. Many researchers have investigated the effect of corrosion on the mechanical properties of steel, and stated notable reductions in yielding and ultimate tensile strengths and a significant reduction in the ultimate strain and elongation of corroded rebar. Almusallam [57] tested 6-mm and 12-mm steel bars embedded in concrete and subjected them to accelerated corrosion. Using the actual cross-sectional area, the ultimate tensile strength of steel bars was marginally reduced as the degree of steel corrosion increased. Correspondingly, the total elongation of the steel bars decreased with the increasing degree of corrosion. Apotolopoulos and Papadakis [58] studied the tensile behavior of corroded steel bars of Class BSt 420, and found that the effective yield strength remained nearly constant while the apparent yield strength and both effective and apparent ultimate strengths decreased as the corrosion rate increased. Cairns et al. [59] investigated the effect of local pitting, which was simulated by removing a section of a bar using a multifluted, hemispherical end mill with a cylindrical shank, and found that the reduction of the maximum load was proportional to the damaged area while reduction in the force at the yield point was slightly less proportional to the cross-section. Du et al. [60] experimentally studied 108 reinforcement steel bars, and they concluded that the residual yield strength and the ultimate strength of corroded steel bars in concrete decreased with an increasing corrosion level. Apostolopoulos et al. [61] used advanced image analysis to investigate the effects of corrosion on mechanical properties and pit depths on B500c steel bars embedded in concrete. Wang et al. [62] used a three-dimensional (3D) laser scanner to determine the residual cross-sectional areas of corroded bars recently.

1.2.3.3 Bond degradation due to corrosion. Corrosion products of reinforcing steel bars occupy more space than the steel itself, exert an expansive radial pressure at the steel-concrete interface, develop the hoop tensile stress in the surrounding concrete, and therefore results in concrete cracking as the maximum hoop tensile stress exceeds the tensile strength of the concrete. Corrosion also causes the reduction in rib height of the deformed bars and the subsequent reduction of the interlocking force between the ribs and their surrounding concrete, thereby weakening the bond and anchorage between the concrete and reinforcement.

Bond behavior of corroded reinforcement bars has been experimentally studied by many researchers. Fang et al. [63, 64] investigated the effect of steel corrosion on the bond between steel bars and their surrounding concrete under confinement, and analyzed the results with the finite element method. They concluded that the confinement provided an effective means to counteract the bond loss of corroded steel bars at a medium corrosion level. Li et al. [65] studied the effect of corrosion on the bond strength between steel strands and concrete, and found that corrosion of strands in a prestressed concrete structure reduced the tensile strength of the strands more significantly than their bond strength in concrete. Tang et al. [66] investigated the effects of the concrete cover depth, bar diameter, degree of corrosion and the surface crack width on the bond strength between concrete and the corroded rebar, and found a strong correlation between the average bond strength and the average surface crack width, and an unclear relationship between the average bond strength and the degree of corrosion. Yalciner et al. [67] proposed an empirical equation for the steel-concrete bond strength considering two concrete mix designs, three concrete cover depths, and the degree of corrosion.

1.3 RESEARCH OBJECTIVES AND SCOPE OF THIS WORK

This study takes a new barrier approach to control the corrosion of steel rebar in concrete. Specifically, enamel coating will be developed and applied to steel rebar in RC structures in order to meet the societal needs for cost-effective corrosion mitigation measures. In addition, the main components in a probabilistic, corrosion-induced

deterioration model of RC structures are investigated statistically, including concrete cover cracking, steel strength reduction, and rebar-concrete bond degradation.

The main objectives of this study are (1) to investigate the corrosion-induced structural deterioration in terms of concrete cracking, mechanical property variations of corroded steel bars, and loss of the bond between steel bars and concrete, and (2) to characterize three types of enamel coatings for corrosion protection of reinforcing steel in RC structures. To achieve the main objectives, seven research tasks are designed and planned as follows:

1. Investigate corrosion-induced concrete cover cracking and its relation with the cross section loss of steel rebar,
2. Develop statistical models for various mechanical properties of corroded steel rebar,
3. Study the rebar-concrete bond degradation and degradation mechanism as a result of rebar corrosion in concrete
4. Develop new enamel coatings, evaluate the short-term corrosion resistance of enamel-coated steel plates,
5. Evaluate the long-term corrosion resistance of enamel-coated smooth rebar in 3.5wt.% NaCl solution and investigate the effect of mortar cover,
6. Study the corrosion resistance and mechanism of enamel-coated deformed rebar in 3.5 wt.% NaCl solution with and without coating damage,
7. Study the deterioration mechanism and rate of enamel-coated deformed rebar in mortar, and the effects of water cement ratio and exposure condition,

Tasks 1-3 are focused on the corrosion-induced deterioration of RC structures and address the first objective of this study. Tasks 4-7 deal with material characterization and corrosion performance of enamel-coated steel plates and bars and address the second objective.

1.4 ORGANIZATION OF THIS DISSERTATION

This dissertation consists of nine chapters. Each main chapter (2-8) will be organized as a stand-alone paper including a detailed introduction section. Chapter 1

introduces the overall objectives and scope of work in this study, literature reviews on related topics such as electrochemical corrosion test techniques, corrosion prevention methods, and corrosion-induced structural deterioration, and seven technical tasks that will be addressed in the following seven chapters. Chapter 2 is related to the corrosion-induced concrete cracking and the relationship between the mass loss of corroded steel and the change in crack width, which will be submitted to *Magazine of Concrete Research* (journal). Chapter 3 deals with the reductions in mechanical properties and ductility of corroded steel rebar in terms of yield strength, ultimate strength, and elongation, which will be submitted to *Construction and Building Materials* (journal). Chapter 4 deals with the corrosion-induced bond loss between concrete and its reinforcing steel bar, which will be submitted to *Cement and Concrete Research* (journal). Chapter 5 deals with the development and application of three types of enamel coating in structural steel and their electrochemical characteristics in simulated concrete pore solution with different chloride concentrations, which has been published in *Electrochimica Acta* (journal). Chapter 6 deals with the corrosion resistance of three types of enamel coating applied on smooth steel rebar that was embedded in mortar cylinder and then immersed in 3.5 wt% NaCl solution for 173 days, which has been published in *Cement and Concrete Composites* (journal). Chapter 7 studies the corrosion rate and mechanism of three types of enamel coating applied on deformed steel rebar in 3.5 wt% NaCl solution, which has been published in *Corrosion Science* (journal). Chapter 8 studies the deterioration mechanism and rate of three types of enamel coating applied on deformed steel bar embedded in mortar cylinder in 3.5 wt.% NaCl solution for 244 days, which will be submitted to *Corrosion Science* (journal). The main research outcomes, findings, and future studies are summarized in Chapter 9.

2. CORROSION-INDUCED CONCRETE COVER CRACKING

2.1 INTRODUCTION

Reinforced concrete (RC) structures often suffer from damage due to reinforcement steel corrosion that is caused by either carbonization or chloride contamination in concrete [68-70]. The main visual indicator of corrosion presence is the cracking of concrete cover in combination with rust stains. Generally, excessive cracks appear before corrosion has any significant influence on the strength of structures [71, 72]. As a result, the time for structural repair/replacement due to corrosion is usually controlled by the serviceability limit state associated with corrosion-induced cracking of the concrete cover.

Cracks are very small immediately after their initiation, and generally do not represent any immediate effect on the serviceability of a RC structure. However, they can accelerate the structural deterioration due to the exposure of steel reinforcement to environmental factors such as moisture and oxygen. Once cracked, the concrete cover becomes softer than un-cracked. As such, the widening of crack will not be strongly correlated to the corrosion level [73, 74]. The overall relationship between concrete cracks and steel corrosion is strong in the initiation stage, and gradually becomes weak in the propagation stage. This trend of crack width development makes it difficult to evaluate structural performance based on the corrosion-induced crack width.

Both laboratory and field tests have been performed to investigate corrosion-induced concrete cracking behaviors using empirical and analytical models [75-78]. Most of the investigations are focused on the initiation of cracking from the penetration of aggressive chemical to the onset of cracks in concrete cover, instead of the propagation stage of cracks. A few researchers studied the relationship between corrosion level and crack width [79-81]. However, the established relationship was applicable at low corrosion level for a single crack without taking into account the interaction between multiple cracks along the length of steel rebar. The effects of corrosion on structural behaviors such as the time of cracking initiation and crack width are non-uniform in

space due to non-homogeneity of concrete itself and other causative parameters such as corrosion environments.

This study aims to statistically investigate the propagation of corrosion-induced concrete cracks in RC blocks. The effect of rebar corrosion on the spatial distribution of concrete cracks over time was considered as a random field in spatial-temporal space. Concrete cover was the main parameter to consider in this study. Block specimens were tested in a corrosion bath filled with sands that were kept in moisture and salty environments. All steel bars in the block specimens were subjected to a constant electrical potential in accelerated corrosion tests.

2.2 EXPERIMENTAL PROCEDURE

2.2.1 Materials and Specimens. The steel bars (Grade 60) tested in this study have a diameter of 19.1 mm, and their chemical composition was determined and listed in Table 2.1. The yield and ultimate strengths of the steel bars are 420 MPa and 620 MPa, respectively.

Table 2.1 Chemical composition of steel rebar

Element	C	Si	Mn	P	S	Cr	Mo	Ni	Co	Cu	V	Sn	Fe
Wt.%	0.38	0.18	1.00	0.12	0.06	0.10	0.07	0.20	0.01	0.37	0.02	0.03	97.40

To consider the randomness of corrosion effects along the length of steel bars, two types of specimens were prepared and tested: 279.4 mm × 228.6 mm × 508 mm concrete blocks and 127 mm × 228.6 mm × 508 mm concrete blocks. A total of 32 concrete blocks were casted for corrosion tests: 16 large specimens and 16 small specimens. As shown in Figure 2.1, each large concrete block has 8 parallel pieces of 457 mm long steel bars through the 279.4 mm concrete with a middle 203 mm of the steel bars exposed to a corrosive environment. As shown in Figure 2.2, each small concrete block has 8 parallel pieces of 305 mm short steel bars through the 127 mm concrete with

a middle 50.8 mm of the steel bars exposed to a corrosive environment. For each type of specimens, four concrete cover thicknesses were considered: 25.4 mm, 38.1 mm, 50.8 mm, and 63.5 mm as shown in Figure 2.3.

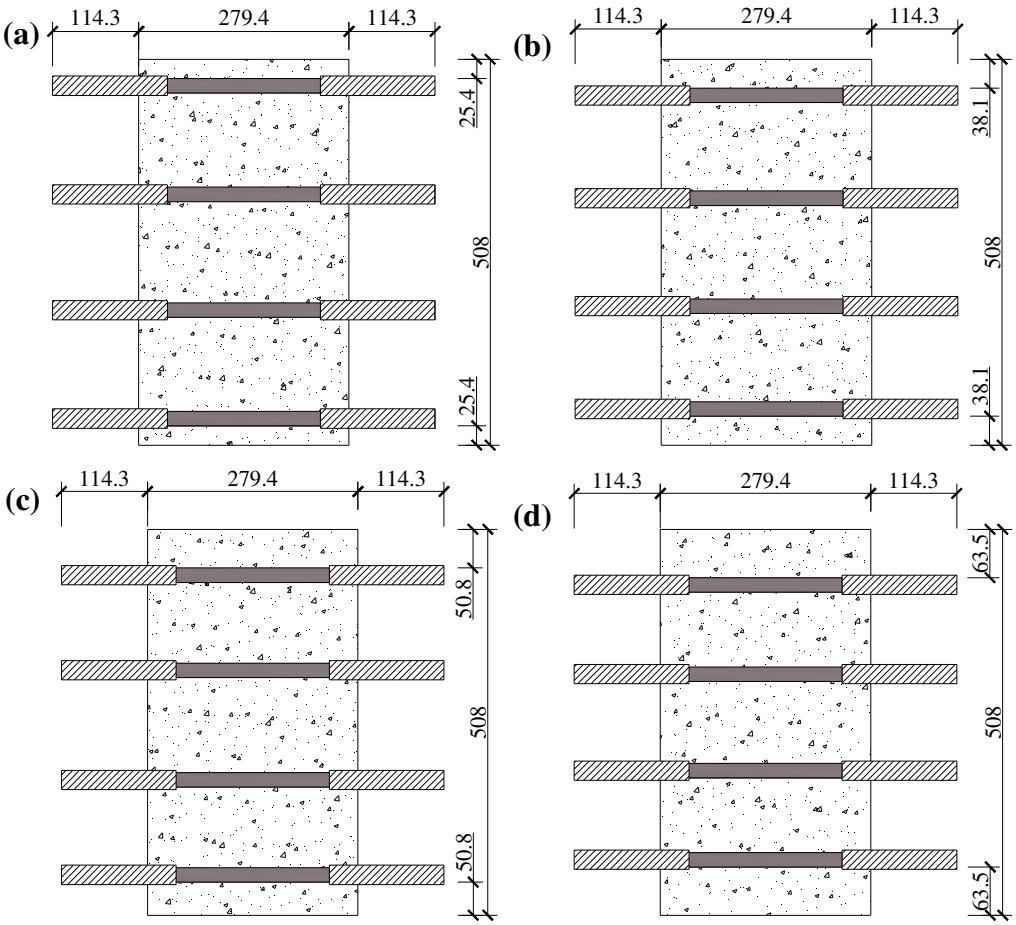

Figure 2.1 Side views of large concrete blocks with four concrete cover thicknesses: (a) 25.4 mm, (b) 38.1 mm, (c) 50.8 mm, and (d) 63.5mm (unit: mm).

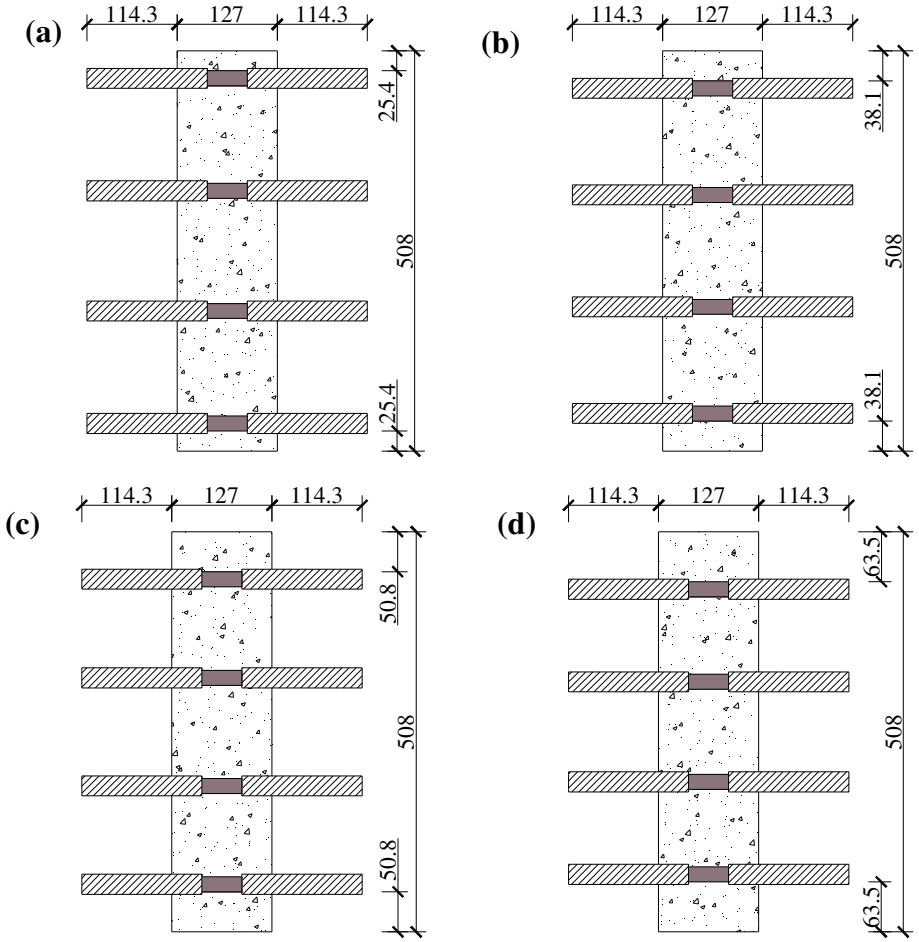

Figure 2.2 Side views of small concrete blocks with four concrete cover thicknesses: (a) 25.4 mm, (b) 38.1 mm, (c) 50.8 mm, and (d) 63.5mm (unit: mm).

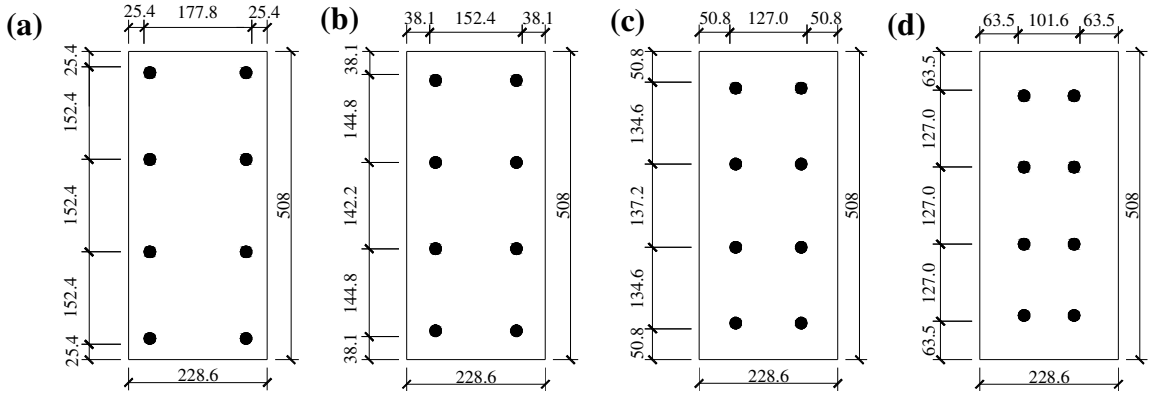

Figure 2.3 Cross section views of concrete blocks with four concrete cover thicknesses: (a) 25.4 mm, (b) 38.1 mm, (c) 50.8 mm, and (d) 63.5mm (unit: mm).

To reduce the effect of crevice corrosion at the end of a steel bar in concrete, each end of the steel bar was encased in a PVC pipe filled with epoxy resins as shown in Figure 2.4 so that only the middle portion was subjected to corrosion. A copper wire was welded at one end of the rebar and connected to an external power supply.

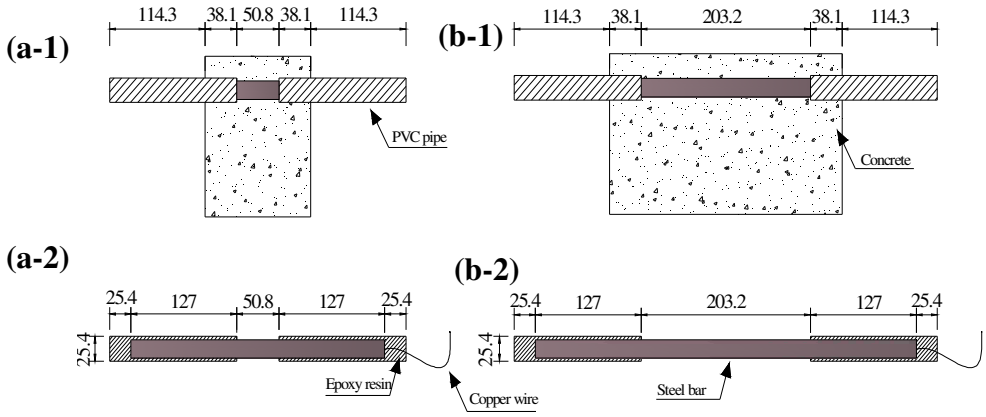

Figure 2.4 Details of short steel bars (a-1, a-2) and long steel bars (b-1, b-2) (unit: mm).

The concrete used in this study was prepared with cement, coarse aggregates, fine aggregates and tape water. Type I Portland cement was used, and its chemical composition is listed in Table 2.2. Limestones with a maximum diameter of 19 mm were used as coarse aggregates, and river sands with a fineness modulus of 2.78 were used as fine aggregates. The water-cement ratio is 0.45 with no admixtures. The compressive 28-day strength of concrete was determined with standard concrete cylinder tests to be 38.58 MPa.

Table 2.2 Chemical composition of Type-I Portland cement (wt. %).

Loss on ignition	SiO_2	Al_2O_3	CaO	MgO	SO_3	Na_2O	K_2O	Cl	TiO_2	Fe_2O_3	P_2O_5	Total
3.98	19.48	6.80	55.35	3.32	4.35	2.39	1.00	0.02	0.20	2.18	0.19	99.27

For the casting of concrete, two molds were built with plywoods as shown in Figure 2.5. Each of the two long sides of plywoods has 8 holes with a diameter of 28.6 mm to accommodate the 8 steel bars encased in PVC pipes at both ends. The void between the plywood holes and the PVC pipes was sealed with silicon resins. Before casting, a layer of oil was applied to avoid water penetration to the plywood during and after casting of concrete.

(a)  **(b)** 

Figure 2.5 Plywood molds for: (a) small concrete block, and (b) large concrete block.

2.2.2 Accelerated Corrosion Test. All the concrete blocks were placed in a corrosion bath established with wet sands, as shown in Fig. 2.6(a). 3.5 wt% NaCl water was sprayed weekly on the sands to provide moisture and chloride ions in corrosion tests. The two sides of each specimen were in contact with wet sands to test the effect of various concrete cover thicknesses. To accelerate the corrosion of steel bars, direct current with a constant electrical potential was applied on the steel bars embedded in concrete using an external power supply. As schematically illustrated in Figure 2.6(b), each steel bar and a graphite rod with a diameter of 6.35 mm were respectively connected to the positive and negative ends of the power supply. To monitor the electrical current through the steel bar and ultimately the loss of steel cross section, one 10 ohm resistor was added to the electrical circuit in between the graphite rod and the power supply. The voltage of the resistor was recorded with a DataLogger 880 system to monitor and used to determine the electrical current applied.

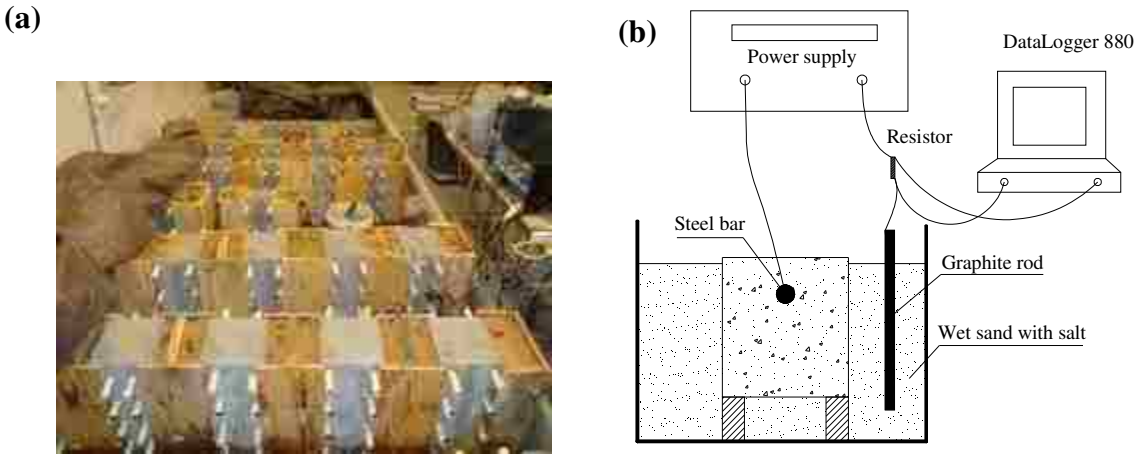

Figure 2.6 Accelerated corrosion test: (a) corrosion bath, and (b) test setup.

After the power supply was turned on, the current flowing through each steel bar was recorded at a 1 min. interval. The amount of corrosion in terms of mass loss is related to the electrical energy consumed, which is a function of voltage, amperage, and time interval. The amount of corrosion can be estimated from the following equation:

$$\Delta m = \frac{MIt}{zF} \tag{2.1}$$

where Δm is the mass of steel consumed (g), M is the atomic weight of the metal (56 g for iron), t is the time in seconds, z is the ionic charge (2 for iron), and F is a constant (96,500 coulombs/equivalent).

2.2.3 Crack Width Measurement. At specified corrosion levels, photos were taken on the top of each test specimen with a crack width meter as the scale as shown in Figure 2.7. The images were processed in AutoCAD 2010 to determine the widths of concrete cracks along the length of steel bars every 1.0 mm.

Figure 2.7 Typical corrosion-induced cracks on the concrete surface with a crack meter.

2.3 RESULTS AND DISCUSSION

2.3.1 Concrete Cracking. At the end of accelerated corrosion tests, two types of cracks were observed on all the test specimens. For the side steel bars through the middle portion of concrete blocks, one crack appeared through the concrete cover as schematically indicated in Figure 2.8(a). For the corner steel bars in some concrete blocks, two cracks were present through the concrete covers on two faces as shown in Figure 2.8(b).

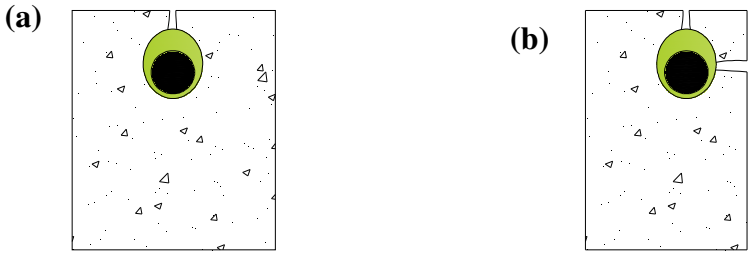

Figure 2.8 Representative concrete cracks: (a) near the side steel bar, and (b) near the corner steel bar.

Figure 2.9 exemplifies the surface cracks on the side of small and large concrete blocks at the end of corrosion tests. Cracks occurred on the side concrete cover of each corroded steel bar and penetrated through the concrete along the length of the bar. Some

corrosion products were diffused out and distributed around the cracks. However, the width of each crack seemed not uniform along its length. The crack location also varied slightly in relation to the bar location.

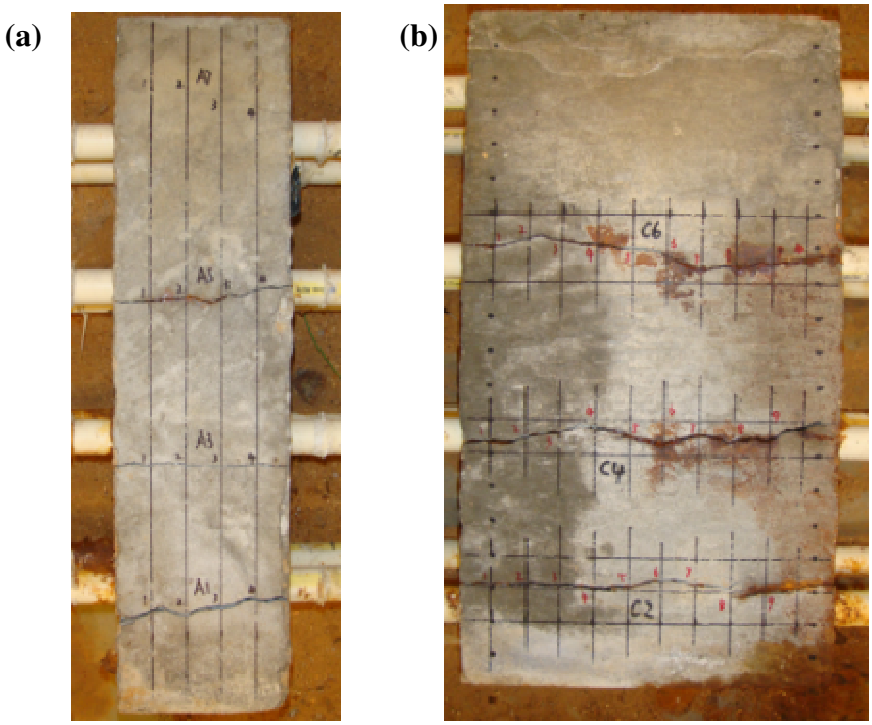

Figure 2.9 Cracks on the side of: (a) small concrete blocks, and (b) large concrete blocks after corrosion tests.

Figure 2.10 shows the cross sectional photos of cracks penetrating from the steel bar to the outer surface of concrete cover. As shown in Figure 2.10(a), the crack width decreases from approximately 1 mm near the steel bar to a hair size at the concrete surface. As indicated in Figure 2.10(b), although the steel bar already corroded to some degrees, the nearby crack did not penetrate through the concrete cover so that no visible crack was observed on the outer surface. Therefore, just because no cracks were observed on a concrete surface does not necessarily mean no corrosion in the embedded steel bar nearby.

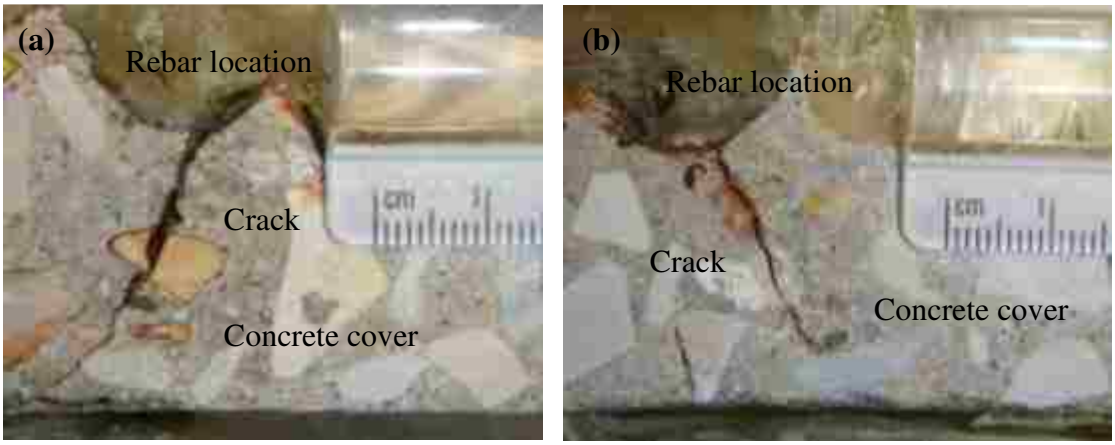

Figure 2.10 Cracks underneath concrete covers: (a) hairline crack on concrete surface, and (b) no crack on concrete surface.

2.3.2 Histograms of Crack Width. Figure 2.11 shows the typical histograms of crack width and its fitting probability density functions (PDF) of a Gaussian random variable for large and small block specimens. It can be seen from Figure 2.11 that the crack width follows a Gaussian distribution pretty well. Overall, it was observed that the Gaussian distribution is applicable to all test cases.

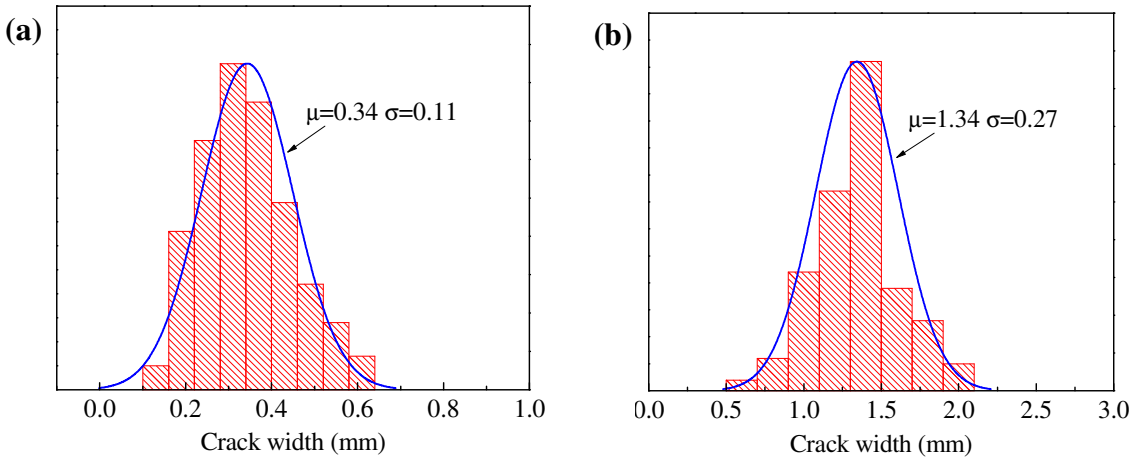

Figure 2.11 Typical histograms of crack width and fitting pdf curves for: (a, b) for small specimens, and (c, d) for large specimens.

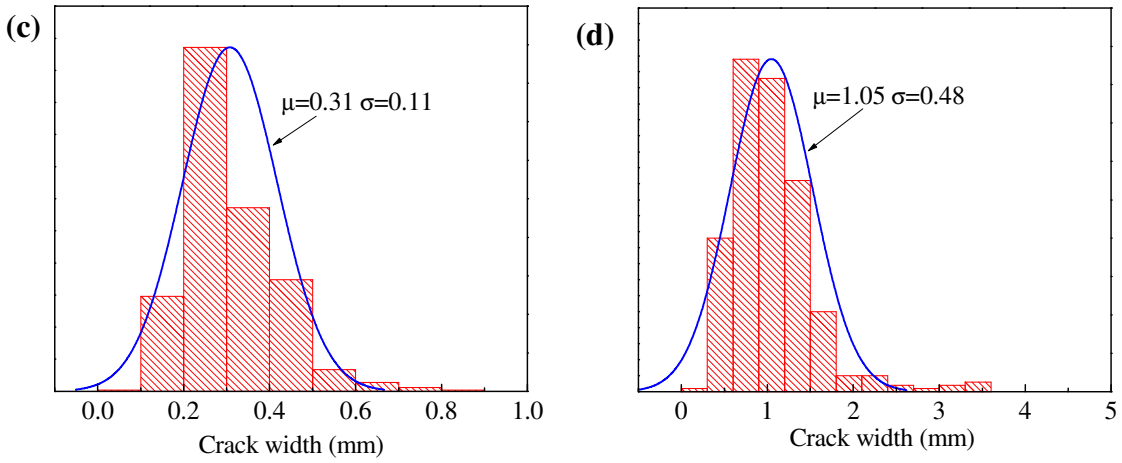

Figure 2.11 Typical histograms of crack width and fitting pdf curves for: (a, b) for small specimens, and (c, d) for large specimens. (cont.)

2.3.3 Evolution of Crack Width. Figures 2.12 and 2.13 show the PDF of crack width on the surface of large and small concrete blocks with different concrete cover thicknesses. The PDF curves were developed based on the test data obtained from multiple cracks on the specimens with the same concrete cover thickness at different corrosion levels over time. It can be clearly seen from Figures 2.12 and 2.13 that the standard deviation of crack width increased with an increase in mean value over time.

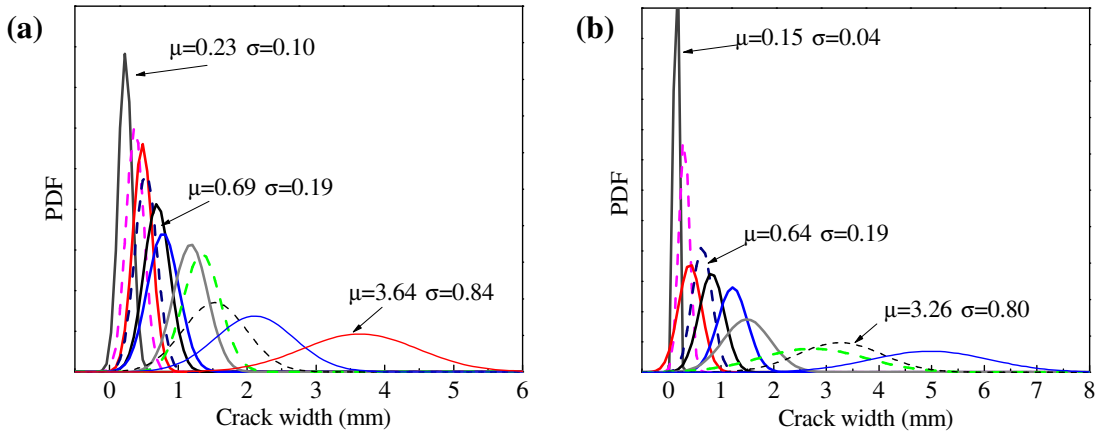

Figure 2.12 PDF evolution of crack width on small specimens with various cover thicknesses: (a) 25.4 mm, (b) 38.1 mm, (c) 50.8 mm, and (d) 63.5 mm.

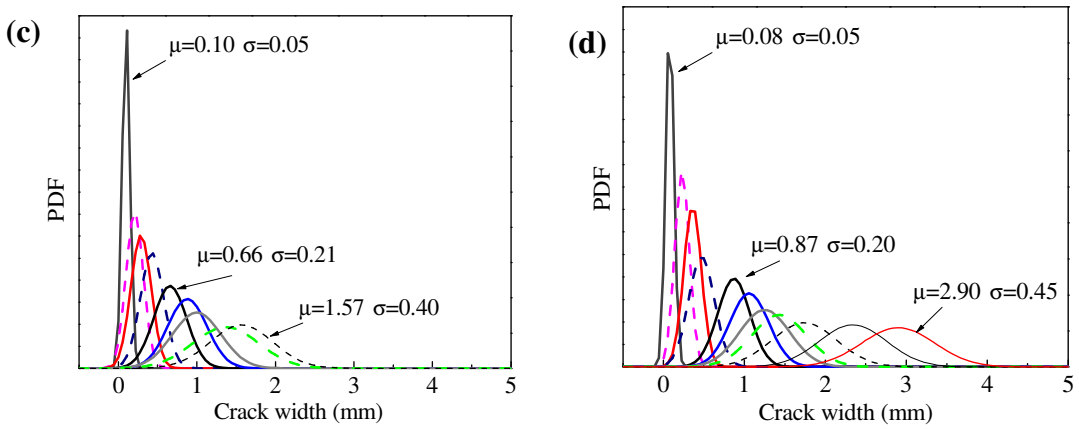

Figure 2.12 PDF evolution of crack width on small specimens with various cover thicknesses: (a) 25.4 mm, (b) 38.1 mm, (c) 50.8 mm, and (d) 63.5 mm. (cont.)

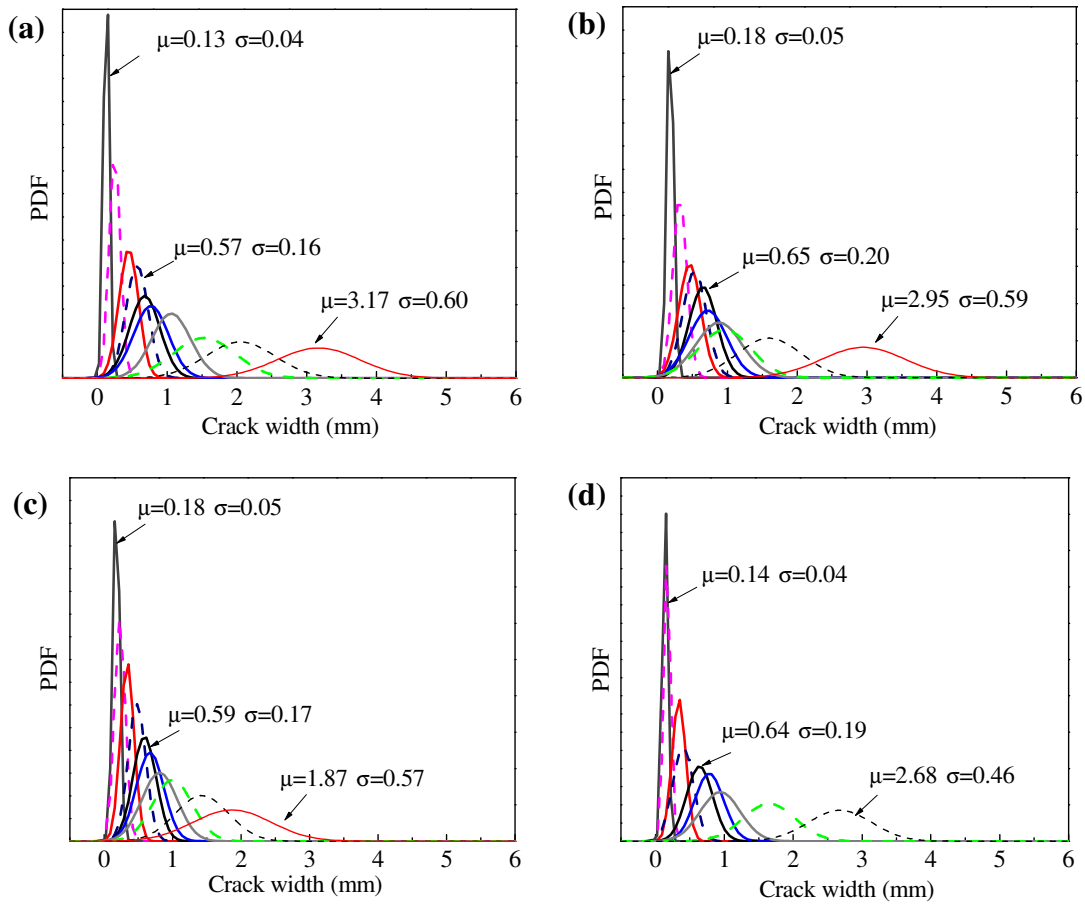

Figure 2.13 PDF evolution of crack width on large specimens with various cover thicknesses: (a) 25.4 mm, (b) 38.1 mm, (c) 50.8 mm, and (d) 63.5 mm.

2.3.4 Relationship between Mean Value and Standard Deviation of Crack Width. Figures 2.14 and 2.15 display the relationship between the mean value and the standard deviation of crack width for the small and large concrete blocks, respectively, with the given concrete cover thicknesses. Each scattered point on the plot shows the statistical property of one crack. A linear regression analysis indicated a good correlation between the mean and the standard deviation of crack width with a correlation coefficient of 0.67 to 0.90. The slopes of all the fitted straight lines are in the range of 0.147 to 0.302.

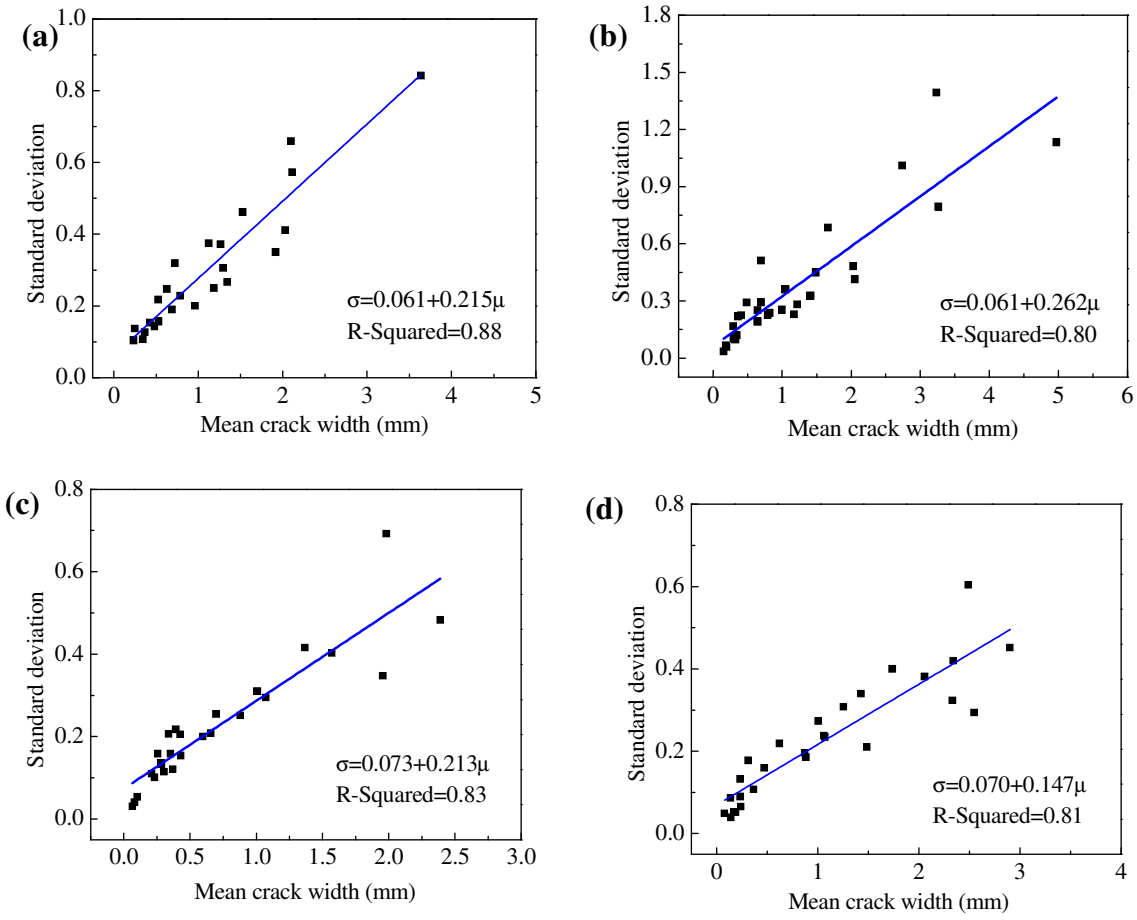

Figure 2.14 Relations between the mean value and standard deviation of crack width on small specimens with various cover thicknesses: (a) 25.4 mm, (b) 38.1 mm, (c) 50.8 mm, and (d) 63.5 mm.

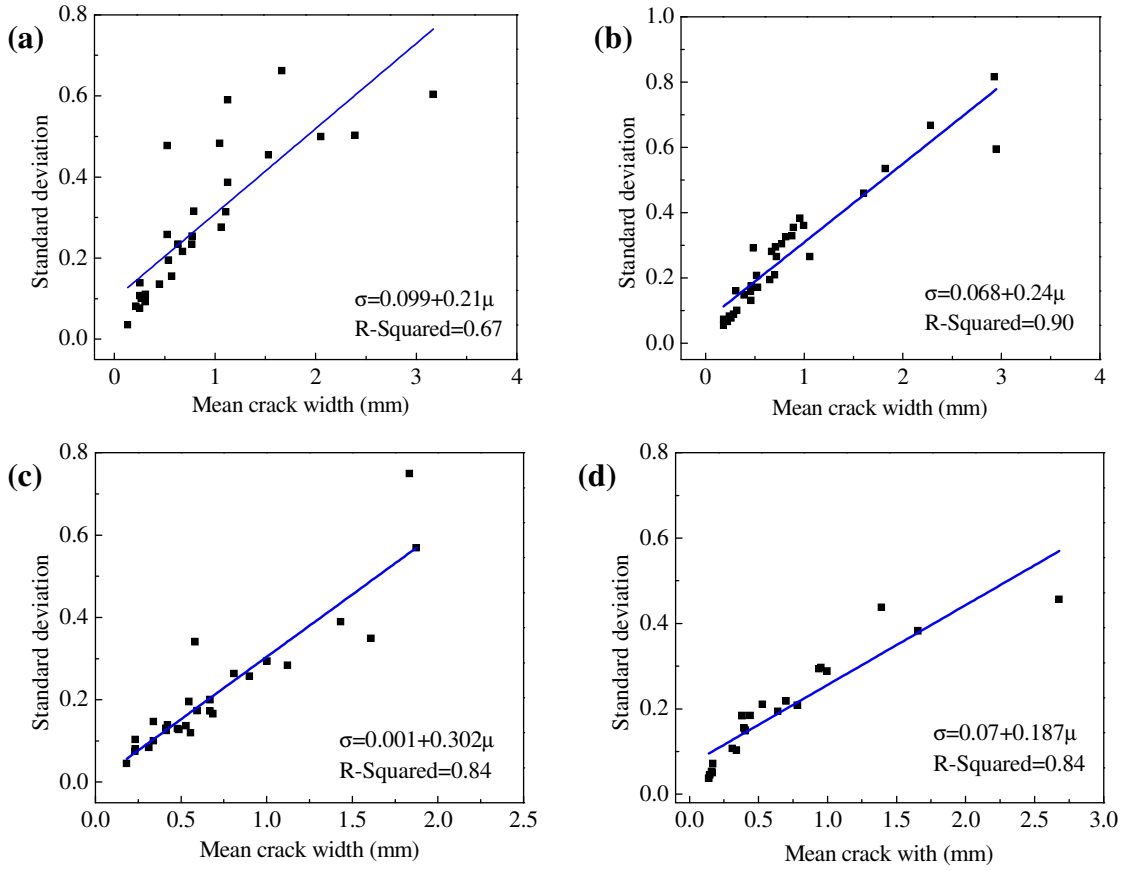

Figure 2.15 Relations between the mean value and standard deviation of crack width on large specimens with various cover thicknesses: (a) 25.4 mm, (b) 38.1 mm, (c) 50.8 mm, and (d) 63.5 mm.

2.3.5 Relationship between Crack Width and Corrosion Level. Many researchers attempted to relate the width of cracks in concrete cover with the corrosion level. For example, Alonso et al. [80] investigated the effects of concrete cover, steel bar diameter, proportions of cement, water-cement ratio, cast position of the bar, transverse reinforcement and corrosion rate on such a relationship. They concluded that the cracking process of concrete can be characterized in two distinct steps: initiation and propagation. The first visible crack was initiated after the steel bar has lost 15-50 μm in radius, and then propagated with increasing length that is proportional to the corrosion-induced loss of steel.

Figures 2.16 and 2.17 show the relationship between the mean crack width and the mean mass loss for the small and large concrete blocks, respectively, with the given

concrete cover thicknesses. A linear regression analysis revealed that the linear relationship is very weak with a correlation coefficient of 0.22 to 0.73, which is inconsistent with the previous finding by Alonso et al. [80]. The fitted straight line intersects with the vertical axis instead of the horizontal axis, indicating that cracks may occur even before corrosion has taken place. These two inconsistencies with the previous results [80] are likely attributed to the following three main reasons. First, this study takes a statistical approach and analyzes data collected under the same condition from multiple specimens and multiple cracks on each specimen while Alonso et al. [80] took a deterministic approach and was focused on one specimen and one crack location. Second, the mean crack width in this study reached a maximum of approximately 5 mm while the crack width was limited to 1 mm in [80]. Third and last, the relationship between the crack width and corrosion level is not linear particularly for large crack widths considered in this study. This is because the concrete cover becomes softened and delaminated as the crack width reaches some critical value.

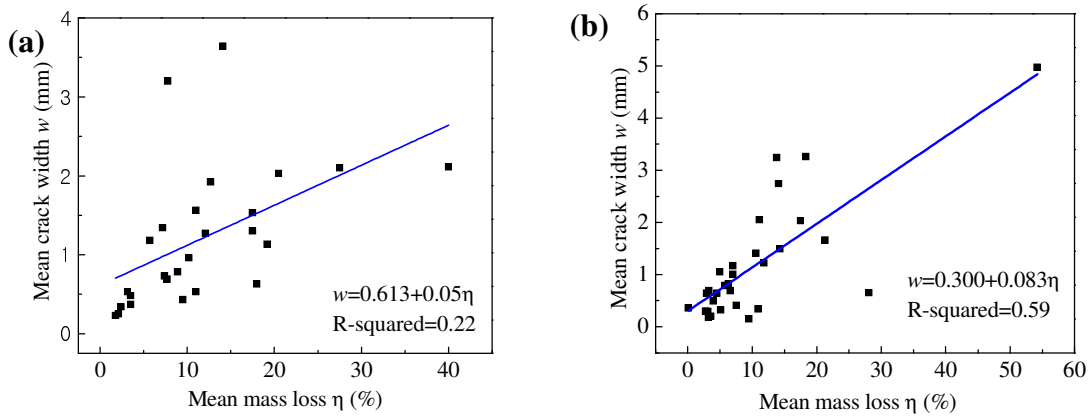

Figure 2.16 Relationship between the mean crack width and the mean mass loss of steel bars for small specimens with various cover thicknesses: (a) 25.4 mm, (b) 38.1 mm, (c) 50.8 mm, and (d) 63.5 mm.

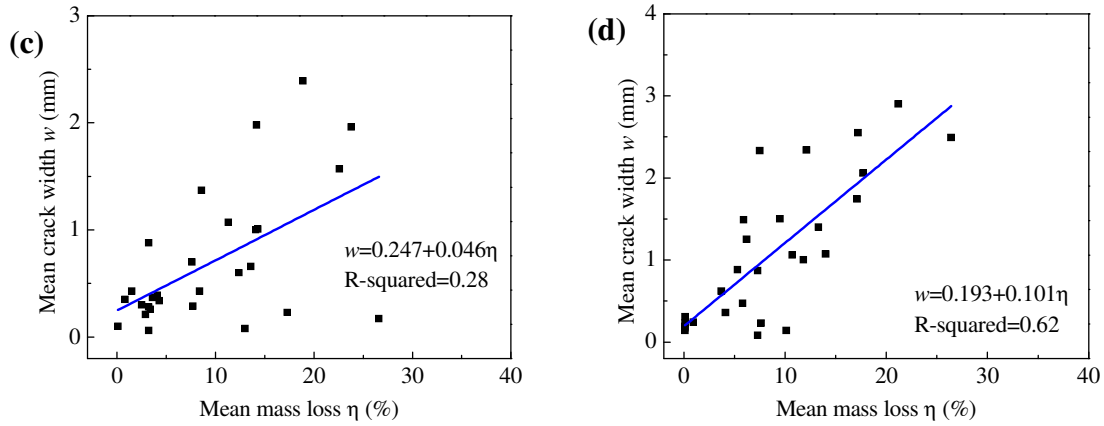

Figure 2.16 Relationship between the mean crack width and the mean mass loss of steel bars for small specimens with various cover thicknesses: (a) 25.4 mm, (b) 38.1 mm, (c) 50.8 mm, and (d) 63.5 mm. (cont.)

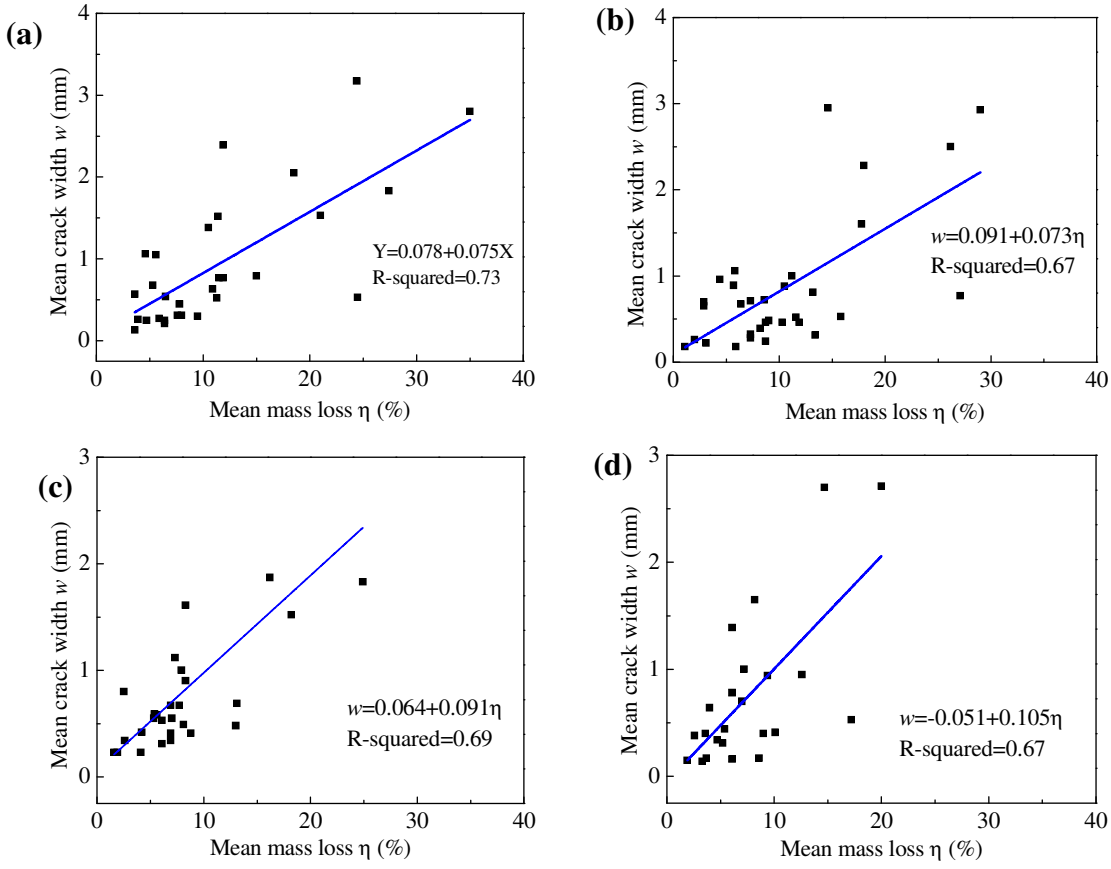

Figure 2.17 Relationship between the mean crack width and the mean mass loss of steel bars for large specimens with various cover thicknesses: (a) 25.4 mm, (b) 38.1 mm, (c) 50.8 mm, and (d) 63.5 mm.

2.3.6 PDF of Crack Width for Rebar with Two Cracks in the Corner of Specimen. Figure 2.18 shows four pairs of PDF curves, each comparing the typical distributions of two cracks around a steel bar in one of the four corners of concrete blocks with 25.4 mm concrete cover. The two comparative PDFs for each bar appear quite different in terms of their shape and mean crack width. These results further justify the need for a statistical analysis of crack widths.

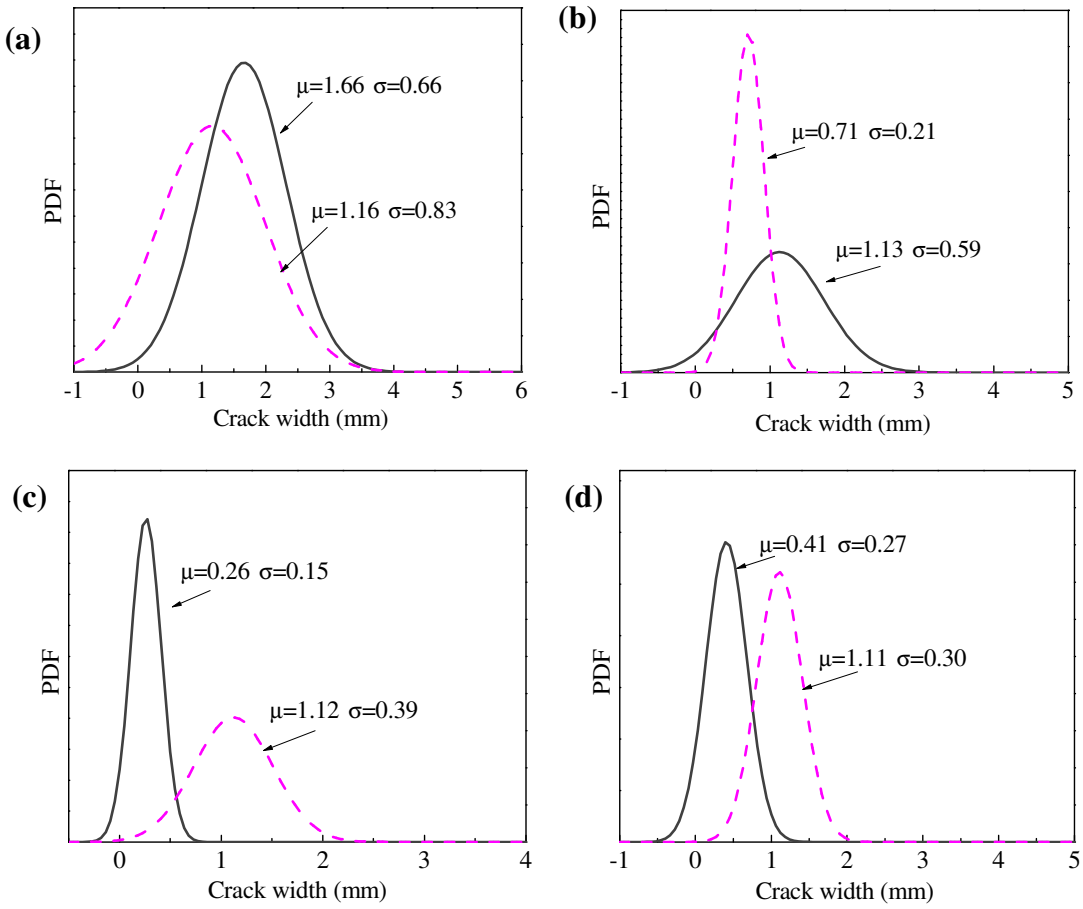

Figure 2.18 Representative PDF curves of cracks around corner steel bars in the large concrete blocks with 25.4 mm concrete cover: (a) Corner 1, (b) Corner 2, (c) Corner 3, and (d) Corner 4.

2.3.7 Crack Propagation Mechanism. Figures 2.19 and 2.20 schematically show the evolution of corrosion induced crack width over time as the corrosion level increases. In general, the crack evolution can be divided into four stages. Stage I is from the completion time of new construction to the initiation of cracking on the surface of concrete specimens. This stage takes a long time and can be further divided into three steps: penetration of carbon dioxide or chloride ions, onset of corrosion, and propagation of internal crack to the outer surface of concrete. Therefore, stage I is controlled by both the property of concrete cover itself and environmental factors such as concentrations of aggressive chemicals, moisture, and availability of oxygen. To date, most of the findings reported in the literature are limited to this stage.

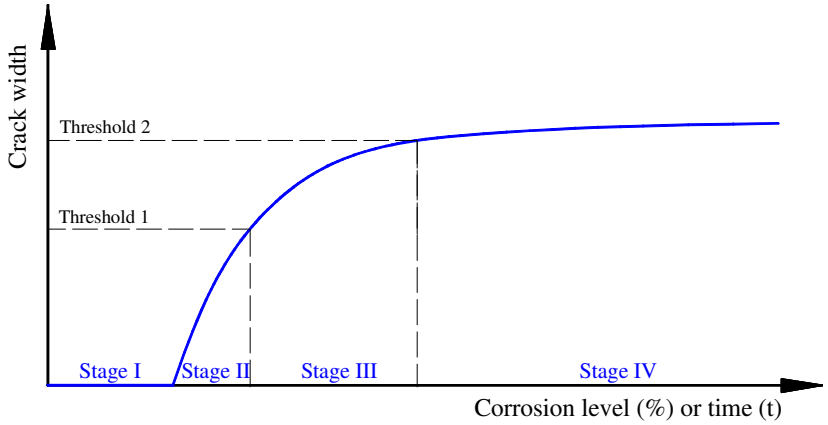

Figure 2.19 Schematic illustration of corrosion-induced concrete cracking as a function of corrosion level or time.

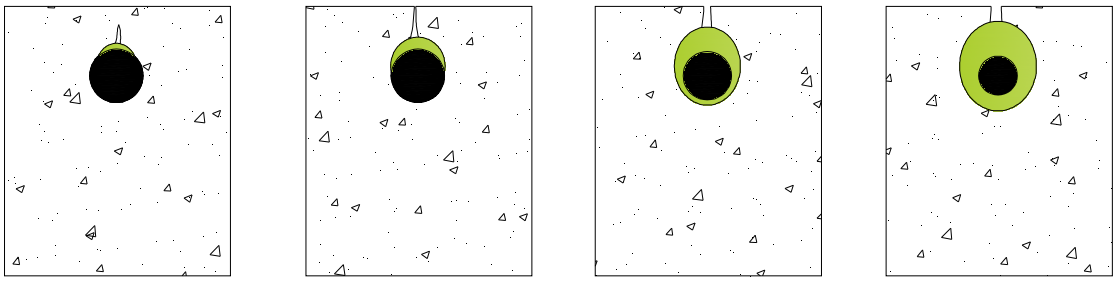

Figure 2.20 Schematic diagram of crack width development.

Stage II is from the initiation of cracking on the surface of concrete to the reach of a critical crack width referred to as threshold 1 in Figure 2.19. Threshold 1 can be defined as the deceleration of crack opening due to the softening of cover concrete. Stage III is the transition from Stage II to Stage IV, in which the crack width will increase gradually with an increase of corrosion level. Stage IV is reached when the crack width no longer increases or changes little over time. This stage is attributed to two reasons. One is that the concrete cover starts to separate from the steel bar, and the other is that the corrosion products would diffuse out of the concrete cover through the wide open crack.

As pointed out previously, the relationship between the crack width and corrosion level becomes more uncertain over time. In the initiation stage of cracking (Stage II in Figure 2.19), the crack width is strongly correlated with corrosion level because the concrete cover at that stage remains intact with the corroded steel bar. However, in the propagation stage (Stage IV in Figure 2.19), the concrete cover becomes softened and begins to lose contact with the corroded bar, and the relationship becomes less obvious.

2.4 SUMMARY

This study experimentally investigated the complete process of corrosion-induced concrete cracking as a function of corrosion level. It will thus provide new knowledge to the after-initial-crack behavior that is lacking in the literature, and potentially provide new insights to the life-cycle evaluation of reinforced concrete structures. Based on the test data and analysis, the following conclusions can be drawn:

(1) The crack widths on the concrete cover surfaces of 32 tested specimens were measured along the length of 256 steel bars and then analyzed statistically. The large data set indicated that the crack width can be well represented by a normal distribution, regardless of bar length, concrete cover thickness, and corrosion level.

(2) The standard deviation of crack width linearly increased with the mean value of crack width. Their correlation appeared strong independent of crack length and concrete cover thickness, but affected by the corrosion level over time.

(3) The relationship between the crack width and corrosion level changed significantly over time. In the initiation stage of cracking, a strong correlation was observed because the concrete cover remained intact with the corroded steel bar. As the corrosion became severe and the crack width reached a critical threshold value, their correlation became weakened due to concrete cover spalling or corrosion products diffusion through wide cracks.

3. MECHANICAL DEGRADATION OF CORRODED STEEL BAR

3.1 INTRODUCTION

Reinforcement steel in concrete structures is generally protected by a passive film formed in the alkaline environment due to the hydration product of cement [82, 83]. However, this passive film could be destroyed by ingress of aggressive ions such as chloride and carbon dioxide [84, 85]. Due to the heterogeneity of external environment and concrete cover as well as the spatial variation of the cover thickness, the breakdown of this passive film on the surface of reinforcing steel bars is not uniform along the rebar length, resulting in local pitting corrosion. Corrosion pits reduce the cross section of steel rebar locally, resulting in stress concentration and significantly degrading the structural performance [86-88]. With further penetration of aggressive ions, more corrosion pits would form and propagate randomly along the surface over time. Therefore, corrosion of reinforcement steel in RC structures is generally a random/stochastic field problem with probabilistic temporal and spatial distributions. This randomness increases the failure probability of corroded RC members as the corroded rebar may fail at cross sections that are not subjected to the maximum load.

The irregular shape of corrosion pit formed on the steel bar surface makes it difficult to accurately measure the loss of cross section. One conventional method is to compare the difference of steel bar weight before and after corrosion, and the mass loss was used as the only parameter to quantify the corrosion level [89-91]. However, this method is not scientific due to the random distribution of corrosion pits (size and location) on the steel bar. Corrosion pits could also be measured using a caliper [92]. However, there is no easy way to calculate the area loss based on these data, which is sometimes overestimated because this method could not measure the corrosion pit when curved down from the rebar surface. Other researchers tried to cut the corroded steel bar into many small pieces, and then measured the mass of each piece to determine the non-uniformity of corroded cross section [93-95]. Apostolopoulos et al. [61] used image analysis technique to determine the size of corrosion pits. Recently, a 3-D laser scanner was used to determine the depth of corrosion pits; it proved to be a relatively more

precise measurement than other conventional methods [62]. With the aid of 3D scanner, any required physical dimensions, such as pit depth, cross-sectional area loss and weight loss could be measured precisely and conveniently.

In the literatures, the spatial variation of the cross-sectional area of corroded rebar can be quantified either by the pitting factor $R_p=p_{max}/p_{avg}$ or the cross-sectional spatial heterogeneity factor $R= A_{avg}/A_{min}$, where p_{max} and p_{avg} are the maximum and average penetration depths of corrosion pits, respectively, A_{min} and A_{avg} are the minimum and average cross-sectional areas of corroded rebar, respectively. Previous researchers showed that the average value of R_p ranged from 4.0 to 23.8 [96, 97]. Stewart et al. [98, 99] and Zhang et al. [100] proposed that R_p can be characterized by the Gumbel distribution. However, these two mathematical descriptions on the variation of steel bar geometry are either oversimplified (pitting factor) or too complicated (cross-sectional spatial heterogeneity factor).

This study aims to (1) compare two methods of characterization for the cross-sectional area loss of steel rebar due to corrosion and (2) reevaluate the mechanical properties of corroded steel rebar. The two methods include a conventional gravimetric analysis and a geometric analysis based on 3D laser scanner data. Moreover, a critical cross section with the minimum area will be identified and used as an indicator for mechanical properties degradation. The relationships among yield strength, ultimate strength, and elongation will be reevaluated based on the critical cross section.

3.2 EXPERIMENTAL PROCEDURE

3.2.1 Specimen Preparation. The steel bar used in this study had a diameter of 19.05 mm, and its chemical composition was determined and listed in Table 3.1. The yield and ultimate strengths of the steel bar are 420 MPa and 620 MPa, respectively.

Table 3.1 Chemical composition of steel rebar

Element	C	Si	Mn	P	S	Cr	Mo	Ni	Co	Cu	V	Sn	Fe
Wt.%	0.38	0.18	1.00	0.12	0.06	0.10	0.07	0.20	0.01	0.37	0.02	0.03	97.40

Eight pieces of steel rebar were embedded in each 228.6 mm×279.4 mm×508 mm concrete block as shown in Figure 3.1. To reduce the effect of crevice corrosion at the intersection of steel bar and concrete, each end of the rebar was encased in a PVC pipe filled with epoxy resin so that only the middle portion was subjected to corrosion, as shown in Figure 3.2. To have an electrical connection with external power supply, a copper wire was welded at one end of the rebar. A total of 32 specimens were prepared in this study.

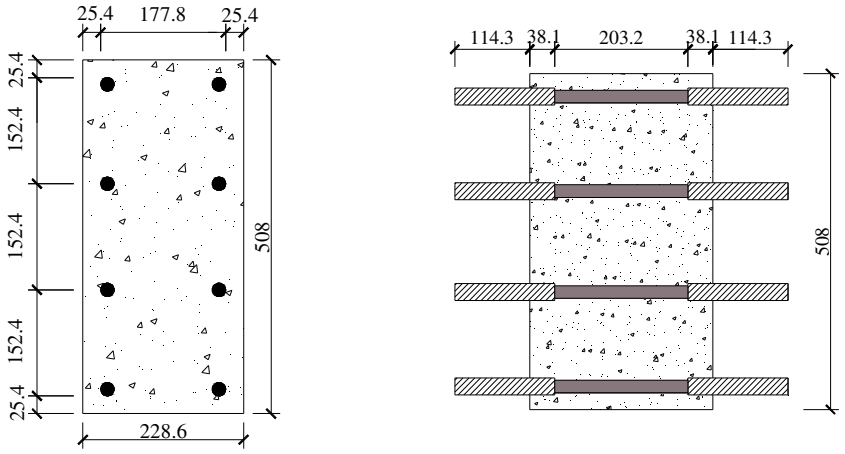

Figure 3.1 Dimensions of concrete block specimen (unit: mm).

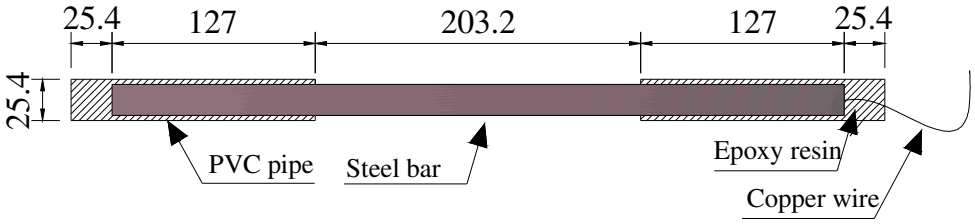

Figure 3.2 Details of steel bar (unit: mm).

The concrete used in this study was a mixture of Portland cement, coarse aggregates, fine aggregates, and tap water with a ratio of 1:1.47:3.29:0.45 by weight. Type I Portland cement was used, and its chemical composition is listed in Table 3.2. Limestone with a maximum diameter of 19 mm was used as coarse aggregates, and river

sands with a fineness modulus of 2.78 were used as fine aggregates. The water cement ratio is 0.45 with no admixtures. The 28-day compressive strength of concrete was determined to be 38.58 MPa with standard concrete cylinder tests.

Table 3.2 Chemical composition of Type-I Portland cement (wt. %).

Loss on ignition	SiO_2	Al_2O_3	CaO	MgO	SO_3	Na_2O	K_2O	Cl	TiO_2	Fe_2O_3	P_2O_5	Total
3.98	19.48	6.80	55.35	3.32	4.35	2.39	1.00	0.02	0.20	2.18	0.19	99.27

Figure 3.3 Mold to cast concrete block.

For the casting of concrete, plywood molds were built as shown in Figure 3.3. Sixteen holes with a diameter of 28.6 mm were drilled in two side plywoods at the location of steel bars. After that, silicon resins were applied to seal the void between the plywood hole and the encasement PVC pipe. Before casting, a layer of oil was applied to avoid water penetration to the plywood during and after casting of concrete.

3.2.2 Accelerated Corrosion Test. All the concrete blocks were placed in a corrosion bath established with wet sands, as shown in Figure 3.4(a). To accelerate reinforcement corrosion, direct electric current was impressed on the steel bar embedded in concrete using an external power supply that provides a constant electrical potential. The steel rebar was connected to the positive end, while a graphite rod was connected to

the negative end of the power supply as schematically shown in Figure 3.4(b). The specimens were placed side by side and the space between them was filled with sands flush with the top face of specimens. To create a corrosion environment, 3.5 wt% NaCl solution was sprayed weekly on the sands to provide moisture and chloride ions. In order to monitor the electrical current through the steel bar, one 10 ohm resistor was connected in the circuit. The voltage of the resistor was recorded with a DataLogger 880 system and the electrical current was determined.

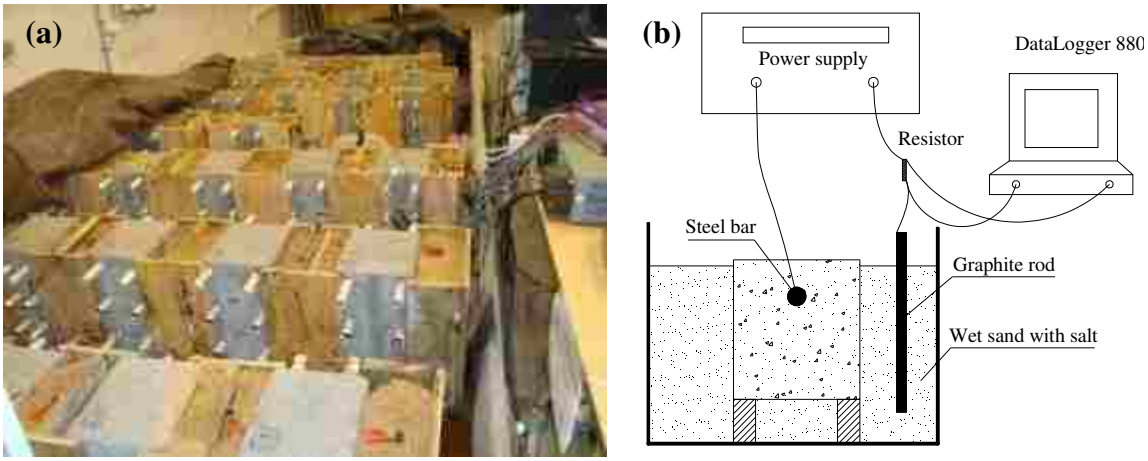

Figure 3.4 Accelerated corrosion test setup: (a) corrosion bath, and (b) electrical circuit to accelerate corrosion.

3.2.3 3D Laser Scan. After the accelerated corrosion test, the corroded bars were taken out of the concrete specimens and then sand blasted to remove the attached concrete debris and corrosion products. After cleansing, all the surface morphology was measured using a 3D laser scanner (see Figure 3.5) to determine the remaining cross section, and the 3D coordinates of each point on the surface of the corroded rebar were acquired. Data not belonging to the corroded rebar were cleansed by ScanStudio software to get cleaner point cloud files with a higher signal-to-noise ratio of the data. The acquired 3D point cloud data were processed using ImageWare software to get the boundary of the cross sections of corroded steel rebar.

Figure 3.5 3D laser scanning of deformed steel bar.

3.2.4 Tensile Test Setup. The tensile tests were conducted on the MTS880 testing machine, as shown in Figure 3.6 (a). An extensometer with an effective range of 50 mm was attached to the most probable failure zone where the severest corrosion was observed on each corroded rebar. The applied load and deformation within the gauge length were recorded using an automatic data sampling and processing system. The test results were used to calculate the stress in the test specimen.

To further measure the total elongation of a corroded bar, two steel collars as shown in Figure 3.6(b) were made and attached at the two ends of the corroded portion. One collar supported a plastic pulley with its axle welded onto the side of steel collar and the other collar supported a screw by welding. During tests, a soft and strong copper wire went through the pulley and the screw fixed on the two steel collars and was then connected to a strain port to measure the elongation of the corroded rebar between the two steel collars. To ensure a good contact with the bar under testing, particularly when a significant load is applied, several layers of plastic adhesive tapes were wrapped around the steel bar at the location of steel collars as shown in Figure 3.6(b), and a threaded steel rod was then screwed through each steel collar against the plastic tapes.

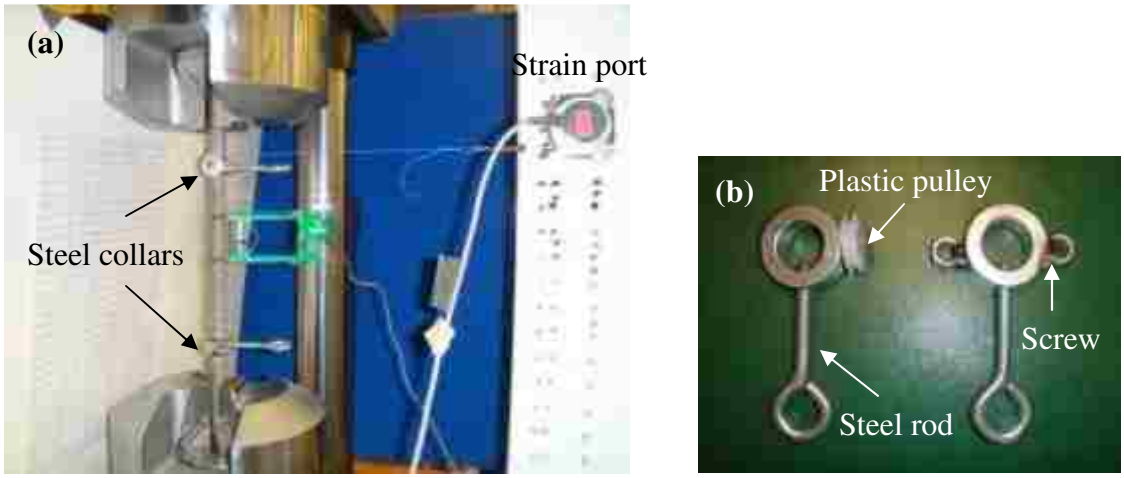

Figure 3.6 Tensile tests: (a) setup, (b) two steel collars mounted on steel bar.

3.3 RESULTS AND DISCUSSION

3.3.1 Histograms of Cross Sectional Area of Corroded Rebar. Figure 3.7 shows the scanned 3D images of one uncorroded (reference) and two corroded steel bars. Figure 3.7(a) indicates a uniform reference bar. Figures 3.7(b, c) clearly show that the corrosion-induced mass loss was not evenly distributed both around the circumference and along the length of the steel bar. In particular, the corroded steel bar as shown in Figure 3.7(c) had two large corrosion pits at its two ends, which is likely attributed to the crevice corrosion at the intersection of steel bar and PVC pipe. This case is referred to as the non-uniformly corroded bar. In Figure 3.7(b), the corrosion pits had similar sizes and almost evenly distributed along the length of the steel bar. This case is thus referred to as the almost uniformly corroded bar.

The distributions of their cross-sectional area along the length of the steel bars are plotted in Figure 3.8. For the uncorroded steel bar, a very good and consistent pattern was observed along the length of the bar. The valleys and peaks in the black and solid line in Figure 3.8 represent the minimum cross section between two ribs and the cross section through a rib. For the almost uniformly corroded steel bar, the cross-sectional area fluctuated around a certain average value. However, for the non-uniformly corroded bar, two distinct valleys appeared near its two ends. The plots in Figure 3.8 are very consistent with their corresponding 3D images in Figure 3.7.

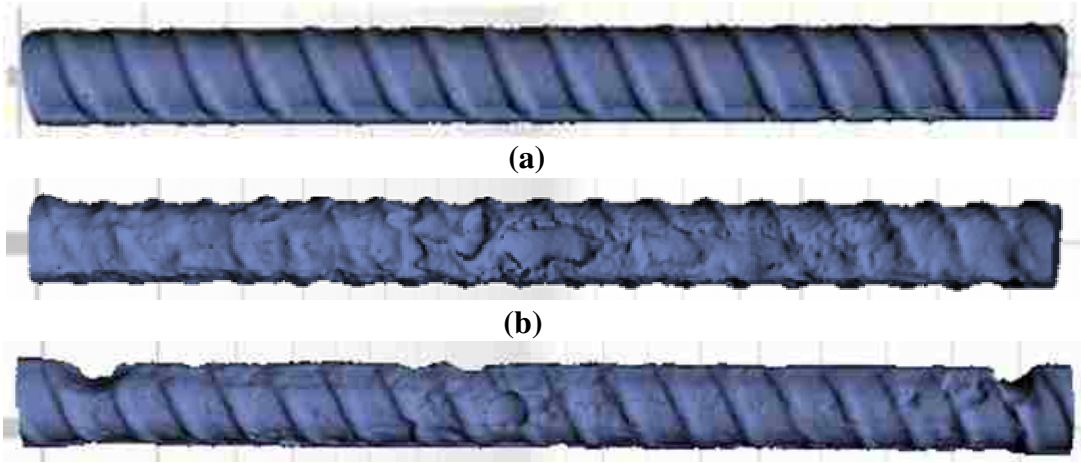

Figure 3.7 3D images of: (a) uncorroded, (b) almost uniformly corroded, and (c) non-uniformly corroded steel bar.

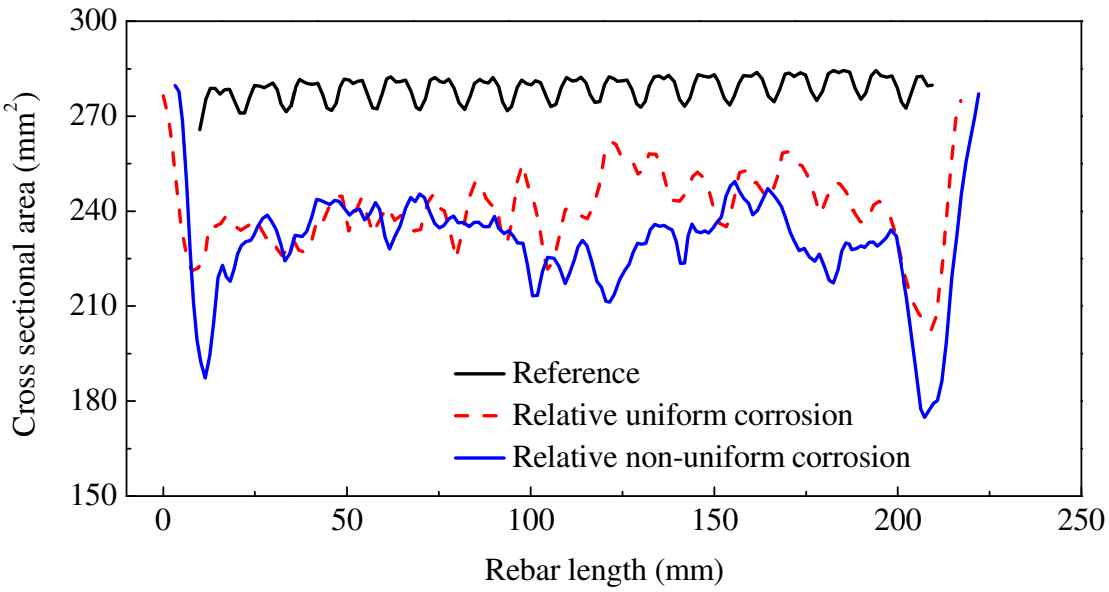

Figure 3.8 Distribution of cross sectional area along the rebar length of: (a) uncorroded (reference), (b) almost uniformly corroded, and (c) non-uniformly corroded steel bar.

The histograms of the cross-sectional area of the uncorroded and corroded steel bars in Figure 3.7 are plotted in Figure 3.9. It can be seen from Figure 3.9 that a bimodal distribution for the uncorroded steel bar seems reasonable, considering the effect of rebar

ribs. The mean areas are 282 mm^2 and 275 mm^2 for the cross sections near ribs and between two ribs, respectively. For the almost uniformly corroded bar, the histogram seems like a normal distribution since the original ribs were smoothed out in the corrosion process and the corrosion pits were not significant. For the non-uniformly corroded bar, two peaks appeared in the cross section histogram. The first peak in the small area represents the average area of the sections with large pits, and the second peak in the large area represents the average area of the sections without large pits. Therefore, a bimodal distribution is a better fit for corroded steel bars with large corrosion pits.

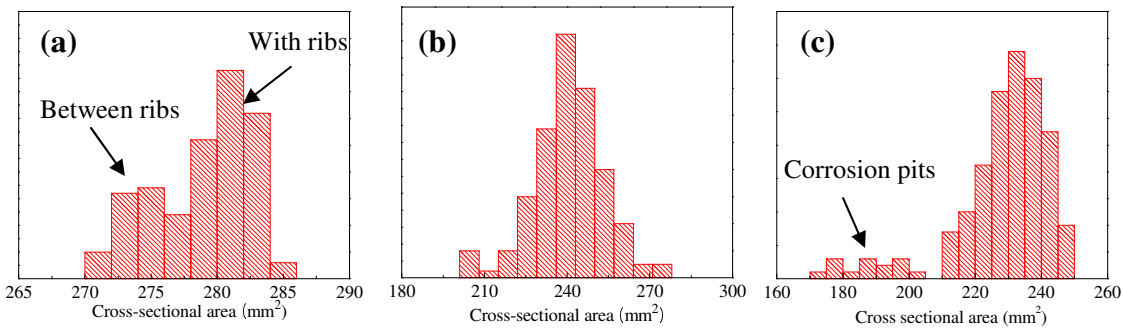

Figure 3.9 Histograms of: (a) the uncorroded, (b) almost uniformly corroded, and (c) non-uniformly corroded steel bar.

Figure 3.10 shows some typical cross sections of the uncorroded (a-1, a-2, a-3), almost uniformly corroded (b-1, b-2, b-3), and non-uniformly corroded (c-1, c-2, c-3) steel bars. The deformation and two ribs can be seen on the uncorroded steel bar. For the corroded steel bars, corrosion pits with various shapes and sizes can be observed.

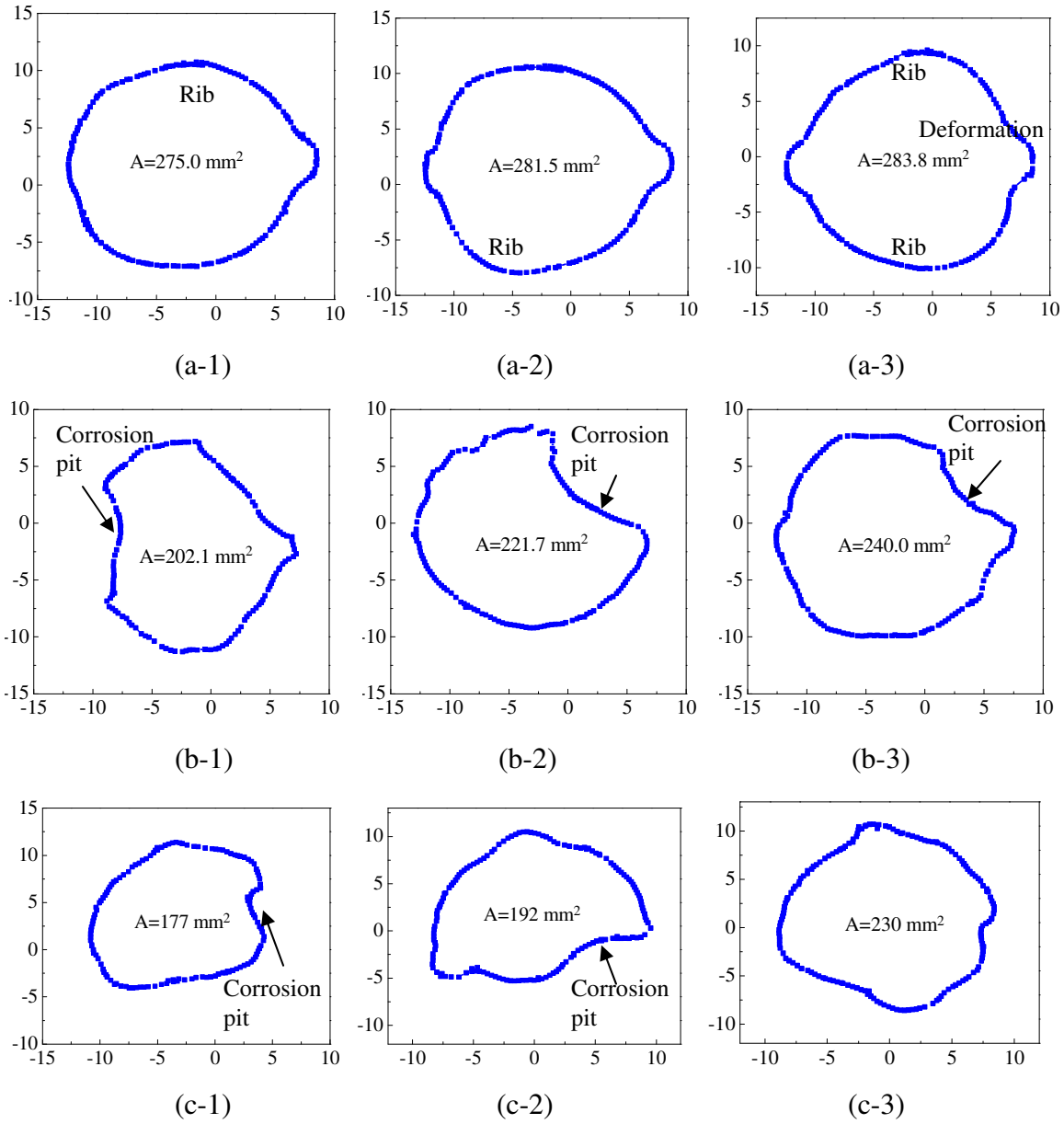

Figure 3.10 Cross sections of: (a-1, a-2, a-3) for the uncorroded, (b-1, b-2, b-3) for almost uniformly corroded, and (c-1, c-2, c-3) for non-uniformly corroded steel bar (unit: mm).

Figure 3.11 shows the probability density functions (PDF) of residual cross section area of nine representative corroded steel bars as a function of corrosion area loss. These curves were obtained by fitting the PDF of a Gaussian random variable into the histograms based on the mean and standard deviation of measured residual cross section areas. The mean and standard deviation of the residual cross section area are specified in

Figure 3.11, together with the average area loss in percentage. Obviously, the standard deviation increased with an increase of corrosion level (area loss). This indicated that the more severe the corrosion, the more non-uniform the corrosion effect.

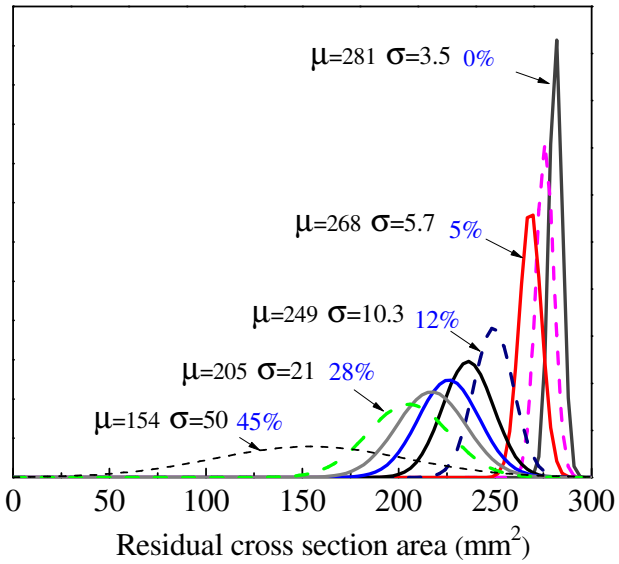

Figure 3.11 PDF curves of the residual cross section area of corroded steel bar as a function of corrosion area loss.

3.3.2 Comparison with Gravimetric Analysis. Figure 3.12 compares the area loss with the mass loss of corroded bars, both representing the level of corrosion. The area loss was based on the 3D laser scan data, and the mass loss was determined by comparing the mass difference before and after corrosion using the gravimetric analysis. Both the average cross-sectional area loss and the maximum area loss at the minimum cross section were considered. It can be seen from Figure 3.12 that the mass loss is linearly related to the cross sectional area loss, being the average or maximum area loss definition used. However, the correlation between the average area loss and the average mass loss (R-squared = 0.96) is stronger than that between the maximum area loss and the average mass loss (R-squared = 0.90). This is because the average area loss is an indicator of the entire steel rebar while the maximum area loss represents a small number of steel sections. The former is a more robust describer for the area loss than the latter.

The slope of the regression line based on the minimum cross section is greater than that based on the average cross section. Their ratio is 1.76, which is an indirect representation of the cross-sectional spatial heterogeneity factor *R*.

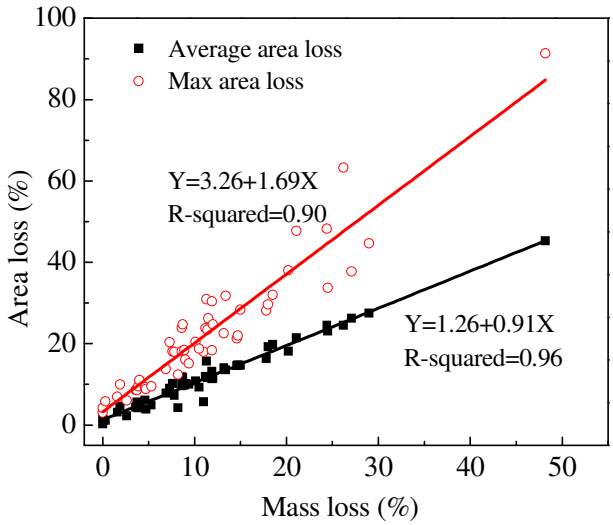

Figure 3.12 Correlation between the area loss and mass loss.

3.3.3 Mechanical Property Degradation. Figure 3.13 shows the typical load-elongation curves for the uncorroded (reference) and corroded steel bars tested in this study. It can be seen that both the yielding and ultimate loads decreased with an increase of average cross-sectional area loss. The yield plateau became shorter and even disappeared when the corrosion loss reached some values. In addition, the total elongation also decreased from 15 mm to 1.5 mm when the corrosion level increased from 0% to 48%.

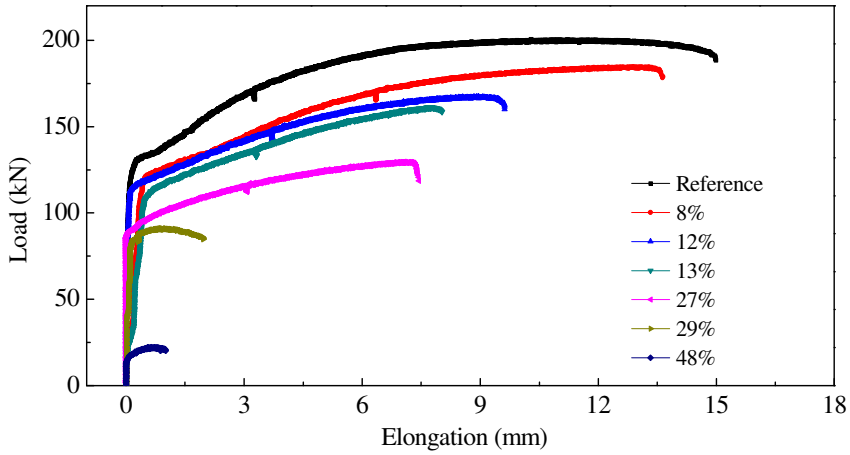

Figure 3.13 Load-slip curves of the uncorroded and corroded steel bars.

Under tension, steel bars typically fractured at the minimum cross section with a large corrosion pit. Therefore, the mechanical properties of steel rebar, such as yield and ultimate strengths, were intuitively related to the corrosion loss at the minimum cross section instead of the average corrosion loss over the entire steel bars as done by other researchers [60, 89].

Figure 3.14 shows the yielding and ultimate loads as a function of cross section area loss. Both the average cross sectional area loss (solid points) and the area loss at the minimum cross section (hollow points) were considered. A linear regression analysis was performed based on 50 test data points. It can be seen from Figure 3.14 that both the yielding and ultimate loads decreased with an increase of area loss, being it the average or minimum area considerations. The load capacities in relation to the area loss at the minimum cross section were greater than those to the average area loss since they were presented at the greater cross-sectional area loss. Their linear correlation with the area loss at the minimum cross section was also stronger with R-squared equal to 0.94 and 0.96 for yield and ultimate strengths, respectively, in comparison with R-squared equal to 0.85 and 0.88 based on the average area loss. The small data scattering based on the area loss at the minimum cross section is attributed to the eccentric loading during the tensile tests. For the uncorroded steel bar, the loading center likely coincided with the center of cross section. However, due to the effect of corrosion pits on cross sections as indicated

in Figure 3.10, the applied load likely created an eccentricity of various degrees at the minimum cross section of corroded steel bars.

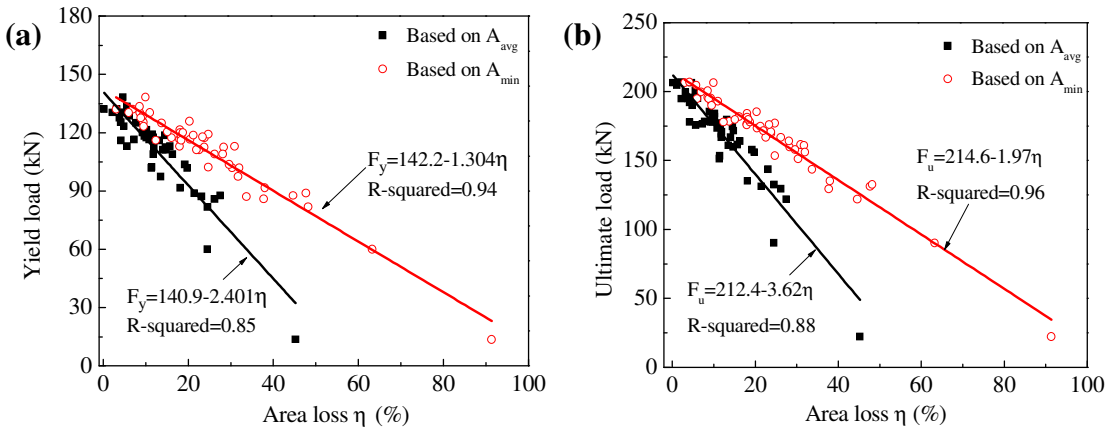

Figure 3.14 Yielding load (a) and ultimate load (b) as a function of area loss.

The effect of corrosion can be normalized by dividing the yielding load of a corroded bar by that of a corresponding uncorroded bar. To estimate the yielding load of uncorroded bars, the two fitted straight lines in Figure 3.14(a) were extended to intersect with the loading capacity coordinate axis and give the yielding load of 140.9 kN based on the average area loss and 142.2 kN based on the area loss at the minimum cross section. The yielding load can then be determined by:

$$F_y = (1.0 - 0.017\eta) F_{y0-avg} \tag{3.1}$$

$$F_y = (1.0 - 0.009\eta) F_{y0-crt} \tag{3.2}$$

where F_y is the yielding load of corroded steel rebar, $F_{y0\text{-avg}}$ (=140.9 kN) is the fitted yielding load at 0% corrosion level based on the average cross section area loss, $F_{y0\text{-crt}}$ (=142.2 kN) is the fitted yielding load at 0% corrosion level based on the area loss at the critical/minimum cross section, and η is the corrosion level in terms of area loss.

Similarly, the ultimate loads at 0% corrosion level are 212.4 kN and 214.6 kN based on the average area loss and the area loss at the critical cross section, respectively. The ultimate load can be determined by:

$$F_u = (1.0 - 0.017\eta)F_{u0-avg} \tag{3.3}$$

$$F_u = (1.0 - 0.009\eta)F_{u0-crt} \tag{3.4}$$

where F_u is the ultimate load of corroded steel rebar, $F_{u0\text{-}avg}$ (=212.4 kN) is the fitted ultimate load at 0% corrosion level based on the average cross section area loss, and $F_{u0\text{-}crt}$ (=214.6 kN) is the fitted ultimate load at 0% corrosion level based on the area loss at the critical cross section.

It can be clearly seen by comparing Eq. (3.1) with Eq. (3.3) and by comparing Eq. (3.2) and Eq. (3.4), the effects of corrosion on the normalized yielding and ultimate loads are basically the same so long as the same cross-sectional area loss is used. The reduction of loading capacity based on the average cross section area loss is more rapid than that based on the maximum area loss at the maximum cross section.

The mechanical properties of steel rebar are usually expressed by the stress/strength instead of load carrying capability. Therefore, both the yield and ultimate strengths were calculated based on the average and the minimum cross sectional areas, respectively. Figure 3.15(a) shows the plots of yield strength as a function of both the average and the maximum cross-sectional losses. As one can be seen, the yield strength of all corroded steel bars exceeds 420 MPa based on the minimum/critical cross section, indicating that corrosion has not affected the yield strength of steel bars. However, the yield strength decreased with an increase of corrosion level based on the average cross-sectional area loss as observed by other researchers [60, 89]. Considering that the failure mode in fracture is governed by the critical cross section of a steel bar instead of the "fictitious" average cross section of the entire steel bar, this definition of yield stress for corroded bars based on the average cross-sectional area loss is not reasonable in

engineering applications. Therefore, corrosion changes the cross section but not the yield strength of steel bars.

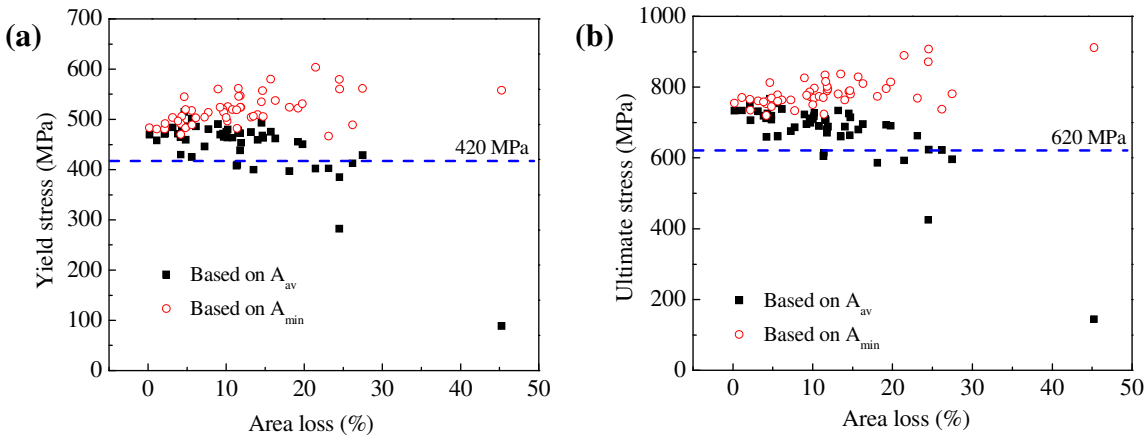

Figure 3.15 Yield strength (a) and ultimate strength (b) as a function of corrosion area loss.

Similarly, the ultimate strength based on the critical/minimum cross section as shown in Figure 3.15(b) always exceeds 620 MPa while the ultimate strength based on the "fictitious" average cross section decreases with an increase of area loss. Therefore, corrosion does not change the ultimate stress, either, based on the critical cross section.

3.3.4 Ductility. Figure 3.16 presents the elongation as a function of area loss. Unlike the strong linear correlation between the strength reduction and the area loss as discussed in Section 3.3.3, the linear correlation between the elongation and the area loss is significantly weaker, regardless of the use of average or maximum area loss. The R-squared values for the two straight lines fitting into the elongation data are 0.43 and 0.56 based on the average cross-sectional area loss and the area loss at the minimum cross section, respectively.

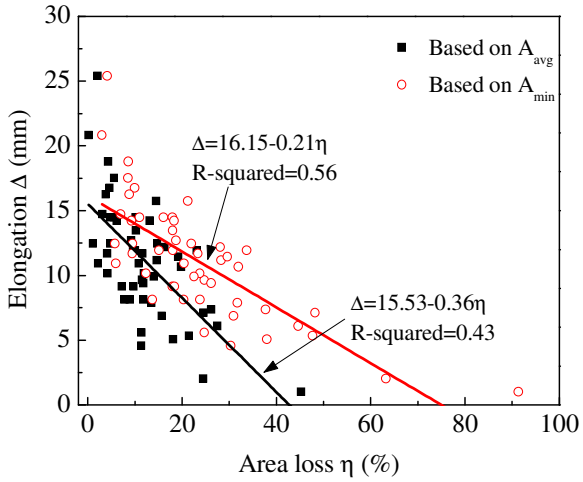

Figure 3.16 Elongation of steel bars as a function of area loss.

While both the yielding and fracture of a steel bar occur at the critical cross section with minimum area, elongation depends on the distribution of cross-sectional area along the length of the steel bar. The recognition of this difference is less significant for uncorroded steel bars since all the cross sections have nearly the same area, resulting in the uniformly distributed stress and deformation of the bar under tension. It becomes important for corroded steel bars due to randomly distributed corrosion pits and thus cross-sectional areas along the steel bars. Therefore, relating the elongation to the average cross-sectional area loss instead of the area loss at the critical section is more reasonable in engineering applications.

3.3.5 Fracture Cross Section. Figure 3.17 shows the representative fracture cross sections of uncorroded and corroded steel bars. As one can see, the fracture surface of the uncorroded steel bar is quite uniform with a significant necking area as illustrated in Figure 3.17(a). However, the fracture of the corroded bar initiated at the corrosion pits and propagated into other areas as illustrated in Figure 3.17(b). No obvious necking behavior was observed. This is probably due to the eccentric loading effect since the area center is not the same as the loading center with corrosion pits in the corroded steel bar.

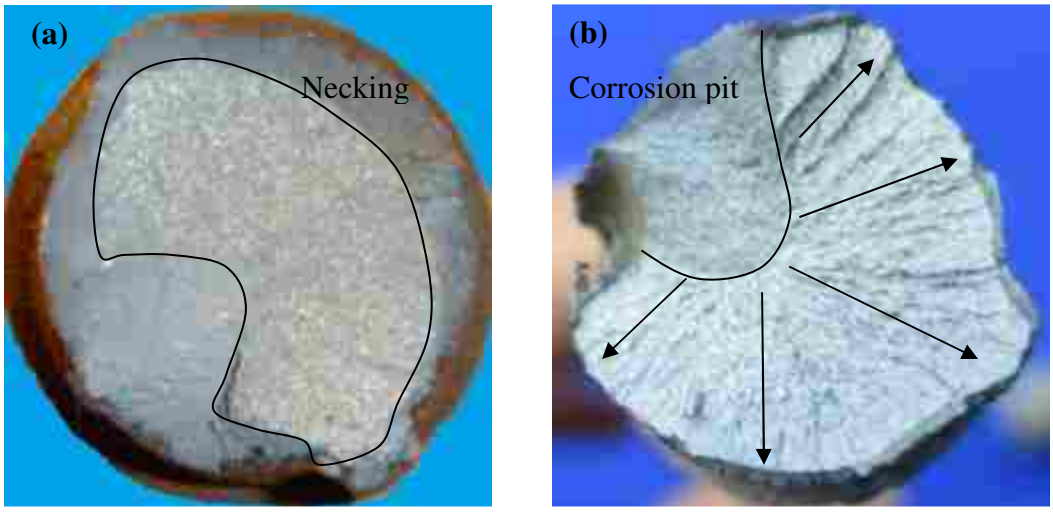

Figure 3.17 Fracture cross sections of (a) uncorroded and (b) corroded steel bars after tensile tests.

3.4 SUMMARY

This study experimentally investigated the tensile behavior of corroded steel bars in a corrosion bath filled with sands sprayed with 3.5% NaCl solution weekly. Both mechanical strengths and elongation of corroded bars under tension were considered. The corrosion loss was evaluated based on two methods: the mass loss and the 3D laser scan. Based on the test data and analysis, the following conclusions can be drawn:

(1) The cross-sectional area of uncorroded deformed bars followed a bimodal distribution due to the effect of ribs. The two peaks on the probability density function corresponded to a mean area of 275 mm^2 and 282 mm^2, respectively.

(2) Corrosion changed the distribution of cross-sectional area of steel bars. For steel bars with relatively uniform corrosion, a normal distribution was observed. However, for steel bars with obvious corrosion pits, a bimodal distribution was found.

(3) Corrosion resulted in a reduction of the cross section of steel bars, but did not change both yield and ultimate strengths at the critical cross section of steel bars with minimum area. The yield and ultimate strengths can be linearly correlated with the area loss at the critical cross section with little scattering that is attributed to the load eccentricity.

(4) Unlike the mechanical strengths, the elongation of corroded steel bars was less correlated with the area loss due to the non-uniform distribution of cross section. Due to the accumulative effect of cross-sectional changes, the average area loss is more appropriate when correlated to the elongation.

(5) Uncorroded steel bars fractured at the critical cross section after significant necking while the fracture of corroded steel bars initiated at the corrosion pits and then propagated to the other area without obvious necking.

4. CORROSION-INDUCED BOND DEGRADATION

4.1 INTRODUCTION

The concrete and reinforcing steel in reinforced concrete (RC) structures can work together due to their mechanical interaction through bonding and anchorage. However, the effectiveness of concrete-steel interfaces could be significantly reduced by deterioration of the concrete, steel, or both. Corrosion is one of the main deterioration processes in RC structures; it can impair the structural integrity by weakening concrete-steel interfaces and generating concrete cover cracking as corrosion products grows between the concrete and steel [101-103].

Many studies have been conducted on the influence of corrosion on bond between steel and concrete. They can be categorized into two main groups: experimental investigation and numerical simulation. Small concrete specimens with one embedded steel bar were often used in direct pullout tests. Chung et al. [104] investigated the impacts of corrosion to the bond behavior and proposed the bond equations with corrosion effects properly taken into account level, using two types of specimens with a steel bar subjected to corrosion before and after concrete casting, respectively. Tang et al. [66] investigated the influence of surface crack width on the bond strength, observed a strong relationship between the average surface crack width and the average bond strength, and concluded with an inconclusive correlation between the surface crack width and the degree of corrosion. Fang et al. [63, 64] studied the effect of corrosion on the bond strength under both static and cyclic loading.

Flexural tests were also conducted to study the effect of corrosion on the bond strength. For example, Al-Sulainmani et al. [105] tested RC beams. Stanish et al. [106] and Chung et al. [107] tested RC slabs. To date, the only parameter used in previous studies to quantify the corrosion effect on steel bars is the average mass loss. It was usually determined by comparing the weight before and after corrosion tests. Other corrosion effects on structural behavior are seldom investigated, including the spatially non-uniform reduction of steel bar cross section and the spatially non-uniform cracking in concrete cover.

The objectives of this study are: (1) to investigate the effect of corrosion non-uniformity on the bond strength between concrete and corroded steel bars, (2) to better understand the bond deterioration mechanism and bond failure modes, and (3) to observe the effects of average corrosion level and average crack width on the bond degradation.

4.2 EXPERIMETAL DETAILS

4.2.1 Materials and Specimens. The steel bars used in this study met the requirements of ASTM A615 Guidelines. Their chemical composition is listed in Table 4.1. Their average yield and ultimate strengths were determined to be 420 MPa and 620 MPa, respectively. Type I Portland cement was used in this study; its chemical composition is listed in Table 4.2. The water cement ratio is 0.45 with no admixtures. Their compressive strength at the day of pull-out tests was determined to be 32.42 MPa, based on the standard concrete cylinders tests using 102 mm in diameter and 203 mm tall specimens. The concrete splitting tensile strength was evaluated with testing of a simply-supported beam under third-point loading and determined to be 1.62 MPa.

Table 4.1 Chemical composition of steel rebar

Element	C	Si	Mn	P	S	Cr	Mo	Ni	Co	Cu	V	Sn	Fe
Wt.%	0.38	0.18	1.00	0.12	0.06	0.10	0.07	0.20	0.01	0.37	0.02	0.03	97.40

Table 4.2 Chemical composition of Type-I Portland cement (wt. %).

Loss on ignition	SiO_2	Al_2O_3	CaO	MgO	SO_3	Na_2O	K_2O	Cl	TiO_2	Fe_2O_3	P_2O_5	Total
3.98	19.48	6.80	55.35	3.32	4.35	2.39	1.00	0.02	0.20	2.18	0.19	99.27

The pullout test specimen used in this study is a 152.4 mm×139.7 mm×177.8 mm concrete block with one embedded deformed bar as schematically illustrated in Figure 4.1. The steel bar is located near the top face with a clear concrete cover of approximately 41.3 mm to replicate the application condition in RC beams and restrain the potential cracking within the top portion. The embedment length of the steel bar was selected to be

127 mm, which is 6.7 times the bar diameter. To reduce the potential arching effect and end restraint, the steel bar was encased in a 25.4 mm long PVC pipe at both ends (within concrete). The above design offered ideal bond breakers for the steel bar as will be confirmed by the failure modes of tested specimens. The steel bar at its both ends can slide freely without causing any noticeable anchoring effect on concrete. To limit the corrosion on the embedment portion yet minimize the effect of the PVC pipes on the pull-out strength of the steel bar in concrete, only the ends of the PVC pipes near the embedment portion were sealed with epoxy resin. The millscale formed on the steel bar was cleaned off before casting concrete using a steel wire wheel brush.

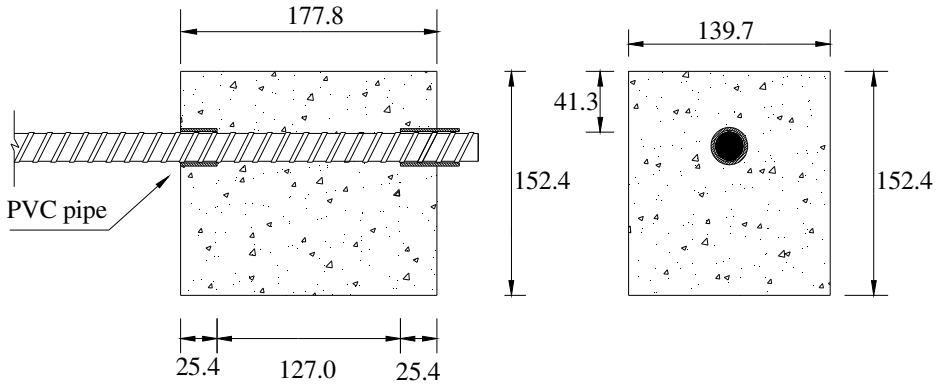

Figure 4.1 Pull-out test specimen dimensions (unit: mm).

For the casting of concrete, formworks were constructed using 13 mm plywoods as shown in Figure 4.2. Two holes with a diameter of 28.6 mm were drilled on the two opposite side walls for bar placement at the predetermined location. Once the steel bar is in place, silicon resin was applied to seal the void between the holes and the PVC pipes. Two epxoy coated steel bar stirrups with a diamter of 12.7 mm were used as confinement. To ensure the placement of stirrups at the certain location, four palstic ties were used to mount the stirrups against the sidewalls. Before casting, a layer of oil was applied to avoid water penetration to the plywoods.

Figure 4.2 Plywood mold for pull-out specimen casting.

4.2.2 Accelerated Corrosion Test. Figure 4.3 shows a schematic view of corrosion test setup. The concrete block was placed in a corrosion test container with the steel bar oriented horizontally and the spaces between the block and two container side walls were filled with sands nearly flush with the top face of the concrete block. In its final position, the steel bar was located underneath the top face of sands on which 3.5 wt% NaCl solution was sprayed weekly to provide moisture and chloride ions. To accelerate steel corrosion, direct current was impressed on the steel bar embedded in concrete using an external power supply as schematically shown in Figure 4.3. The steel bar was connected to the positive end of the power supply while a graphite rod with a diameter of 6.35 mm plugged into sands was connected to the negative end. In order to monitor the electrical current through the steel bar and the predetermined corrosion mass loss, one 10 ohm resistor was connected in the circuit. The voltage of the resistor was recorded with a DataLogger 880 system and used to evaluate the electrical current through the resistor.

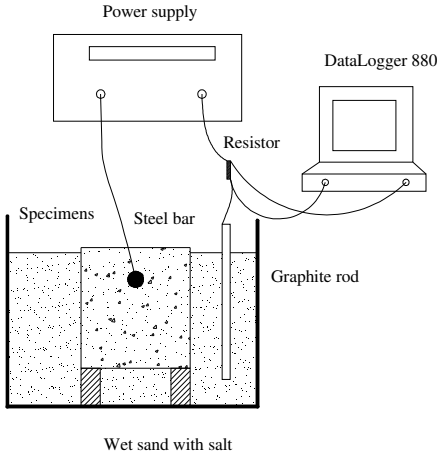

Figure 4.3 Accelerated corrosion test setup.

4.2.3 Pullout Test Setup. Each specimen was tested on a Tinius Olsen machine as shown in Figure 4.4 (a) and (b) with the steel bar pulled downward. A 12.7 mm thick steel plate was used to provide an upward reaction to the bottom face of the concrete specimen. Between the steel plate and the concrete block was a 6.35 mm thick rubber pad with a center hole that was used to avoid stress concentrations caused by any potentially uneven concrete surface introduced during the casting process. To ensure that the applied force go downward without any potential eccentricity, a ball bearing was placed between the rubber pad and the reaction frame as illustrated in Figure 4.4(a). The steel bar went through the hole in the center of the ball bearing.

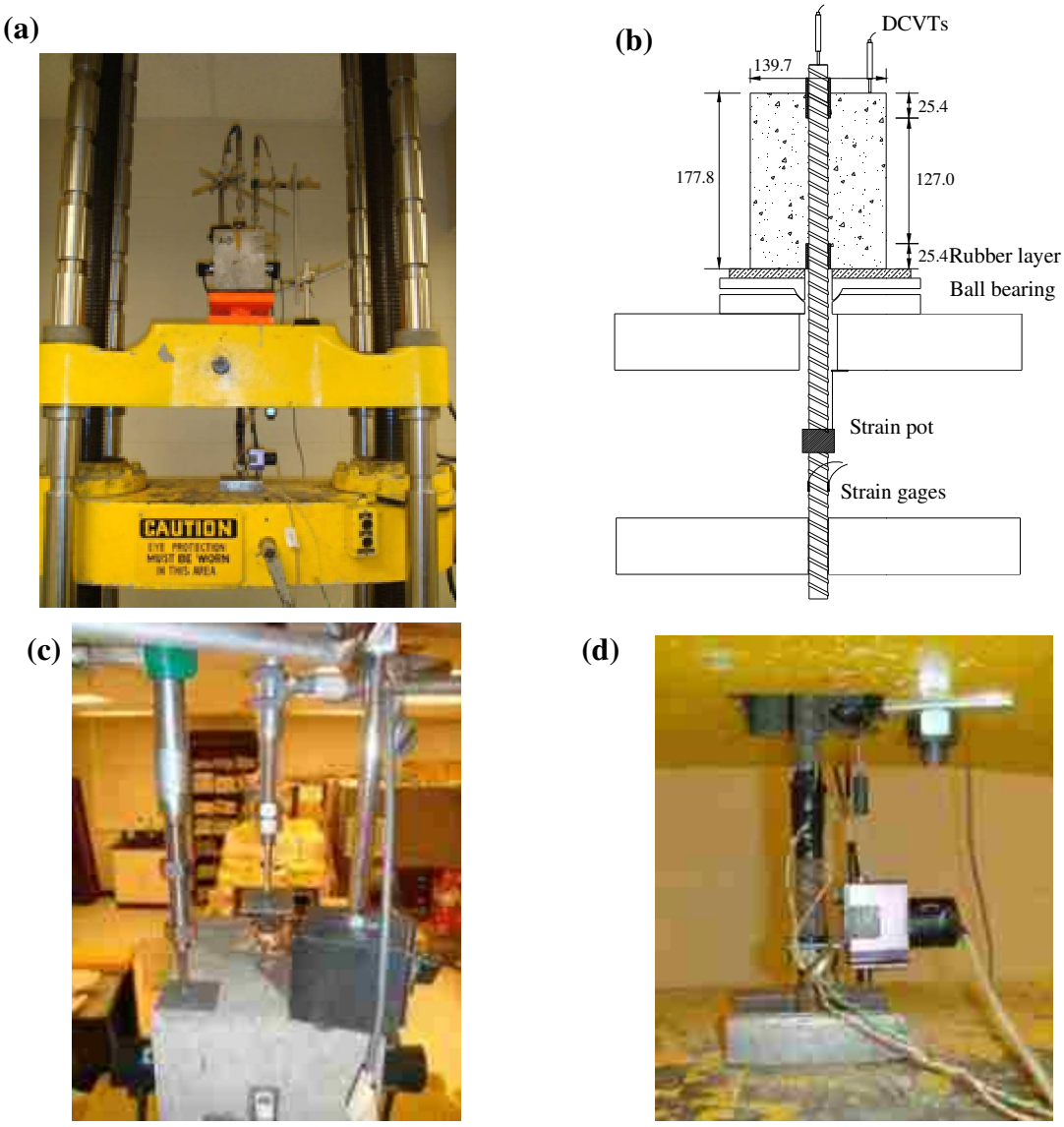

Figure 4.4 Pullout test setup: (a) specimen during testing, (b) schematic view of specimen, (c) two DCVTs mounted on top of the specimen, and (d) strain pot for deformation recording.

As detailed in Figure 4.4(c), each specimen was instrumented with two Linear Variable Differential Transformers (LVDTs) at the top end of the steel bar and the top concrete surface of the concrete block, respectively. One strain pot was mounted around the bar as shown in Figure 4.4(d) to measure the bar elongation. Two strain gages were attached on the bar surface to measure the strain during tests, which would be used to calculate the bar slip at the bottom of concrete block.

4.2.4 3D Laser Scan. After pullout tests, the corroded bars were taken out of the concrete specimens and cleansed with sand blaster. After cleansing, the surface morphology of the bars was measured using a 3D laser scanner to determine the residual cross section as indicated in Figure 4.5. After this operation, the 3D coordinates of each point on the surface of the corroded bar were acquired. Data not belonging to the corroded rebar were cleansed by ScanStudioHD software to give point cloud files with higher signal-to-noise ratios. The acquired 3D point cloud data were processed using ImageWare software.

Figure 4.5 3D laser scanning of the deformed steel bar.

4.2.5 Acoustic Emission Test. Acoustic emission tests were performed with the pullout test specimens. The objective was to capture the acoustic signal of concrete cracking and the friction between concrete and the steel bar embedded in concrete. A 24-channel Micro-II PCI-8 module system from Physical Acoustics Corporation was used to acquire data. The acoustic sensor (Model R1.5I) used in this study incorporated a built-in low noise input, 40 dB preamplifier and a filter. Its resonant frequency is 20 kHz.

In order to potentially locate the source of cracks, three sensors were placed on three faces of a concrete block. As shown in Figure 4.6, two sensors were mounted on the

two side faces and one sensor was mounted on the back face. The front face near the steel bar was left for the monitoring of crack opening during loading as will be discussed later. Each sensor was fixed to a steel angle that was in turn attached to the concrete surface with super glue and silicone grease. Such an attachment scheme can couple the acoustic sensor and the concrete surface for a better transition of acoustic signals.

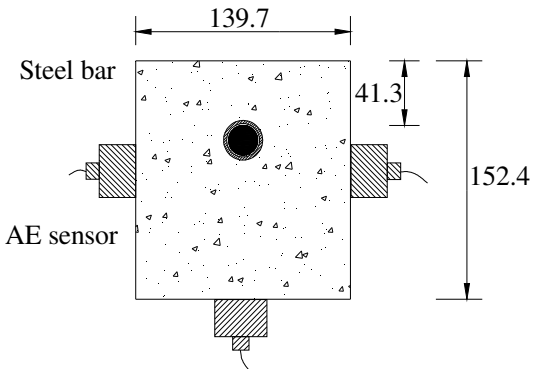

Figure 4.6 Layout of AE sensors (unit: mm).

4.3 RESULTS AND DISCUSSION

4.3.1 Average Bond Loss. Bond stress was calculated based on the cross section of an uncorroded steel bar. During the tests, it was observed that corrosion effects were quite non-uniform over the embedment length and large corrosion pits appeared sometimes. Therefore, the use of the cross section of the uncorroded bar can simplify the calculation of bond stress as follows:

$$u_{avg} = \frac{P}{\pi d_b l_d} \tag{4.1}$$

where u_{avg} is the average bond stress, P is the applied load, l_d is the embedment length, and d_b is the bar diameter.

The bar slip at the bottom of concrete block was determined based on the following equation:

$$\delta = \Delta_s - L\varepsilon_s - \Delta_R \tag{4.2}$$

where δ represents the bar slip at the bottom of a concrete specimen, Δ_s is the elongation of steel bar measured from the strain port, L is the distance from the bottom face of the specimen to the strain port, ε_s is the strain in the steel bar, and Δ_R is the deformation of the rubber layer which was recorded from the DCVT mounted on the top frame of the test machine.

4.3.2 Cross Section of Corroded Bar. Figure 4.7 shows the scanned surface profiles of one uncorroded and three corroded steel bars (#2, #3, and #10) over the embedment length. Note that the corrosion area losses of the corroded bars are given in Table 4.3. As shown in Figure 4.7(a), the ribs of the uncorroded bar are periodically distributed along the length of the bar and their geometry and texture can be seen clearly. As shown in Figures 4.7(c) and (d), the residual cross sections of severely corroded bars change irregularly over the embedment length due to the presence of large corrosion pits.

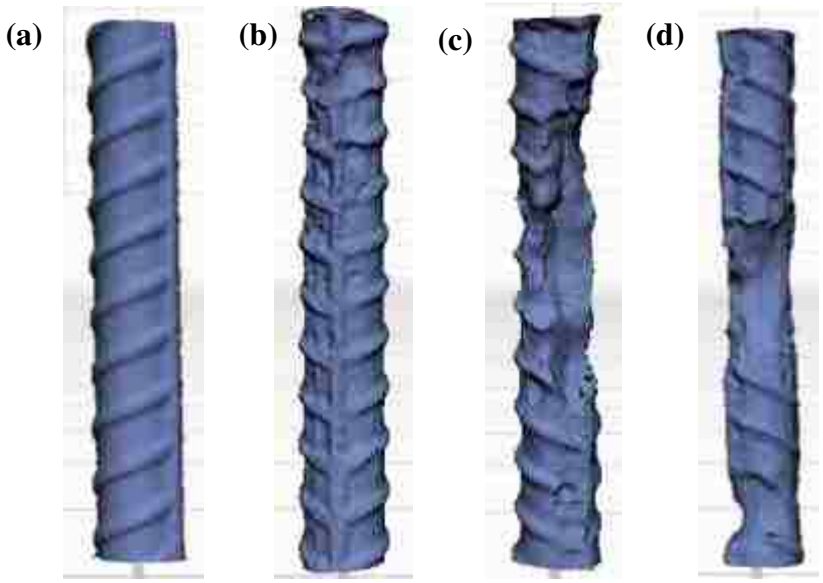

Figure 4.7 Scanned surface profiles of (a) uncorroded bar, (b) corroded bar #2, (c) corroded bar #3, and (d) corroded bar #10.

Figure 4.8 gives the histograms of cross sectional area for the uncorroded steel bar and the corroded steel bars as shown in Figure 4.7. Two peaks of cross sectional area appeared in the histogram of the uncorroded steel bar around 273 mm^2 and 280 mm^2, respectively. Due to the effect of ribs, the area of cross sections at ribs is larger than that between two ribs as seen in Figure 4.7(a). The effect of corrosion on the bar cross section can be divided into two groups. One is for the steel bar with relatively uniform corrosion, and the other is for the steel bar with obvious corrosion pits. The residual cross sectional area of the bar with uniform corrosion follows a normal distribution as seen in Figure 4.8(b). The steel bar with corrosion pits has a bimodal distribution with one peak on the cross section without corrosion pits and the other peak on the cross section with corrosion pits as shown in Figures 4.8(c) and (d).

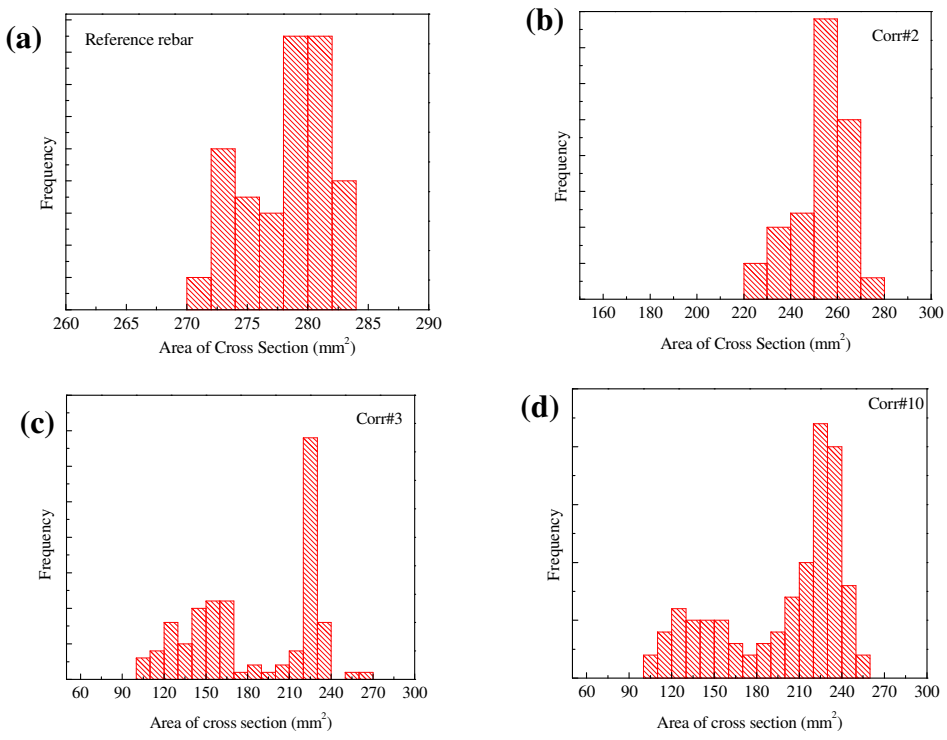

Figure 4.8 Histograms of the cross section of corroded bars for (a) uncorroded bar, (b) corroded bar #2, (c) corroded bar #3, and (d) corroded bar #10.

4.3.3 Crack Pattern and Opening. The typical crack patterns of specimens with corroded bars prior to pullout tests are shown in Figure 4.9. Four types of cracking

patterns were observed: one small crack through the concrete cover in Figure 4.9(a), two small cracks through the two side faces in Figure 4.9(b), two small cracks with one through the concrete cover and the other through one side face as shown in Figure 4.9(c), and three cracks through both the concrete cover and the two side faces as shown in Figure 4.9(d). The widths of the cracks on all specimens were recorded and listed in Table 4.3. For each specimen, crack widths along a crack were sampled every 1.0 mm so that the statistical mean and standard deviation were obtained as listed in Table 4.3.

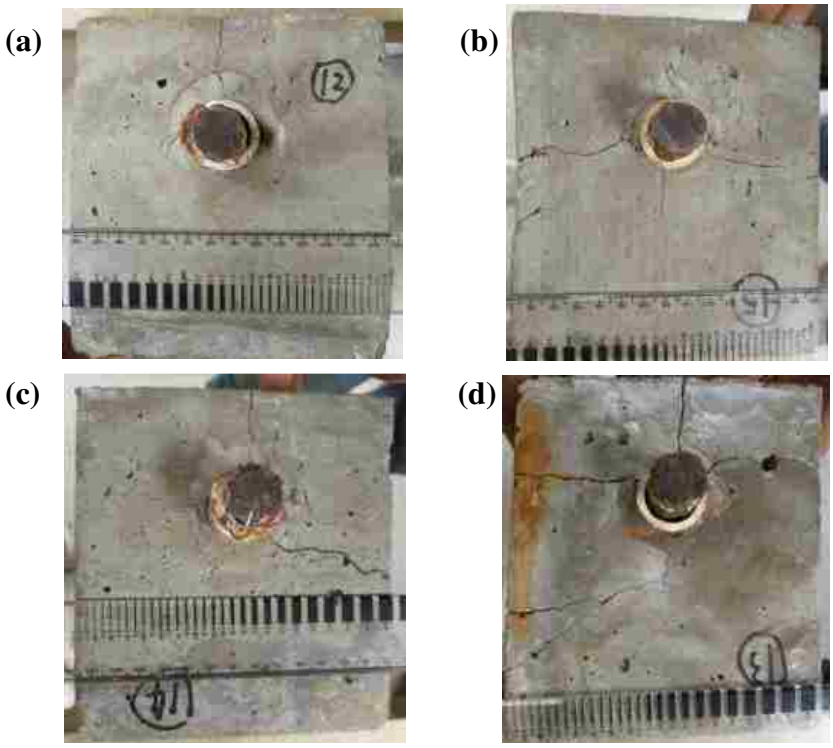

Figure 4.9 Representative corrosion-induced cracking: (a) one small crack through the concrete cover, (b) two cracks through the two side faces, (c) two cracks with one though the concrete cover and the other through one side, and (d) three cracks though both the concrete cover and two side faces.

For the specimen with embedded uncorroded steel bar as shown in Figure 4.10, a crack was initiated near the loading point and subsequently propagated parallel to the reinforcing bar as the applied load increased. However, for the specimen with embedded corroded steel bar, one additional crack was induced by corrosion and widened with an

increasing load as shown in Figure 4.11. At the same time, some other minor cracks may occur. During the tests, more small cracks were observed along the steel bar at low corrosion level, and less new cracks were generated but the old cracks continued to be widened at relatively high corrosion level.

Table 4.3 Crack width before pullout tests

Specimen	Corrosion Area loss (%)	Top (mm)	Left side (mm)	Right side (mm)
#1	17.8	0.84±0.30	1.14±0.55	
#2	9.1	0.64±0.12	0.76±0.22	
#3	35	0.98±0.30	0.78±0.19	0.79±0.32
#4	2.2	0.50±0.11	0.25±0.09	
#5	15.6	0.24±0.15	0.87±0.43	1.56±0.51
#6	1.8	0.34±0.12		
#7	12.2	0.26±0.09	0.27±0.13	
#8	7.1	0.39±0.10		
#9	18.1	1.07±0.44	1.00±0.33	1.28±0.92
#10	29.5	0.26±0.18	1.71±0.84	1.51±0.66
#11	10.3	0.21±0.11	0.30±0.16	
#12	4.1	0.42±0.14		
#13	7.7	0.30±0.14	0.48±0.24	1.39±0.47
#14	1.5	0.31±0.17	0.32±0.17	
#15	7.8		0.44±0.16	0.20±0.05

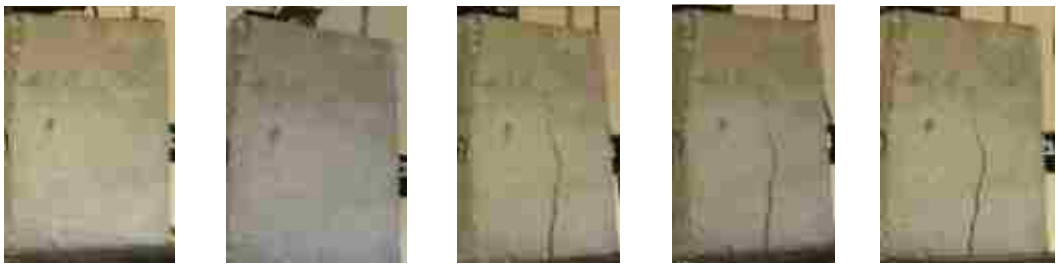

(1) 0 kN (2) 69.8 kN (3) 56.0 kN (4) 50.3 kN (5) 29.8 kN

Figure 4.10 Crack initiation and propagation of the concrete block with uncorroded bar under applied loads from (1) 0 kN through (3) 69.8 kN to (15) 29.8 kN.

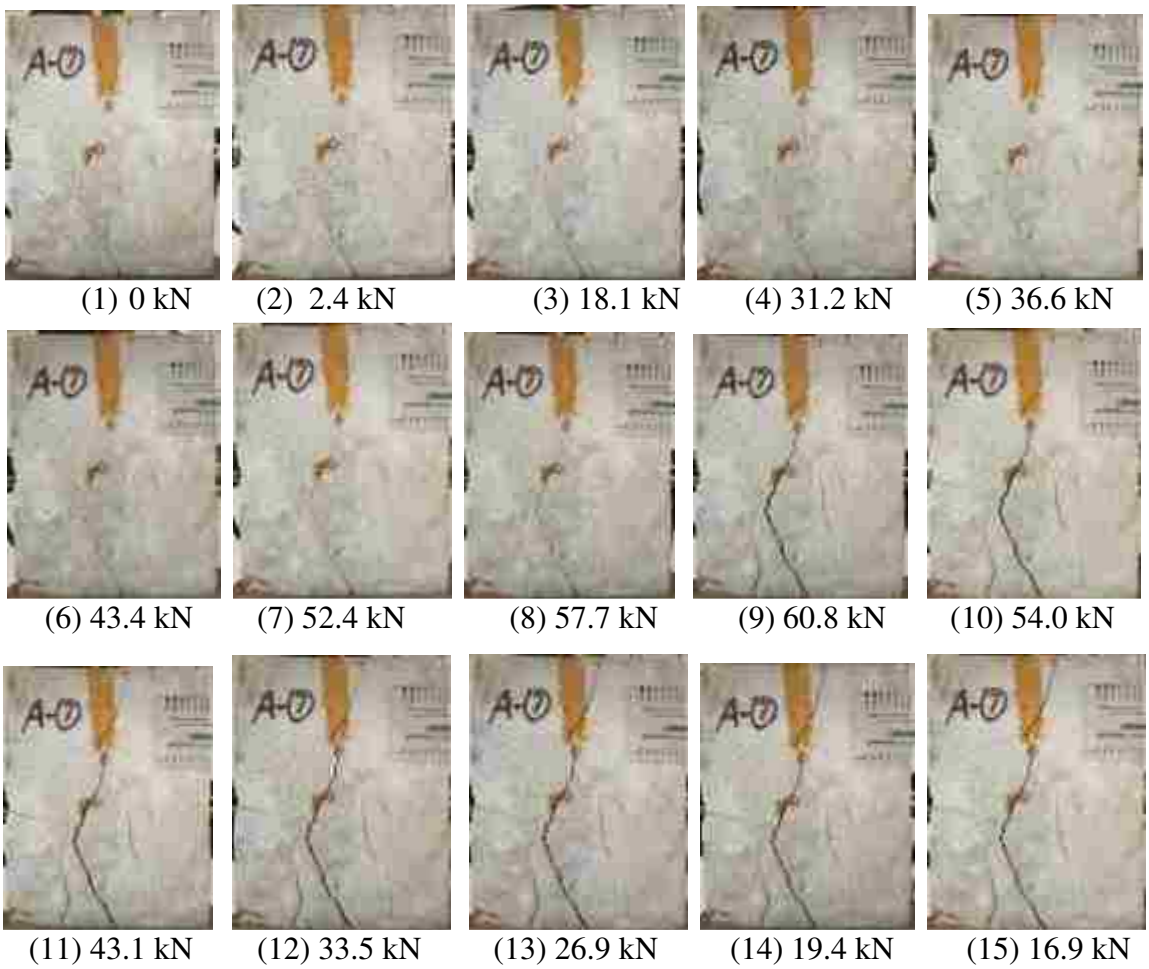

Figure 4.11 Crack widening of corroded specimen #7 at loads from (1) 0 kN through (9) 60.8 kN to (15) 16.9 kN.

4.3.4 Load-slip Curves. Figure 4.12 shows representative load-deformation in rubber layer, load-strain in steel bar, and load-slip curves. As indicated in Figure 12(a), the load-deformation in rubber layer seems to show a hardening material behavior, which is not realistic for rubber materials. The initial hardening-like behavior was likely due to slack in the test setup. As a result, the deformation increased rapidly in the beginning of loading and less rapidly after the applied load reached a critical value or the initial slack was removed completely. Thereafter, the deformation increased almost linearly with the applied load. When unloaded to the critical value, the deformation fluctuated around the loading curve. The fluctuation was due to the cracking and crushing of concrete bottom face next to the rubber layer.

The relation between the applied load and strain in steel bar is linear, elastic, and non-hysteretic in a loading-unloading cycle as displayed in Figure 4.12(b). This is because the maximum pullout load of 80 kN applied to all specimens is lower than the yield strength in terms of loading capability.

Figure 4.12(c) shows two representative load-slip curves. One is for the slip between the top end of the steel bar and the top face of concrete as shown in Figure 4.4(b) and the other is for the slip where the steel bar exits out of concrete. The latter is always greater than the former because the latter represents the accumulative deformation over the embedment length and corresponds to the maximum steel-concrete interface force. This explanation is also supported by the crack initiation and propagation pattern as shown in Figure 4.10. The difference between the two slips measured at the top and bottom faces of concrete increased in the loading process and decreased in the unloading process. The maximum difference in slip was reached at the maximum load or bond force since the steel-concrete interface gradually damaged after the maximum load and the interfacial reaction force from the concrete and then the deformation in steel bar were reduced. The effect of corrosion on the maximum slip difference will be discussed later.

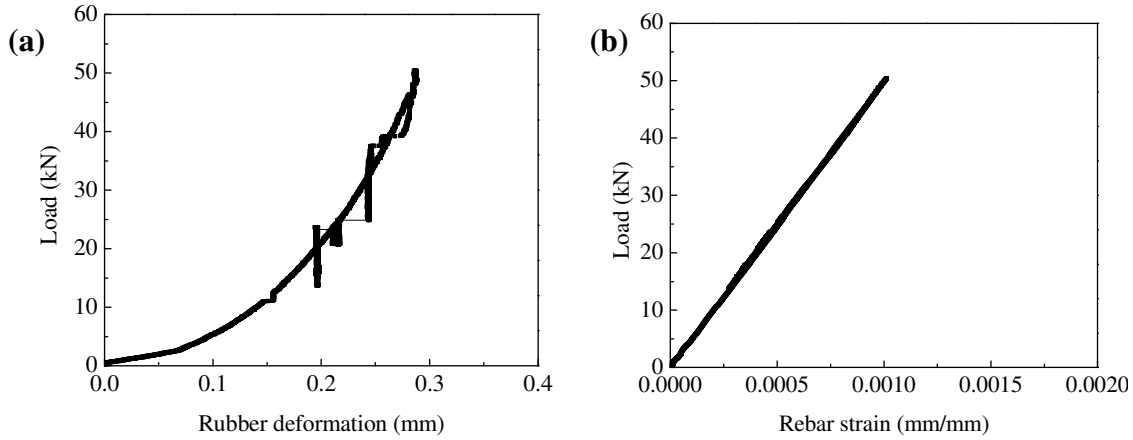

Figure 4.12 Representative curves: (a) load-deformation in rubber layer, (b) load-strain in steel bar, and (c) load-slip.

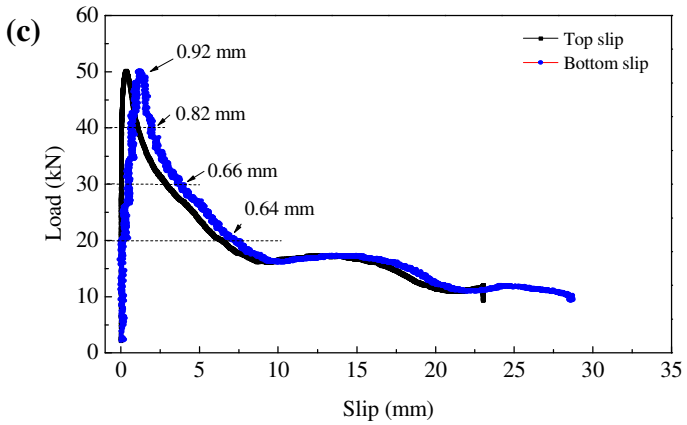

Figure 4.12 Representative curves: (a) load-deformation in rubber layer, (b) load-strain in steel bar, and (c) load-slip. (cont.)

Figure 4.13 shows the relationships between the bond stress and the top slip at the end of steel bar for all specimens. The specimens were divided into three groups based on their characteristics that are closely related to the number of cracks and crack width appeared on concrete surface instead of average corrosion level. As shown in Figure 4.13(a), the bond stress for the specimens with uncorroded (reference) steel bars suddenly dropped after initiation of the first crack, then increased to some extent, and finally decreased in a relatively rapid rate with the slip. When the bond stress dropped to 15% of its maximum load, the slip at the top end of the steel bar is approximately 7 mm. As shown in Figure 4.13(b), the specimens with less cracks on the concrete surface exhibited the same behavior as the specimens with uncorroded steel bars. However, the slip when the bond stress is 15% of its maximum value is much greater than that with the uncorroded steel bars, which is approximately 12 mm. For the specimens with two and more wide cracks, there is no sudden drop in the loading process, indicating that no new crack occurred as indicated in Figure 4.13(c). In the unloading process, the maximum slip is as large as that for the specimens with less narrow cracks, which is approximately 18 mm.

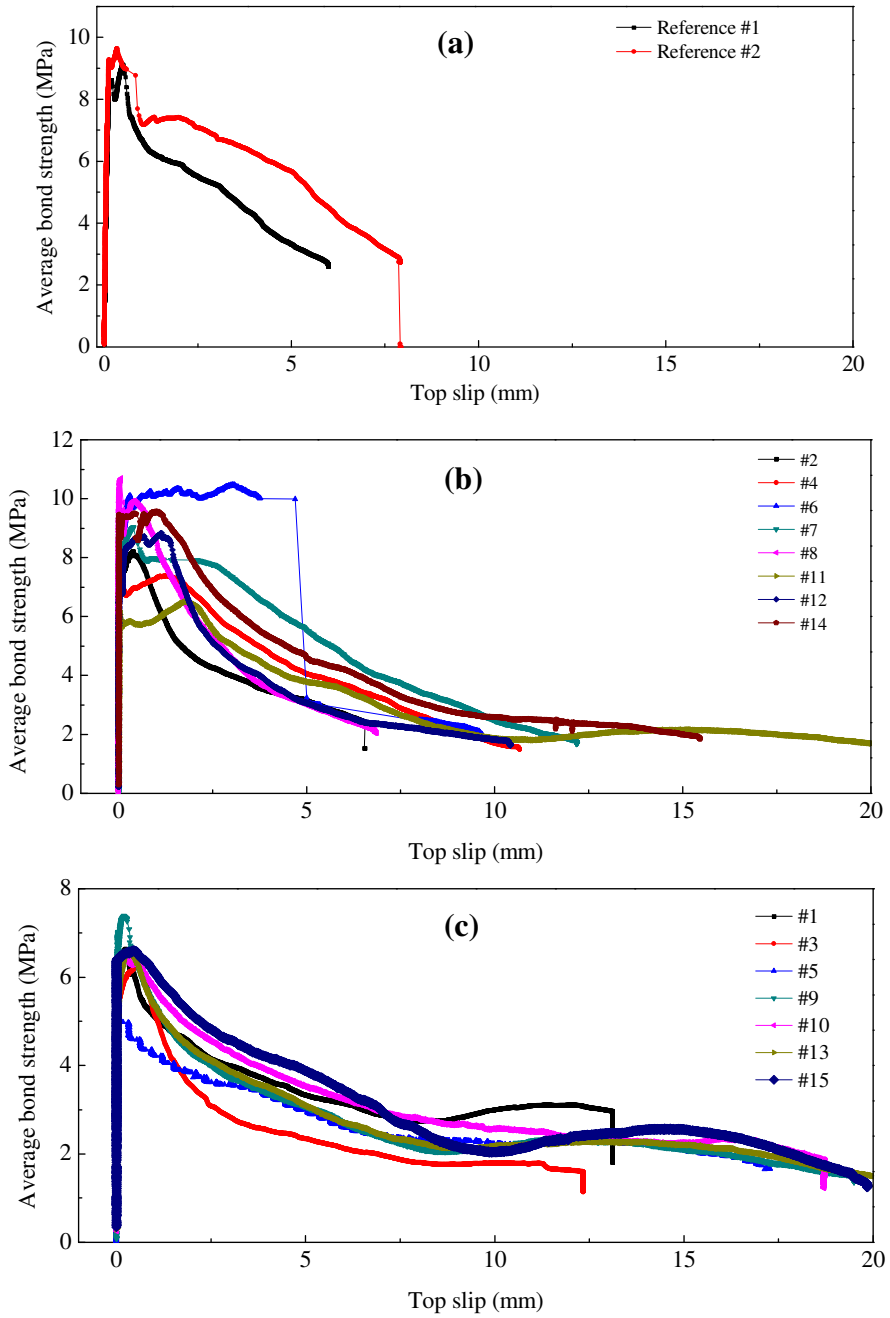

Figure 4.13 Bond stress-slip curves of all specimens: (a) specimens with unocrroded steel bar, (b) specimens with less crack, and (c) specimens with more cracks.

4.3.5 AE Results. During pullout tests, two types of acoustic signal can potentially be captured by the AE system: concrete cracking and the friction between concrete and steel bar. The specimen with the uncorroded steel bar experienced three

major stages that were dominated by concrete cracking, both concrete cracking and steel-concrete friction, and steel-concrete friction, respectively. The frequency characteristics in each stage can be identified because the acoustic wave generated from concrete cracking propagated in nearby hard materials so that more acoustic energy is distributed over high frequencies while the acoustic wave from the friction between the steel bar and concrete propagated in nearby softened materials during previous concrete cracking so that more energy is distributed over low frequencies.

In order to identify the frequency characteristics corresponding to different mechanisms, each signal was divided into three stages based on the bond-slip curves. Stage I is from the beginning of loading to maximum bond strength, stage II corresponds is from maximum bond strength to the end of rapid decrease of bond strength, and stage III is from the end of rapid decrease of bond strength to the termination of test. Figure 4.14 presents the acoustic energy spectra for six specimens. During the pullout test of each specimen, two dominant peaks were identified from each of the three acoustic energy spectra in three stages. The low- and high-frequency peaks represent the friction and cracking effects, respectively. In Stage I, the energy released due to concrete cracking is generally higher than that from the friction as indicated by the solid line in Figure 4.14 (except the corroded bars #1 and #13). In contrast, in Stage III, the energy released from the steel-concrete friction is higher than that from concrete cracking as shown in blue dashed line in Figure 4.14 (except the corroded bar #15). In stage II, the energy levels released from concrete cracking and steel-concrete friction are generally comparable as shown in red dashed line in Figure 4.14 (except the corroded bar #15). Overall, the friction generated acoustic energy is mainly distributed in a low frequency range of 3 kHz to 15 kHz while the cracking generated acoustic energy is in a high frequency range of 35 kHz to 41 kHz.

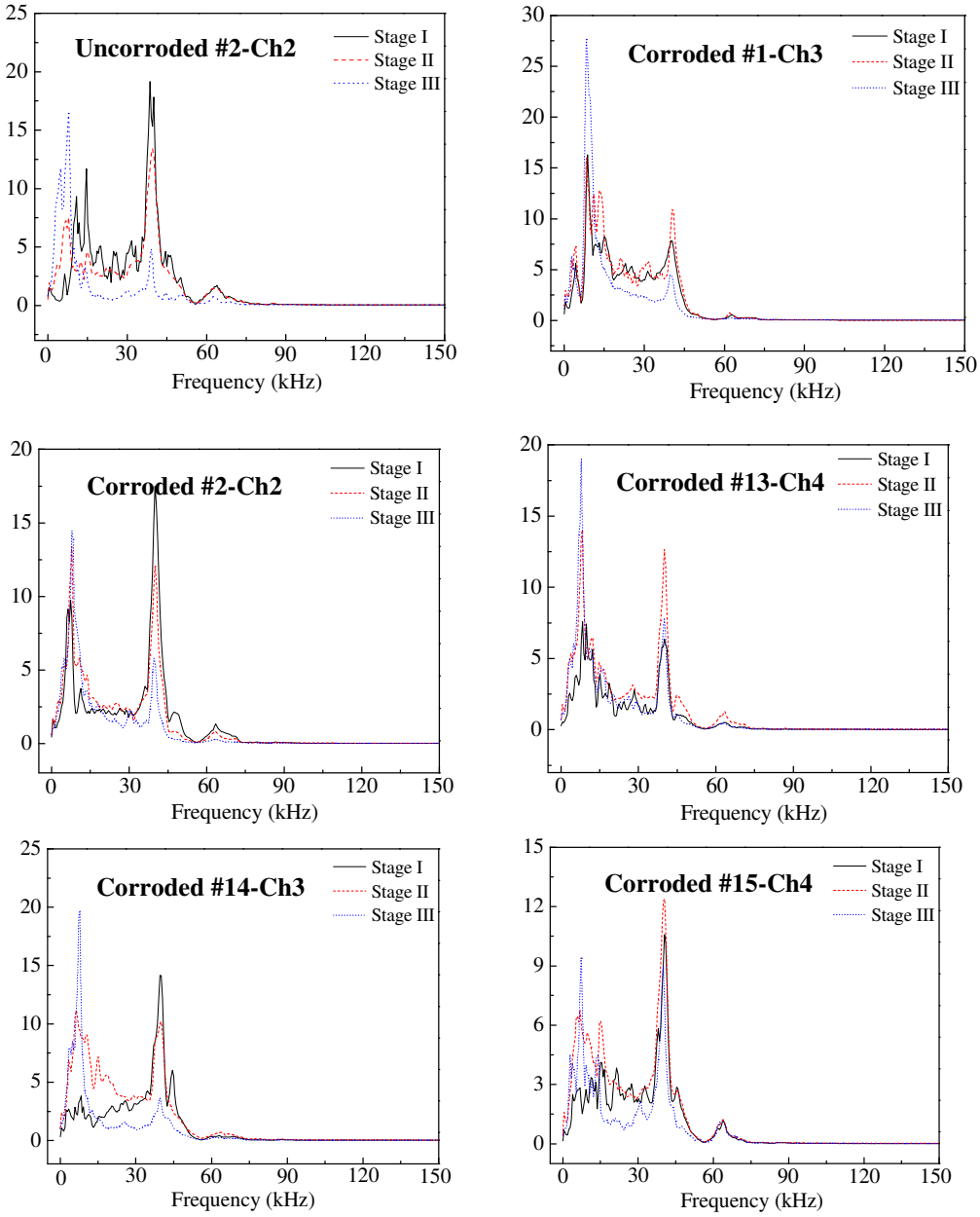

Figure 4.14 Acoustic energy spectra of various specimens.

The dominant frequency ranges at Stages I and III of seven representative specimens are presented in Table 4.4. Specimen R2 was with the uncorroded steel bar as a reference for other specimens, Specimens #1, #2, and #14 were with corroded steel bars but less small cracks, and Specimens #3, #13, and #15 were with corroded steel bars and many large cracks. For each specimen, three sets of signal corresponding to three AE

sensors on the concrete block surface were taken at each stage; their mean and standard deviation were evaluated. Both the mean and standard deviation are reported in the form of mean ± standard deviation in Table 4.4. It can be clearly seen from Table 4.4 that the frequencies identified at Stage I for concrete cracking are almost the same with or without corrosion. The is because many new cracks would be induced as the specimens with uncorroded steel bars are loaded; and propagation of old cracks and generation of few new cracks would occur for the specimens with corroded steel bars, both of which released significant energy.

Table 4.4 Frequencies identified at Stages I and III (kHz)

Specimen	Stage III (steel-concrete friction)	Stage I (concrete cracking)
#1	8.138±0.746	39.88±0.746
#2	8.138±0.746	39.71±0.564
#3	7.812±0.000	40.36±0.746
#13	7.486±1.409	39.71±0.282
#14	7.975±0.282	40.04±0.489
#15	7.812±1.760	40.04±0.489
R2	12.04±2.255	39.71±1.227

Effect of corrosion on the dominant frequency can be observed at Stage III due to the steel-concrete friction. The specimen (R2) with the uncorroded steel bar had a much higher friction-associated frequency than that for the other specimens with corroded steel bars. This is because the steel-concrete interfacial materials through which the friction-induced acoustic wave propagated are much harder with the uncorroded specimen (R2), less harder with the corroded specimens (#1, #2, and #14), and relatively loose with the corroded specimens (#3, #13, and #15). In addition, the acoustic energy is more sensitive to the number and size of cracks and less to the level of corrosion as will be demonstrated in Section 4.6.3. Overall, the average friction frequency is 12 kHz for the specimen with uncorroded steel bar (R2), 8 kHz for the specimens with less and small cracks (#1, #2, and #14), and 7.7 kHz for the specimens with many large cracks (#3, #13, and #15).

4.3.6 Bond Degradation. Figure 4.15 shows the relationship between the maximum bond stress and average corrosion level, and the relationship between the maximum bond stress and average crack width for all specimens. With an increase of corrosion level and average crack width, the maximum bond stress decreased. A linear regression analysis made for both cases demonstrated that the reduction of maximum bond stress due to corrosion was more sensitive to the average crack width and less to the average corrosion level. This is consistent with studies in the literature [5]. The bond stress depends on the confinement of concrete, which can be reduced significantly by concrete cracking. However, high corrosion level means more corrosion products that may penetrate into the concrete void and cracks rather than generate tensile stress on the cover concrete.

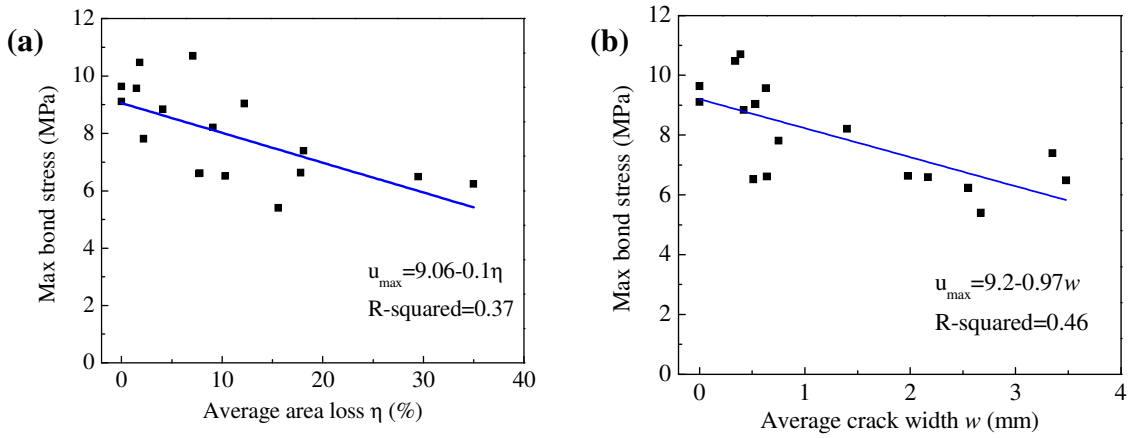

Figure 4.15 Relationships between (a) maximum bond stress and corrosion level, and (b) maximum bond stress and crack width.

Figure 4.16 shows the corrosion effects on the difference of slips at the top and bottom concrete faces and corresponding to the maximum bond strength, and on the average crack width. It can be seen from Figure 4.16(a) that the slip difference likely increased with an increase of corrosion level with a weak correlation (R-square = 0.50). This is because corrosion reduced the cross section of steel bar embedded in the concrete, and some part of the embedment may yield under the maximum load and produce

significant deformation. Figure 4.16(b) indicated that the average crack width generally increased with an increase of corrosion level. However, their correlation is weak (R-squared = 0.57).

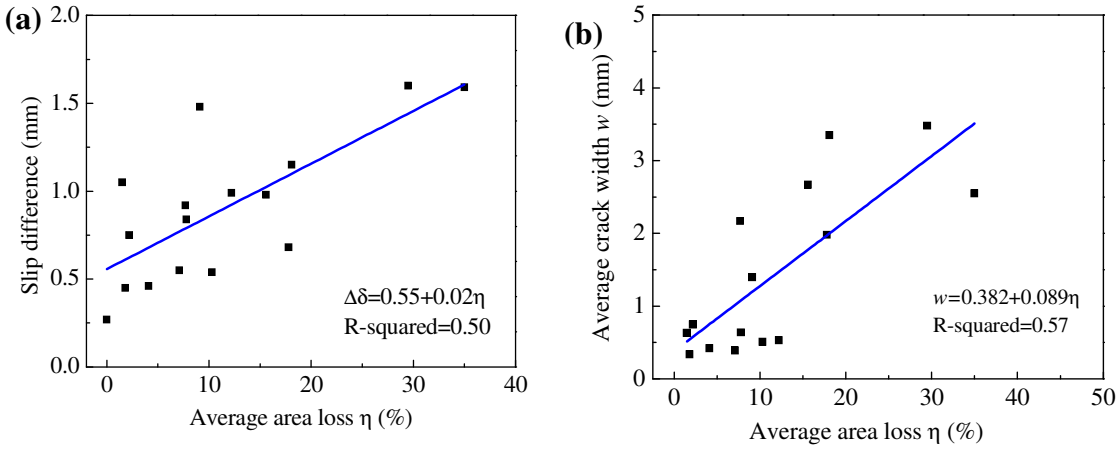

Figure 4.16 Effects of steel bar corrosion on: (a) top-bottom slip difference, (b) average crack width.

4.3.7 Bond Degradation Mechanism. In general, bond between concrete and deformed steel bar in RC structures is controlled by three mechanisms: chemical adhesion, bearing force of ribs against concrete (mechanical interlocking), and friction between concrete and steel. Adhesion is the chemical bond at the interface between the reinforcement and the concrete. At relatively low loads, the chemical adhesion is the dominant bond mechanism. Bearing of ribs against concrete is considered to be the most significant transfer mechanism at high loads. The friction mechanism depends on the surface characteristics of the reinforcing bar.

As reported by Tassios [108], the ideal bond-slip curve of deformed steel bars in concrete can be divided into several stages. In this study, five stages were observed for specimens with uncorroded steel bar, six stages were observed for specimens with slightly corroded steel bar, and four stages were observed for specimens with severely corroded steel bar. The bond-slip curves for various specimens are schematically shown in Figure 4.17. In Stage I, the chemical adhesion between the reinforcing bar and

concrete plays a major role, corresponding to an unnoticeable slip due to strain localization at the bar-concrete interface layer.

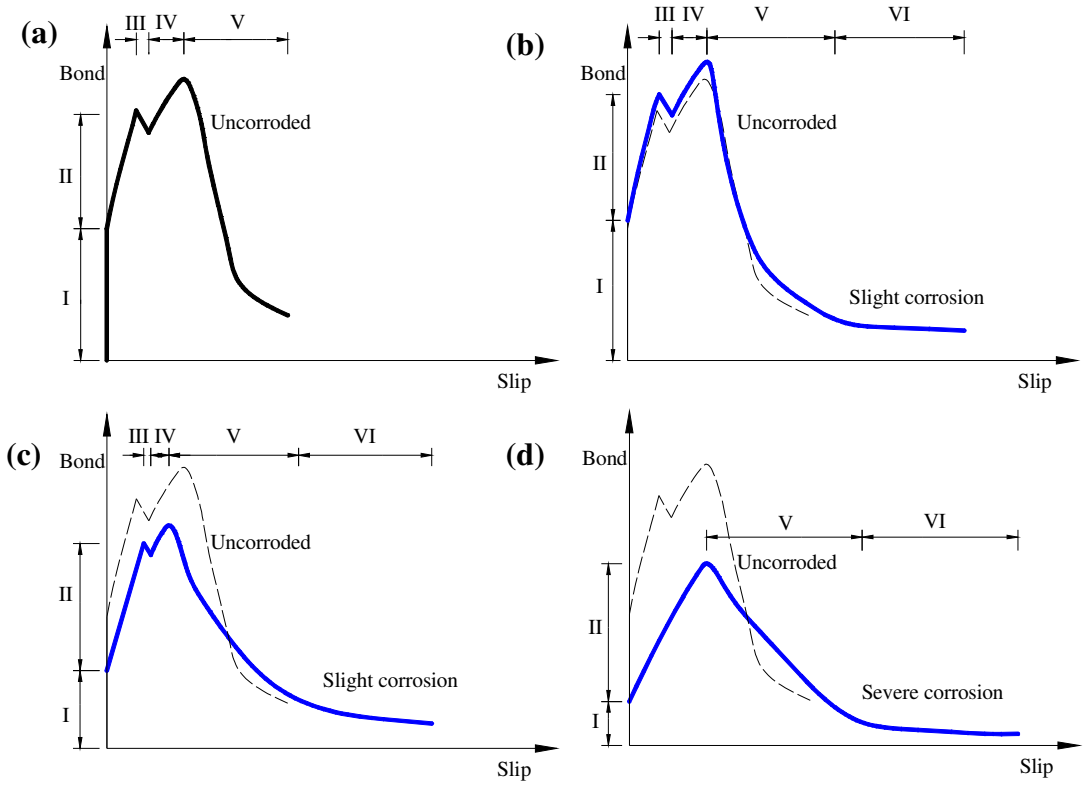

Figure 4.17 Bond-slip curves for: (a) specimens with uncorroded steel bar, (b) specimens with slightly corroded steel bar concentrated at lugs, (c) specimen with slightly corroded steel bar concentrated at ribs, and (d) specimens with severely corroded steel bar.

In Stage II, micro-cracks initiate in concrete near the ribs of the reinforcing bar due to the increased bearing force against surrounding concrete, and continue to penetrate towards the outer face of concrete with an increase of loading. At the same time, the micro-cracks continue to propagate upwards the top portion of the embedded steel bar. Therefore, the crack width continues to increase as shown in Figure 4.10. When the number of micro-cracks that penetrate through the concrete cover and propagate upwards along the steel bar reaches a critical value, a significant drop of bond stress occurs, which is referred to as Stage III. Due to the confinement of stirrups, the outward movement of

cracked concrete will stop and hold the steel ribs tightly again. Therefore, the bond force increases again, which is referred to as Stage IV. For specimens without stirrup confinement, no further bond increase can be observed.

After the bond force increases to a certain value, significant concrete crushing occurs locally and the shear forces of steel bar ribs against the concrete diminish, resulting in a rapid decrease of the bond stress, which is Stage V. With further loading, the steel bar can move for a distance of rib spacing, which is Stage VI. In this study, the friction stage was not observed for specimens with uncorroded steel bar since the applied load dropped rapidly corresponding to 15% of its maximum bond stress. For specimens with slightly corroded steel bar, a relatively flat and smooth friction stage started to appear when the slip of steel bar reached approximately 12.7 mm (rib spacing) as observed in Figures 4.13 (b) and (c).

Corrosion changes the geometry of steel bar particularly for the depth of ribs. Due to varying external environment and non-homogenous concrete cover, corrosion is not uniform along the length of steel bar. This non-uniformity of corrosion makes the interface between the steel bar and concrete change over the embedment length. The ribs of the steel bar may corrode off at some locations and the lugs between two adjacent ribs may deepen due to local active corrosion as indicated in Figures 4.18 (b-2) and (c-2). In some cases, all steel bar ribs might corrode off as shown in Figure 4.18 (d-2). Therefore, the effect of corrosion on the bond behavior of steel bars in concrete is difficult to quantify.

(a-1)

(a-2)

Figure 4.18 Visual observations on steel-concrete interfaces after pullout tests: (1) concrete interface, (2) steel bar surface; (a) uncorroded specimen, (b) slightly corroded specimen on ribs, (c) slightly corroded specimen on lugs, and (d) severely corroded specimen.

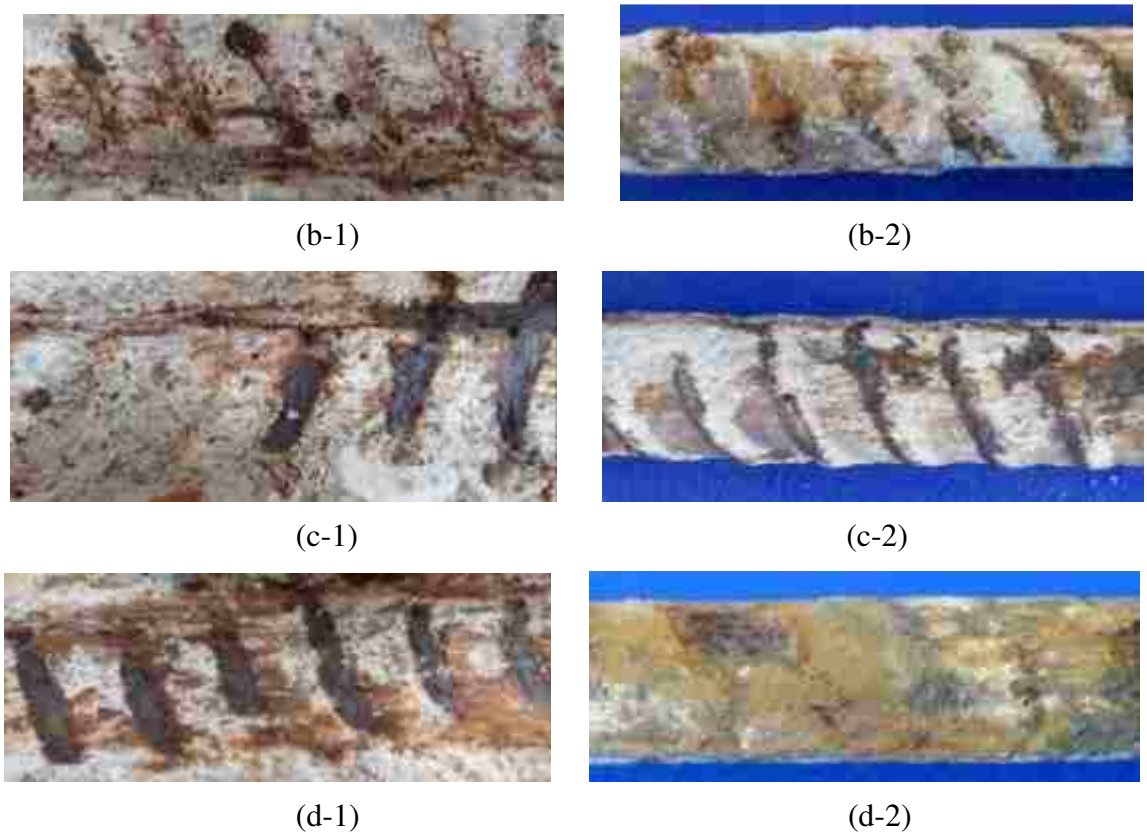

(b-1) (b-2)

(c-1) (c-2)

(d-1) (d-2)

Figure 4.18 Visual observations on steel-concrete interfaces after pullout tests: (1) concrete interface, (2) steel bar surface; (a) uncorroded specimen, (b) slightly corroded specimen on ribs, (c) slightly corroded specimen on lugs, and (d) severely corroded specimen. (cont.)

In this study, the corrosion-induced bond degradation is divided into three scenarios as illustrated in Figure 4.19: steel bar with slight corrosion concentrated on ribs (Figure 4.19(c)), steel bar with slight corrosion concentrated on lugs (Figure 4.19(b)), and steel bar with severe corrosion with all ribs corroded (Figure 4.19(d)). Figure 4.19(a) illustrates the bond condition of the uncorroded steel bar. Their corresponding load-slip curves in comparison with the uncorroded steel bar are schematically demonstrated in Figure 4.17(b-d).

In Stage I, corrosion reduced the chemical adhesion between the steel bar and surrounding concrete. Consequently, the initial bond stress of the corroded steel bar is lower than that of uncorroded steel bar. Stages II-V for specimens with slightly corroded steel bar are similar to those for the specimens with uncorroded steel bar. However, the

specimens with the corrosion of steel concentrated on the lugs may exhibit a higher maximum bond stress than the specimens with uncorroded steel bar (Figure 4.17(b)). The specimens with the corrosion of steel concentrated on the ribs exhibited the lower maximum bond stress than that for the specimens with uncorroded steel bar (Figure 4.17(c)). They can be explained with the aid of their corresponding failure mechanisms in Figures 4.19(b) and (c). The steel bar with corrosion concentrated on the ribs would reduce the bearing force against concrete, thus resulting in a reduced bond stress. The steel bar with corrosion concentrated at the lugs would increase the bearing force against the concrete due to relatively high ribs.

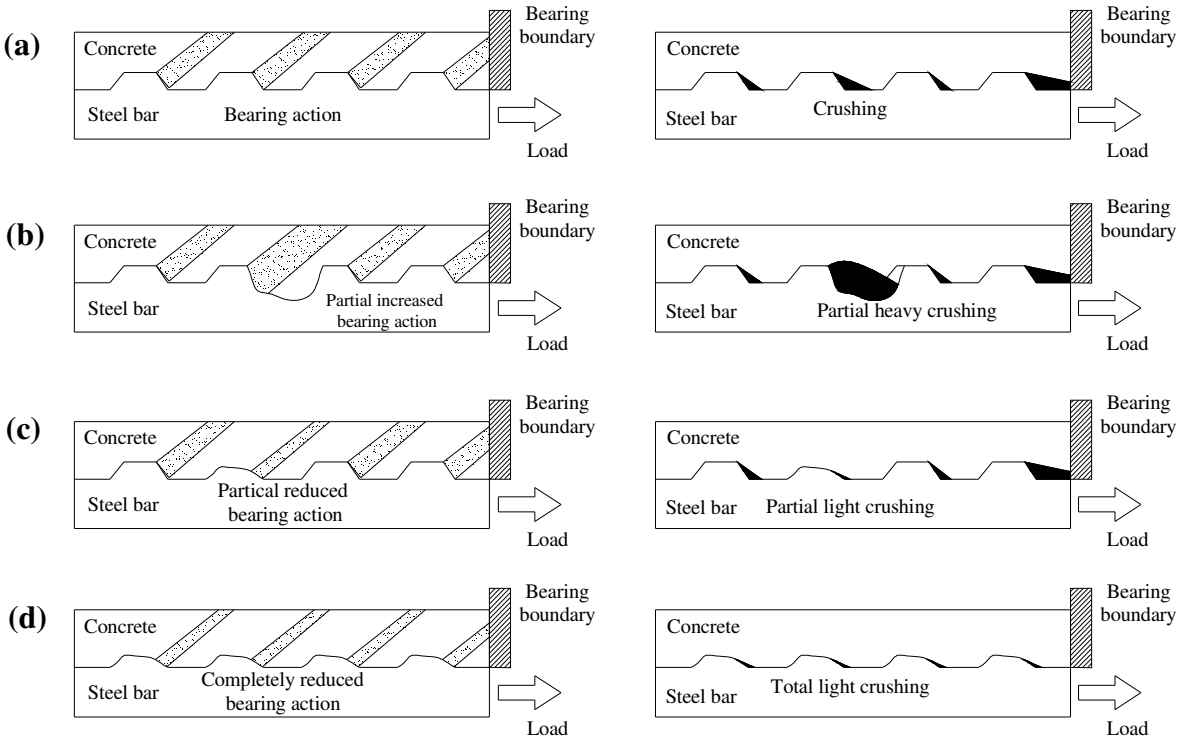

Figure 4.19 Bond degradation mechanisms for specimens with: (a) uncorroded steel bar, (b) slightly corroded steel bar concentrated at lugs, (c) slightly corroded steel bar concentrated at ribs, and (d) severely corroded steel bar.

Specimens with severely corroded steel bar can be characterized with four stages as shown in Figure 4.17(d). This particular characterization can be explained using Figure

4.18(d) and Figure 4.19(d). The absence of Stages III and IV is attributed to the disappearance of the bearing force of bar ribs against the concrete. As shown in Figure 4.19(d), all the ribs stayed attached to the concrete, and a relatively smooth surface could be observed.

4.4 SUMMARY

Based on the test data and analysis, the following conclusions can be drawn:

(1) The cross sectional area of uncorroded steel bars followed a bi-modal distribution due to the effect of bar ribs. The cross sectional area of corroded steel bars was well represented by a normal distribution for relatively uniform corrosion and a bi-modal distribution for non-uniform corrosion with large corrosion pits.

(2) Three stages of acoustic energy release were identified from two types of acoustic emission signals acquired during pullout tests: dominant concrete cracking, balanced concrete cracking and steel-concrete friction, and dominant steel-concrete friction. The acoustic wave generated from concrete cracking propagated in nearby hard materials so that more acoustic energy was distributed over high frequencies (35 – 41 kHz) while the acoustic wave from the friction between the steel bar and concrete propagated in nearby softened materials during previous concrete cracking so that more energy was distributed over low frequencies (3 – 15 kHz).

(3) Acoustic energy is more sensitive to the number and size of cracks and less to the level of corrosion. As such, the frequencies identified from concrete cracking are almost the same with or without corrosion since both many new cracks on uncorroded specimens and few new cracks plus old crack propagation on corroded specimens released significant acoustic energy. On the other hand, the average frequency of friction-induced acoustic signals is 12 kHz for uncorroded specimens, 8 kHz for corroded specimens with less and small concrete cracks, and 7.7 kHz for corroded specimens with many large concrete cracks.

(4) The maximum bond stress decreased with an increase of corrosion level in terms of average area loss and with an increase in crack width. At the same time, the difference between the bar slips at the top and bottom concrete faces and the average crack width increased with the area loss. However, all the above correlations are weak

with R-square values ranging from 0.37 to 0.50. The number and size of concrete surface cracks were found to result in more reduction of bond stress than the corrosion-induced area loss.

(5) Three mechanisms of corrosion-induced bar-concrete bond degradation were identified: chemical adhesion, mechanical interlocking, and bar-concrete friction. With no noticeable slip, chemical adhesion was reduced when the passive film formed on steel bar surface started degrading due to the attack of aggressive chloride ions. With significant slipping, the bar-concrete friction was reduced due to the soft corrosion products formed in between the steel bar and concrete.

(6) With intermediate slipping, the mechanical interlocking degraded in a more complicated way. Corrosion at a lug between two adjacent ribs likely increased the local bearing force of the ribs against surrounding concrete. On the other hand, corrosion at a rib likely reduced the local bearing force of the rib against surrounding concrete. For severely corroded steel bars, the commonly-observed local increase and decrease bond stress stages on a bond-slip curve, associated with micro-cracking and propagation, disappeared since severe corrosion made the bar ribs become flattened.

5. ELECTROCHEMICAL BEHAVIOR OF ENAMEL COATED CARBON STEEL IN SIMULATED CONCRETE PORE WATER SOLUTION WITH VARIOUS CHLORIDE CONCENTRATIONS

5.1 INTRODUCTION

Enamel coating has been widely used to protect metals or alloys from corrosion due to its strong adherence to the substrate and its chemical stability in various environments including acid, alkaline, high temperature, and harsh working conditions [109, 110]. Enamel coated carbon steel has long been used for chemical reactors, heat exchangers, and food-processing vessels in industry as well as cookware in domestic applications. Commercial enamel is a silica-based glass-forming material containing various oxides to obtain optimum properties for specified applications. The enamel is typically fused to the substrate metals at temperatures between 750°C and 850°C. The properties of enamel can be controlled either by adjusting the components or percentages of oxides or by pretreating substrate metals [111]. For example, acid resistance is obtained by increasing the SiO_2 content and reducing B_2O_3 and BaO; water resistance is achieved by adding TiO_2; alkaline resistance is improved by adding ZrO_2 [112]; adherence to substrate metals is increased by adding CoO and NiO [113]; and the hardness of coating is improved by crystallization treatment [114].

Recently, a number of studies have been performed at Missouri University of Science and Technology to investigate the performance of enamel as a coating material applied on reinforcement steel to (i) reduce the corrosion rate [23, 115] and (ii) enhance the bond strength with steel and surrounding concrete [116, 117]. Three types of enamel coatings were investigated including pure enamel (PE), mixed enamel (ME) and double (DE). The PE is a commercially available product (PEMCO International) and used as a benchmark in this study. It was selected because it contains ZrO_2 for improved durability of glasses in alkaline environments, and NiO and CoO for increased adherence with steel substrates. The ME is a mixture of 50% PE with 50% calcium silicate by weight. Calcium silicate was added to modify the mechanical property of the PE, improving the interface transition zone between the concrete and steel rebar that has traditionally been a weak link due to bleed water and lack of small cement particles in the shadow of the

concrete aggregates [118]. Our previous studies showed that an average increase of approximately 15% in bond strength was observed for deformed steel rebar in concrete and as much as a seven times increase in bond strength for smooth steel rods in mortar in comparison with uncoated rods [116, 117]. The DE has an inner PE layer and an outer ME layer; it was developed to enhance the corrosion resistance of steel rebar by the inner layer and increase the bond strength of steel rebar with surrounding concrete by the outer layer.

For deformed steel rebar tested in 3.5 wt.% NaCl solution, all three enamel coatings can reduce the corrosion rate of the steel by 12-20 times [115] even though the coating thickness on the surface of deformed rebar was non-uniform due to the rebar deformation and limitations in the chosen fabrication process. For smooth steel rebar in mortar cylinders tested in 3.5 wt % NaCl solution, the PE and DE coatings can reduce the corrosion current density of the steel rebar by 50 and 360 times, respectively; the ME coating only reduced the current density by three times [23]. However, due to the influence of mortar cover, particularly with its non-homogeneity and diffusion behavior, both the coating properties and the coating/steel interface properties could not be accurately evaluated particularly for DE coated samples. Moreover, the thickness of enamels applied on the smooth steel rebar was relatively thin due to curvature effects, making it difficult to compare the properties of the three enamel coatings.

To avoid the complexity involved in mortar or concrete, saturated $Ca(OH)_2$ solutions often have been used to simulate the alkaline environment of concrete pore water [119-121] because it is the main product from the hydration process of cement as follows [118]:

$$2Ca_3SiO_5 + 11H_2O = 3CaO{\cdot}2SiO_2{\cdot}8H_2O + 3Ca(OH)_2 \quad (5.1)$$

$$2Ca_2SiO_4 + 9H_2O = 3CaO{\cdot}2SiO_2{\cdot}8H_2O + Ca(OH)_2 \quad (5.2)$$

Therefore, in the present study, the electrochemical properties of enamel coatings applied on structural steel plates are studied in saturated $Ca(OH)_2$ solution with different chloride concentrations. The phase compositions of the three different enamel coatings and the morphologies of the coatings and the coating-steel interfaces were characterized by X-ray diffraction (XRD) and scanning electron microscopy (SEM). Moreover, the tensile strength of each enamel coating was determined with direct pull-off tests.

5.2 EXPERIMENTAL

5.2.1 Preparation of Enamel Coatings and Test Samples. Carbon steel plates of 76.2 mm × 38.1 mm in size and 3.18 mm in thickness were used in this study. The chemical composition by weight is: 0.27% C, 0.28% Si, 1.03% Mn, 0.05% S, 0.03% P, and the balance Fe. The plates were coated by Pro-Perma Engineered Coatings with three types of enamel (PE, ME, and DE). Prior to coating, all steel plates were sand-blasted and cleansed with a commercially available cleansing solvent.

Table 5.1 Chemical composition of alkali borosilicate glass frits.

Composition	SiO_2	B_2O_3	Na_2O	K_2O	CaO	CaF_2	Al_2O_3	ZrO_2	MnO_2	NiO	CoO	Total
Amount (wt.%)	44.0	19.3	15.8	2.8	0.0	4.7	4.6	5.3	1.5	1.0	0.9	100

The commercially available alkali borosilicate glass frit (PEMCO International) was used to prepare the PE coating [122], and its chemical composition is given in Table 5.1. The PE slurry was made by first adding 454 kg of glass frit into 189.3 liters of water and mixing them for 20 min., and then adding 31.8 kg of clay and 2.3 kg of borax as suspension agents and mixing again for 3.5 hrs. The ME coating was obtained by adding 50% calcium silicate to 50% the alkaline borosilicate glass frit by weight, and then following the same procedure to produce a slurry. Calcium silicate was directly taken from Portland cement as specified in ASTM C150-07 [123]. The DE coating consists of two layers: an inner PE layer and an outer ME layer.

For PE and ME coatings, the steel plate samples were dipped into their corresponding slurries, heated at 150 °C for 2 min. to drive off moisture, then fired at 810 °C for 10 min., and finally cooled to room temperature. For the DE coating, the steel plates were first dipped into the PE slurry, heated at 150 °C for 2 min. to drive off moisture, and fired at 810 °C for 10 min. They were then dipped into the ME slurry, heated at 150 °C for 2 min. again to drive off moisture, and finally fired at 810 °C for 10 min. The firing treatment melted the glass frit and chemically bonded the enamel to the steel substrate.

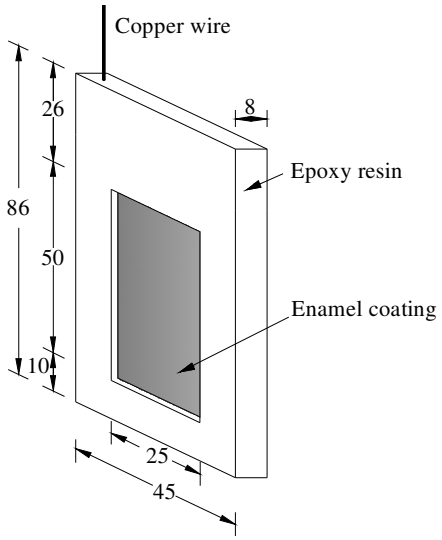

Figure 5.1 Schematic view of the steel plate sample used in the electrochemical experiments (unit: mm).

For each enamel coated steel plate schematically illustrated in Figure 5.1, one corner was ground off to expose the steel for a soldering connection with a copper wire for electrochemical measurements. All four side edges and the back face of the steel plate were covered with EpoxyMount (ALLIED). Therefore, only the center portion on the front face of all steel plates, approximately 12.5 cm^2, was potentially exposed to the test solution. For comparison, uncoated steel plates were also prepared and characterized. Three steel plate samples were prepared and tested in each condition to ensure the repeatability of the test data.

5.2.2 Characterization of Enamel Coating. The morphologies of enamel coated samples were investigated by SEM (Hitachi S4700). A small piece of an enamel coated steel plate, 20 mm×5 mm in size, was sectioned with a diamond blade, and directly used for the surface SEM imaging. Another small piece of the sample was cut across the cross section and cold-mounted with EpoxyMount. The cross section was then ground with silicon carbide papers to 1200 grit. The ground sample was rinsed with deionized water, cleansed with acetone, and finally dried in an oven preset at 60°C prior to SEM imaging. The phase composition was directly examined with XRD (Philip X' Pert) tests on the surface of enamel coated steel plates.

5.2.3 Pull-off Test. The tensile strength of enamel coatings on steel plates was determined following ASTM D4541-09 with an automatic PosiTest pull-off tester. To reduce the risk of adhesive failure, the bottom face of a 14-mm-diameter dolly and the enamel coating surface were slightly abraded with sandpaper and cleansed with acetone. The dolly was then adhered to the enamel surface of an enamel coated steel plate with Araldite multi-purpose adhesive. After the adhesive was cured for 24 hrs, the enamel coating was scored around the perimeter of the dolly before the dolly was pulled off perpendicular to its interface with the enamel coated plate at a stress rate of 0.41 MPa s^{-1}. The maximum strength of each test sample was recorded.

5.2.4 Electrochemical Tests. Saturated $Ca(OH)_2$ solution was prepared by mixing certified $Ca(OH)_2$ powder (Fisher Scientific) into distilled water in a 500 mL glass beaker. The chloride concentration in the simulated concrete pore solution was incrementally increased to 0.01, 0.05, 0.10, 0.50, and 1.00 mol L^{-1} by adding NaCl granules (Fisher Scientific) into the glass beaker. A steel plate sample was first immersed in the saturated $Ca(OH)_2$ solution for three days so that a relatively stable passive film would be developed on the uncoated steel [84, 121]. Electrochemical measurements were then performed with the coated steel before the pH value of the solution was measured. After the first electrochemical test, NaCl granules were added into the solution to achieve a chloride concentration of 0.01 mol L^{-1}, and the steel plate sample continued to be immersed for another three days prior to the next pH and electrochemical measurements. This process was repeated until the chloride concentration in the solution reached 1.00 mol L^{-1} and the tests were completed. For proper chloride concentration adjustments, a

magnetic stirring bar was placed at the bottom of the glass beaker and was set to rotate and continuously mix the test solution for 10 min. per day in between two electrochemical tests. To reduce the potential carbonation of the saturated $Ca(OH)_2$ solution, all glass beakers remained covered with plastic sheets except when the NaCl was added or during electrochemical testing.

Open circuit potential (OCP), lineal polarization resistance (LPR) and electrochemical impedance spectroscopy (EIS) tests were used to monitor the electrochemical behavior of uncoated and enamel coated steel plates. The three-electrode system used for the electrochemical tests included a platinum sheet (25.4 mm×25.4 mm×0.254 mm) as counter electrode, a saturated calomel electrode (SCE)as reference electrode, and a steel plate as working electrode. All three electrodes were connected to a Gamry, Reference 600 potentiostat/galvanostat/ZRA for data acquisition. A stable OCP was recorded before each EIS measurement, which used a sampling rate of 5 points per decade with an applied sinusoidal potential of 10 mV amplitude around the OCP and with frequency ranging from 100 kHz to 0.005 Hz. The LPR curves were measured within 15 mV around the OCP at a scan rate of 0.167 mV s^{-1}. The polarization resistance, R_p, is equal to the slope of the polarization curve around zero current and is calculated by:

$$R_p = \Delta V / \Delta I \tag{5.3}$$

in which ΔV and ΔI represents the applied potential difference and the measured current difference, respectively, in the linear portion of the polarization curve around I=0. The polarization resistance was used to evaluate the corrosion current density, j, according to the Stern-Geary equation [12]:

$$j = B / AR_p \tag{5.4}$$

where A is the surface area of a sample exposed to the test solution (12.5 cm^2), and B is a constant related to the anodic and cathodic Tafel slopes. In this study, B = 26 mV was used for simplicity [84, 124].

5.3 RESULTS AND DISCUSSION

5.3.1 Characterization of the Coatings.

5.3.1.1 Phase composition. X-ray diffraction patterns of the calcium silicate powder from Portland cement and the three enamel coatings are presented in Figure 5.2. It can be clearly seen from Figure 5.2(a) that the primary crystalline phase of the cement power is tricalcium silicate, Ca_3SiO_5, which is in agreement with the principle constituents of cement. The PE is dominated by an amorphous hump centered at 2θ=27°, which is consistent with the glassy nature of this borosilicate material as will be discussed below. Other small peaks indicate the presence of a small amount of crystalline SiO_2 (quartz).

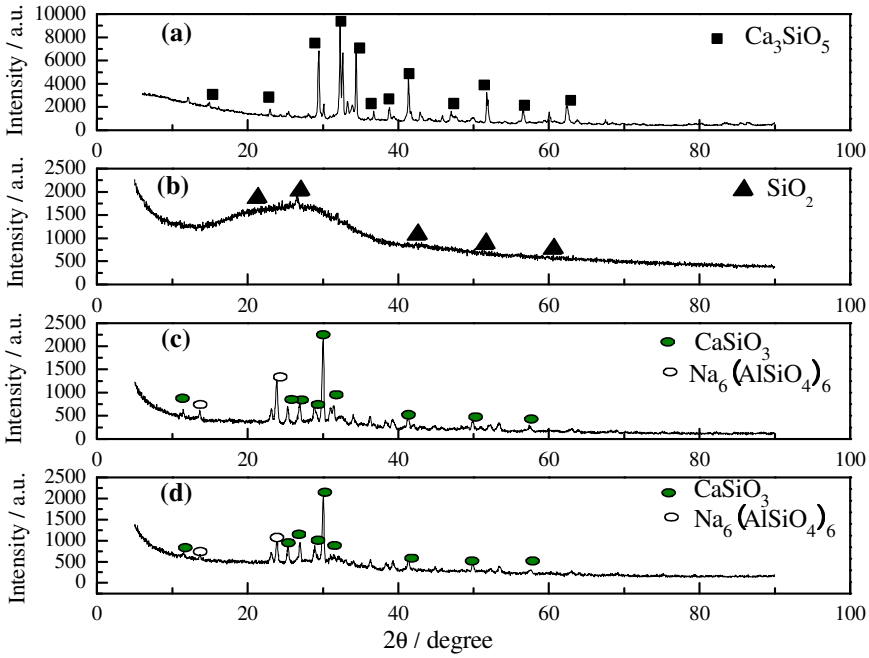

Figure 5.2 XRD patterns for: (a) ordinary Portland cement, (b) PE, (c) ME, and (d) DE coatings.

The ME and DE coatings are dominated by a principal phase of crystalline wollastonite $CaSiO_3$ as illustrated in Figures 5.2(c) and 5.2(d). A minor phase of $Na_6(AlSiO_4)_6$ is also detected. It can be observed that the dominant phase Ca_3SiO_5 in cement has been transformed to $CaSiO_3$ as a result of the combined effect of cement

hydration in the slurry, reaction with the borosilicate frit, and the thermal treatment used to bond the enamel to the steel.

5.3.1.2 Surface, cross-sectional and enamel-steel interfacial morphologies. Figure 5.3 shows the SEM images of the surface and cross-sectional views of three enamels coated on carbon steel. It can be clearly observed that the surface and cross-sectional morphologies of the three enamel coatings are quite different. The PE has a smooth and glassy surface with a few pin-holes resulting from bubbles in the frit, as shown in Figure 5.3(a-1). From the cross-sectional view in Figure 5.3(a-2), the PE coating (300 μm thick) has a microstructure with isolated air bubbles trapped during the firing process, which is typical of enameled steel. These air bubbles were formed from gases such as CO_2, CO, H_2O and H_2 as a result of high temperature chemical reactions between the carbon, iron and other elements in the steel and the water and oxides in the enamel frits [125]. Figure 5.3(a-2) also indicates that no trace of fish scaling was observed at the steel-enamel interface due to the occurrence of large bubbles as pointed out by Yang et al. [126]. The ME and DE surfaces, shown in Figures 5.3(b-1) and 5.3(c-1), are also both much rougher than the PE surface due to the altered microstructures from the added calcium silicate. As illustrated in the cross-sectional view in Figure 5.3(b-2), the ME coating (250 μm thick) has a number of open channels that are interconnected in the outer portion of the coating thickness with no large air bubbles. This is because the addition of calcium silicate formed small open channels through which the gases generated during the enameling process were released. As illustrated in Figure 5.3(c-2), the DE coating (300 μm thick) has two distinctive layers. The inner PE layer (150 μm thick) has larger air bubbles than those in the PE coating, which were likely accumulated due to the high viscosity of the outer ME layer. The largest air bubble was approximately 300 μm on a side, which is several times greater than that in the PE coating. There is no evidence of interconnected channels through the DE coating thickness as was observed in the ME coating.

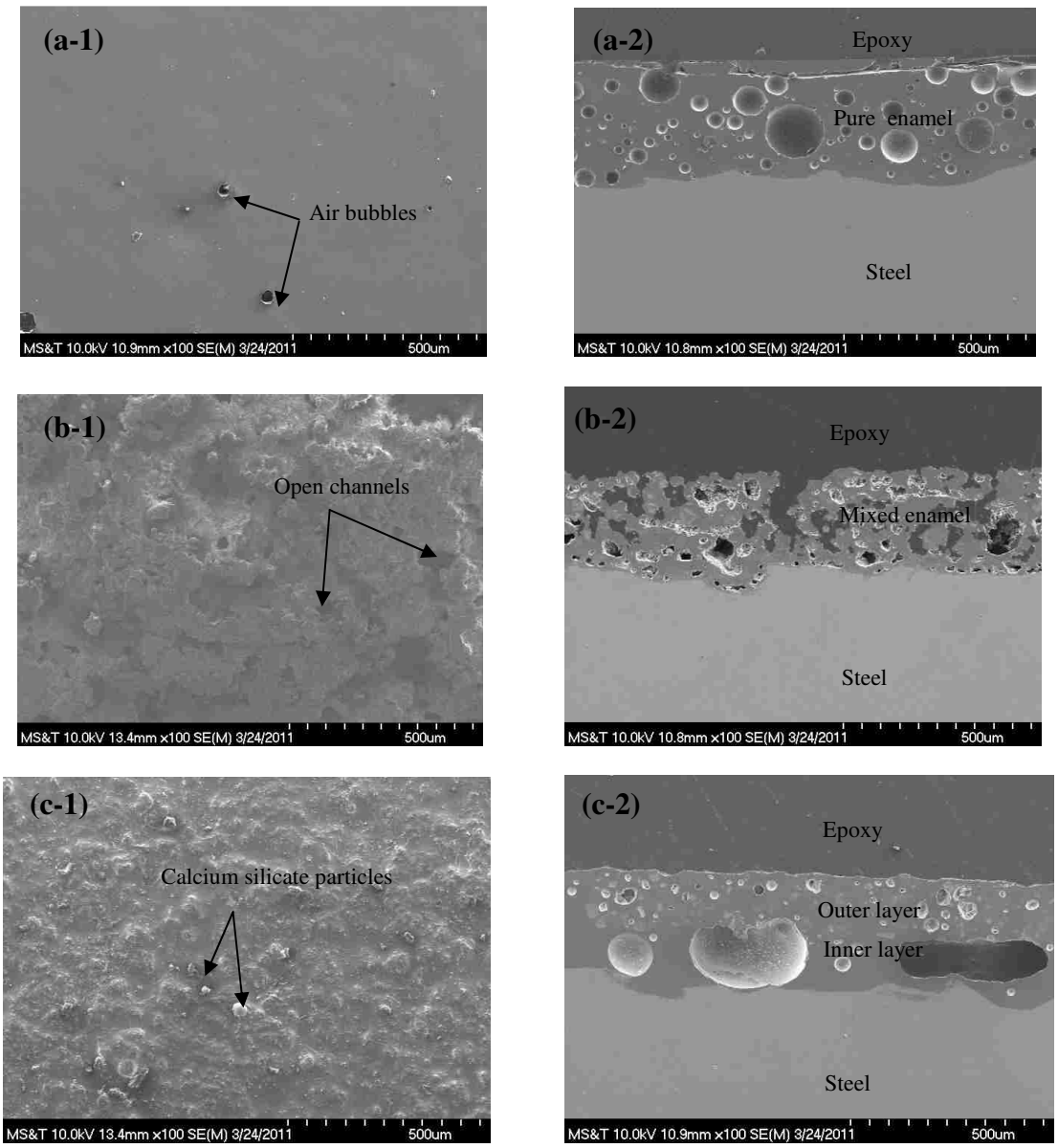

Figure 5.3 SEM images for (1) surface and (2) cross-sectional morphologies of: (a) PE, (b) ME, and (c) DE coatings.

Figure 5.4 shows highly magnified SEM cross-sectional images of the three enamel coatings and their corresponding enamel-steel interfaces. As depicted in Figure 5.4(a-1), the PE coating is relatively uniform with the largest bubbles approximately 50 μm in diameter. The ME (Figure 5.4(b-1)) has a complex structure with the calcium silicate distributed in the enamel matrix and the epoxy filled in the open channels. The epoxy was used to prepare the samples for SEM imaging. Calcium silicate is also present

in the outer layer of DE coating but absent in the inner layer (Figure 5.4(c-1)). Both the PE and DE coatings are wetted well to the underlying steel as shown in Figures 5.4(a-2) and 5.4(c-2). There exist small pores at the enamel-steel interface of the ME coated samples as indicated in Figure 5.4(b-2).

It can be seen from enamel-steel interfacial morphologies as shown in Figure 5.4 that, for all three enamel coatings, many small, Fe-rich protrusions were interconnected to form the so-called anchor points at the enamel-steel interface. These features have been described in the literature as resulting from the following reaction [113]:

$$FeO + [CO, H_2] = Fe + [CO_2, H_2O] \quad (5.5)$$

$$2FeO + SiO_2 = Fe_2SiO_4 \quad (5.6)$$

These protrusions increase the roughness and adherence strength of the enamel-steel interface [127-129].

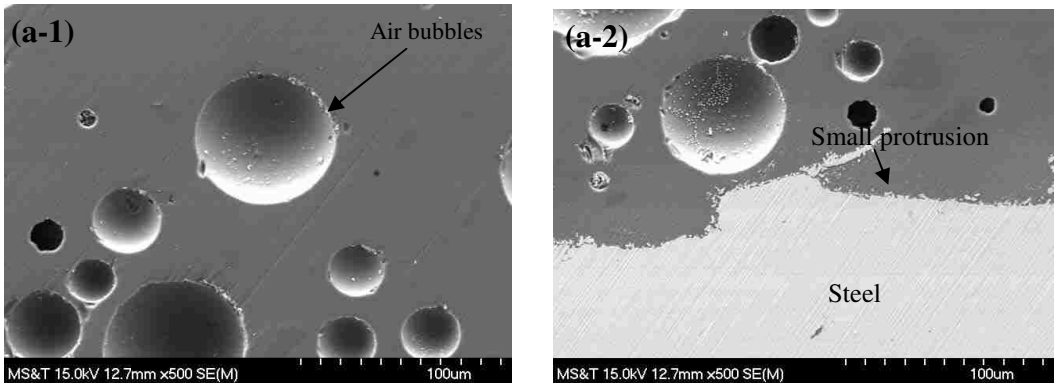

Figure 5.4 SEM images for (1) cross section and (2) steel-enamel interface of (a) PE, (b) ME, and (c) DE coating at high magnification.

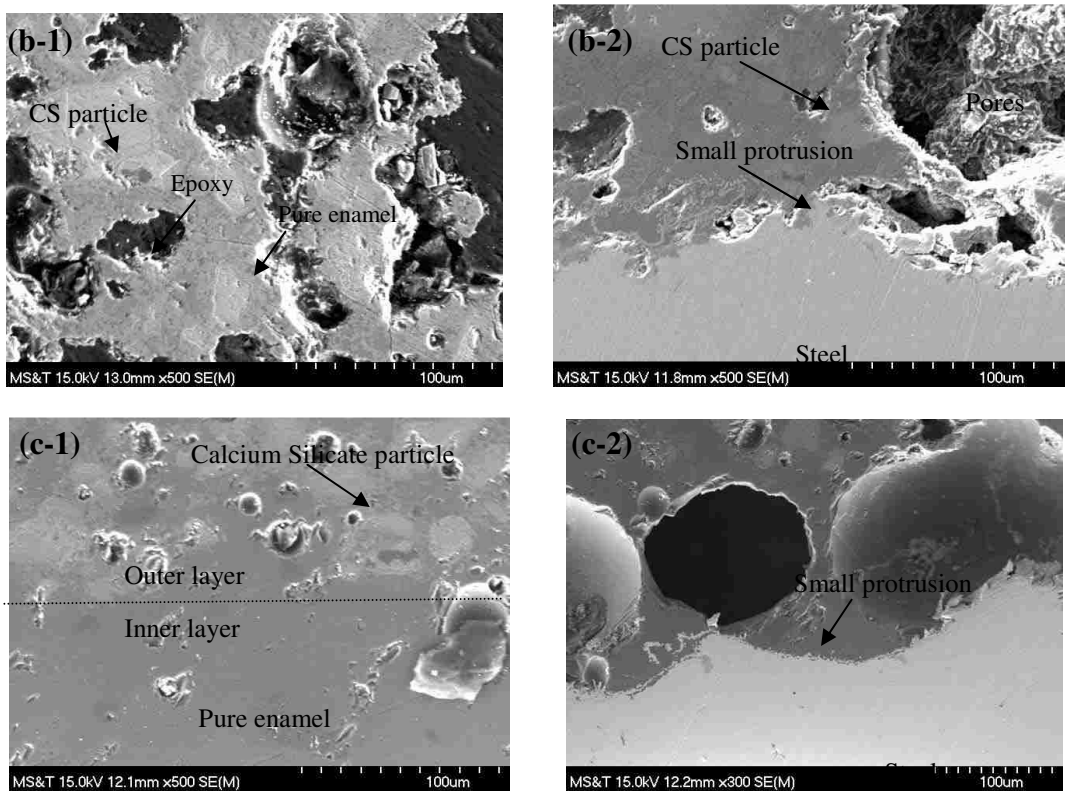

Figure 5.4 SEM images for (1) cross section and (2) steel-enamel interface of (a) PE, (b) ME, and (c) DE coating at high magnification. (cont.)

5.3.2 Tensile Strength of Enamel Coatings. At the completion of the pull-off tests, the dollies were separated from their steel plate substrates. Optical micrographs of representative peeled steel plates are presented in Figures 5.5(a-1), 5.5(b-1) and 5.5(c-1) for PE, ME and DE coated samples, respectively. It was observed that all samples fractured within the enamel coatings – typical cohesive failure modes. The optical microscopic fracture interfaces are displayed in Figures 5.5(a-2), 5.5(b-2) and 5.5(c-2).

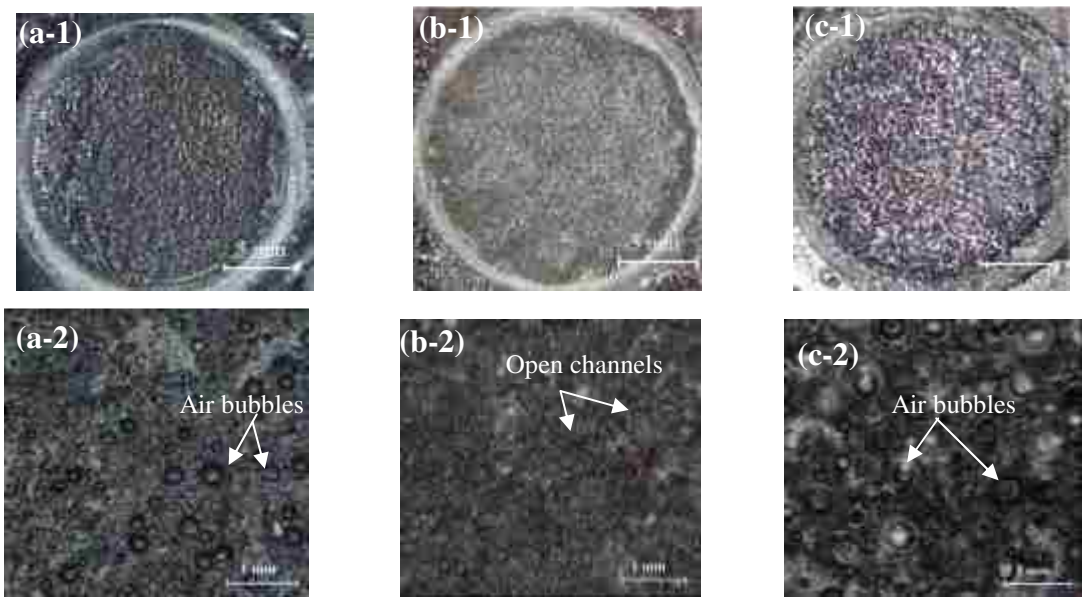

Figure 5.5 Optical micrographs of the fracture interfaces after pull-off tests at (1) low magnification and (2) high magnification of (a) PE, (b) ME, and (c) DE coated steel plates.

Table 5.2 Cohesive strength of various enamel coatings

Coating type	Pure enamel	ME	DE
cohesive strength / MPa	6.36±0.66	7.87±0.33	4.90±0.67

As shown in Figure 5.5(a-2), the PE coating fractured across the large air bubbles. Similar to the PE coating, the fracture surface of the DE coating as shown in Figure 5.5(c-2) was also across the air bubbles in the inner layer, which are even larger than those in the PE coating, as illustrated in Figure 5.5(a-2). The ME has a relatively dense fracture interface despite the presence of small interconnected channels as depicted in Figure 5.5(b-2). The average cohesive strengths of the three enamel coatings and their variations are given in Table 5.2. The variation of cohesive strengths for each enamel coating is less than 14% of their corresponding average strength. The ME and DE coatings have the highest and lowest cohesive strength, respectively, among the three coating systems. This is because the added calcium silicate altered the microstructure of the PE with isolated air bubbles to that of the ME with open channels, which released gases generated during the firing process and avoided the occurrence of large air bubbles

as discussed previously. However, the air bubbles in the inner layer of the DE coating are larger than those in the PE coating since the gases formed in the inner layer of the DE coating during the firing process appear to have been trapped by the highly viscous outer layer of the DE coating, resulting in a weaker link under the tensile load.

5.3.3 Electrochemical Measurements.

5.3.3.1 Open-circuit potential and corrosion current density. The pH values of the saturated $Ca(OH)_2$ solution were approximately 12.7 without addition of sodium chloride, then dropped to a value of around 12.5 when the chloride content reached 1.00 mol L^{-1}. This appears to be due to the carbonation of the solution during various tests and the addition of sodium chloride. No significant difference of pH values among the four samples was observed even after the initiation of corrosion had occurred in the uncoated steel plate.

Figure 5.6(a) presents the average and the standard deviation of open circuit potentials (OCPs) for various samples in the saturated $Ca(OH)_2$ solution with various chloride concentrations. In general, the variation of three data points for each test condition is small, indicating consistent test results. The PE and DE coated samples have relatively stable values with an average of approximately -100 mV and -240 mV, respectively. The OCPs of the uncoated steel samples decreased from -110 to -430 mV when the chloride concentration was increased from 0.01 to 0.10 mol L^{-1}, and continued to gradually decrease as the chloride content increased. With regard to the ME coated steel samples, the potentials decreased gradually except for a significant drop from -410 to -490 mV when the chloride content reached 0.5 mol L^{-1}. The significant drop of OCPs in uncoated and ME coated steel plates indicated the initiation of pitting corrosion due to a local breakdown of the passive film. The chloride concentration at the breakdown of passive film in this study agrees well with that in the literatures [84, 130, 131]. When the chloride concentration is less than 0.05 mol L^{-1}, the OCPs of all the test samples are ranked in descending order as: -122 mV for the uncoated steel plate, -211 mV for the PE coated steel plate, -245 mV for the DE coated steel plate, and -382 mV for the ME coated steel plate. These differences in potential are likely related to the microstructures of the passive film as affected by the enamel coatings.

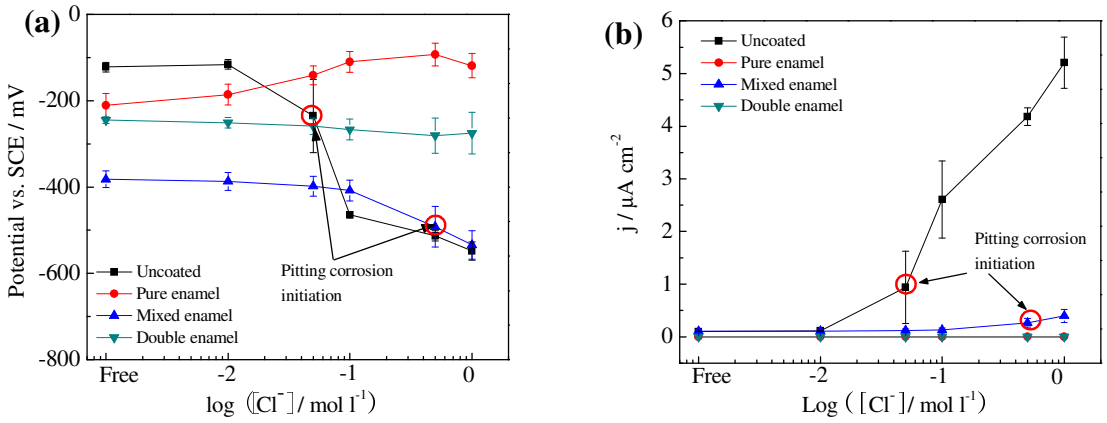

Figure 5.6 Changes of (a) open circuit potential, and (b) corrosion current density of various steel plate samples in the saturated $Ca(OH)_2$ solution with different chloride concentrations.

Figure 5.6(b) displays the average and standard deviation of corrosion current densities calculated from equation (5.4) as a function of chloride concentration. Except for the uncoated steel plate samples, the three data points for each condition are quite consistent. Throughout the testing, the corrosion current densities of the PE and DE coated steel samples remained at 0.05 nA cm^{-2} and 0.50 nA cm^{-2}, respectively. The corrosion current density of the uncoated steel sample increased from 0.11 to 0.94 μA cm^{-2} when the chloride content increased from 0.01 to 0.05 mol L^{-1}, and the corrosion current density of the ME coated sample increased from 0.10 μA cm^{-2} to 0.50 μA cm^{-2} when the chloride content increased from 0.10 to 0.50 mol L^{-1}. The significant increase of corrosion current densities for uncoated and ME coated steel plates are attributed to the initiation of pitting corrosion as observed in the OCPs.

5.3.3.2 EIS tests with plate samples. Figure 5.7 shows representative EIS diagrams for uncoated and three types of enamel coated steel plate samples in the saturated $Ca(OH)_2$ solution with different chloride concentrations. It is noted that the Nyquist diagrams are not in the same unit scale, the scattered symbols are the experimental data, and the solid line represents the fitted results using equivalent circuits as will be discussed later. After immersion in the saturated $Ca(OH)_2$ for three days, the impedance magnitude of the uncoated steel plate reached approximately 100 kΩ cm^2 at 5

mHz as shown in Figure 5.7(a-2). This is attributed to the formation of a dense passive film on the steel surface. The passive film remained effective until the chloride content reached 0.05 mol L^{-1} when a significant decrease of impedance was observed due to the initiation of pitting corrosion. Unlike the uncoated steel sample, the PE coated sample possesses a capacitive behavior until the chloride content reached 0.05 mol L^{-1} as shown in Figure 5.7(b-1). The radius of the capacitive arc decreased with the increase in chloride concentration. When the chloride content reached 0.10 mol L^{-1}, a small tail appeared at low frequencies. This tail was associated with the diffusion of oxygen throughout the corrosion products formed around the small coating defect [132, 133], and it gradually became more significant as the chloride content in the solution increased.

When the chloride concentration was less than 0.50 mol L^{-1}, little change was observed in the impedance diagrams of the ME coated samples. However, as the chloride reached 0.50 mol L^{-1}, a notable decrease of impedance magnitude appeared as shown in Figure 5.7(c-2). This is attributed to the initiation of pitting corrosion on the exposed steel in the open channels of the ME coating as discussed previously. Figure 5.7(d) shows the EIS results of the DE coated steel sample. Two depressed loops are present in the impedance diagram with a chloride concentration of less than 0.50 mol L^{-1}. Similar to the PE coated steel sample, the DE coated steel sample experienced the diffusion behavior when the chloride content reached 1.00 mol L^{-1} due to precipitation of corrosion products on the coating defects. The reason that the diffusion behavior was observed on the PE and DE coated steel samples but not on the uncoated and ME coated samples is that the coating defects on the PE and DE coating are relatively small while the passive film on the uncoated sample and the ME coating are porous with numerous open channels. Therefore, the precipitation of corrosion products at small active sites (corrosion pits) on the uncoated and ME coated samples did not change the overall behavior even after the chloride content became significant.

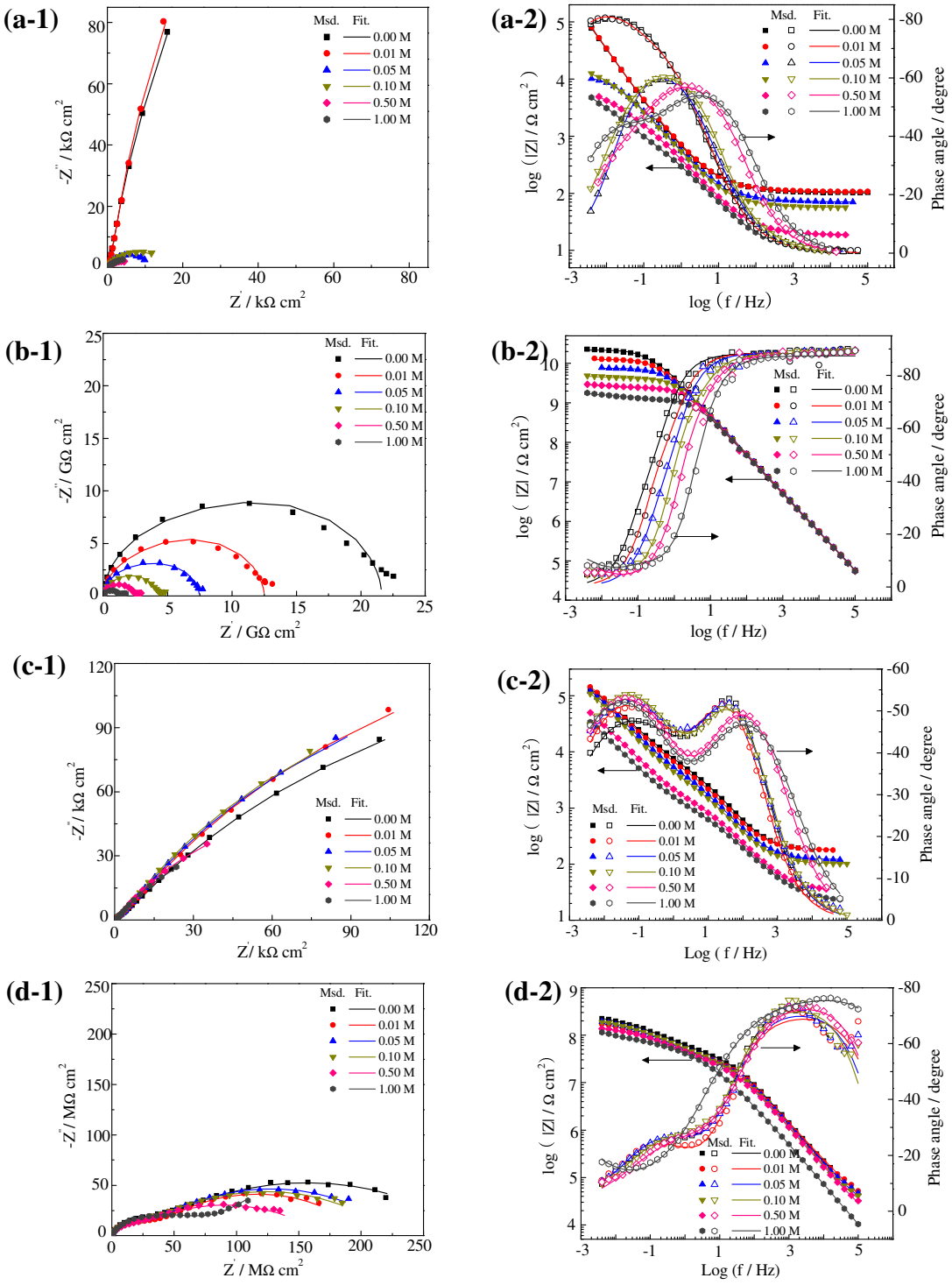

Figure 5.7 Representative EIS diagrams: (1) Nyquist plot and (2) Bode plot for (a) uncoated, (b) PE coated, (c) ME coated, and (d) DE coated steel plates in the saturated $Ca(OH)_2$ solution with different chloride concentrations.

Various equivalent electric circuit models have been used to interpret impedance spectra on passive and active metal surfaces as well as metal surfaces with different coatings [134-137]. In this study, two equivalent electrical circuits as shown in Figure 5.8 were used to fit the EIS test data with ZsimpWin software [138-140]. The suitability of these fits was measured by a threshold Chi-squared value of 10^{-3} for all cases. Model (a) was used for samples with a PE coating, and Model (b) was for uncoated, ME and DE coated samples. Although the PE coated sample appeared to be dominated by one capacitive behavior as indicated in Figure 5.7(b-1), it can be more accurately simulated with two time constants because both the PE properties and the electrochemical reaction at the steel-electrolyte interface were closely related to small coating defects, which are too small to distinguish in the EIS diagram [141]. Model (a) excluded the solution resistance due to the dominant properties of the PE while Model (b) included the solution resistance due to their relatively poor properties in comparison with the PE. The Warburg impedance *W* was included both in Model (a) and (b) to simulate the observed diffusion behavior.

In each equivalent circuit model, a constant phase element (CPE) instead of a pure capacitor is used to represent the non-homogeneity of the corrosion system under study. The non-homogeneity mainly comes from the non-uniform thickness of the passive film and enamel coatings, coating defects, formation of corrosion pits and precipitation of corrosion products [142-145]. A CPE is defined by two parameters *Y* and *n,* and its impedance is represented by:

$$Z_{CPE} = Y^{-1}(j\omega)^{-n} \tag{5.7}$$

where *Y* is a parameter with dimension of Ω^{-1} $cm^{-2}s^{n}$, which is directly proportional to the capacitance of a pure capacitive electrode [119], ω is the angular frequency in rad s^{-1}, and *n* is an index that represents the deviated degree of the capacitance of the electrode from a pure capacitor. A CPE resembles a pure capacitor with capacitance *Y* when $n = 1$, the Warburg element with admittance *Y* when $n = 0.5$, a resistor with resistance Y^{-1} when $n = 0$, and an inductor when $n = -1$.

In the equivalent circuits shown in Figure 5.8, R_s is the solution resistance, R_c and CPE_c represent the coating capacitance and coating resistance for the enamel coated samples and the passive film property for the uncoated steel sample; R_{ct} and CPE_{dl} are associated with the charge transfer resistance and the double layer capacitance of the underlying steel/electrolyte interface; and W is the Warburg impedance. CPE_c is represented by Y_c and n_c; and CPE_{dl} is by Y_{dl} and n_{dl}. An effective capacitance can be evaluated by [146, 147]:

$$C = Y^{1/n} R^{(1-n)/n} \tag{5.8}$$

where R is referred to R_c and R_{ct}, Y is referred to Y_c and Y_{dl} , and n is referred to n_c and n_{dl} when the coating capacitance C_c and the double layer capacitance C_{dl} are calculated, respectively.

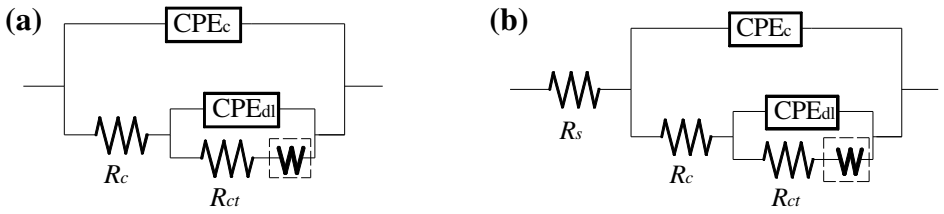

Figure 5.8 Equivalent electrical circuits for: (a) PE coated samples, and (b) uncoated, ME and DE coated samples.

The solution resistance is associated with the ionic mobility in a solution. It is affected by the position of either the reference electrode or the working electrode or both, and it can also be affected by the thickness of the passive film and the porosity of the enamel coating [148]. As the chloride concentration was increased from 0 to 0.50 mol L^{-1}, the conductivity of the saturated $Ca(OH)_2$ solution was increased and, therefore, the average solution resistance decreased from 106 to 11 Ω cm^2 for uncoated steel samples, from 180 to 22 Ω cm^2 for ME coated samples, and from 42 to 3 kΩ cm^2 for DE coated samples, respectively. The solution resistance of ME coated samples is approximately 1.7

to 2.0 times that of uncoated steel plates and 136 to 233 times that of DE coating. This is probably because the passive film was thinner than both the ME and DE coating, and the defect area of the DE coating is significantly smaller than the area of open channels in the ME coating.

The coating resistance measures the barrier performance of a coating against the penetration of water and ions. The coating capacitance indicates the water uptake ability of a coating. The higher the water uptake amount, the larger the coating capacitance since the dielectric constant of electrolytes is generally higher than that of the coating itself. Both of these two parameters are closely related to the dielectric property, microstructure, thickness, and defect of the coating itself. The coating resistances of three enamels generally decreased and the coating capacitances generally increased with increasing chloride concentrations as shown in Figure 5.9(a) and Figure 5.9(b), respectively, since chloride increased the conductivity of the solution within the coatings due to water uptake. At the same chloride concentration, the PE coating has the highest coating resistance and the lowest coating capacitance whereas the ME coating has the lowest coating resistance and the highest coating capacitance. The properties of the DE coating lie between the PE and ME. This is because the ME coating, with numerous open channels, allows easier water uptake than the PE and DE, and the defect area in the PE coating is smaller than that in the DE coating. In comparison with the enamel coatings, the passive film of the uncoated steel samples has a lower coating resistance and a higher coating capacitance. Note that the variation of three data points for each test condition is generally small except for n_c values.

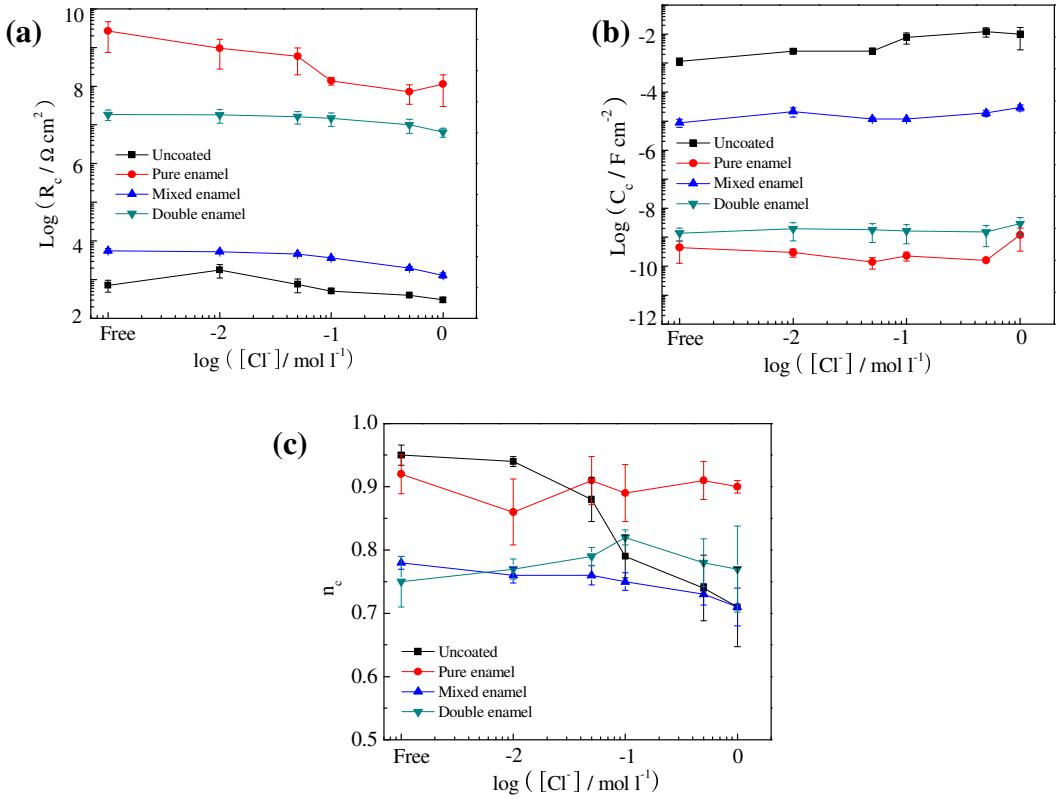

Figure 5.9 Comparison of coating properties: (a) coating resistance R_c, (b) coating capacitance C_c, and (c) n_c.

The charge transfer resistance measures the ease of electron transfer across the metal surface, which is inversely proportional to corrosion rate [149]. As shown in Figure 5.10(a), the charge transfer resistance of all samples decreased with increasing chloride concentration since more corrosion pits were formed on the passive film of the uncoated steel samples and around the coating defects or open channels of the enamel coated samples. A significant drop of charger transfer resistance was observed at a chloride concentration of 0.05 to 0.1 mol L^{-1} for uncoated steel samples due to breakdown of the passive film. The double layer capacitance for all samples increased with the increase of chloride concentration as shown in Figure 5.10(b). Specifically, the double layer capacitance of the uncoated steel plate was increased for two possible reasons: 1) the passive layer became thinner or broke down, and/or 2) the electrode surface became more porous, which were closely associated with the chloride-induced pitting corrosion [150].

The PE coating has the highest charge transfer resistance and the lowest double layer capacitance, the ME coating has the lowest charge transfer resistance and the highest double layer capacitance, and the DE coating was ranked in between the two coatings. This is because the coating defect size in the DE coating is larger than that in the PE coating; and the ME coating has numerous open channels.

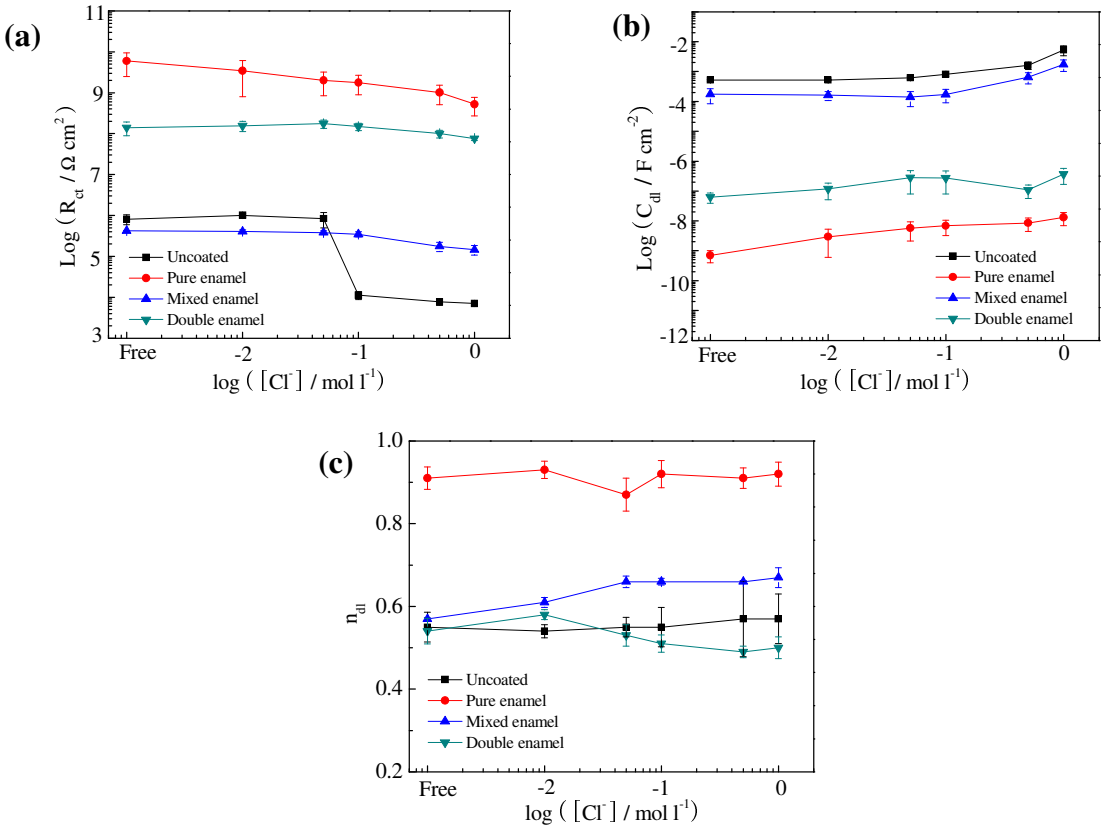

Figure 5.10 Comparison of steel-solution interfacial parameters: (a) charge transfer resistance R_{ct}, (b) double layer capacitance C_{dl}, and (c) n_{dl}.

The indices related to the non-homogeneities of both coating and steel-solution interface are presented in Figures 5.9(c) and 5.10(c). The coating index n_c for the uncoated steel samples significantly decreased when the chloride concentration reached 0.05 mol L^{-1} since the pitting corrosion increased the non-homogeneity of the passive film. For the three enamel coatings, n_c did not change considerably with the increase of

chloride concentration. However, the n_c values of the PE coated samples are higher than both the ME and DE coated samples since the former has a significantly smoother surface than the latter as indicated in Figure 5.3 [142]. The steel-solution interface index n_{dl} fluctuated around 0.90 for the PE coated samples and ranged from 0.50 to 0.70 for the uncoated, ME coated, and DE coated samples. In comparison with the other coatings, the PE coating provided a closer-to-capacitor behavior, which is desirable in the design of corrosion barriers (n_{dl} = 1 for a pure capacitor). The less desirable barrier behavior (n_{dl} << 1) is mainly attributed to the large air bubbles in the DE coating, open channels in the ME coating, and local breakdown of the passive film in the uncoated samples.

The diffusion behavior observed from testing of the PE and DE coated steel samples reflected the transport of charged ions, electrons and dissolved oxygen through the corrosion products around defects in the coatings, which depends on both the size of defect and the porosity of corrosion products. Considering similar corrosion products of steel in the same solution in this study, the impedance difference among the test samples mainly depends on the size of coating defects. The Warburg parameter for the PE coated steel sample (approximately 7.0 $n\Omega^{-1}$ cm^{-2} $s^{1/2}$) is about 350 times smaller than that of the DE coated steel sample (2.5 $\mu\Omega^{-1}$ cm^{-2} $s^{1/2}$). This is because the defects in the PE coating are smaller than those in the DE coating.

5.4 SUMMARY

Based on the microstructure and mechanical characterization of enamel coatings, and the electrochemical tests of enamel coated steel plates in simulated concrete pore water solution, the following conclusions can be drawn:

(1) All three types of enamel coatings (PE, ME, and DE) are stable in a high alkaline environment and improve the corrosion performance of carbon steel in the presence of chloride. Overall, the PE coated steel plate has a better corrosion resistance than the DE coated steel plate, and both substantially outperform the ME coated plate.

(2) At a chloride concentration between 0.01 mol L^{-1} and 0.05 mol L^{-1}, pitting corrosion initiated on the uncoated steel plate due to breakdown of the passive film. The pitting corrosion of the ME-coated steel plate initiated at a chloride concentration

between 0.1 mol L^{-1} and 0.5 mol L^{-1} partly because the open channels of the ME coating provide a direct access of chloride ions to the steel surface. Both the PE and DE coated steel plates appear to remain in a passive state throughout the corrosion tests due to small coating defects.

(3) All three types of enamel coatings mechanically failed across large air bubbles within the coating layers away from the enamel-steel interfaces. In comparison with the PE coating, the cohesive strength of the ME coating was about 24% greater because the open channels in the ME coating prevented the accumulation of bubbles. However, the cohesive strength of the DE coating was about 23% lower than that for the PE coating because bubbles were trapped, accumulated and enlarged in the DE coating during the high temperature enameling process.

6. CEMENT-MODIFIED ENAMEL COATING FOR ENHANCED CORROSION RESISTANCE OF STEEL REINFORCING BARS

6.1 INTRODUCTION

Steel rebar in concrete is generally protected by a thin passive film formed due to the high alkalinity of fresh concrete pore solution [82, 83]. However, this thin film can be degraded by the penetration of carbon dioxide and aggressive ions such as chloride [84, 85]. When this happens, corrosion will initiate in the presence of moisture and oxygen, resulting in formation of corrosion products which are usually several times greater volume than the original steel consumed. The expansive corrosion products lead to cracking and spalling of concrete cover which is one usual consequence of corrosion of steel in concrete. In addition, it may impair structural capacity through reduction of reinforcement cross section and the loss of bond between reinforcement and concrete [87, 91, 93]. Corrosion protection of steel rebar is often achieved by adding inhibitors in concrete [152-154], use of high performance concrete mixtures [155-157], using protective coatings [158-161], using stainless steel [162, 163], and applying cathodic protection [164, 165]. Among these methods, use of protective coatings is the most economical and effective method since it can establish a physical barrier between aggressive ions and the steel rebar.

Porcelain enamel is a vitreous or glassy inorganic coating bonded to the substrate metal by fusing glass frits at a temperature of 750 °C to 850 °C. It has been extensively used in domestic and industrial applications that require chemical, high temperature, corrosion and mechanical protection [109]. The properties of enamel coating are flexible and can be controlled by altering the chemical composition or microstructure, and pre-treating the metal substrate [111, 112]. For example, replacing B_2O_3 with SiO_2/TiO_2 can increase the corrosion resistance of enamel in acidic environments; adding ZrO_2 can improve the performance of enamel in alkaline environments; increasing CoO and NiO can promote adherence of the enamel to a metal substrate; and crystallization treatment can improve the hardness of the coating [114]. Therefore, enamels can be designed and used to improve corrosion resistance in an alkaline environment with an enhanced

chemical bond to the steel substrate [116], resulting in an alternative coating for steel rebar applied in concrete structures.

In a recent study by the authors [166], the microstructure and phase composition of three types of enamel coating (pure, mixed, and double enamels) have been examined using SEM and XRD techniques, and their corrosion resistances were characterized in 3.5 wt.% NaCl solution with open-circuit potential, electrochemical impedance spectroscope and potentiodynamic polarization methods. The test results showed that all three enamel coatings can improve the corrosion resistance of steel rebar to various extents. However, the effectiveness of these enamel coatings to protect steel rebar from corrosion in an application environment in concrete/mortar, and more importantly, the change in their corrosion resistance over time have not been well understood. In addition, a comprehensive evaluation of the corrosion process over time, including chloride ion ingress, passive film degradation, and corrosion resistance degradation of enamel coated rebar have never been studied systematically.

This study aims to investigate the time-varying corrosion performances of three types of enamel coating in 3.5 wt. % NaCl solution with enamel coated, smooth steel rebar embedded in ordinary Portland cement mortar cylinders. The chloride ion ingress, passive film degradation, and corrosion resistance degradation of enamel coatings were investigated over a period of 173 days, using chloride content, open-circuit potential (OCP), linear polarization resistance (LPR), and electrochemical impedance spectroscope (EIS) tests. After various tests, each mortar cylinder was removed and the exposed rebar surface was visually inspected and examined with an optical microscope for signs of corrosion.

6.2 EXPERIMENTAL PROCEDURES

6.2.1 Preparation of Enamel Coatings and Mortar Cylinders. Enamels are typically silicate-based oxides that are deposited from slurries and fused at high temperature. The enamel slurry is prepared by milling glass frits, clay and certain electrolytes, then mixing with water to provide a stable suspension. Three types of enamels were investigated in this study: pure enamel, mixed enamel, and double enamel.

The mixed enamel was used to enhance the bond strength with surrounding concrete by increasing its surface roughness, and the double enamel consisted of an inner pure enamel layer and an outer mixed enamel layer to increase its corrosion resistance through inner layer as well as to enhance its bond strength with concrete through outer layer.

The pure enamel slurry was made by first adding 454 kg alkali borosilicate glass frits to 189.3 L water and mixing them for 20 min., and then adding 31.8 kg clay and 2.3 kg borax as suspension agents, and mixing again for 3.5 hr. The chemical composition of alkali borosilicate glass frit is given in Table 6.1 [122]. This glass frit was selected because it contains ZrO_2 to improve the resistance of enamels in alkaline environments, and NiO and CoO to enhance the adherence strength with steel rebar. The mixed enamel was prepared by mixing 50% calcium silicate directly taken from the Portland cement [123] with the 50% pure enamel. The mixed enamel slurry was made following the same procedure as the pure enamel slurry.

Commercial steel rebar (12.7 mm diameter) was used in this study, and its chemical composition was determined and is given in Table 6.2. Prior to enamel coating, all steel rebar was sand-blasted and cleansed with a commercially available cleansing solvent. For PE and ME coatings, the cleaned steel rebar was dipped into their corresponding liquid slurry, heated for 2 min. at 150 °C to drive off moisture, fired at 810 °C for 10 min., and finally cooled to room temperature. For the DE coating, the steel rebar was first dipped into the PE slurry and heated for 2 min. at 150 °C to drive off moisture, then dipped into the ME slurry and heated to 150 °C again to drive off moisture, finally fired for 10 min. at 810 °C. The firing treatment at high temperature was used to melt the glass frit and chemically bond the enamel to the steel rebar.

Table 6.1 Chemical composition of alkali borosilicate glass frit.

Materials	SiO_2	B_2O_3	Na_2O	K_2O	CaO	CaF_2	Al_2O_3	ZrO_2	CoO	MnO_2	NiO
wt.%	44.0	19.3	15.8	2.8	0.0	4.7	4.6	5.3	0.9	1.5	1.0

Mortar was prepared using a mixture of cement, fine aggregate and water. Type I Portland cement was used, and its chemical composition is listed in Table 6.3. Missouri

River sands were used as fine aggregates with a maximum size of 6.35 mm and a fineness modulus of 2.80. The water/cement ratio was 0.55. The proportion of sand used in the mix was 2.81 times the weight of the cement.

Table 6.2 Chemical composition of steel rebar.

Element	C	Si	Mn	P	S	Cr	Mo	Ni	Co	Cu	V	Sn	Fe
wt.%	0.43	0.22	0.95	0.15	0.07	0.17	0.03	0.10	0.01	0.46	0.02	0.02	97.37

Table 6.3 Chemical composition of Type-I Portland cement (wt. %).

Loss on ignition	SiO_2	Al_2O_3	CaO	MgO	SO_3	Na_2O	K_2O	Cl	TiO_2	Fe_2O_3	P_2O_5	Total
3.98	19.48	6.80	55.35	3.32	4.35	2.39	1.00	0.02	0.20	2.18	0.19	99.27

Cylindrical mortar specimens were prepared as shown in Figure 6.1(a); each cylinder is 38.1 mm in diameter and 114.3 mm tall. One 88.9 mm long steel rebar specimen, either uncoated or enamel coated, was placed along the centerline of the cylinder as shown in Figure 6.1(a). A copper wire was welded to the top end of the rebar to provide an electrical connection. To force the corrosion activity in the middle portion of the steel rebar and avoid any potential crevice corrosion at the two ends, each end of the rebar was encased in a PVC tube filled with epoxy resin. Therefore, the actual length of rebar potentially exposed to the corrosive environment was approximately 50.8 mm, with a surface area of approximately 20.3 cm^2. The clear cover of mortar around the exposed portion of the rebar was 12.7 mm. For the casting of each specimen, a PVC pipe with a nominal inside diameter of 38.1 mm was used as a mold, and the steel rebar and the PVC mold were held in place by grooves pre-cut on a bottom plywood sheet as shown in Figures 6.1(b) and 6.1(c). To ensure a proper consolidation, each mortar specimen was cast in three layers, each compacted 25 times with a 6.35-mm-diameter steel rod and tapped 15 times with a small rubber mallet on the PVC mold to close the potential void generated by each rodding/compaction. All specimens were de-molded after 24 hr, placed in a curing room at room temperature and 100% relative humidity, and

cured for 28 days prior to testing. Three identical specimens were prepared for each condition, and the specimen whose test result lies in between the other two was selected to represent the coating system. For reference, mortars with uncoated steel rebar were also prepared at the same time.

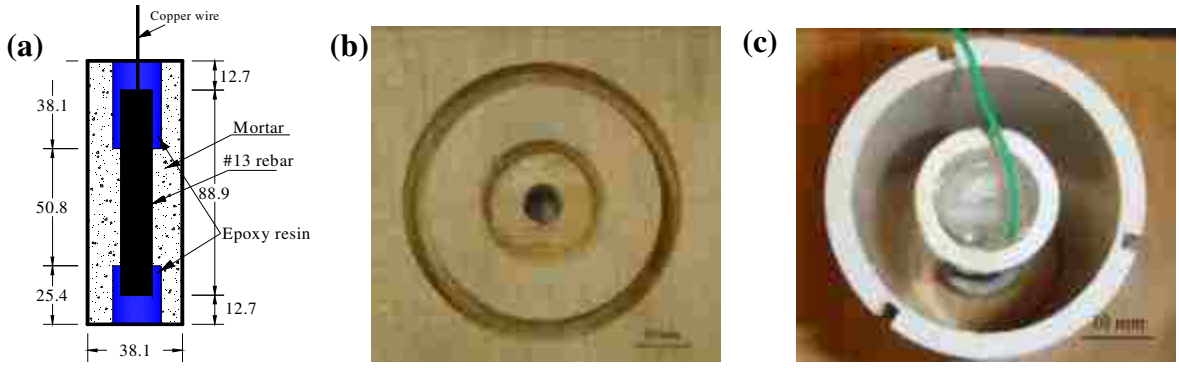

Figure 6.1 Mortar cylinder specimens: (a) geometries (unit: mm), (b) groove precut on plywood, and (c) PVC mold for casting.

6.2.2 Mortar/Steel Interface. The microstructure of the interfaces between the mortar and steel rebar was investigated through scanning electron microscope (SEM, Hitachi S4700). One 8.0 mm thick cross section of mortar was sectioned with a diamond blade for each of the uncoated, PE, ME, and DE coated steel rebar reinforced specimens. The slices were polished using silicate carbide papers with grits of 80, 180, 320, 600, 800 and 1200, rinsed with de-ionized water, and placed in an oven prior to the SEM study. Mounting epoxy was cast around each specimen to protect the mortar and enamel coating from damage during the sample preparation.

6.2.3 Chloride Measurement. Six additional mortar cylinders without steel rebar were prepared to monitor the diffusion process of chloride ions over time. One cylinder was removed from the NaCl solution approximately every 30 days and sectioned with a diamond blade into two halves with one cross section schematically illustrated in Figure 6.2. Mortar powder samples were taken directly from the middle cross section to avoid disproportionately high chloride contents at the top and bottom of the specimen. The samples were collected using a 3.175-mm-diameter masonry drill bit at each of three

depths from the cylinder side face: 3.1 mm, 7.9 mm, and 12.7 mm, as indicated in Figure 6.2. To collect representative data points, powder samples were taken from three locations evenly distributed around the circumference of the cylinder. The three samples at each respective depth were mixed together for chloride analysis, totaling 1.5 g. Using Rapid Chloride Testing equipment manufactured by German Instruments, Inc., the concentration of water soluble chlorides contained within each powder sample was determined.

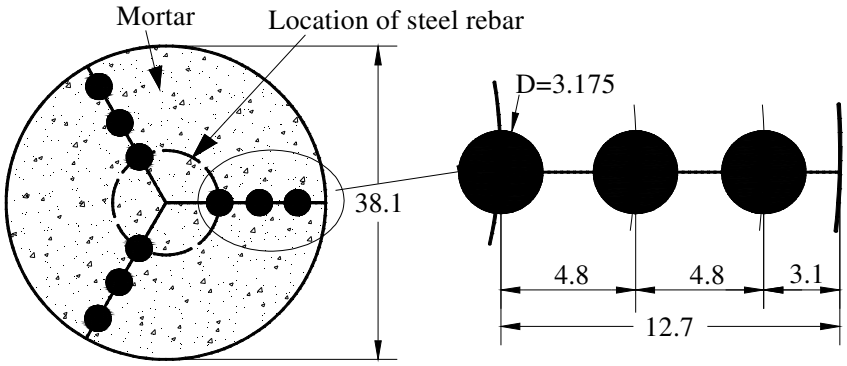

Figure 6.2 Locations of mortar powder samples for chloride content analysis (unit: mm)

6.2.4 Electrochemical Measurements. All mortar cylinders were immersed up to 173 days in glass beakers that contained 3.5 wt.% NaCl solution at room temperature and open to the air. The solution was made by mixing the purified sodium chloride with distilled water. To maintain a constant concentration of the test solution, distilled water was added every two days to compensate for any evaporative loss. OCP, LPR and EIS measurements were performed approximately every 30 days, and prior to testing, the NaCl solution was replaced with fresh solution to avoid any contamination of the electrolyte. All electrochemical measurements used a three-electrode test setup consisting of a 25.4 mm × 25.4 mm × 0.254 mm platinum sheet as a counter electrode, a saturated calomel electrode (SCE) as a reference electrode, and the mortar cylinder and rebar as a working electrode. These electrodes were connected to a Gamry, Reference 600

potentiostat/galvanostat/ZRA for data acquisition. EIS measurements were taken at 5 points per decade with a sinusoidal potential of 10 mV applied around the open-circuit potential E_{ocp} with a frequency range of 5 mHz to 100 kHz. The LPR curves were measured within E_{ocp}± 15 mV at a scan rate of 0.167 mV/s. Representing the slope of the polarization curve, the polarization resistance, R_p, can be calculated by:

$$R_p = \Delta V / \Delta i \tag{6.1}$$

where ΔV and Δi represent the voltage and current increments, respectively, in the linear portion of the polarization curve at i=0. LPR measurements were used to calculate the corrosion current density by the Stern-Geary equation [12]:

$$i_{corr} = \beta_a \beta_c / [2.303(\beta_a + \beta_c) R_p] = B / R_p \tag{6.2}$$

where i_{corr} is the corrosion current density, β_a is the anodic Tafel slope, β_c is the cathodic Tafel slope, and B is a constant related to β_a and β_c. In this study, a tentative value of 26 mV for the B constant was used [84, 124].

6.2.5 Visual Observation. After 173 days of immersion testing, all mortar cylinders were removed from the NaCl solution and dried in an oven at 60 °C for one day. The dry mortar cylinders were removed from the steel rebar using a steel hammer, and the surface condition of the exposed steel rebar was examined with an optical microscope.

6.3 RESULTS AND DISCUSSION

6.3.1 Mortar/Steel Interfaces. Figure 6.3 shows SEM images of the interfaces between the mortar and coated/uncoated steel rebar prior to immersion test. For uncoated steel rebar, a passive film was formed due to the high alkaline mortar pore solution. This passive film is very thin, less than 10 nm as observed with XPS techniques by other

researchers [167, 168]. Therefore, it cannot be identified with the relatively low magnification in Figure 6.3(a). Figure 6.3(b) shows that the pure enamel coating has bubbles that were released from the reaction of the enamel coating with the steel during the enameling process. These bubbles are isolated and smaller than the coating thickness (150 μm). As shown in Figure 6.3(c), the mixed enamel coating, 300 μm thick, has a porous structure with interconnected channels that were generated due to an increase in the viscosity of the mixed enamel slurry as it was heated during firing. The double enamel coating, 250 μm thick, has similar microstructure to the pure enamel coating as indicated in Figure 6.3(d).

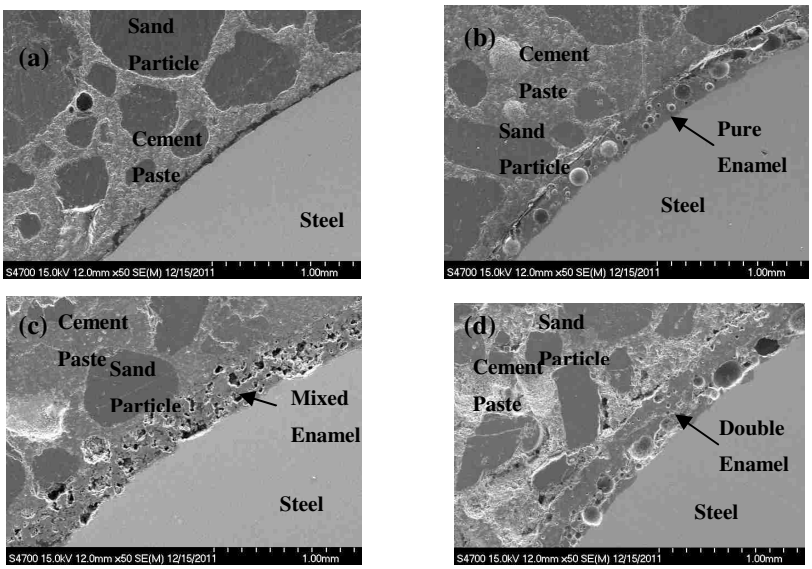

Figure 6.3 Cross sectional SEM images of the interface between mortar and steel rebar for: (a) uncoated, (2) pure enamel coated, (c) mixed enamel coated, and (d) double enamel coated.

6.3.2 Open-circuit Potential, Corrosion Rate and Chloride Profile. Figure 6.4 is a plot of the OCP as a function of time up to 173 days for mortar samples with uncoated and enamel coated steel rebar immersed in 3.5 wt. % NaCl solution. The OCP values of all cylinders were larger than -273 mV/SCE at the beginning of testing and dropped below -273 mV/SCE at 27 days. According to ASTM C876 [6], the probability

of the initiation of corrosion is 90% at 27 days. The OCP values then remained approximately -700 mV/SCE and -520 mV/SCE for mortar specimens with uncoated and enamel coated steel reinforcement, respectively. Initiation of corrosion for mortar cylinders with uncoated steel rebar is due to breakdown of the passive film induced by chloride ions. For cylinders with mixed enamel coated steel rebar, the penetration of chlorides through connected channels inside the coating initiated corrosion. For pure enamel and double enamel coated samples, the initial decrease in OCP may indicate the onset of corrosion due to small defects that are inherent in the enamel coating process.

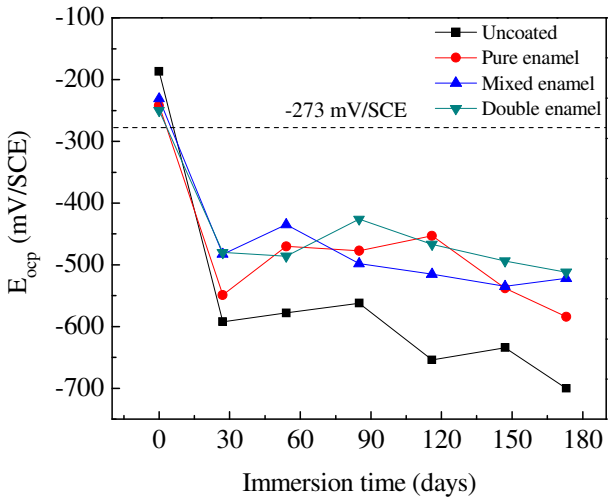

Figure 6.4 Open-circuit potential evolution with time for mortar cylinders reinforced with uncoated and three types of enamel coated steel rebar in 3.5 wt.% NaCl solution.

Figure 6.5 shows the change of corrosion current density as a function of time by the LPR tests. According to the Durar Network Specification [124], the corrosion level may be divided into four levels: passivity when i_{corr}<0.1 μA/cm^2, low corrosion when 0.1 μA/cm^2 <i_{corr}<0.5 μA/cm^2, high corrosion when 0.5 μA/cm^2 <i_{corr}<1.0 μA/cm^2, and very high corrosion when 1.0 μA/cm^2 <i_{corr}. Cylinders with uncoated steel rebar experienced all four states: passive state at the beginning of immersion, low corrosion after 27 days, high corrosion from 54 days to 85 days, and very high corrosion after 116 days. Cylinders with the mixed enamel coated steel rebar had similar behaviors but reached a

high corrosion level after 116 days of immersion, which indicated a greater corrosion resistance than the uncoated steel rebar. Mortar cylinders with the pure enamel and double enamel coated steel rebar remained in the passive state throughout the test. The corrosion current density ranged from 0.019 to 0.039 μA/cm^2 for mortar cylinders with the pure enamel coated rebar and from 0.003 to 0.004 μA/cm^2 for mortar cylinders with the double enamel coated rebar. The fact that the double enamel coated samples have a lower corrosion current density than the pure enamel coated rebar is mainly attributed to the thicker double enamel coating as illustrated in Figures 6.3(b) and 6.3(d). Note that the corrosion current density from LPR tests seems inconsistent with the OPC results at a first glimpse. This is because the areas of the defects in the pure enamel and double enamel coatings are very small, resulting in an overall small corrosion current density defined over the entire coating area exposed to the corrosive solution. For the mixed enamel coating, the defects formed during the high temperature firing are interconnected and covered a more significant area. As a result, the corrosion current for the mixed enamel coating is substantially higher than those of the pure and double enamel coatings as indicated in Figure 6.5.

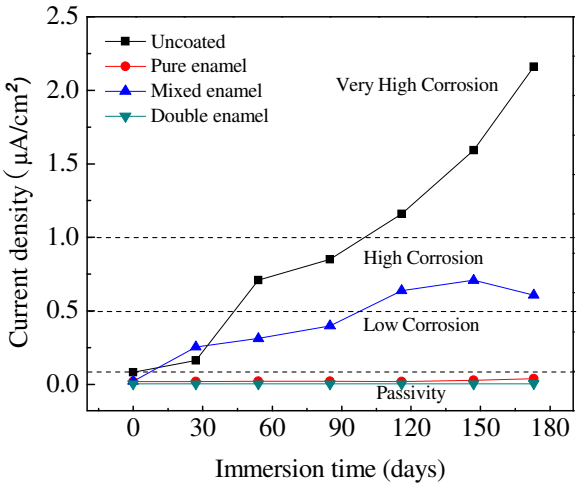

Figure 6.5 Corrosion current density evolution with time for mortar cylinders reinforced with uncoated and three types of enamel coated steel rebar in 3.5 wt.% NaCl solution.

Corrosion of steel rebar initiates when the chloride content on the rebar surface exceeds the chloride threshold, which is a function of mortar mix, exposure condition, cement type, and so on. ACI Building Code 318 [36] specifies the maximum water-soluble chloride content in concrete in a chloride rich environment to be 0.15% by weight of cement. According to Mehta [169], the level of chloride content that causes the breakdown of passive film on the surface of steel ranges from 0.23 to 1.5%. Figure 6.6 shows the change in chloride distribution over time for mortar cylinders in 3.5 wt. % NaCl solution. It can be observed from Figure 6.6 that the chloride content at the location of the steel rebar surface (11 mm from the mortar surface) in similar mortar cylinders with steel rebar was 0.25% after the mortar cylinders had been immersed in the NaCl solution for 27 days, and increased to 1.25% after 173 days. Therefore, the mortar cylinders had accumulated sufficient chloride ions for breakdown of the passive film and the initiation of corrosion when the initial tests were made.

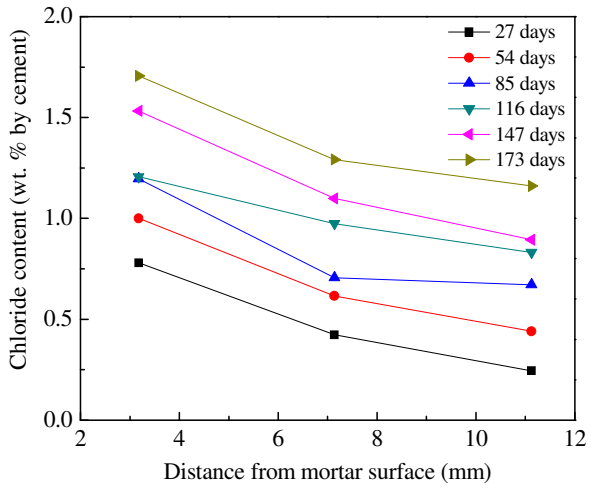

Figure 6.6 Chloride distribution in mortar with time in 3.5 wt.% NaCl solution.

6.3.3 EIS Results. Figure 6.7 shows the impedance diagrams of mortar cylinders with uncoated and three types of enamel coated steel rebar up to 173 days. The phase-frequency plots in Figures 6.7(a-3) and 6.7(c-3) indicated three time constants for cylinders with the uncoated and mixed enamel coated steel rebar, regardless of

immersion time. The first time constant in the high frequency range (>10^4 Hz) is associated with the dielectric properties of the mortar or combined mortar and mixed enamel coating [21]. The second time constant in the middle frequency range (1~10^4 Hz) is likely attributed to the dielectric properties of the passive layer formed on the steel rebar surface due to the high alkalinity of the fresh mortar pore solution during cement hydration process. The presence of the passive layer for cylinders with the mixed enamel coated steel rebar is due to the penetration of mortar pore solution through the connected channels to the steel surface. The third time constant in the low frequency range (<1 Hz) is closely related to the interface properties between steel rebar and mortar or enamel coating where corrosion occurs, namely the double layer capacitance and charge transfer resistance. The change of impedance spectra over time can only be reflected by the third time constant in the low frequency range.

Mortar cylinders with the pure enamel and double enamel coated steel rebar had different behaviors from those with the uncoated and mixed enamel coated reinforcement. Regardless of the immersion time, these specimens can be represented by two time constants as indicated in Figures 6.7(b-3) and 6.7(d-3). The impedance magnitudes of these two types of mortar cylinders, Figures 6.7(b-2) and 6.7(d-2), were higher than those with the uncoated and mixed enamel coated steel rebar at all frequencies, Figures 6.7(a-2) and 6.7(c-2). The time constant in the high frequency range (>10^3 Hz for pure enamel and >10^2 Hz for double enamel) is associated with the dielectric properties of combined mortar and enamel coating. The second time constant in the low frequency range (<10^3 Hz for pure enamel and <10^2 Hz for double enamel) originated from the interface properties due to the charge transfer resistance and double layer capacitance.

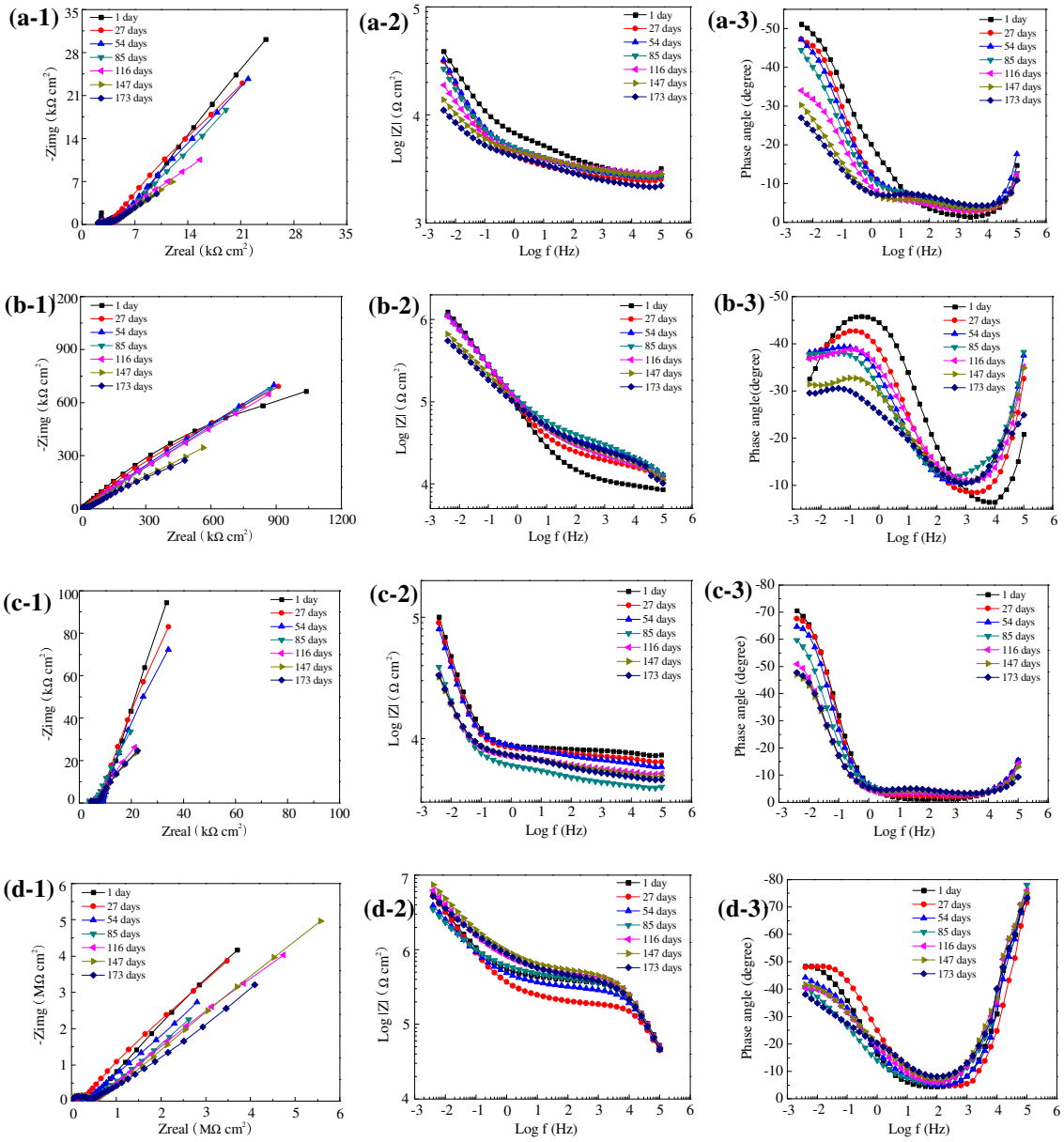

Figure 6.7 Typical EIS diagrams of mortar cylinders in 3.5 wt.% NaCl solution with: (a) uncoated, (b) pure enamel, (c) mixed enamel, and (d) double enamel coated steel rebar in the format of Nyquist plots(1), and Bode plots (2) & (3).

The intrinsic dielectric properties of mortar/enamel coating and passive film as well as the electrochemical behavior at the mortar-steel interface can be obtained by fitting an appropriate equivalent electrical circuit (EEC) model to the EIS test data. As illustrated in Figure 6.8, two EEC models were used in this study: (a) with two

distributed constant phase elements (CPEs) for mortar cylinders with the pure enamel and double enamel coated steel rebar, and (b) with three distributed CPEs for mortar cylinders with the uncoated and mixed enamel coated steel rebar. Model (a) consists of a salt solution resistance R_s, capacitance CPE_m and resistance R_m of bulk-matrix (combined mortar and enamel coating for pure enamel and double enamel), charge transfer resistance R_{ct}, and double layer capacitance CPE_{dl}. Such a model was used by other researchers to study steel corrosion in carbonated alkali-activated slag concrete [29]. Model (b) consists of a solution resistance R_s, bulk-matrix (mortar or mortar and mixed enamel coating) capacitance CPE_m and resistance R_m, passive film capacitance CPE_f and resistance R_f, charge transfer resistance R_{ct}, and double layer capacitance CPE_{dl}. A model similar to (b) was used to study the electrochemical characteristics of reinforced concrete corrosion [170].

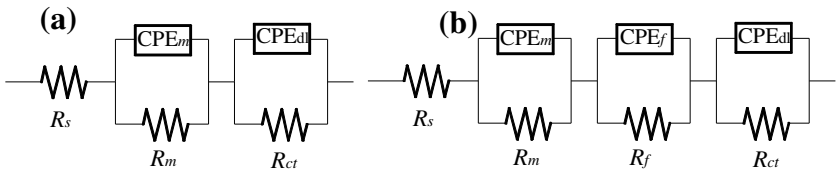

Figure 6.8 Equivalent electrical circuits for mortar cylinders with: (a) pure enamel and double enamel coated steel rebar, and (b) uncoated and mixed enamel coated steel rebar.

Application of CPEs in the EEC models is attributed to the non-homogeneity of the system under study. The non-homogeneity mainly comes from the irregularities on the steel surface, surface roughness, fractal surface, and in general certain processes associated with an irregular distribution of the applied potential [162]. The CPE is defined by two parameters Y and n, and its admittance representation is:

$$Y_{CPE} = Y(j\omega)^n \tag{6.3}$$

where Y is a parameter with dimension of Ω^{-1} $cm^{-2}s^{n}$, which is directly proportional to the capacitance of pure capacitive electrode [119], ω is the angular frequency in rad/s, and n represents the deviated degree of the capacitance of the electrode from the ideal condition of a pure capacitor. When n = 1, the CPE resembles a capacitor with capacitance Y; when n=0.5, it represents Warburg impedance; when n =0, the CPE represents a resistor with resistance Y^{-1}, and when n=-1, it is an inductor.

ZsimpWin software [171] was used to fit all EIS data. The Chi-squared value was found to be on the order of 10^{-3} for all results, indicating a good simulation with the proposed two EEC models. Figure 6.9 shows the excellent agreement between the EEC models and the results of four types of mortar cylinders after 116 days of immersion.

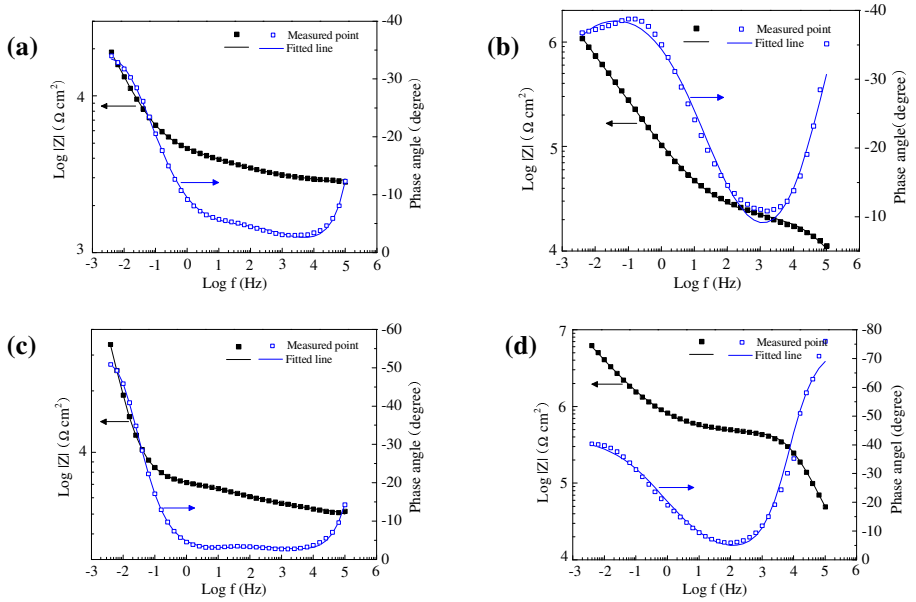

Figure 6.9 Impedance spectrum and fitting results for: (a) uncoated, (2) pure enamel, (c) mixed enamel, and (d) double enamel coated steel rebar after 116 days of immersion in 3.5 wt. % NaCl solution.

Tables 6.4 and 6.5 summarize the EEC model parameters for mortar cylinders with the uncoated and three types of enamel coated steel rebar. The solution resistance R_s was close to zero when the dielectric properties of the bulk-matrix were extracted by

extending the small arc in the high frequency range to the real axis. It was therefore not listed in the tables.

Table 6.4 EEC model (b) parameters for mortar cylinders with uncoated and mixed enamel coated steel rebar in 3.5 wt.% NaCl solution.

Time (day)	R_m ($k\Omega$ cm^2)	n_m	Y_m ($n\Omega^{-1}$ cm^{-2} s^{-} $^{n}{}_{m}$)	R_f ($k\Omega$ cm^2)	n_f	Y_f ($\mu\Omega^{-1}$ cm^{-2} $s^{n}{}_{f}$)	R_{ct} ($k\Omega$ cm^2)	n_{dl}	Y_{dl} ($\mu\Omega^{-1}$ cm^{-2} $s^{n}{}_{dl}$)
Uncoated steel rebar									
0	2.79	0.80	1.03	1.04	0.44	16.8	285	0.70	164
27	2.68	1.00	0.11	4.71	0.20	28.2	188	0.71	629
54	3.05	1.00	0.10	3.07	0.26	11.5	198	0.62	652
85	2.95	0.96	0.21	3.13	0.29	92.2	102	0.59	770
116	3.41	0.55	4.06	1.15	0.47	54.3	76	0.48	502
147	3.39	0.77	2.07	1.81	0.41	48.6	43	0.49	757
173	3.18	0.87	0.46	2.25	0.38	52.7	36	0.52	795
Mixed enamel coated steel rebar									
0	6.41	0.87	0.47	2.36	0.19	42.5	960	0.84	226
27	6.91	0.72	3.25	1.46	0.47	42.9	829	0.87	274
54	6.11	0.74	2.57	3.22	0.35	58.5	677	0.86	299
85	3.96	0.80	1.48	2.41	0.38	62.1	634	0.79	308
116	5.23	0.76	2.07	2.05	0.41	45.9	193	0.78	559
147	5.15	0.64	9.98	2.20	0.47	34.1	148	0.76	530
173	4.87	0.60	13.2	2.60	0.46	34.9	143	0.77	536

The bulk-matrix resistance and capacitance reflect the ability of the mortar/enamel coating to resist the penetration of electrolytes containing aggressive ions and the dielectric properties of the mortar/enamel coating, respectively, both closely related to the porosity of mortar and enamel coatings. As shown in Table 6.4, for mortar cylinders with the uncoated steel rebar, the bulk-matrix (mortar) resistance is in the range of 2.68 to 3.41 $k\Omega$ cm^2. For cylinders with the mixed enamel coated steel rebar, the mortar and mixed enamel coating resistance is in the range of 3.96 to 6.91 $k\Omega$ cm^2, which is approximately twice as high as that for the uncoated steel rebar. This is likely because

the mixed enamel coating has a higher resistivity than the mortar, despite the presence of connected channels. Capacitance Y_m of the bulk-matrix is in the range of 0.10 to 4.06 $n\Omega^{-1}$ cm^{-2} s^n_m for the uncoated and 0.47 to 13.2 $n\Omega^{-1}$ cm^{-2} s^n_m for the mixed enamel coated specimen, respectively. This range is in reasonable agreement with other studies in the literature [124, 170].

Table 6.5 EEC model (a) parameters for mortar cylinders with pure enamel and double enamel coated steel rebar in 3.5 wt.% NaCl solution.

Time (day)	R_m ($k\Omega$ cm^2)	n_m	Y_c ($n\Omega^{-1}$ cm^{-2} s^n_m)	R_{ct} ($k\Omega$ cm^2)	n_{dl}	Y_{dl} ($\mu\Omega^{-1}$ cm^{-2} s^n_{dl})
Pure enamel coated steel rebar						
0	8.21	0.84	0.57	2410	0.54	4.12
27	14.2	0.71	3.78	3790	0.46	4.80
54	12.9	0.92	0.33	1910	0.58	8.54
85	20.5	0.81	1.22	3750	0.52	8.69
116	26.9	0.78	1.74	3460	0.43	7.07
147	21.4	0.67	7.85	3810	0.32	6.43
173	21.3	0.73	3.39	3350	0.48	11.9
Double enamel coated steel rebar						
0	387	0.85	0.23	$>10^4$	0.58	1.64
27	193	0.86	0.22	$>10^4$	0.57	1.62
54	303	0.85	0.26	$>10^4$	0.51	1.78
85	388	0.83	0.33	$>10^4$	0.46	1.75
116	455	0.84	0.27	$>10^4$	0.48	1.01
147	483	0.83	0.32	$>10^4$	0.47	0.81
173	381	0.83	0.34	$>10^4$	0.40	0.92

As shown in Table 6.5, the bulk-matrix resistance of mortar cylinders with the pure enamel coated rebar is in the range of 8.21 to 26.9 $k\Omega$ cm^2, which is higher than that for the uncoated and mixed enamel coated rebar. This is attributed to the improved barrier behavior of the pure enamel coating, despite the isolated pores in the coating. The bulk resistance of the double enamel coating is in the range of 193 to 483 $k\Omega$ cm^2, which is approximately 100 times higher than that with the uncoated steel bar. This is because

the double enamel coating has a relatively thicker coating than the pure enamel coating. The capacitance of the bulk-matrix is in the range of 0.67 to 0.92 $n\Omega^{-1}cm^{-2}\ s^n_m$ for the pure enamel coated and 0.83 to 0.86 $n\Omega^{-1}cm^{-2}\ s^n_m$ for the double enamel coated, respectively. These values are smaller than the uncoated and mixed enamel coated, indicating substantial protection from the penetration of electrolytes through the pure and double enamel coatings.

For the uncoated and mixed enamel coated steel rebar, the resistance of the passive films varies between 1.0 and 3.2 $k\Omega\ cm^2$, and the capacitance is in the range of 10 to 60 $\mu\Omega^{-1}\ cm^{-2}\ s^n_f$. No change in passive film dielectric property was observed for the uncoated steel rebar even when the passive film was broken down by chloride attack. This is likely because the dielectric property of the passive film is close to that of the corrosion products.

The two most direct parameters to reflect corrosion resistance are charge transfer resistance and double layer capacitance. These parameters are related to the charge transfer during the corrosion process at the interface between the exposed steel and the electrolyte inside mortar pore structure; they are a measure of ease of corrosion [172]. For specimens with the uncoated steel rebar, the charge transfer resistance displayed a continuous reduction with time of immersion from 285 to 36 $k\Omega\ cm^2$, indicating a transition from the passive state to the active state. The same trend was also observed for the mixed enamel coated steel rebar from 960 to 143 $k\Omega\ cm^2$. The charge transfer resistance of the double enamel coating exceeded $10^4\ k\Omega\ cm^2$ and cannot be accurately obtained from the simulation since the obvious diffusion behavior appeared in the low frequency range. The charge transfer resistance of the pure enamel coated rebar is also large, ranging from 1910 to 3810 $k\Omega\ cm^2$. Like the double enamel coating, the pure enamel coated rebar appeared to remain in a passive state over the entire duration of testing. These results were in agreement with the LPR results.

The double layer capacitance increased from 164 to 795 $\mu\Omega^{-1}\ cm^{-2}\ s^n_{dl}$ for mortar cylinders with the uncoated steel rebar and from 226 to 536 $\mu\Omega^{-1}\ cm^{-2}\ s^n_{dl}$ for mortar cylinders with the mixed enamel coated steel rebar, respectively. These results indicate that the diffusion of chloride ions increased the activity of corrosion at the double layer interface. The double layer capacitance ranged from 4.12 to 11.9 $\mu\Omega^{-1}\ cm^{-2}\ s^n_{dl}$ for mortar

cylinders with the pure enamel coated steel rebar and from 0.81 to 1.78 $\mu\Omega^{-1}$ cm^{-2} s^{n}_{dl} for mortar cylinders with the double enamel coated steel rebar. The smaller double layer capacitance of the pure and double enamel coatings also indicated a higher corrosion resistance than the uncoated and mixed enamel coating.

6.3.4 Visual Observation. Figure 6.10 shows the surface condition of the uncoated and three types of enamel coated steel rebar after they were removed from mortar cylinders at the end of the 173 days of corrosion testing. As shown in Figure 7.10, rust stains are apparent on the uncoated and the mixed enamel coated steel rebar only. No rust was observed on the pure enamel and double enamel coated steel rebar as shown in Figures 6.10(b) and 6.10(d). This observation verified the superior corrosion resistant performance of the pure and double enamel coatings as indicated by the LPR and EIS test results.

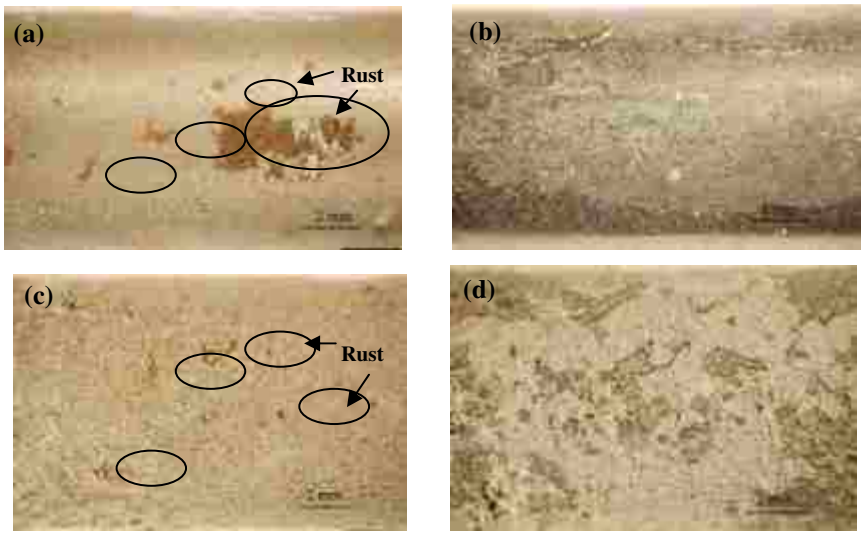

Figure 6.10 Surface conditions of (a) uncoated, (b) pure enamel, (c) mixed enamel, and (d) double enamel coated steel rebar embedded in mortar after 173 days of immersion in 3.5 wt.% NaCl solution.

6.4 SUMMARY

Based on the test data and analysis of 38.1-mm diameter mortar cylinders with embedded #13 smooth steel rebar, both uncoated and coated with three types of enamel, the following conclusions can be drawn:

1. Corrosion of the uncoated and mixed enamel coated steel rebar embedded in mortar cylinders initiated within 27 days of immersion in 3.5 wt.% NaCl solution, as supported by both the OCP and LPR tests. Based on the chloride analysis in mortar, the level of chloride content at the mortar-steel interface also indicated that the passive film on the steel rebar was most likely broken down and corrosion initiated after 27 days of immersion in the solution. The OCP of the tested specimens significantly decreased from above to below -273 mV/SCE and their corrosion current density increased from below the passivity threshold to a very high corrosion level and high corrosion level for uncoated and mixed enamel coated steel rebar at 173 days, respectively.

2. There was no sign of corrosion in pure enamel and double enamel coated steel rebar embedded in mortar cylinders. This finding was confirmed by visual inspections on the tested specimens at the end of corrosion testing. Although the OCP indicated a high probability of corrosion, the corrosion current density remained below the passivity threshold until the end of corrosion testing at 173 days.

3. The corrosion behavior of either uncoated or enamel coated rebar in mortar can be characterized by a single model throughout the corrosion tests. EIS tests indicated three time constants for mortar cylinders with uncoated and mixed enamel coated steel rebar, and two time constants for mortar cylinders with pure enamel and double enamel coated steel rebar. The first and last time constants correspond to the high and low frequency behaviors of the capacitive responses of mortar/enamel coating and the double layer interface, respectively. The middle time constant for uncoated and mixed enamel coated rebar in the middle frequency range is attributed to the dielectric property of the passive film since the mixed enamel coating has interconnected pore channels, extensively exposing steel rebar to the NaCl solution.

7. CORROSION RESISTANCE AND MECHANISM OF STEEL REBAR COATED WITH THREE TYPES OF ENAMEL

7.1 INTRODUCTION

Corrosion of reinforcing steel is common in reinforced concrete structures around the world. It causes premature deterioration of civil infrastructures such as highway and railway bridges, offshore platforms, pipelines, and dams. According to Koch et al. [1], the annual cost of corrosion in the United States is approximately $8 billion for highway bridges alone. Corrosion of reinforcing steel in concrete results from two main sources: carbonization and chloride penetration [9]. Chloride mainly comes from road deicing salts in winter for highways and bridges, and marine climate for offshore and coastal structures. One effective way to prevent or slow down the penetration process of these aggressive ions is to apply a coating on the rebar surface that would establish a physical barrier between the steel and concrete.

Ceramic porcelain enamel coatings for steel possess chemical and mechanical stability in various environments including acid, alkaline, high temperature and harsh working conditions [112], and so are widely used for a variety of consumer applications and for the protection of steel in many industrial chemical applications. The degradation mechanism of enamel coated steel has been investigated by several researchers [173, 174]. Recently, enamel coated reinforcing steel for pavement and stay-in-place forms have been investigated by researchers with the Army Corps of Engineers [175-177]. They modified standard enamel compositions by adding a reactive phase, like Ca-silicate, that would bond to the surrounding concrete matrix, and concluded that enamel coatings improve the corrosion resistance and enhance the bond strength with surrounding concrete. However, corrosion resistance of different enamel coatings and their tolerance to existing damage have not been studied and quantified systematically. In particular, the concept of a two-layer coating, one to enhance bond strengths and the other to improve corrosion resistance, has never been explored prior to this study.

In this study, corrosion resistances of enamel coated steel rebar were evaluated in 3.5 wt. % NaCl solution by electrochemical impedance spectroscopy (EIS). The enamel coating systems tested include a pure enamel, an enamel mixed with 50% calcium silicate

(by weight), and a double enamel with an inner layer of pure enamel and an outer layer of the mixed enamel. Their corrosion performance was compared with commonly used fusion bonded epoxy (FBE) coating in reinforced concrete structures. The phase composition and microstructure of enamel coatings were characterized by X-ray diffraction (XRD) and scanning electron microscopy (SEM) coupled with an energy-dispersive X-ray spectroscopy (EDS). Impact tests were performed on some samples to investigate the effect of coating damage on its corrosion resistance. The barrier ability of enamel coatings to aggressive ions was confirmed by mapping the chloride distribution in the coating of tested rebar.

7.2 EXPERIMENTAL DETAILS

7.2.1 Preparation of Enamel Coatings. Enamels are typically silicate-based materials that are deposited from slurries and fused at high temperature. The enamel slurry is made by milling glass frits, clay and certain electrolytes, then mixing with water to provide a stable suspension. In this study, a commercially-available alkali borosilicate glass frit from PEMCO (Product No. PO2025) was used for the pure enamel (PE). Its chemical composition is given in Table 7.1 [178]. This composition was selected because it contains ZrO_2 which is known to improve the durability of glasses exposed to alkaline environments, including cement [122]. A slurry of the pure enamel was made by first adding 454 kg of enamel frit to 189.3 litres of water and mixing them for 20 minutes, and then adding clay (31.8 kg) and borax (2.3 kg) as suspension agents, and mixing again for 3.5 hours. The mixed enamel (ME) coatings were prepared by adding 50% (by weight) calcium silicate into pure enamel frits. Calcium silicate particles from the Portland cement specified in ASTM C150-07 [123] were used. Double enamel coating (DE) consists of two layers, the first (inner) layer is a PE coating and the second (outer) is an ME coating.

Table 7.1 Chemical composition of alkali borosilicate glass frit

Element	SiO_2	B_2O_3	Na_2O	K_2O	CaO	CaF_2	Al_2O_3	ZrO_2	MnO_2	NiO	CoO
Wt.%	44.0	19.3	15.8	2.8	0.1	4.7	4.6	5.3	1.5	1.0	0.9

Commercial steel rebar (12.7 mm diameter) was used in this study. Its chemical composition was determined and is given in Table 7.2. Before coating, all rebar was sand-blasted and cleaned with commercially available cleansing solvent. For PE and ME coatings, the cleaned rebar was dipped into their corresponding liquid slurry, and heated for 2 minutes at 150 °C to drive off moisture then fired at 810 °C for 10 minutes, and finally cooled to room temperature. For the double enamel (DE) coating, the rebar was first dipped into the PE slurry and heated for 2 minutes at 150 °C to drive off moisture, then dipped into the ME slurry and heated to 150 °C again to drive off moisture, then moved into furnace to fire for 10 minutes at 810 °C. The firing treatment at high temperature was used to melt the glass frit and chemically bond the enamel to the steel. During enameling, the deformed bar was hung vertically in the furnace; thus, the coating thickness around rebar ribs may not be uniform due to gravity effect.

Table 7.2 Chemical composition of steel rebar

Element	C	Si	Mn	P	S	Cr	Mo	Ni	Co	Cu	V	Sn	Fe
Wt.%	0.38	0.18	1.00	0.12	0.06	0.10	0.07	0.20	0.01	0.37	0.02	0.03	97.40

7.2.2 Preparation of the Samples. The coated steel bars were cut into 89.0 mm lengths with two ends encased in PVC tubes containing epoxy resin. A copper wire was connected electrically at one end of the rebar. The actual length of steel rebar exposed to the corrosive environment was approximately 50.8 mm in the middle portion, as shown in the schematic view of samples in Figure 7.1. In addition, commercial FBE coated rebar samples with the same rebar size were also prepared for comparison.

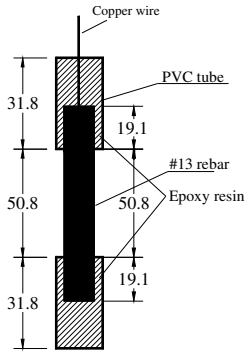

Figure 7.1 Geometry of rebar samples (unit: mm)

To study the effect of coating damage on the corrosion resistance, some samples were pre-damaged using an impact test apparatus designed according to the ASTM Standard G14 [179]. The apparatus consists of a 0.91 kg steel rod with a hemispherical head, a vertical section of hollow aluminum tubing to guide the rod, and a horizontal section of steel angle to position the coated rebar sample. The coated rebar was secured to the steel angle with clamps, and the weight rod was dropped from a height of 45.7 cm to damage the coatings. Two damage extents were considered, samples with 6 impact points and samples with 12 impact points. Examples of the rebar samples ready for corrosion tests with no coating (UN), with different coatings, and with impact points, are shown in Figure 7.2. A total of 39 rebar samples were prepared as detailed in Table 7.3, taking into account the rebar coating (UN, FBE, PE, ME, and DE) and damage extent (0 = no damage, 1 = 6 impact points, or 2 = 12 impact points). Each sample was designated by a string of letters and numbers. The designation starts with two letters for the type of coating and then two numbers for the number of impact points, which were followed by a # sign and another number representing the number of samples in the same group. The uncoated rebar samples were undamaged and not cleaned prior to corrosion tests, to simulate their as-received condition at a construction site, and so a black oxide layer (mill scale) was initially present on their surfaces.

Table 7.3 Test matrix: 39 samples total

Surface condition	Numbers of impact point		
	0	6	12
FBE coating	EP00#1 EP00#2 EP00#3	EP01#1 EP01#2 EP01#3	EP02#1 EP02#2 EP02#3
Pure enamel	PE00#1 PE00#2 PE00#3	PE01#1 PE01#2 PE01#3	PE02#1 PE02#2 PE02#3
Mixed enamel	ME00#1 ME00#2 ME00#3	ME01#1 ME01#2 ME01#3	ME02#1 ME02#2 ME02#3
Double enamel	DE00#1 DE00#2 DE00#3	DE01#1 DE01#2 DE01#3	DE02#1 DE02#2 DE02#3
Uncoated	UN00#1 UN00#2 UN00#3	-	-

Note: Sample ME00#3 was damaged before testing and thus no data is reported in this paper.

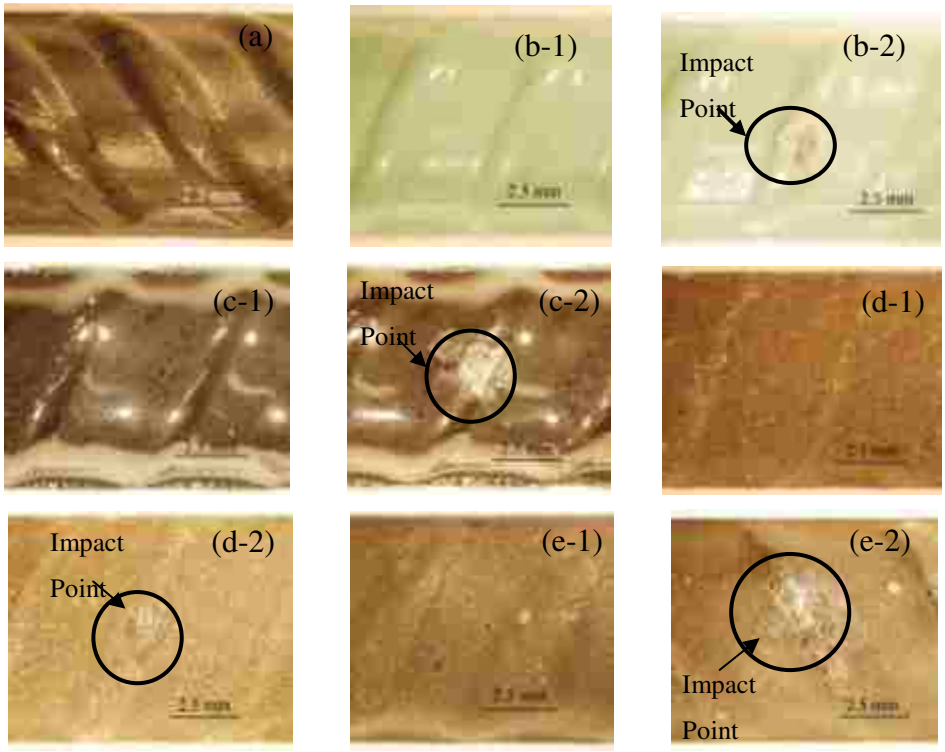

Figure 7.2 Steel rebar samples tested in this study: (a) uncoated rebar, (b-1, b-2) FBE coated rebar without and with impact points, (c-1, c-2) pure enamel coated rebar without and with impact points, (d-1, d-2) mixed enamel coated rebar without and with impact points, and (e-1, e-2) double enamel coated rebar without and with impact points

7.2.3 Characterization and Barrier Ability of Enamel Coatings. The phase composition of three types of enamel coatings and the oxide layer of uncoated rebar before and after corrosion tests were examined directly on the rebar surface with X-ray diffraction (XRD, Philip X' Pert). The microstructure and the elemental analysis of the coatings before corrosion test were investigated by scanning electron microscopy (SEM,

Hitachi S4700) coupled with an energy-dispersive X-ray spectroscopy (EDS). At the completion of corrosion tests, the ability of enamel coatings as a barrier to aggressive ions was investigated with SEM by mapping the chloride profile in the enamel coating of rebar. For SEM measurements, one 4.0 mm thick cross-section sample, mounted in epoxy, was cut from each of the coated and uncoated rebar, and then abraded with silicon carbide papers with grits of 80, 180, 320, 600, 800 and 1200. After abrading, all samples were rinsed with deionized water and dried prior to microscopy study.

7.2.4 Electrochemical Studies. All samples were immersed in 3.5 wt. % salt solution consisting of distilled water and purified sodium chloride. Samples were tested at room temperature with a typical three-electrode setup, including a 25.4 mm × 25.4 mm × 0.254 mm platinum sheet as a counter electrode, saturated calomel electrode (SCE) as a reference electrode, and one rebar sample as a working electrode. All three electrodes were connected to a Gamry, Reference 600 potentiostat/galvanostat/ZRA for data acquisition. The electrochemical impedance spectra were obtained with an applied sinusoidal potential wave of 10 mV amplitude and frequency ranging from 100 kHz to 0.005 Hz at a sampling rate of 5 points per decade.

7.3 RESULTS AND DISCUSSION

7.3.1 Microstructures and Elemental Analysis. Figure 7.3 shows cross-sectional SEM images and representative EDS analyses of uncoated and enamel coated rebar samples. These cross-sections were taken between two ribs, where the coating is relatively uniform and thicker than that over the ribs. EDS analyses were performed on the coating sample taken within the small square in the respective SEM images. The uncoated rebar, Figure 7.3(a-1), has a thin (about 25 μm thick) oxide layer (mill scale) on the rebar surface, which mainly consists of iron (Fe) and oxygen (O) as shown in Figure 7.3(a-2). This was likely formed during the hot rolling process of steel production. The pure enamel (PE) coating is approximately 150 μm thick, and has air voids with the maximum diameter of approximately 50 μm, Figure 7.3(b-1). The air voids result from bubbles that typically form in the molten glass during the high temperature enamel firing process. EDS analysis as shown in Figure 7.3(b-2) indicates that the principal

components in the PE coating include sodium (Na), calcium (Ca), silicon (Si) and aluminum (Al); boron, a major component of the glass frit, could not be detected by the EDS system used. The ME coating is approximately 250 μm thick and it possesses a more complex structure with irregular pore characteristics and relatively high porosity as illustrated in Figure 7.3(c-1). This porous structure was further verified by the penetration of mounting epoxy during preparation of the SEM sample as shown in Figure 7.3(c-2). EDS analysis revealed that the ME coating includes a higher content of Ca than the PE coating, Figure 7.3(c-3), which is consistent with the addition of calcium silicate. The EDS spectrum from the ME coating also exhibited a significant peak of iron (Fe) that presumably originates from the rebar substrate during the chemical reaction at firing temperature. Figure 7.3(d-1) shows an SEM image of the DE coating. It clearly indicates the presence of two distinct layers, approximately 160 μm and 240 μm thick for the inner and outer layers, respectively. The inner pure enamel layer exhibits the same microstructure of trapped air voids as found in the PE sample in Figure 7.3(b-1). Its EDS spectrum, Figure 7.3(d-2), is consistent with the components of enamel glass with a small peak of iron (Fe) from the rebar substrate. The outer 50/50 enamel layer has a slightly different microstructure from the ME sample in that less mounting epoxy was found to have penetrated through the outer layer. This is likely because, during the second firing process, some of the inner melted pure enamel flowed towards the outer 50/50 enamel, and partially filled and isolated what would otherwise be connected pores in the outer layer as observed in the ME coating, Figure 7.3(c-1). Even though the pores in outer layer of the DE sample become disconnected, the EDS spectrum of the outer layer is similar to the ME sample, Figure 7.3(d-3), except that no iron (Fe) was detected since the outer layer was separated from the steel substrate by the inner layer.

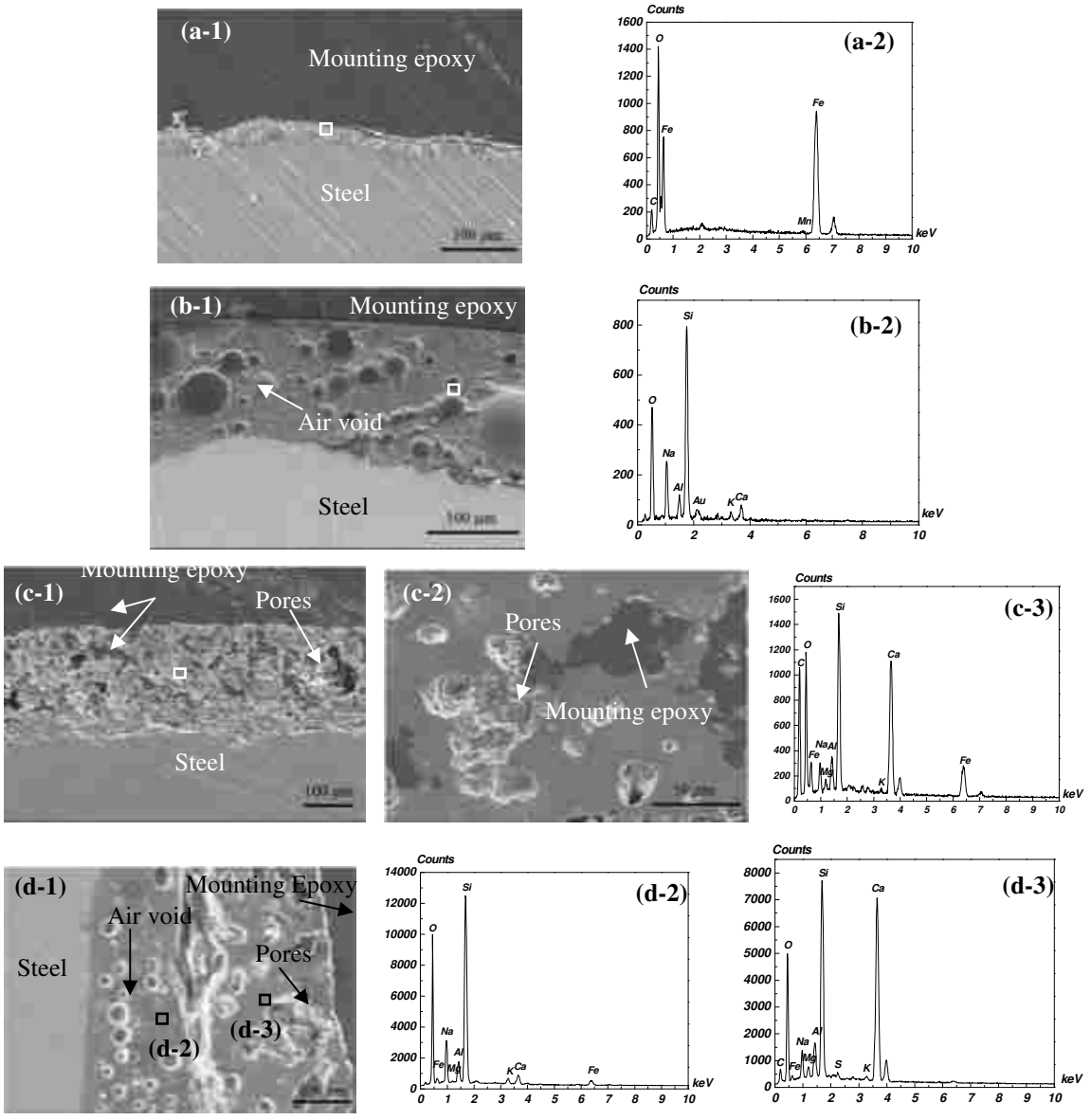

Figure 7.3 Cross sectional SEM images and EDS analysis before corrosion tests: (a-1, a-2) uncoated rebar, (b-1, b-2) pure enamel coated rebar, (c-1, c-2, c-3) mixed enamel coated rebar, and (d-1, d-2, d-3) double enamel coated rebar

7.3.2 Coating Analysis. Figure 7.4 shows the X-ray diffraction analyses on the surface of the uncoated and three enamel coated rebar samples prior to and after corrosion tests immersed in 3.5 wt. % NaCl solution. Magnetite (Fe_3O_4) and Maghemite (Fe_2O_3) are the two main oxides on the uncoated steel rebar surface prior to the corrosion test, consistent with reports on the nature of the mill scale on rebar [180, 181]. After the

corrosion test, one rust layer was formed and mainly consisted of lepidocrocite (γ-FeOOH) and akaganeite (β-FeOOH) as shown in Figure 7.4(a-2) [182-184]. As shown in Figure 6.4(b-1), some crystalline quartz (SiO_2), could be detected in an otherwise amorphous PE coating. A similar distribution of phases was found on the PE coating after the immersion test, Figure 7.4(b-2). The presence of some sodium chloride (NaCl) on this latter sample is attributed to the salt solution in which the sample was immersed. Crystalline Ca-silicate phases were detected in both the ME and DE coatings. These phases are present in the Portland cement added to the pure enamel slurry used to produce the ME coating prior to corrosion tests, as shown in Figures 7.4(c-1) and (d-1). After corrosion tests, no change in main components was observed for the DE coating. However, some lepidocrocite (γ-FeOOH) was observed in the ME coating, which is attributed to the corrosion that occurred in the immersion test.

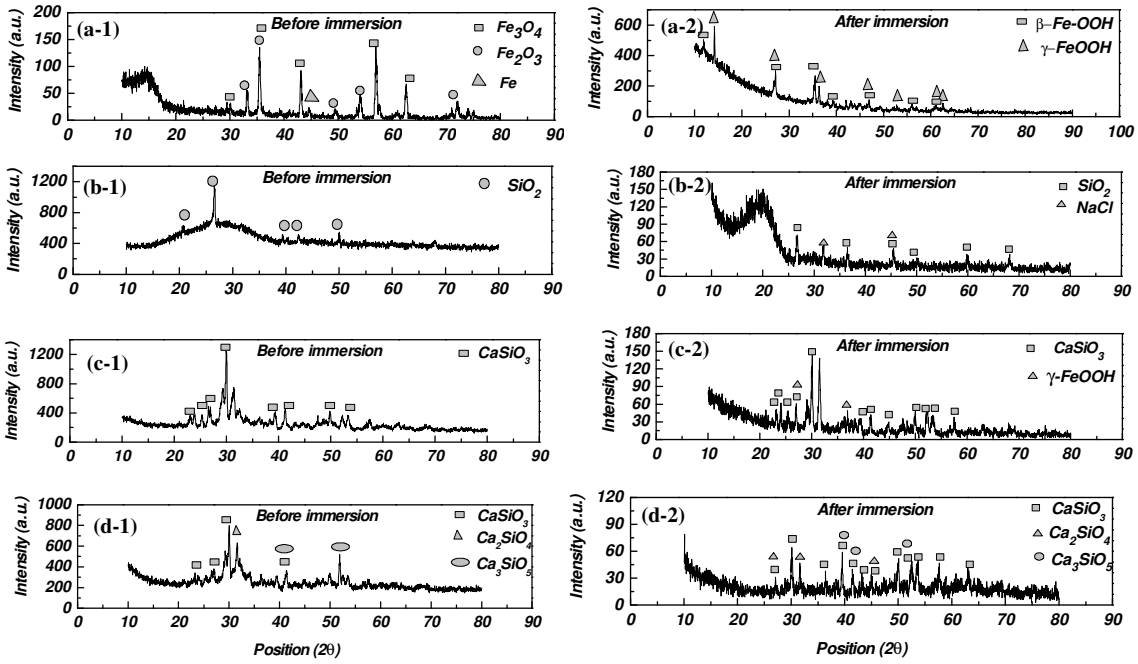

Figure 7.4 XRD patterns on the surface of steel rebar before and after immersion tests in 3.5 wt.% NaCl solution: (a-1, a-2) uncoated rebar, (b-1, b-2) pure enamel coated rebar, (c-1, c-2) mixed enamel coated rebar, and (d-1, d-2) double enamel coated rebar

7.3.3 Electrochemical Study.

7.3.3.1 FBE coated steel bar. Figure 7.5 presents the electrochemical impedance spectra of the FBE coated rebar samples immersed in 3.5 wt.% NaCl solution. Specifically, the modulus and the phase angle of the complex impedance, Z, for intact and damaged samples are plotted as a function of frequency in Figure 7.5(a) and Figure 7.5(b), respectively. It can be seen from Figure 7.5 that the intact FBE coating displayed capacitive behavior since the modulus-frequency curve is a 45° straight line and the phase angle fluctuates around -90°. Therefore, the intact FBE coating is an effective corrosion barrier for steel rebar. However, damaged FBE coating behaved quite differently. The impedance magnitude was significantly reduced from 10^6 MΩ cm^2 to 0.1 MΩ cm^2 at 0.005 Hz, and the phase-frequency plot can be characterized with two time constants. The first time constant at low frequencies was attributed to the resistance and capacitance of the steel-electrolyte interface, the second time constant at high frequencies was due to the resistance and capacitance of the FBE coating. The significant change in the impedance spectra was caused by impact-induced damage that provided a pathway for chloride ions to penetrate through and resulted in corrosion of the coated rebar in the NaCl solution. No significant difference in corrosion performance was observed between the FBE coated rebar with 6 impact points and with 12 impact points. These findings are in reasonable agreement with previous studies on intact and defective paint systems [185, 186].

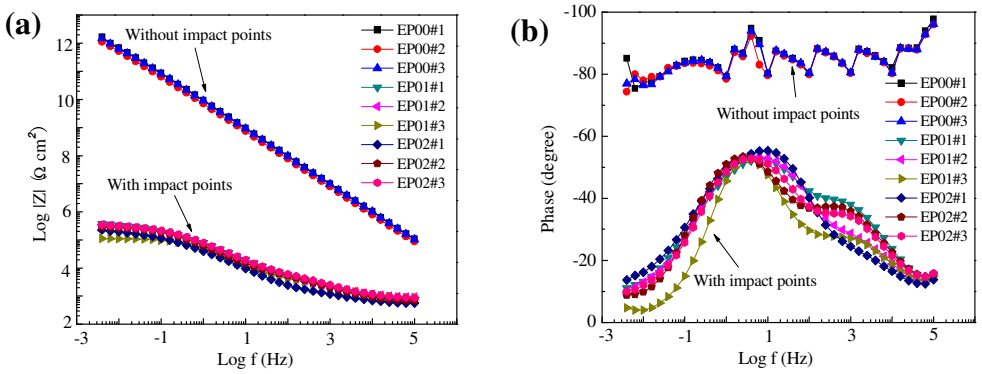

Figure 7.5 EIS test results of FBE coated steel rebar in Bode format: (a) modulus, and (b) phase angle

The electrical equivalent circuit (EEC) as shown in Figure 7.6(a) was used to model the corrosion system with intact FBE coated rebar. Here, R_s represents the solution resistance between the reference electrode and the samples, C_{dl} and R_{ct} represent the double layer capacitance and the charge transfer resistance at the interface between the epoxy coating and the substrate steel. For damaged FBE coating, a different EEC model as shown in Figure 7.6(b) was used to fit the EIS test results. This EEC model is widely used for the evaluation of coating performance and electrochemical behavior of reinforcing steel in concrete [187-189]. The EEC model consists of the solution resistance (R_s), the resistance and capacitance (R_c and CPE_c) of FBE coating, and the charge transfer resistance and double layer capacitance (R_{ct} and CPE_{dl}) of the interface between electrolyte solution and substrate steel. Replacement of the capacitance C for the intact FBE coated rebar in Figure 7.6(a) with the constant phase element (CPE) in Figure 7.6(b) was attributed to the non-homogeneity induced by the coating damage [190, 191]. CPE is defined by two parameters Y and n. When n = 1, CPE resembles a capacitor with capacitance Y. When n =0, CPE represents a resistor with resistance Y^{-1}. The effective capacitance was calculated according to the following equation [192]:

$$C = Y^{\frac{1}{n}} R^{\frac{1-n}{n}} \tag{7.1}$$

where R is referred to R_c and R_{ct} when the coating capacitance C_c and the double layer capacitance C_{dl} are calculated, respectively. Correspondingly, CPE_c is represented by Y_c and n_c, and CPE_{dl} by Y_{dl} and n_{dl}. ZSimpWin software was used to fit the EEC model into the EIS test data. The Chi-squared value in the order of 10^{-3} confirmed a satisfactory fitting process.

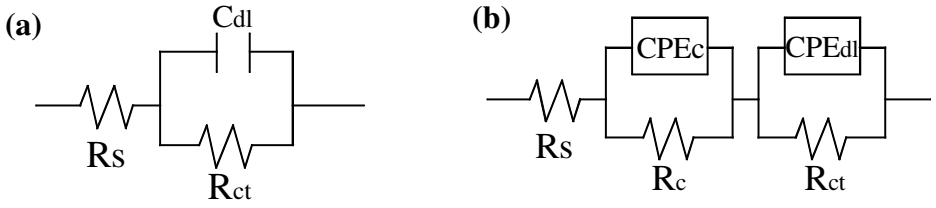

Figure 7.6 EEC model for FBE coated rebar: (a) without impact points, and (b) with impact points

Figures 7.7(a, b) present the effect of coating damage on the charge transfer resistance and the double layer capacitance of FBE coating, respectively. Each point represents the average of three samples with an error bar representing one standard deviation. It can be seen from Figure 7.7 that all parameters vary little except for the exponent n_{dl} of damaged coating with 6 impact points. They indicated a high degree of consistency of FBE coating. For the FBE coating without impact points, a low double layer capacitance of 10^{-3} nF/cm^2 and a high charge transfer resistance of 10^6 MΩ cm^2 indicated a high degree of corrosion protection. For the FBE coating with impact points, the double layer capacitance increased to 10 μF/cm^2 and the charge transfer resistance decreased to 0.1 MΩ cm^2, corresponding to a significantly reduced degree of corrosion protection. The significant change in corrosion performance is attributed to the increased conductivity and capacitance as a result of chloride ions penetration through the impact-induced damage area. The numbers of impact points seemed to have little influence on the coating capacitance and charge transfer resistance. Figure 7.7(c) shows a reduction of the exponent n_{dl} of CPE_{dl} from 1.0 for the intact coating to 0.7 for damaged coating, indicating a significant drift of the electrochemical behavior away from a capacitor. This is because the impact-induced damage increased the non-homogeneity of FBE coating. Therefore, FBE coating is very sensitive to the onset of any damage.

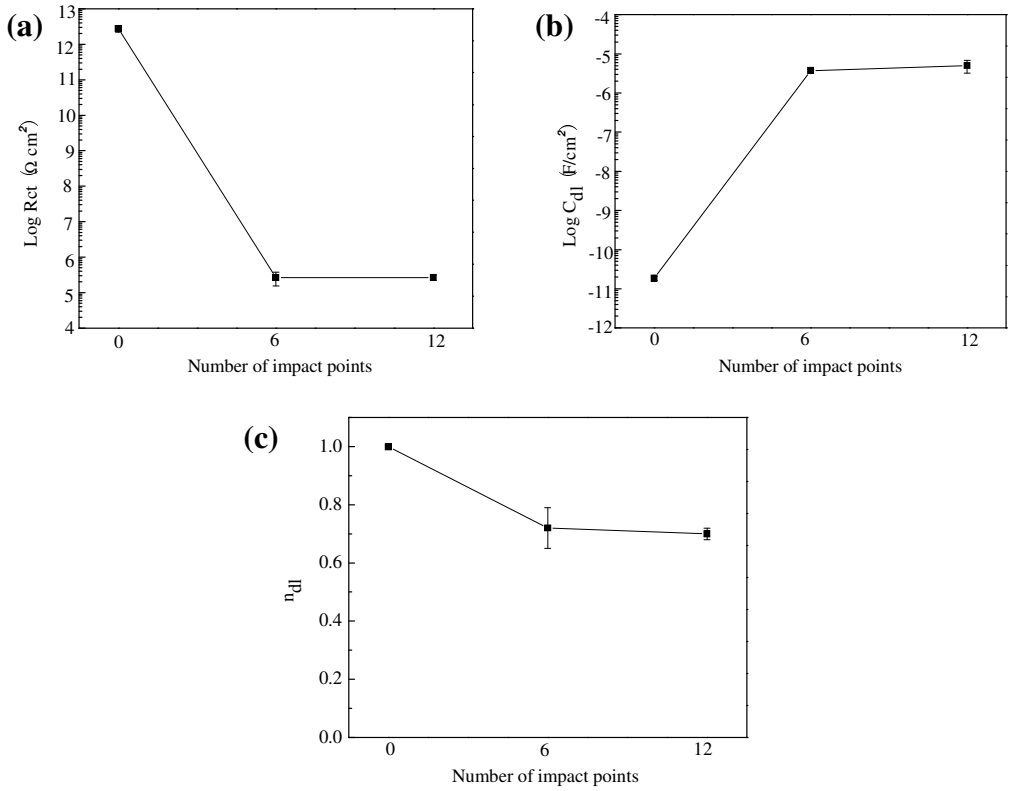

Figure 7.7 Fitted parameters of FBE coated rebar: (a) charge transfer resistance R_{ct}, (b) double layer capacitance C_{dl}, and (c) CPE_{dl} exponent n_{dl}

7.3.3.2 Enamel coated steel bar. The electrochemical impedance spectra of uncoated and three types of enamel coated samples are presented in Figure 7.8 in the format of Bode plots. It can be observed that all the plots featured two capacitive loops, similar to those for damaged FBE coating as shown in Figure 7.5. Therefore, the EEC model in Figure 7.6(b) was used to fit the EIS test results of uncoated and enamel coated rebar samples with or without impact points. In this model, R_c and CPE_c respectively denote the resistance and capacitance of mill scale or enamel coatings. The Chi-squared value in the fitting process to EEC model was in the range between 10^{-4} and 10^{-3}.

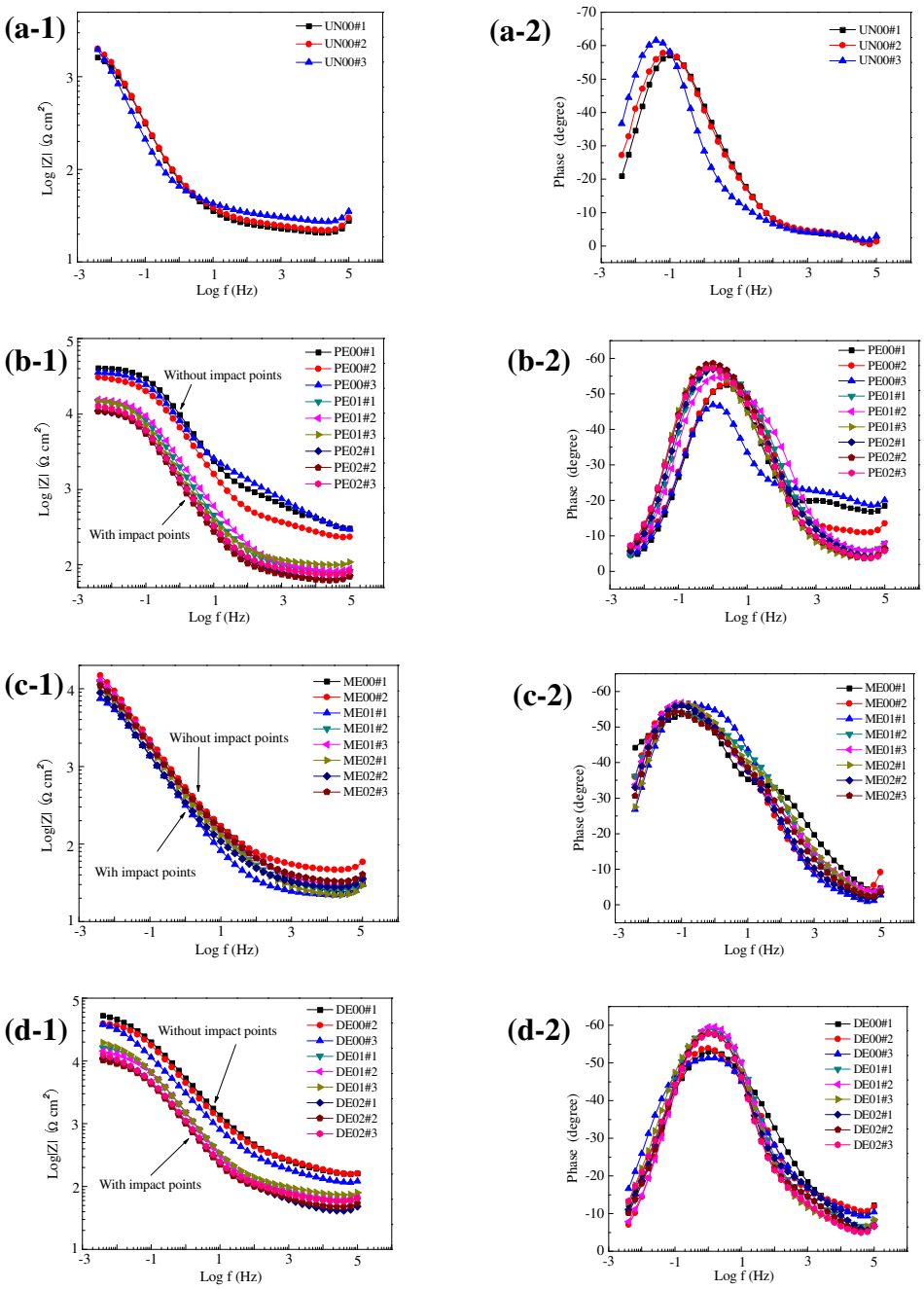

Figure 7.8 EIS test results in Bode format for: (a-1, a-2) uncoated rebar, (b-1, b-2) pure enamel coated rebar, (c-1, c-2) mixed enamel coated rebar, and (d-1, d-2) double enamel coated rebar

The similarity between Figure 7.8 and Figure 7.5 for damaged FBE coating is attributed to the fact that enamel coatings have porous microstructures as illustrated in

Figure 7.3, non-uniform coating thickness due to the influence of rebar ribs, and potential coating defects induced during handling [193]. In particular, the impedance of the ME coating is nearly independent of the number of impact points as shown in Figure 7.8(c). For the PE and DE coatings, a greater number of impact points leads to smaller impedances, as shown in Figures 7.8(b, d).

Figure 7.9 compares the properties of the uncoated and enamel coated rebar samples without impact points in terms of coating resistance R_c, coating capacitance C_c, and CPE_c exponent n_c. In general, coating resistance and coating capacitance represent a degree of ability of coating to resist the penetration of electrolyte solution and the diffusion process of electrolyte solution into the coating, respectively [194]. Among the three enamel coatings as shown in Figure 7.9, the PE coating had the lowest capacitance (0.2 $\mu F/cm^2$) and the highest resistance (1.3 $k\Omega\ cm^2$). These values indicate the best protection of PE coating against chloride ion penetration, which is likely attributed to its less porous microstructure with isolated pores, as shown in Figure 7.3(b-1). On the other hand, the ME coating had the highest capacitance and relatively low resistance, indicating the least degree of prevention to chloride ion penetration. This is attributed to its more porous microstructure, with interconnected pores, as shown in Figure 7.3(c-1). The properties of the DE coating lie in between those of the PE and ME coatings. Compared to the uncoated rebar samples, however, all three enamel coatings had more favorable corrosion-protection properties than the mill scale on the surface of uncoated rebar. The exponent n_c varied from 0.4 to 0.5 for all the uncoated and enamel coated samples, indicating significant non-homogeneities that came from the non-uniform structure of mill scale and the non-uniform coating thickness and defect during handling for the uncoated and enamel coated rebar, respectively.

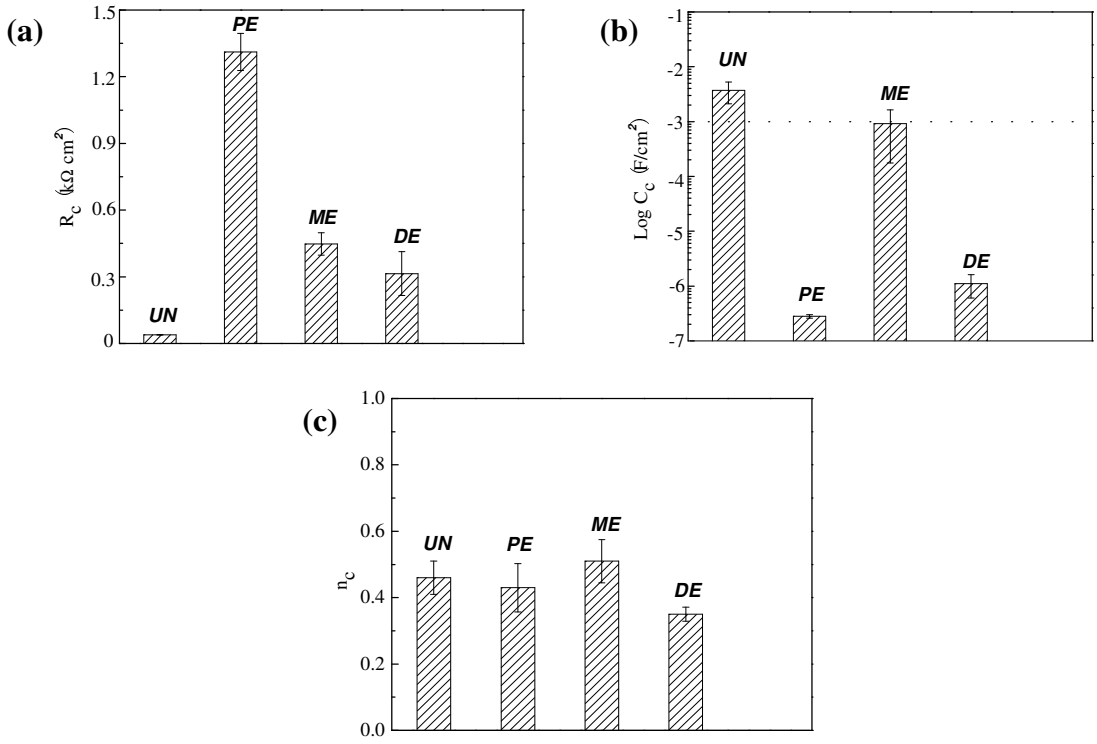

Figure 7.9 Property of intact enamel coatings and mill scale: (a) coating resistance R_c, (b) coating capacitance C_c, and (c) CPE_c exponent n_c

Figure 7.10 shows the sensitivity of three types of enamel coatings to impact points in terms of coating resistance R_c, coating capacitance C_c, and CPE_c exponent n_c. For all three enamel coatings, more impact points resulted in increasing capacitance and decreasing resistance to various extents. The PE and DE coatings were more sensitive to the number of impact points than the ME coating since the intact ME coating already revealed numerous interconnected pores and adding several impact points did not significantly increase the number of chloride ion penetration pathways. On the contrary, the intact PE and DE coatings had better barrier properties with isolated pores. Adding the damage points provided new pathways for chloride ions to penetrate through the coatings. As shown in Figure 7.10(c), the number of damage points did not affect significantly the electrochemical non-uniformity of all three enamel coatings.

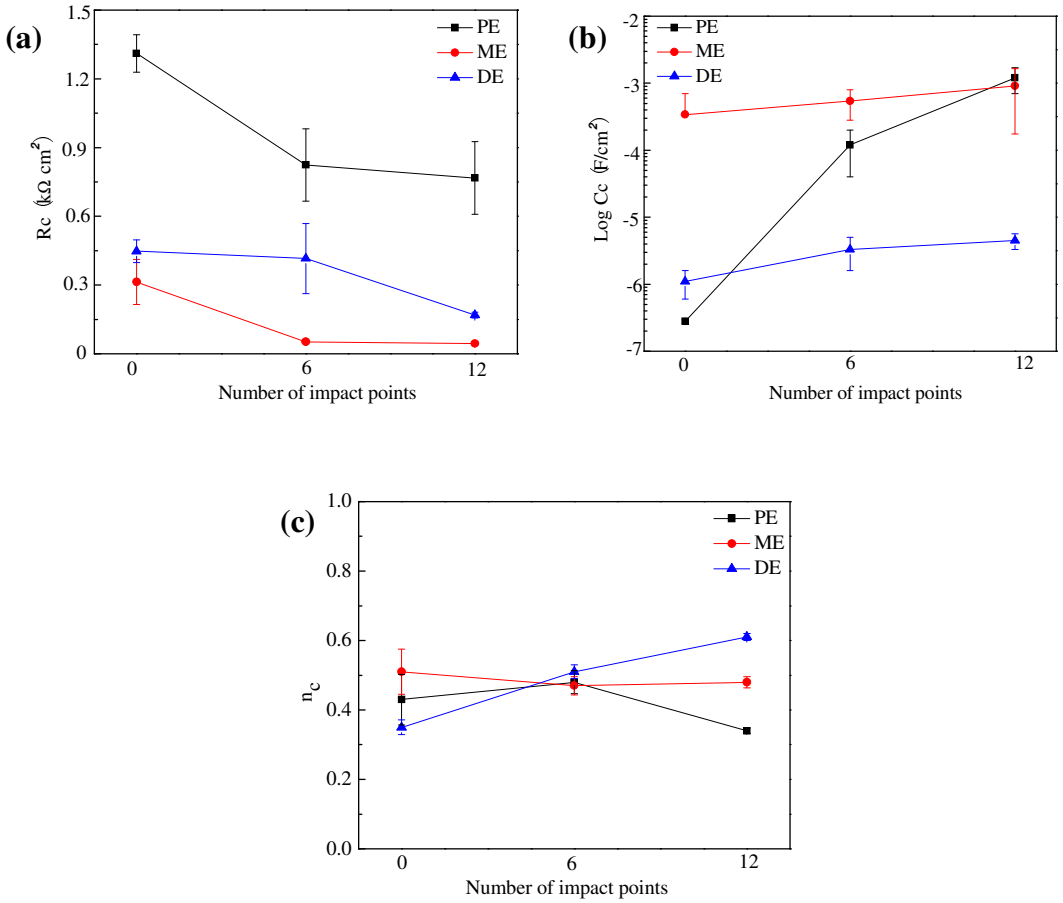

Figure 7.10 Sensitivity of coating properties to impact points: (a) coating resistance R_c, (b) coating capacitance C_c, and (c) CPE_c exponent n_c

Figure 7.11 compares the corrosion resistance of uncoated rebar and enamel coated rebar samples without impact points in terms of charge transfer resistance, R_{ct}, and double layer capacitance, C_{dl}, and CPE_{dl} exponent n_{dl}. The charge transfer resistance is inversely proportional to corrosion rate and is a measure of resistance to the transfer of electrons across the metal surface [172]. The double layer capacitance, calculated from Eq. (1), is a measure of ease of charge transfer. As shown in Figure 7.11, in comparison with the ME coating, the DE and PE coatings had a relatively higher charge transfer resistance and lower double layer capacitance, which is indicative of a smaller exposed area of steel to the electrolyte solution. The uncoated rebar samples had the lowest charge transfer resistance and the highest double layer capacitance compared with the three types

of enamel coated samples. The CPE_{dl} exponents ranged from 0.65 to 0.85, indicating great non-homogeneities of both the uncoated and enamel coated samples.

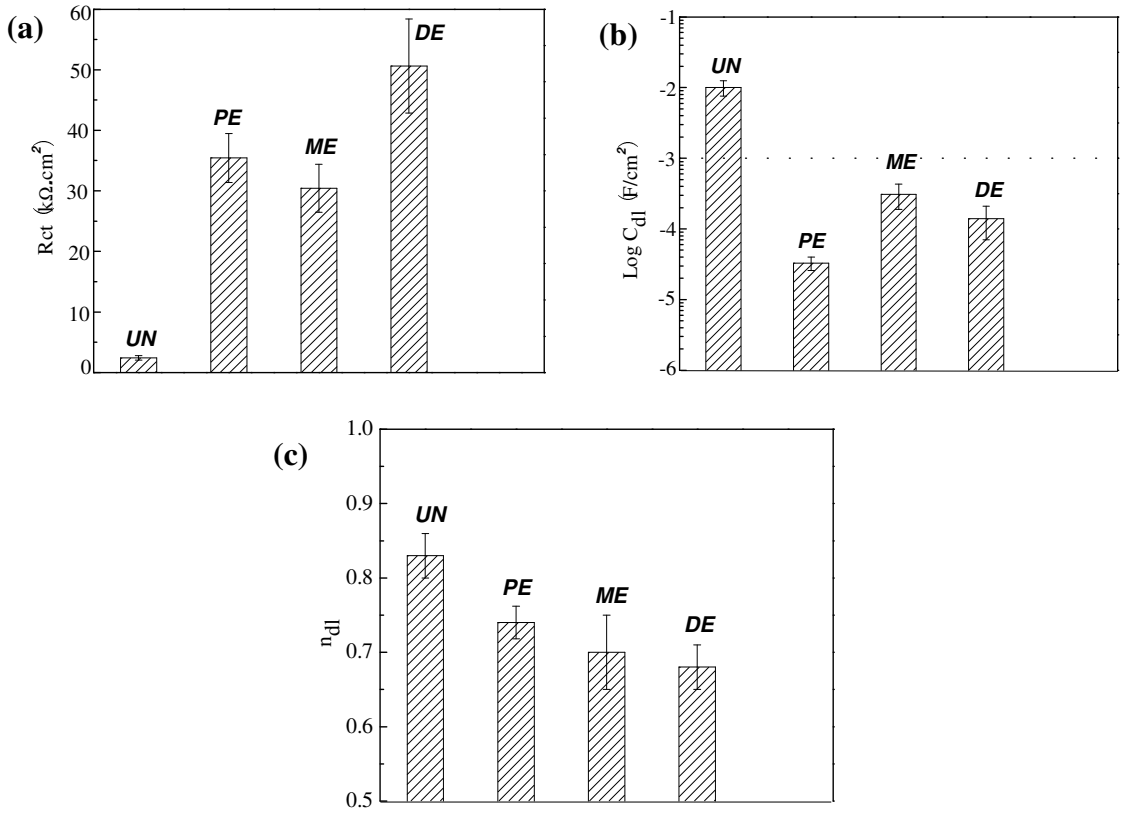

Figure 7.11 Corrosion behavior of three enamel coated versus uncoated samples: (a) charge transfer resistance R_{ct}, (b) double layer capacitance C_{dl}, and (c) CPE_{dl} exponent n_{dl}

Like Figure 7.10 for coating property sensitivity to damage, Figure 7.12 shows the corrosion sensitivity to impact points. Impact points increased the double layer capacitance and decreased the charge transfer resistance for all three types of enamel coatings. No significant difference was observed between the effect of 6 impact points and 12 impact points. As shown in Figure 7.12(c), there seems no obvious influence of impact-induced damage on the non-homogeneity of enamel coatings.

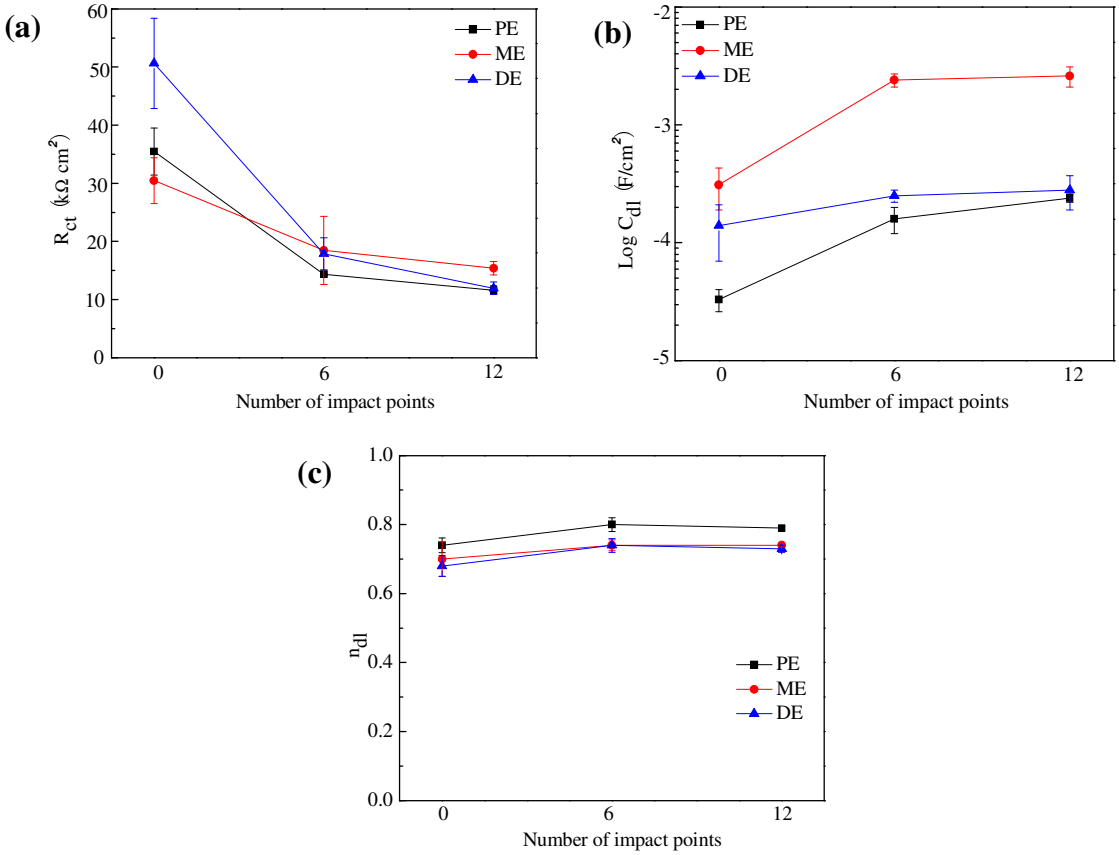

Figure 7.12 Sensitivity of corrosion behavior of enamel coated samples to impact points: (a) charge transfer resistance R_{ct}, (b) double layer capacitance C_{dl}, and (c) CPE_{dl} exponent n_{dl}

Compared with the FBE coating as shown in Figure 7.7, all three enamel coatings, shown in Figure 7.12, are significantly less sensitive to minor damage (0 to 6 points) but equally or more sensitive to further damage (6 to 12 points). This can be explained as follows. Intact enamel coating had some regions of exposed steel that developed during handling; thus, additional minor damage of the coating did not significantly affect corrosion performance of the intact coating; and further coating damage contributed relatively less corrosion degradation. On the other hand, intact FBE coating was an effective corrosion barrier; thus minor damage of the FBE coating added new pathways for chloride ions penetration and significantly degraded corrosion performance, compared to the intact coating. Once initiated under minor damage, corrosion was extended rapidly underneath the FBE coating, which is typically referred to as under-film corrosion and

will be further discussed in Section 7.3.5. In fact, the charge transfer resistance of the enamel coatings with impact points in Figure 7.12(a) is in the same order of magnitudes as that for the damaged FBE coating, Figure 7.7(a).

7.3.4 Chloride Diffusion through Enamel Coatings. Figure 7.13 shows the cross-sectional elemental analysis of uncoated and enamel coated rebar samples after corrosion tests. For enamel coated rebar, the cross-sections were taken from the undamaged coating areas. For each sample, a SEM image and the corresponding distribution mappings for Fe, Cl, and Si were presented. Fe mapping was used for corrosion detection, Cl mapping was used for the detection of chloride ions, and Si mapping was used for the identification of the enamel coating location and thickness.

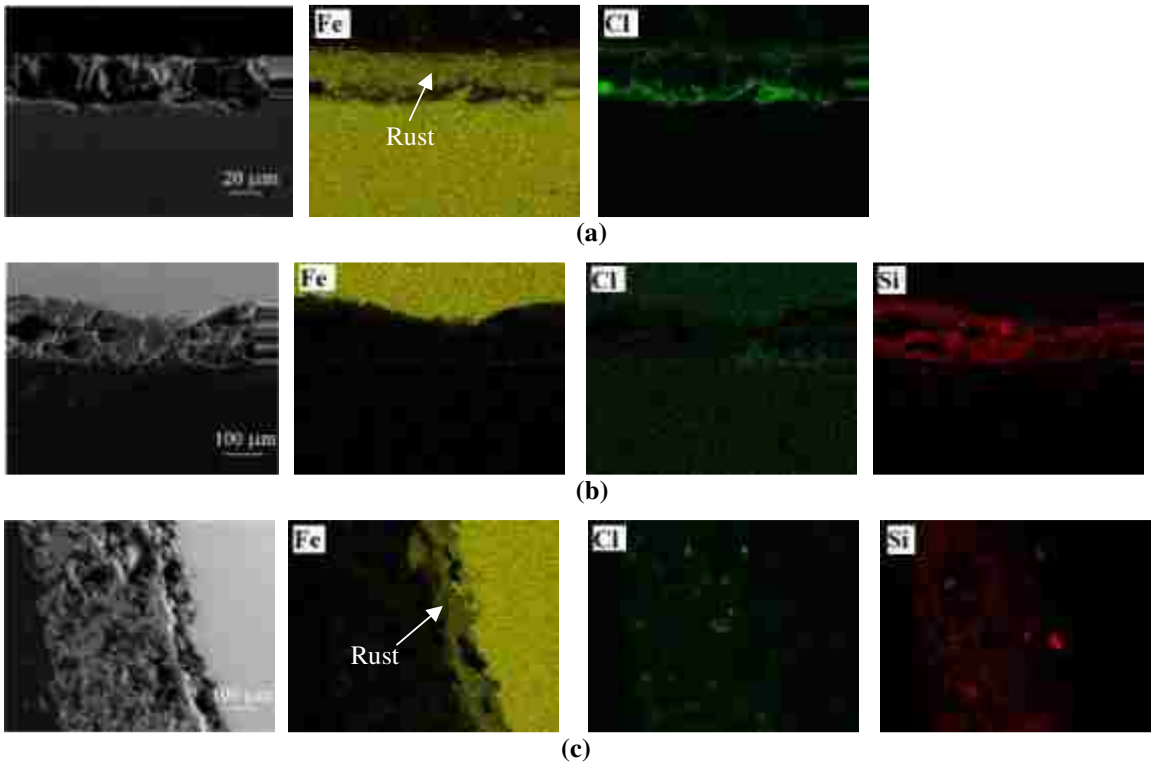

Figure 7.13 Elemental distribution maps of electrochemical tested samples: (a) uncoated rebar, (b) pure enamel coated rebar, (c) mixed enamel coated rebar, and (d) double enamel coated rebar.

(d)

Figure 7.13 Elemental distribution maps of electrochemical tested samples: (a) uncoated rebar, (b) pure enamel coated rebar, (c) mixed enamel coated rebar, and (d) double enamel coated rebar (cont.)

It can be observed from Figures 7.13(a, c) that chloride ions were clearly detected in the rust layer of the uncoated rebar (as-received condition) and in the ME coating, revealing the diffusion of chloride ions through the mill scale and the ME coating. This is further verified by the corrosion product (rust) on the surface of the uncoated rebar and near the interface of the ME coating and its substrate steel. Corrosion products were concentrated near the interface mainly because the sample was immersed in salt solution for a short duration and corrosion products diffused through a part of the coating layer only. As shown in Figures 7.13(b, d), no chloride ions were detected inside the PE and DE coatings even though isolated pores were present as discussed previously. The Fe mappings also verified that little or no corrosion product was detected at the interface between the PE/DE coating and its substrate steel. Therefore, the PE and DE coatings are effective physical barriers that successfully prevented chloride ions from penetration.

7.3.5 Mechanism of the Corrosion Resistance of FBE Coating and Three Enamel Coatings. Based on the SEM images, electrochemical impedance spectra, and chloride distribution mappings, the corrosion mechanisms of the enamel coated steel in 3.5 wt.% NaCl solution can be summarized and illustrated as shown in Figures 7.14(b-d). They are compared with the corrosion mechanism of FBE coated rebar as illustrated in Figure 7.14(a). When it remains intact, the FBE coating is an effective physical barrier to protect the coated steel bar from corrosion. Once damaged, the FBE coating can no longer prevent the electrochemical reaction between the electrolyte and the steel, and its ability for corrosion protection is reduced dramatically. As illustrated in Figure 7.14(a), the damaged coating area provides a pathway for aggressive ions to penetrate through the coating layer and corrosion takes place on the surface of the exposed steel. Furthermore,

once initiated, corrosion can extend beneath the coating, the so-called under-film corrosion as clearly illustrated in Figure 7.15(a). In recent years, such a corrosion mechanism for epoxy coated rebar was supported by several field studies in North America [33, 195, 196] where transportation and handling damage to FBE coatings is a culprit.

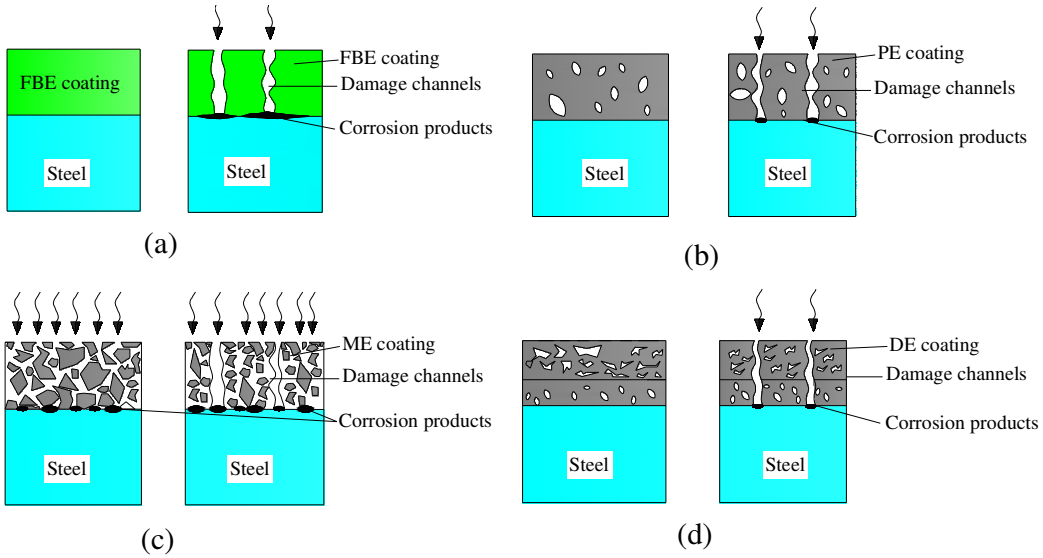

Figure 7.14 Schemes of corrosion process of FBE and enamel coatings: (a) FBE coating (intact & damaged), (b) pure enamel coating (intact & damaged), (c) mixed enamel coating (intact & damaged), and (d) double enamel coating (intact & damaged)

Similar to FBE coating, the intact PE and DE coatings as shown in Figures 7.14(b, d) can also protect the coated steel rebar from corrosion, although the enamel coating with isolated air voids is not uniform, particularly around the rebar ribs. This non-uniformity makes the rib regions susceptible to corrosion attack. Due to its brittleness, enamel coatings are susceptible to impact damage. As a result, the enamel coated rebar often experiences corrosion pits at isolated damage locations as illustrated in Figures 7.14(b, d). Unlike the FBE coating, enamel coating is chemically bonded to its steel substrate [116], limiting the pitted corrosion in the vicinity of the damaged coating area, avoiding the under-film corrosion in the enamel coated rebar as detailed in Figure 7.15(b).

As shown in Figure 7.14(c), the corrosion mechanism of the ME coating differs from those of the PE and DE coatings. Even for an undamaged coated rebar, the ME coating has interconnected pores due to the addition of Ca-silicate particles, potentially providing multiple pathways for aggressive ions to penetrate and resulting in widespread corrosion along the length of coated rebar. Therefore, corrosion in the ME coating takes place early on and is insensitive to additional damage that may be caused during transportation and handling.

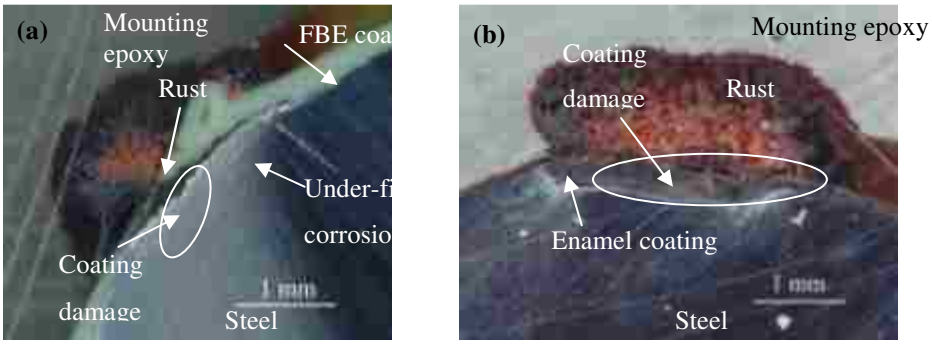

Figure 7.15 Supporting evidences of corrosion mechanisms: (a) damaged FBE coating, and (b) damaged enamel coating

7.4 SUMMARY

In this study, the corrosion resistances of pure, mixed, and double enamel coatings applied on reinforcing steel bars were evaluated by means of electrochemical impedance spectroscopy. Their performance was compared with commercially available FBE coating. Corrosion sensitivity to coating damage was investigated with controlled levels of damage induced by a standard impact tester. Based on the test results, the following conclusions can be drawn about the corrosion performance of these coated samples:

(1) The intact double and pure enamel coatings provided a much higher degree of corrosion protection than the mixed enamel coating with 50% calcium silicate by weight mainly due to the absence of interconnected pores in the double and pure enamel coatings. All enamel coatings were significantly outperformed by the intact FBE coating.

(2) The corrosion performances of the double and pure enamel coatings were more sensitive to damage than the mixed enamel coatings because damage provides corrosion pathways that did not exist in the undamaged DE and PE samples. The corrosion resistance of FBE coating was most sensitive to damage and, once damaged, was in the same order of that for the damaged enamel coatings.

(3) Pitted corrosion of both double and pure enamel coatings was initiated at the location of damaged coating areas but restrained locally due to well-adhered glassy layers on the surface of coated rebar. Interconnected regions of calcium silicate particles in the mixed enamel coating appeared to provide a corrosion pathway to the underlying steel rebar so that both uniform and pitted corrosions occurred on the surface of damaged coated rebar. Although superior when undamaged, the corrosion performance of the FBE coating significantly degraded with local damage of the sort that can occur during transportation and handling due to the well-known under-film corrosion mechanism.

(4) The non-uniformity of coating thickness due to rebar deformation must be overcome with an alternative enameling process to improve the corrosion performance of enamel coatings for practical applications.

8. DETERIORATION MECHANISMS, DETERIORATION RATE, AND TIME-DEPENDENT EQUIVALENT CIRCUIT REPRESENTATION OF MORTAR-COATING-STEEL SYSTEMS BY EIS

8.1 INTRODUCTION

Reinforced concrete (RC) structures are often exposed to a variety of environmental conditions that lead to deterioration and a reduction in service life. For example, corrosion in reinforcing steel bars is a form of the most severe deterioration of transportation infrastructure. In general, the life span of corrosion-affected concrete structures with uncoated reinforcing steel bars can be divided into three stages [72]. Stage I represents the healthy state of RC structures from the completion time of new construction to the initiation of corrosion. This stage is controlled by the diffusion of carbon dioxide or aggressive ions such as chloride through the concrete cover, which mainly depends on the thickness and permeability of the concrete cover and the concentration of aggressive ions on the concrete surface [197-199]. Stage II represents the damage state of the structures from the initiation of corrosion to the end of serviceability. The end of serviceability can be defined to correspond to the code-specified critical concrete crack width or delamination or to the predetermined deflection design criterion associated with corrosion-induced reduction in stiffness. Stage II is controlled by the corrosion rate of the reinforcement steel, which largely depends on environmental factors such as temperature, moisture, and the activities of oxygen, as well as the characteristics of the concrete structures and materials, such as thickness and permeability of concrete cover [80, 93, 200]. Stage III represents the safety state of the structures from the end of serviceability to the ultimate failure [86-91]. The ultimate failure due to corrosion can occur in many modes, including losses of flexural strength and shear strength associated with a significant reduction of reinforcing steel cross section. This stage is primarily controlled by environmental factors when the reinforcing steel is directly exposed to the environment through corrosion-induced cracks in the concrete cover.

In our previous study [115], the corrosion characteristics of deformed steel bars coated with three types of enamel and fusion-bonded epoxy (FBE) were investigated after

immersion in 3.5 wt.% NaCl solution. The enamel coatings improved the corrosion resistance of the steel bars to various degrees, depending on their damage and uniformity. Electrochemical techniques were also used to study the effects of enamel coatings on the corrosion resistance of smooth steel bars embedded in mortar cylinders [23] and it was found that the corrosion performance of enamel-coated smooth bars was significantly better than that of enamel-coated deformed bars. However, deformed instead of smooth steel bars are widely used in RC structures, and their corrosion performance is of great interest to engineering applications. More importantly, the influence of water-cement ratio, exposure conditions, and the state of coating-steel interface on the life-cycle performance of enamel-coated steel bars has not yet been investigated.

In this study, uncoated, enamel-coated, and fusion bonded epoxy (FBE)-coated deformed steel bars embedded in mortar cylinders were tested in 3.5 wt.% NaCl solution for up to 244 days to understand and quantify their deterioration characteristics. The electrochemical behavior of various mortar-coating-steel interfaces was first characterized with EIS tests. The large set of data on the interfacial behavior was then analyzed to produce equivalent electrical circuit models for the mortar-coating-steel interfaces. The deterioration mechanism and rate of enamel- and FBE-coated steel bars in mortar were finally determined from the evolution of various parameters extracted from the equivalent circuits and from visual inspection of the samples at the conclusion of each test. Effects of water-cement ratios and exposure conditions on the deterioration rate of the mortar-coating-steel interfaces were investigated and related to the penetration of chloride ions through the mortar cover.

8.2 MATERIAL AND METHODS

8.2.1 Preparation of Enamel Coating and Cylindrical Specimens. Deformed steel bars (12.7 mm in diameter) used in this study are the same as the ones described in chapter 7 (Figure 8.1(a)). The steel bars were coated by Pro-Perma Engineered Coatings with pure enamel (PE), mixed enamel (ME) with 50% PE and 50% calcium silicate by weight, and double enamel (DE) with an inner PE layer and an outer ME layer. The coating materials and process are described in chapter 6. For comparison, both uncoated

(as-received) steel bars and commercial FBE-coated steel bars were also prepared and tested.

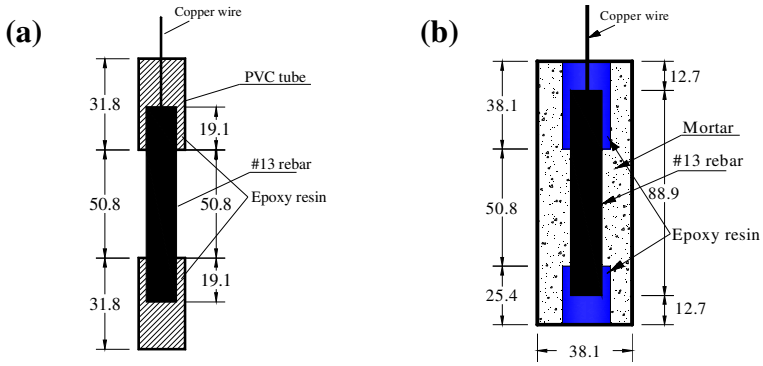

Figure 8.1 Geometry of samples: (a) rebar, and (b) mortar cylinder (unit: mm)

Type-I ordinary Portland cement, described in chapter 6, was used to prepare mortar specimens. In this study, two water-cement ratios were used in the batch design as given in Table 8.1. The fine aggregates used were Missouri River sands with a maximum size of 6.35 mm and a fineness modulus of 2.80.

Table 8.1 Mortar mix proportions

Batch designation	Mix proportions (relative weight ratio)		
	Cement	Sand	Water
40	1	1.83	0.40
55	1	2.81	0.55

Cylindrical mortar specimens were prepared in the same way as described in chapter 6 (Figure 8.1(b)). Each specimen was 114.3 mm tall and 38.1 mm in diameter with one concentrically embedded 88.9 mm long steel bar that is either uncoated, enamel-coated, or FBE-coated. Twenty-four hours after casting, all specimens were moved to the curing room (20 °C, 100% relative humidity) for 28 days prior to testing. Three specimens were prepared for each of four test situations: the two water-cement ratios

shown in Table 8.1 and two different exposure conditions. The mortar cylinder specimens were kept in glass beakers filled solutions prepared from distilled water and 3.5 wt. % NaCl (reagent grade, Fisher Scientific). The specimens were divided into two groups. One group was continuously immersed in the 3.5 wt.% NaCl solution. The other group was subjected to bi-weekly wet-dry cycles, each consisting of one week of continuous immersion (wet) followed by a second week out of solution and exposed to the room ambient (dry). In order to keep a constant concentration of the test solution, a prescribed level of distilled water was added every two days to compensate for the loss due to evaporation. In total, 60 mortar cylinder specimens were prepared and tested, including 12 cylinders with uncoated steel bars, 12 with PE-coated steel bars, 12 with ME-coated steel bars, 12 with DE-coated steel bars, and 12 with FBE-coated steel bars. In addition, one specimen of each type was prepared for microstructure analysis of mortar-coating-steel interfaces.

8.2.2 Microstructure Examination at Mortar-Coating-Steel Interface. Characterization of the microstructure of the mortar-coating-steel interfaces is important to understanding the electrochemical behavior of coated steel bars [201, 202] and more so to the establishment of realistic equivalent electrical circuit models. The relevant interfaces were investigated by scanning electron microscopy (SEM, Hitachi S4700, Tokyo, Japan). One mortar specimen of each type was cross-sectioned through their respective axial centers using a diamond saw, and then abraded using a series of silicon carbide papers to 1200 grit. After abrading, the samples were rinsed with de-ionized water and kept in an oven preset to 60 °C for at least 48 hours to drive off any remaining moisture prior to the microscopic study.

8.2.3 Chloride Profile Analysis. When the mortar specimens with steel bars were cast, an additional 16 mortar cylinders without steel bars were prepared to investigate chloride penetration through mortar over time. These pure mortar cylinders were cast with the same two water-cement ratios (w/c = 0.40 and 0.55), and tested under the same two exposure conditions (continuous immersion in 3.5% NaCl solution and bi-weekly wet-dry cycles) as the steel containing samples. Approximately every two months, one cylinder from each of the four conditions was removed from the test and cross-sectioned across the axis with a diamond saw. Mortar powder (equal weight) was collected from

three evenly-distributed points around the cylinder circumference at depths of 3.1 mm, 7.9 mm, and 12.7 mm, respectively, from the side surface of the cylinder. For each depth, the three samples totaling 1.5 g were combined for a rapid chloride content analysis. The mortar powders were mixed with 9 ml of an extraction liquid (96% de-ionized water and 4% hydrogen peroxide (H_2O_2). After agitating for five minutes, the mixture was then filtered into another container with 1 ml buffer solution (76% de-ionized water and 24% hepes, $C_8H_{18}N_2O_4S$), and a calibrated Cl-ion electrode was inserted into the filtered liquid and, once stabilized to within 0.2 mV, the voltage reading was recorded with the Rapid Chloride Test Water (RCTW) instrument (German Instruments, Inc), and the chloride content was then determined using appropriate calibration references.

8.2.4 Electrochemical Measurement. EIS tests were conducted approximately every 30 days through the 244 days of testing. After each EIS test, the used NaCl solution was replaced. The EIS measurements were taken with a typical three-electrode test setup, consisting of a 25.4 mm × 25.4 mm × 0.254 mm platinum sheet as a counter electrode, a saturated calomel electrode (SCE) as a reference electrode, and a mortar cylinder as a working electrode. These electrodes were connected to a Gamry, Reference 600 potentiostat/galvanostat/ZRA for data acquisition. EIS measurements were taken at 5 points per decade with a sinusoidal potential of 10 mV applied around the open-circuit potential with a frequency range of 5 mHz to 100 kHz.

8.2.5 Forensic Study on Tested Specimens. After 244 days of tests, all mortar cylinders were removed from the NaCl solution and dried in an oven at 60 °C for two days. The dry mortar cylinders were removed from the steel bars using a steel hammer, and the surface condition of the exposed steel bars was examined with an optical microscope.

8.3 RESULTS AND DISCUSSION

8.3.1 Mortar-Coating-Steel Interfacial Microstructures. Figure 8.2 shows cross-sectional SEM images of the mortar-coating-steel interfaces of enamel-coated (three types) and FBE-coated steel bars, and the mortar-steel interface of uncoated steel bars. These images were taken between two ribs on the deformed bars where the enamel

coatings are relatively uniform and thick in comparison with those areas over the ribs. Figure 8.2(a) clearly indicates a thin porous oxide layer approximately 30 μm thick between the mortar and the uncoated steel bar, representing the mill scale formed on the steel surface. As shown in Figure 8.2(b), the PE coating is approximately 150 μm thick and has many small air bubbles, likely produced from the reaction of enamel with the steel during the enameling process. As shown in Figure 8.2(c), the ME coating is approximately 250 μm thick and possesses an amorphous structure with connected channels through the entire coating thickness. As shown in Figure 8.2(d), the DE coating has two distinguishable inner and outer layers that are approximately 150 μm and 250 μm thick, respectively. In comparison with the PE coating, the inner layer of the DE coating has larger but fewer air bubbles. In comparison with the ME coating, the outer layer of the DE coating has fewer connected pores, which is likely attributed to its less reaction with the steel during the second firing. The FBE coating (Figure 8.2(e)) is approximately 300 μm thick and also has air bubbles near the steel surface. These bubbles can weaken the bond between the FBE coating and its substrate, promoting the well-known under-film corrosion as discussed in [115].

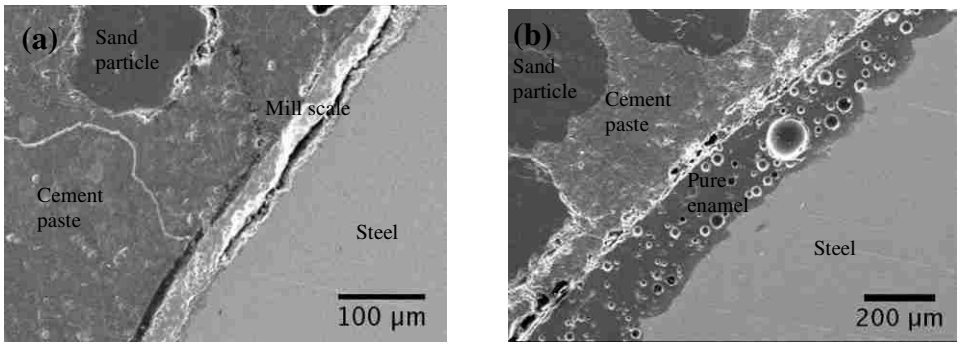

Figure 8.2 SEM images of interfaces for (a) uncoated, (b) pure enamel, (c) mixed enamel, (d) double enamel, and (e) FBE-coated steel bars.

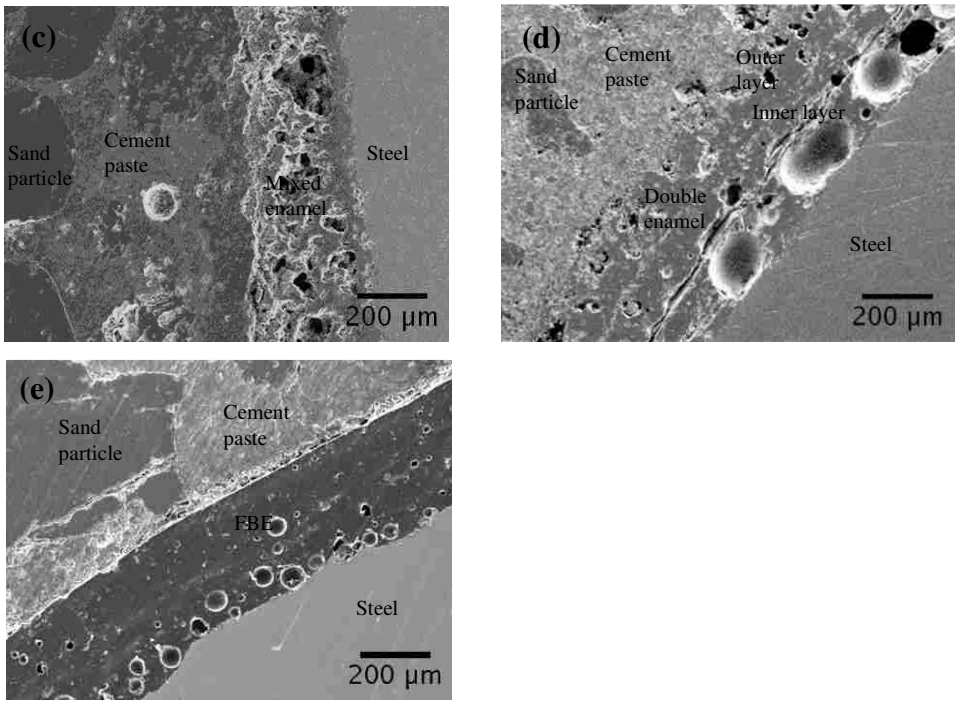

Figure 8.2 SEM images of interfaces for (a) uncoated, (b) pure enamel, (c) mixed enamel, (d) double enamel, and (e) FBE-coated steel bars. (cont.)

8.3.2 Chloride Profiles. Figure 8.3 shows the chloride content variation with mortar cover depth after 61 days, 124 days, 182 days, and 244 days of testing. Chloride transport in concrete is a process that involves ion diffusion, capillary suction, convective flow with flowing water, and physical and chemical binding [203]. For mortar specimens continuously immersed in NaCl solution, ion diffusion is the primary chloride transport mechanism. For mortar specimens subjected to bi-weekly wet-dry cycles, capillary suction plays an important role in chloride transport in addition to ion diffusion. For example, by comparing Figure 8.3(a) with Figure 8.3(c) and comparing Figure 8.3(b) with Figure 8.3(d), it can be clearly observed that the chloride content in mortar with w/c=0.40 is always lower than that with w/c=0.55 under the same exposure conditions since the former is less permeable than the latter [204]. By comparing Figure 8.3(a) with Figure 8.3(b) and comparing Figure 8.3(c) with Figure 8.3(d), it can be seen that the chloride content in mortar subjected to wet-dry cycles is greater than that in the continuously immersed mortar, due to capillary suction that accelerates the transport of chloride [205].

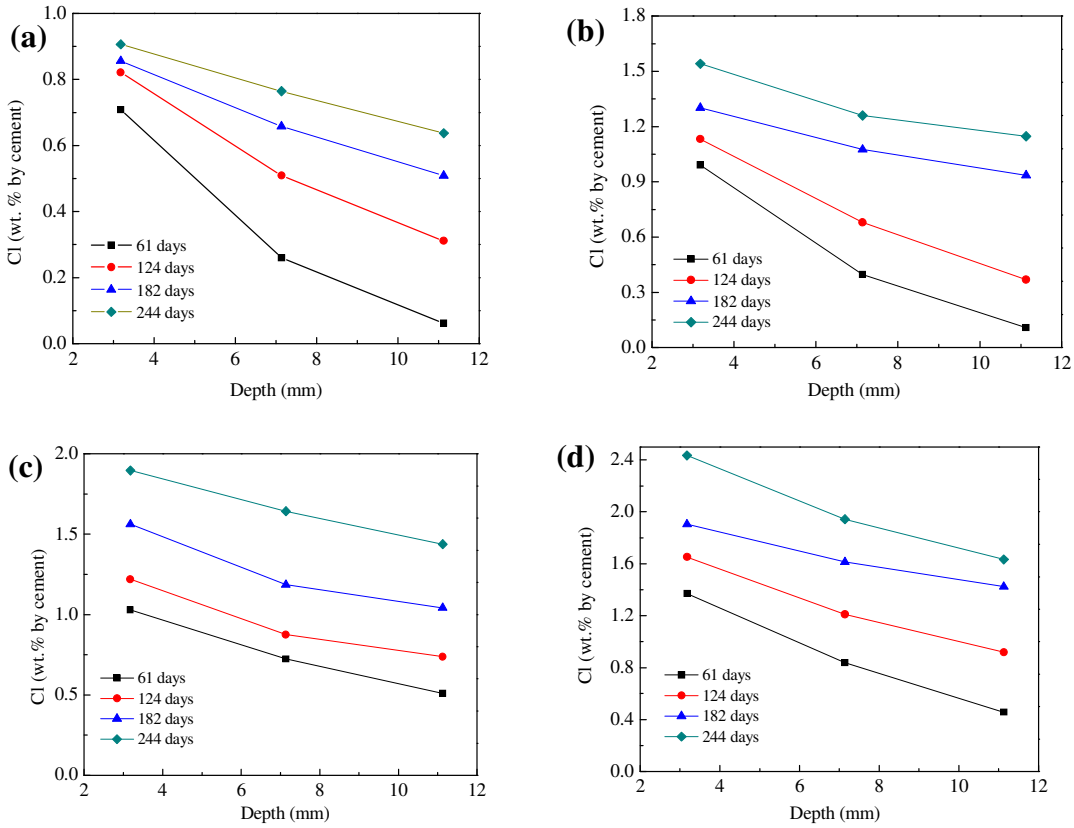

Figure 8.3 Chloride profiles for (a) w/c=0.40 and continuous immersion in 3.5 wt.% NaCl solution, (b) w/c=0.40 and bi-weekly wet-dry cycles, (c) w/c=0.55 and continuous in 3.5 wt.% NaCl solution, and (d) w/c=0.55 and bi-weekly wet-dry cycles.

8.3.3 Visual Observations. Examples of the surface conditions of uncoated, enamel-coated (three types), and FBE-coated steel bars after the conclusion of the 244 days of corrosion testing are shown in Figure 8.4. As clearly seen in Figure 8.4(1-a) to Figure 8.4(1-d), the uncoated bars subjected to the bi-weekly wet-dry cycles displayed more severe corrosion than the bars continuously immersed in NaCl solution.

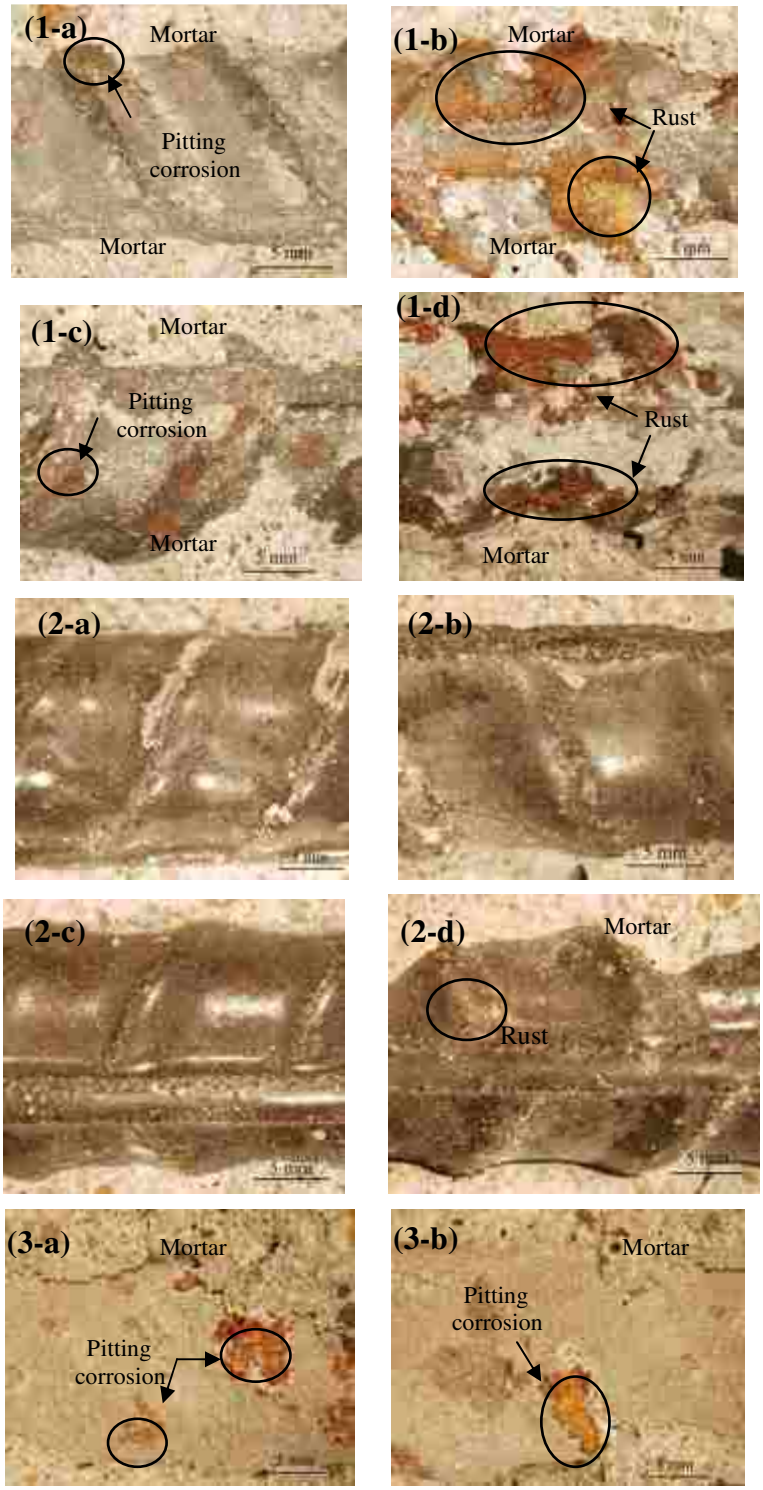

Figure 8.4 Optical images of the surface conditions of 244-day tested samples with (1) uncoated, (2) pure enamel, (3) mixed enamel, (4) double enamel, and (5) FBE- coated steel bars for (a) w/c=0.40 and continuous immersion in 3.5 wt.% NaCl solution, (b) w/c=0.40 and bi-weekly wet-dry cycles, (c) w/c=0.55 and continuous immersion in 3.5 wt.% NaCl solution, and (d) w/c=0.55 and bi-weekly wet-dry cycles.

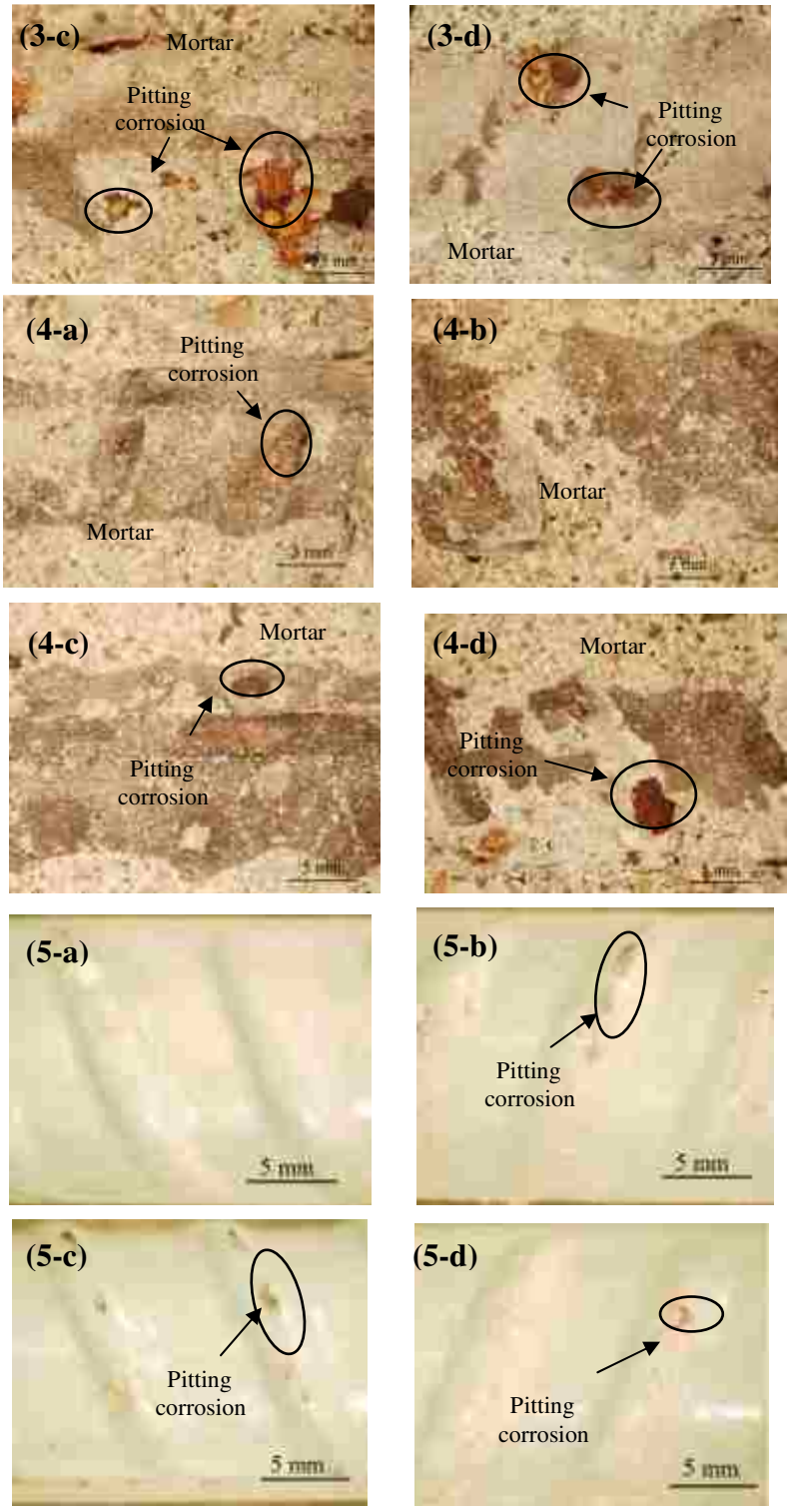

Figure 8.4 Optical images of the surface conditions of 244-day tested samples with (1) uncoated, (2) pure enamel, (3) mixed enamel, (4) double enamel, and (5) FBE- coated steel bars for (a) w/c=0.40 and continuous immersion in 3.5 wt.% NaCl solution, (b) w/c=0.40 and bi-weekly wet-dry cycles, (c) w/c=0.55 and continuous immersion in 3.5 wt.% NaCl solution, and (d) w/c=0.55 and bi-weekly wet-dry cycles. (cont.)

For PE- and DE-coated steel bars, shown in Figure 8.4(2-a) to Figure 8.4(2-d) and Figure 8.4(4-a) to Figure 8.4(4-d), respectively, only a few regions of pitting corrosion were observed and these could be attributed to regions where the coating was damaged during transportation or handling. However, significantly pitting corrosion was found on the surface of the ME-coated steel bars, as shown in Figure 8.4(3-a) to Figure 8.4(3-d). It appears that corrosion products diffused out through the connected channels in the ME coating. Specimens with FBE coating also showed some pitting corrosion around each damaged area as illustrated in Figure 8.4(5-a) to Figure 8.4(5-d).

8.3.4 Electrochemical Testing of Mortar-Coating-Steel Systems. Figures 8.5-8.9 show the impedance spectra (Bode plots) collected from all samples. The spectra from each of the three replicate samples were similar and so only one representative spectrum for each condition is shown. Overall, the phase spectra are more sensitive than the magnitude spectra to the different water-cement ratios and exposure conditions for every set of experiments, and so the phase spectra will be discussed in detail. As indicated in Figures 8.5 and 8.7, the uncoated and ME-coated steel bars have similar phase spectra that can each be clearly divided into three regions at low, intermediate, and high frequency. As shown in Figures 8.6 and 8.8, the peaks between low and intermediate frequency regions in the phase spectra of the PE- and DE-coated steel bars changed with corrosion time. As shown in Figure 8.9, the phase spectra from the FBE-coated bars are different from those of the uncoated and enamel-coated bars. Therefore, all five types of specimens can be divided into three categories: Group A for specimens with uncoated and ME-coated steel bars, Group B for specimens with PE- and DE-coated steel bars, and Group C for specimens with FBE-coated steel bars.

8.3.4.1 Group A: specimens with uncoated and ME-coated steel bars. The phase spectra from the uncoated and ME-coated samples are curved upward over 10 kHz for all specimens throughout the test period (Figures 8.5 and 8.7). The tail portion at high frequency does not change over time; this is related to the dielectric property of bulk matrix materials, mortar cover and the mill scale for the uncoated bars or the ME coating [20, 195]. A time-invariant intermediate frequency region is also present from 10 Hz to 10 kHz for specimens with uncoated steel bars and from 1 Hz to 10 kHz for specimens with ME-coated steel bars. The intermediate frequency region is likely related to the

passive film formed around the open channel in mill scale and ME coating [20]. In the low frequency range (< 10 Hz for uncoated bars and < 1 Hz for ME-coated bars), significant changes of phase spectra are observed over time. In general, corrosion occurs when solution in the micro-pores of cement paste is in contact with steel or when solution in the connected channels of the ME coating is in contact with the steel, resulting in the formation of corrosion microcells [206]. Breakdown of the passive film and the formation and buildup of corrosion products can change the local pore microstructure and chemistry of the microcells, and this is reflected in the low frequency range of impedance spectra [195]. Therefore, the low frequency range of the phase spectra in Figures 8.5 and 8.7 corresponds to the behavior of electrolyte-steel interfaces where corrosion occurred.

After 61 days, the phase spectra show evidence for diffusion behavior [136, 141] associated with the formation of corrosion products on the uncoated steel bars subjected to bi-weekly wet-dry cycles for both w/c=0.40 and w/c=0.55. However, for specimens with w/c=0.55, the low frequency region corresponding to diffusion behavior was gradually shifted to the intermediate frequency range over time, indicating an increase in the number of active sites due to continuing penetration of chloride. On the other hand, no diffusion behavior was observed for ME-coated specimens since the connected channels in the ME coating are larger than the pores in the mill scale and the buildup of corrosion products inside the channels thus does not significantly affect the diffusion of oxygen to the steel surface.

For specimens with uncoated steel bars as shown in Figure 8.5, both the water-cement ratio and exposure conditions affect the impedance spectra in the low frequency region, but the exposure conditions had a more significant influence on the corrosion behavior as indicated by a rapid decrease of phase angle in the low frequency region over time. For specimens with ME-coated steel bars as shown in Figure 8.7, the effect of water-cement ratio or exposure condition on impedance spectra in the low frequency region is not as significant as for the uncoated specimens. This is probably because the ME is 10 times thicker than the mill scale, and thus dominates the diffusion rate of oxygen and chloride prior to arrival to the steel surface even though the oxygen and chloride have penetrated through the mortar cover in different rates under the two exposure conditions.

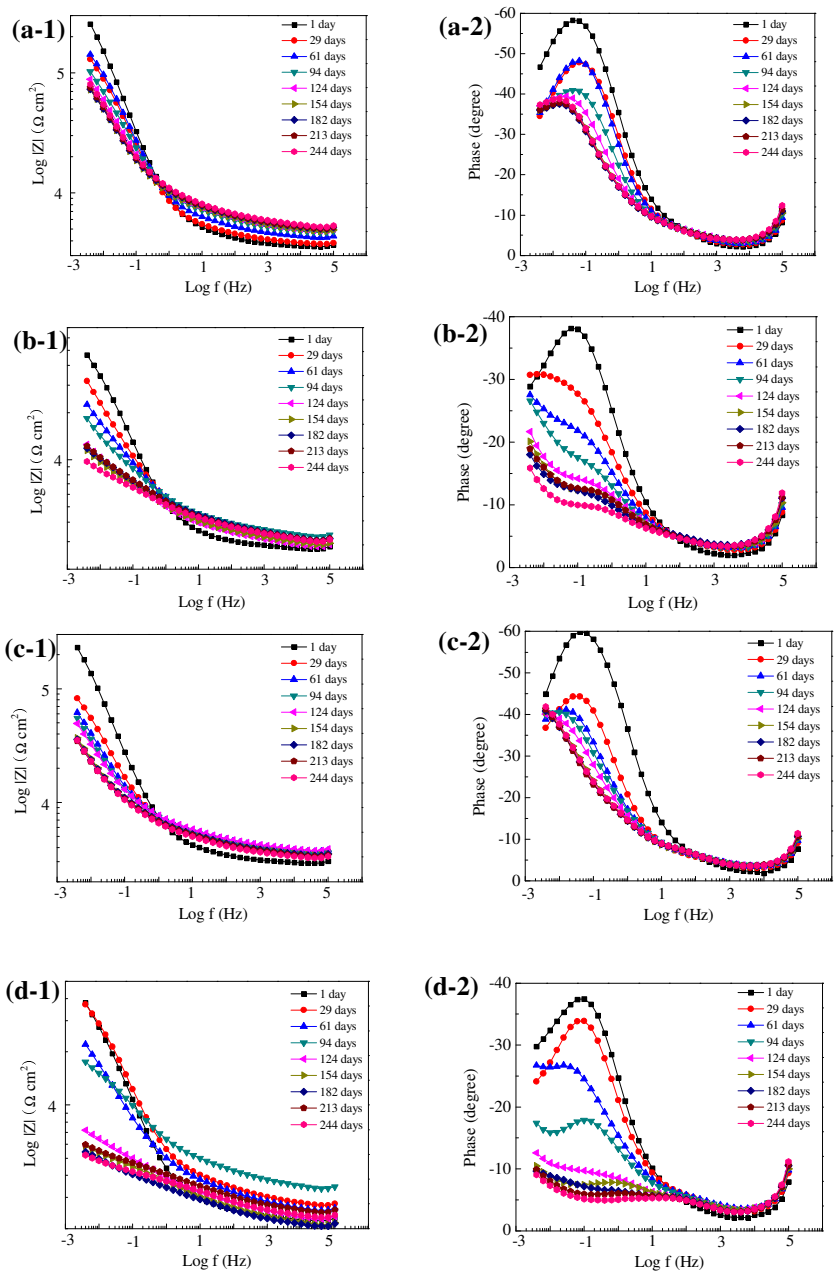

Figure 8.5 Representative Bode plots of mortar cylinders with uncoated steel bars for (a) w/c=0.40 and continuous immersion in 3.5 wt.% NaCl solution, (b) w/c=0.40 and bi-weekly wet-dry cycles, (c) w/c=0.55 and continuous immersion in 3.5 wt.% NaCl solution, and (d) w/c=0.55 and bi-weekly wet-dry cycles.

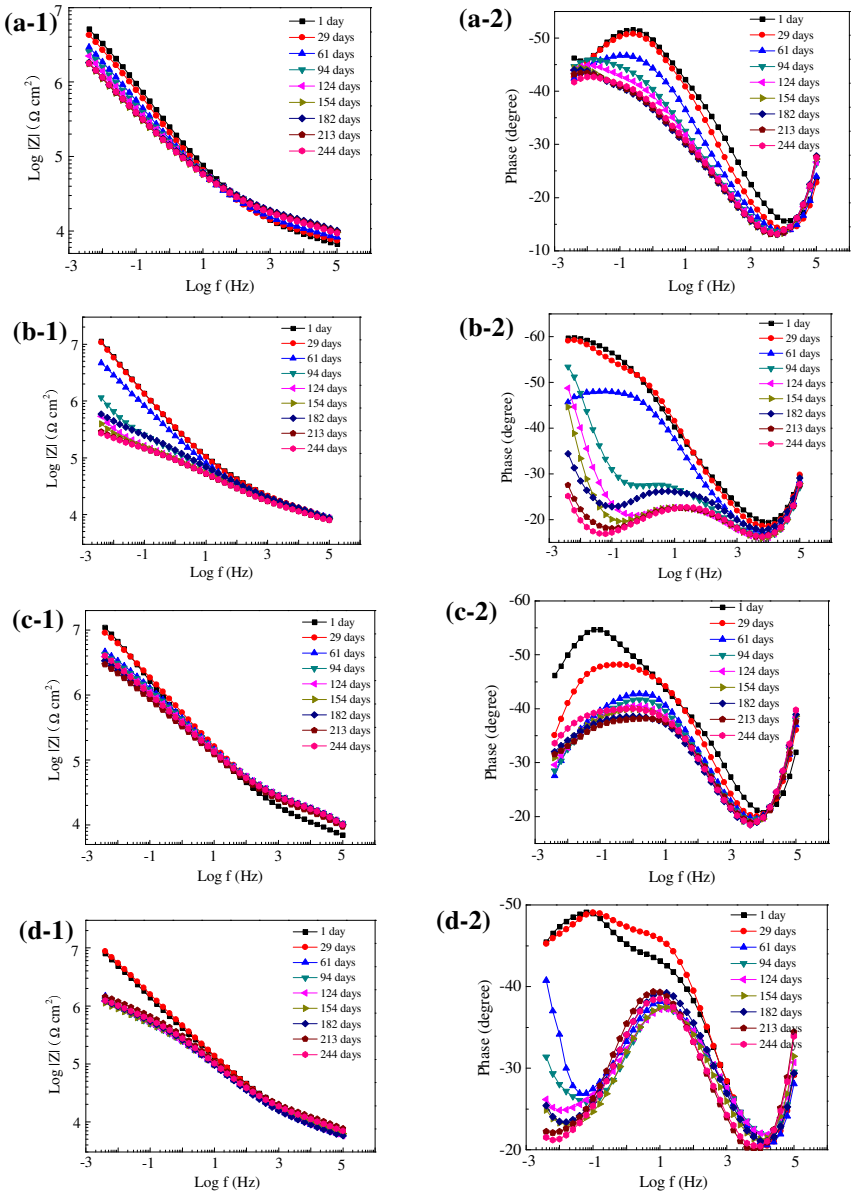

Figure 8.6 Representative Bode plots of mortar cylinders with pure enamel coated steel bars for (a) w/c=0.40 and continuous immersion in 3.5 wt.% NaCl solution, (b) w/c=0.40 and bi-weekly wet-dry cycles, (c) w/c=0.55 and continuous immersion in 3.5 wt.% NaCl solution, and (d) w/c=0.55 and bi-weekly wet-dry cycles.

It can also be observed from Figure 8.7 for the ME-coated specimens that the impedance magnitude suddenly dropped in the low frequency region after 61 days. This significant drop is attributed to the breakdown of passive films as the chloride content

accumulated at the steel interface exceeds a threshold value [130]. On the other hand, the reduction in impedance magnitude over time was progressive for specimens with uncoated steel bars as shown in Figure 8.5, indicating more corrosion pits formed due to the gradual breakdown of passive films.

8.3.4.2 Group B: specimens with PE- and DE-coated steel bars. Figures 8.6 and 8.8 show the impedance diagrams and their changes over time for specimens with PE- and DE-coated steel bars, respectively. Similar to the Group A specimens, the phase spectra are curved upward at a frequency of above 10 kHz, and they do not change over time, corresponding to the combined effects of mortar cover and the PE or DE coatings.

Unlike Group A specimens, the intermediate and low frequency regions of the phase diagrams for the Group B specimens continuously immersed in 3.5 wt.% NaCl solution were shifted throughout the test period, as shown in Figures 8.6(a-2) and 8.6(c-2), and Figures 8.8(a-2) and 8.8(c-2). However, after two or three months, a diffusion behavior appeared for specimens subjected to bi-weekly dry-wet cycles as indicated in Figures 8.6(b-2) and 8.6(d-2) and Figures 8.8(b-2) and 8.8(d-2), completely separating the intermediate frequency region from the low frequency region. The presence of the diffusion response is due to the buildup of corrosion products around the damaged coating areas. The overlapping of intermediate and low frequency regions for specimens continuously immersed in salt solution and the separation of intermediate and low frequency regions for specimens subjected to bi-weekly wet-dry cycles are both attributed to the different diffusion rates of oxygen through the mortar cover. Specimens subjected to bi-weekly wet-dry cycles transported more oxygen and chloride by combined capillary suction and diffusion effects than those continuously in salt solution, where only diffusion occurs, increasing the corrosion rate and resulting in the formation of more corrosion products. The amount of corrosion products accumulated in the active sites significantly affected the overall impedance behavior.

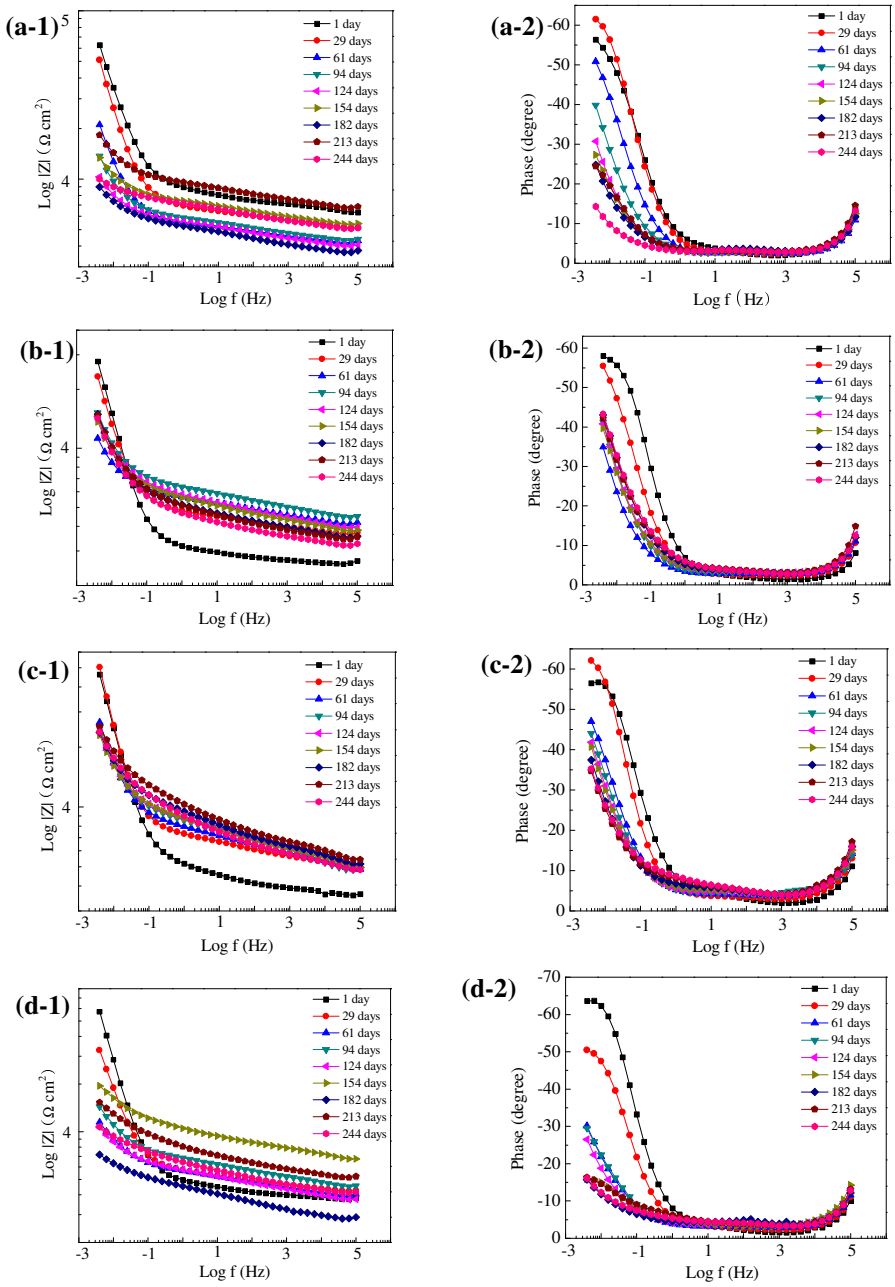

Figure 8.7 Representative Bode plots of mortar cylinders with mixed enamel coated steel bars for (a) w/c=0.40 and continuous immersion in 3.5 wt.% NaCl solution, (b) w/c=0.40 and bi-weekly wet-dry cycles, (c) w/c=0.55 and continuous immersion in 3.5 wt.% NaCl solution, and (d) w/c=0.55 and bi-weekly wet-dry cycles.

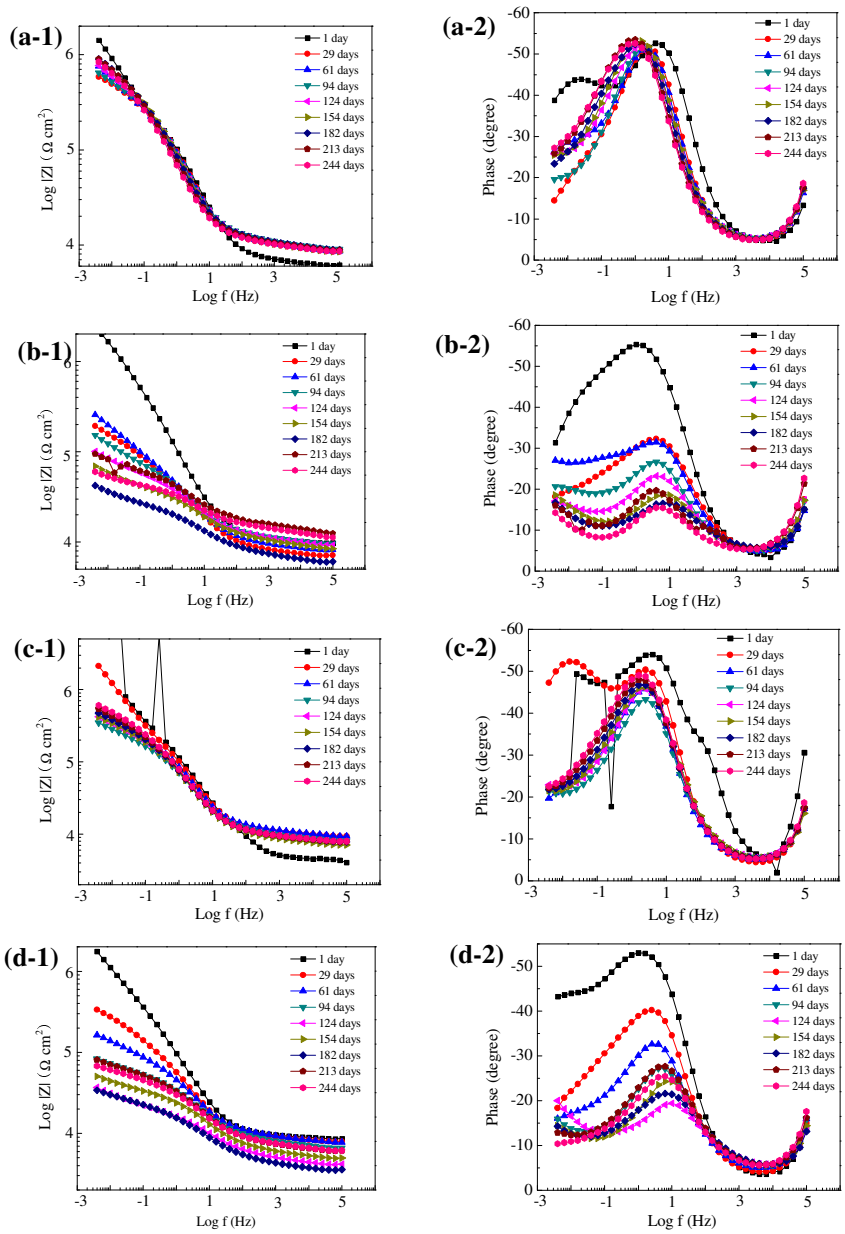

Figure 8.8 Representative Bode plots of mortar cylinders with double enamel coated steel bars for (a) w/c=0.40 and continuous immersion in 3.5 wt.% NaCl solution, (b) w/c=0.40 and bi-weekly wet-dry cycles, (c) w/c=0.55 and continuous immersion in 3.5 wt.% NaCl solution, and (d) w/c=0.55 and bi-weekly wet-dry cycles.

It can also be seen that the reduction in impedance magnitude is small for specimens that were continuously immersed in solution and significant after two or three

months of testing for specimens exposed to bi-weekly wet-dry cycles. The reduction is attributed to the initiation of corrosion as a result of the breakdown of passive films.

8.3.4.3 Group C: specimens with FBE-coated steel bars. Figure 8.9 shows the impedance spectra of mortar cylinders with FBE-coated steel bars over time. Unlike Group A or Group B specimens, inconsistent trends in terms of frequency region separation were observed in the phase diagrams. This is because the impedance spectra of the mortar-coating-steel systems are significantly affected by the barrier property of FBE coating layer and much less by mortar cover (w/c), electrolyte-steel interface, and exposure conditions.

Specifically, FBE coatings that are intact suppress all contributions from other materials and the testing conditions to the impedance spectra, resulting in a large capacitive loop as shown in Figures 8.9(a-2) and 8.9(d-2). With moderate damage, the FBE coating may affect the contributions from other materials and the dielectric properties extracted from the test data are not accurately related to the materials, as observed from Group B specimens and some FBE-coated specimens as shown in Figures 8.9(b-2) and 8.9(c-2). With more severe damage, the FBE coatings had poor barrier properties, the impedance spectra of the mortar-coating-steel system were significantly affected by other materials, and the properties of the other materials could thus be extracted, as discussed for the Group A specimens. The significant scatter in the range of behaviors of the FBE-coated specimens implies that inconsistent corrosion resistances of FBE-coated bars may be expected in field applications [33].

For specimens with w/c=0.40 in NaCl solution (Figure 8.9a), semi-circles in the Nyquist plot were observed throughout the tests with their radius gradually reduced over time. This is because FBE coatings, in perfect condition or with little damage, function as an effective insulating layer like a pure capacitor, and become increasingly conductive as chloride reaches the steel in damaged area of coatings. For specimens with w/c=0.55 subjected to bi-weekly wet-dry cycles (Figure 8.9d), capacitive loops were also observed at the beginning of the tests but gradually replaced by diffusive behaviors towards the end of tests as corrosion products formed and accumulated around tiny damage areas due to the combined diffusion and capillary suction of oxygen. As shown in Figures 8.9b and

8.9c, FBE-coated specimens are similar to PE- and DE-coated specimens in Group B likely because the damage extent in the FBE coating is similar to PE and DE coatings.

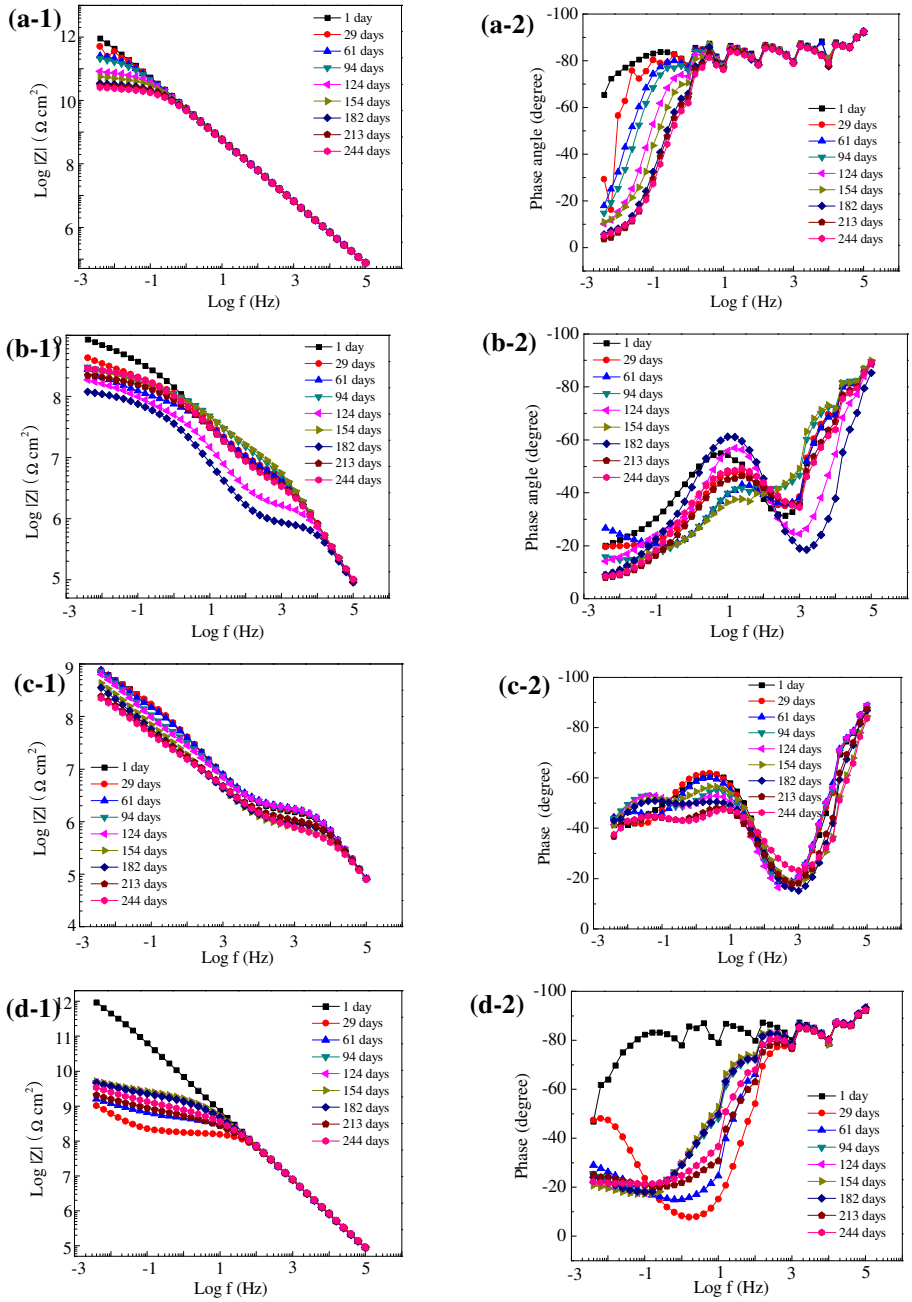

Figure 8.9 Representative Bode plots of mortar cylinders with FBE coated steel bars for (a) w/c=0.40 and continuous immersion in 3.5 wt.% NaCl solution, (b) w/c=0.40 and bi-weekly wet-dry cycles, (c) w/c=0.55 and continuous immersion in 3.5 wt.% NaCl solution, and (d) w/c=0.55 and bi-weekly wet-dry cycles.

8.3.5 Equivalent Electrical Circuit Representations of Mortar-Coating-Steel Interfaces. Equivalent electrical circuit (EEC) modeling of steel-concrete interfaces is a subject of continuing debate due to non-homogeneity and diffusion behavior involved in the electrochemical process [207-209]. Feliu et al. [28] summarized several common features of a steel-concrete system: (i) presence of more than one semi-circle in a Nyquist plot, (ii) possible appearance of low frequency tails, and (iii) existence of a depressed semi-circle. Multiple semi-circles in various frequency regions corresponded to different material layers of the system [21, 22], low frequency tails resulted from a diffusion behavior, and the depressed semi-circle was related to the non-homogeneity of the system. Introduction of a coating layer between the mortar (concrete) and steel interface significantly changed the spectral characteristics as discussed in Section 8.4. Therefore, different EEC models were proposed to simulate the mortar-steel system with different coatings.

As discussed in Section 8.3.4, the relative effects of various material layers may be changed over time, corresponding to overlapping or separating frequency regions in the impedance spectra depending on the coating layer property. In this study, for simplicity, each frequency region is represented by a constant phase element (CPE) and a resistor in parallel, and several of these pairs are connected in series to represent the entire frequency range of a mortar-coating-steel system, as indicated in Figure 8.10. The use of a CPE instead of a pure capacitor was to consider the non-homogeneity of different materials, including the mortar cover, coating layer and coating-steel interface. The non-homogeneity of the mortar cover mainly came from the random distributions of sand particles, voids and other hydration products in the cement paste as well as their different dielectric properties [210]. The non-homogeneity of coating layers mainly came from random distributions of air bubbles (or connected channels), coating damage, and penetration of chemical species such as chloride, water and hydration products into the damaged coating area [115]. The non-homogeneity of steel-coating interface mainly was related to irregularities on the steel surface like a non-uniform passive film, local breakdown of the passive film, local buildup of corrosion products, random distribution of corrosion microcell, and certain processes associated with an irregular distribution of the applied potential [14, 15, 124].

The small tail of an impedance spectrum associated with diffusion behavior in the low frequency range was combined into the impedance model pair related to the coating-steel interface. The diffusion behavior can be generally represented by the Warburg impedance. The Warburg impedance (n=0.5) is theoretically represented by a 45° straight line in the Nyquist plot, but experimentally by a straight line higher or lower than 45°. The underlying cause for the theory-experiment difference in concrete-steel and other systems remains debatable [211, 212]. For example, Zhang et al. suggested that a capacitor and a resistor in parallel be used to fit the impedance spectra when a diffusion behavior revealed [213, 214]. Hu et al. used CPE to represent diffusion impedance because the value of n ranged from 0.1 to 0.3 deviating from the Warburg impedance [215]. In this study, non-ideal diffusion behavior was observed from specimens with coated steel bars, and a CPE was used to represent the diffusion impedance. For specimens with uncoated steel bar, Warburg impedance W was used.

Figure 8.10a shows three equivalent electrical circuits used to model the corrosion of the Group A specimens: (a-I) for the uncoated specimens continuously immersed in NaCl solution and all ME-coated specimens, (a-II) for the uncoated specimens subjected to bi-weekly wet-dry cycles after the appearance of diffusion behavior, and (a-III) for the uncoated specimens after the appearance of significant corrosion products particularly, when w/c= 0.55 and subjected to bi-weekly wet-dry cycles after 182 days. Figure 8.10b shows two EECs of Group B specimens: (b-I) and (b-II) for the specimens without and with diffusion behaviors, respectively. Figure 8.10c show three equivalent circuits for Group C (FBE-coated) specimens: (c-I) for the specimens with w/c=0.4 in solution with a large capacitive loop, (c-II) for the specimens with w/c=0.55 and subjected to bi-weekly wet-dry cycles with a large capacitive loop and a diffusion behavior in the low frequency range, and (c-III) for the specimens with minor coating damage. For the EECs in Figure 8.10, CPE_m and R_m are the impedance and resistance of the bulk matrix, respectively; CPE_f and R_f represent the electrical properties of the passive films formed on each sample, e.g., at the open channels for uncoated and ME-coated specimens, and around the damaged coating area for PE-, DE-, and FBE-coated specimens; CPE_{dl} and R_{ct} represent the electrical properties of the electrolyte-steel interface where corrosion occurred; W is the Warburg impedance, and CPE_D represents the non-ideal diffusion behavior.

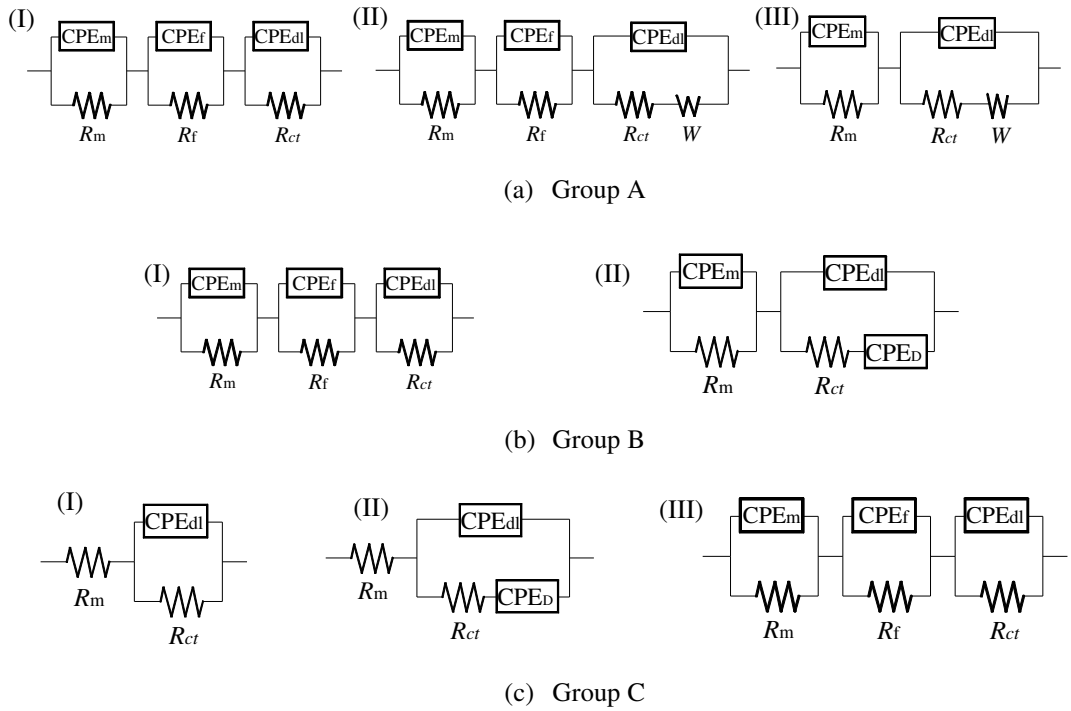

Figure 8.10 Equivalent electrical circuits for mortar cylinders with (a) uncoated and mixed enamel coated steel bars, (b) pure and double enamel coated steel bars, and (c) FBE-coated steel bars.

ZSimpWin was used to fit the EIS data with the different EEC models. The chi-squared values in the fitting to EEC models ranged from 10^{-4} to 10^{-3}, indicating an excellent fitting. Figures 8.11-8.15 present some representative solutions to EEC simulations after different corrosion times. The fitting parameters from the EEC models and the chi-squared values are tabulated in Tables 8.2-8.6.

8.3.6 EEC Parameter Evolution. By analyzing the impedance spectra over a wide frequency range, conclusions may be drawn on the electrochemical properties of various materials in the mortar-coating-steel system. Furthermore, by monitoring the evolution of impedance spectra over a relatively long time, the evolution of the dielectric properties for various materials can be obtained. As discussed previously, the impedance

spectra can be divided into high, intermediate, and low frequency regions related to various materials.

8.3.6.1 High frequency region (mortar cover and coating layer). The high-frequency regions in an EIS spectrum reflects the dielectric properties of the mortar cover and coating layer, both closely related to their microstructure and the electrolyte that might penetrate that microstructure. These dielectric properties largely depend on the water-cement ratio for the mortar cover, the number and size of open channels in the ME coating, and extent of the damaged areas of the PE, DE, and FBE coatings. For the specimens with uncoated steel bars, bulk matrix (mortar) resistances (R_m) are presented in Table 8.2. No clear trend was observed over time. However, influences of water-cement ratio and exposure condition can be seen clearly. With the same water-cement ratio, specimens subjected to bi-weekly wet-dry cycles have lower resistances than those continuously immersed in NaCl solution, and under the same exposure condition, specimens with w/c=0.55 have lower mortar resistances than those with w/c=0.40. For example, R_m = 4.41±0.46 kΩ cm^2 for specimens with w/c=0.40 immersed in solution, 2.70±0.21 kΩ cm^2 for specimens with w/c=0.40 subjected to bi-weekly wet-dry cycles, 3.18±0.26 kΩ cm^2 for specimens with w/c=0.55 immersed in solution, and 2.31±0.87 kΩ cm^2 for specimens with w/c=0.55 subjected to bi-weekly wet-dry cycles. Mortars with higher water-cement ratios are more porous and can thus absorb more NaCl solution, resulting in increased conductivity (lower R_m). Specimens subjected to bi-weekly wet-dry cycles absorb more chloride into the mortar micro-pores than those immersed in salt solution since additional capillary suction increases their conductivity. The R_m values for uncoated steel bar in this study are in good agreement with the reported values from the literature [216, 217].

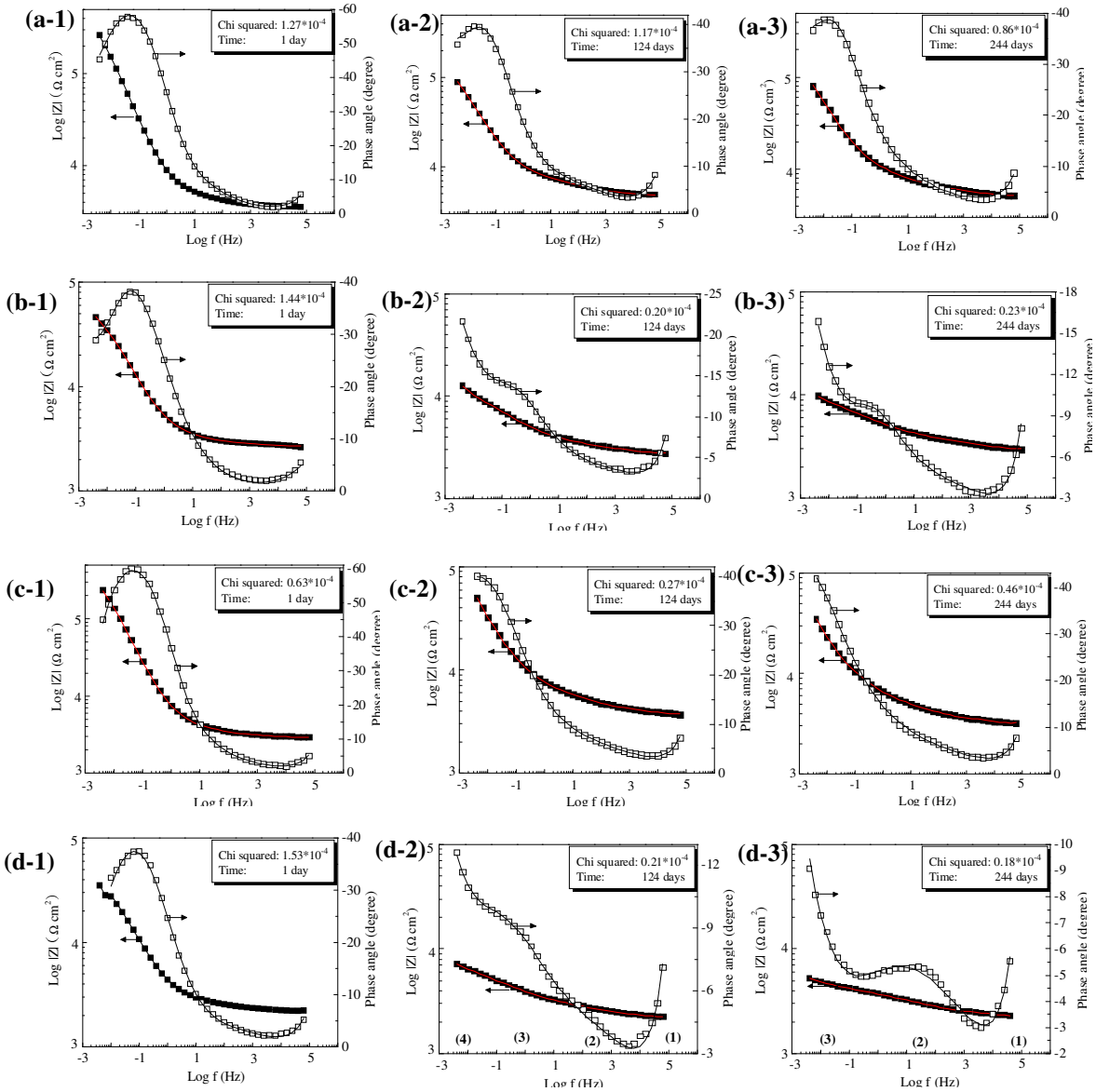

Figure 8.11 Measured versus simulated Bode plots of mortar cylinders with uncoated steel bars for (a) w/c=0.40 and continuous immersion in 3.5 wt.% NaCl solution, (b) w/c=0.40 and bi-weekly wet-dry cycles, (c) w/c=0.55 and continuous immersion in 3.5 wt.% NaCl solution, and (d) w/c=0.55 and bi-weekly wet-dry cycles at (1) 1 day, (2) 124 days, and (3) 244 days test.

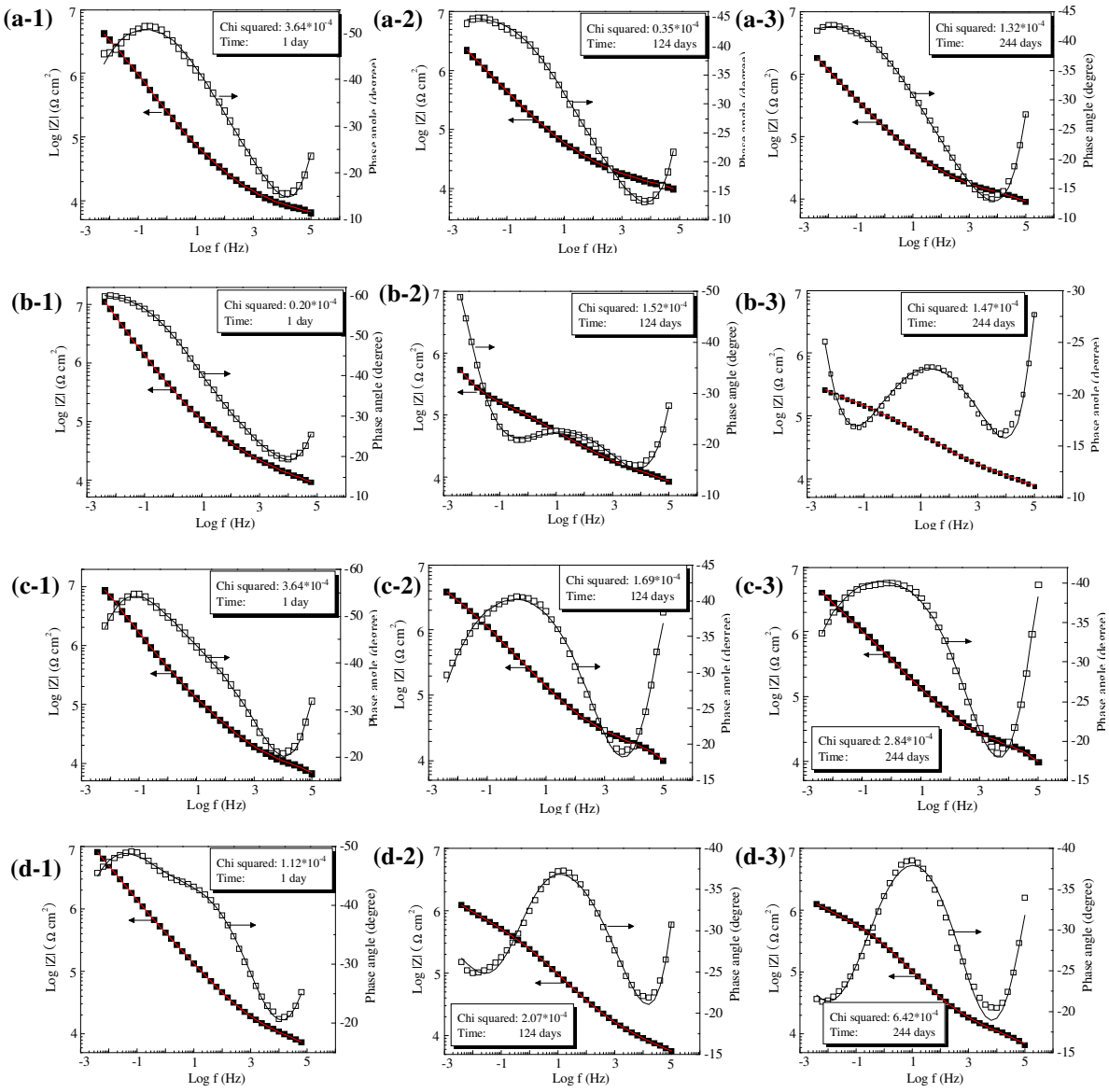

Figure 8.12 Measured versus simulated Bode plots of mortar cylinders with pure enamel coated steel bars for (a) w/c=0.40 and continuous immersion in 3.5 wt.% NaCl solution, (b) w/c=0.40 and bi-weekly wet-dry cycles, (c) w/c=0.55 and continuous immersion in 3.5 wt.% NaCl solution, and (d) w/c=0.55 and bi-weekly wet-dry cycles at (1) 1 day, (2) 124 days, and (3) 244 days test.

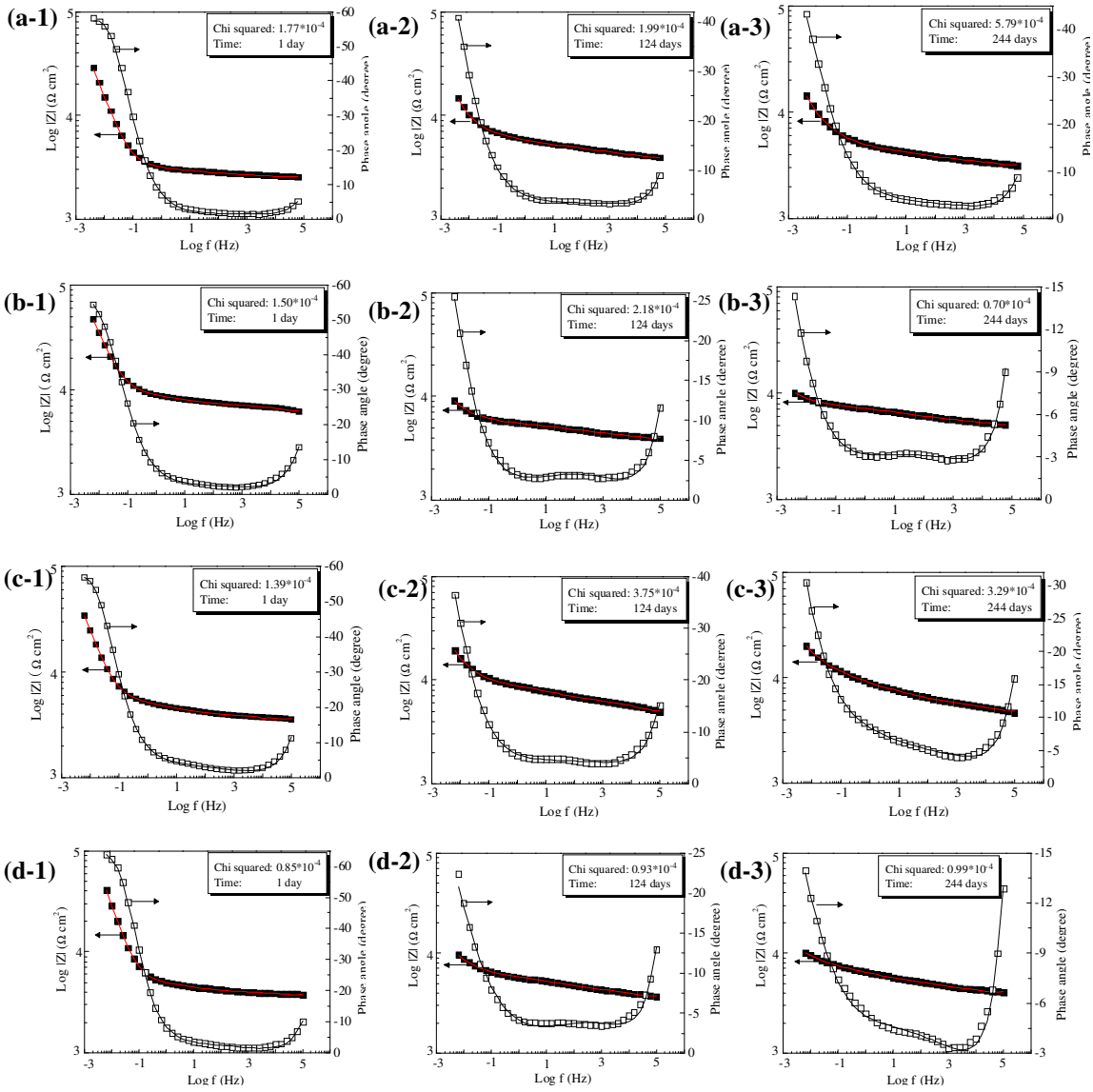

Figure 8.13 Measured versus simulated Bode plots of mortar cylinders with mixed enamel coated steel bars for (a) w/c=0.40 and continuous immersion in 3.5 wt.% NaCl solution, (b) w/c=0.40 and bi-weekly wet-dry cycles, (c) w/c=0.55 and continuous immersion in 3.5 wt.% NaCl solution, and (d) w/c=0.55 and bi-weekly wet-dry cycles at (1) 1 day, (2) 124 days, and (3) 244 days test.

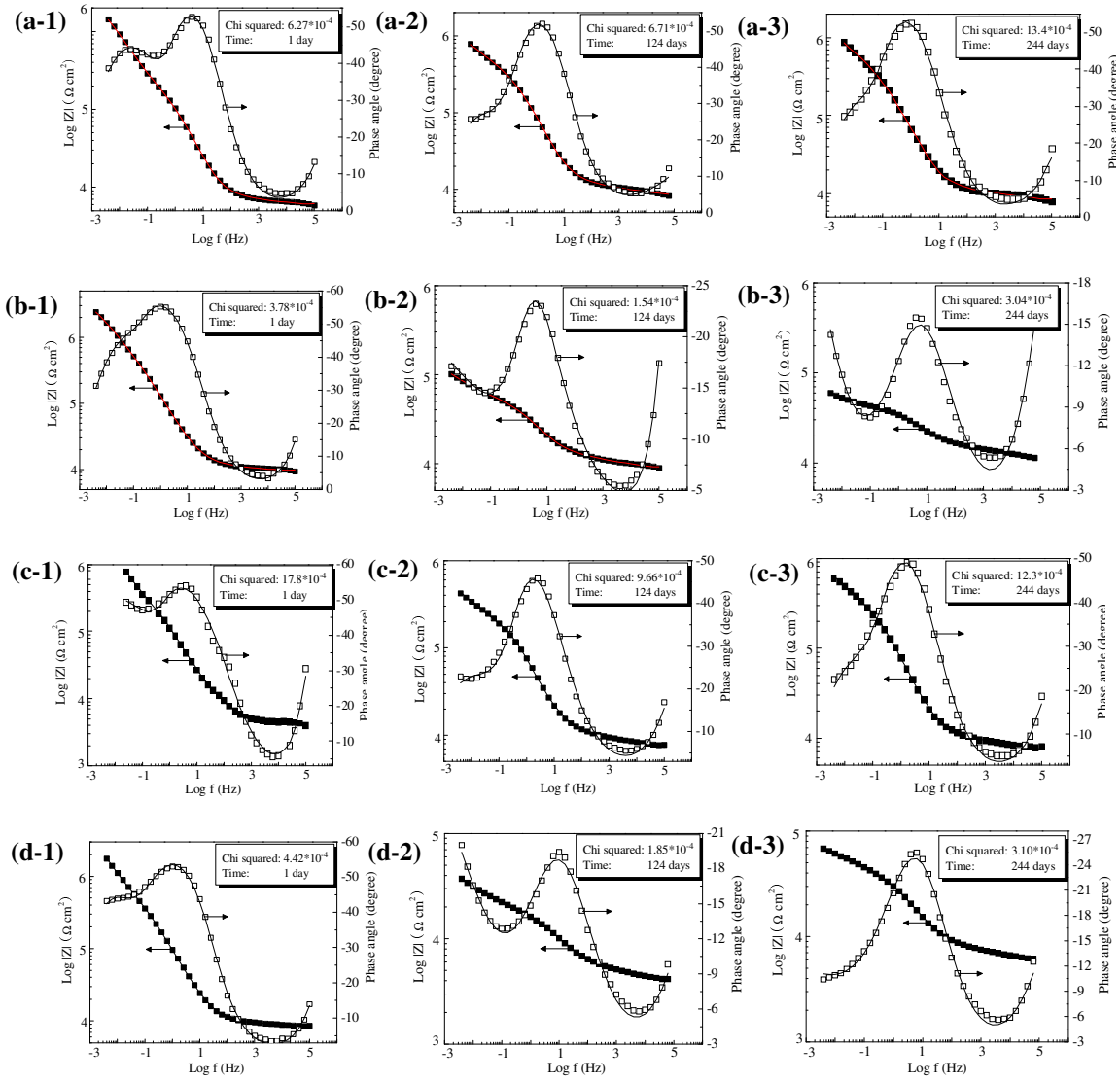

Figure 8.14 Measured versus simulated Bode plots of mortar cylinders with double enamel coated steel bars for (a) w/c=0.40 and continuous immersion in 3.5 wt.% NaCl solution, (b) w/c=0.40 and bi-weekly wet-dry cycles, (c) w/c=0.55 and continuous immersion in 3.5 wt.% NaCl solution, and (d) w/c=0.55 and bi-weekly wet-dry cycles at (1) 1 day, (2) 124 days, and (3) 244 days test.

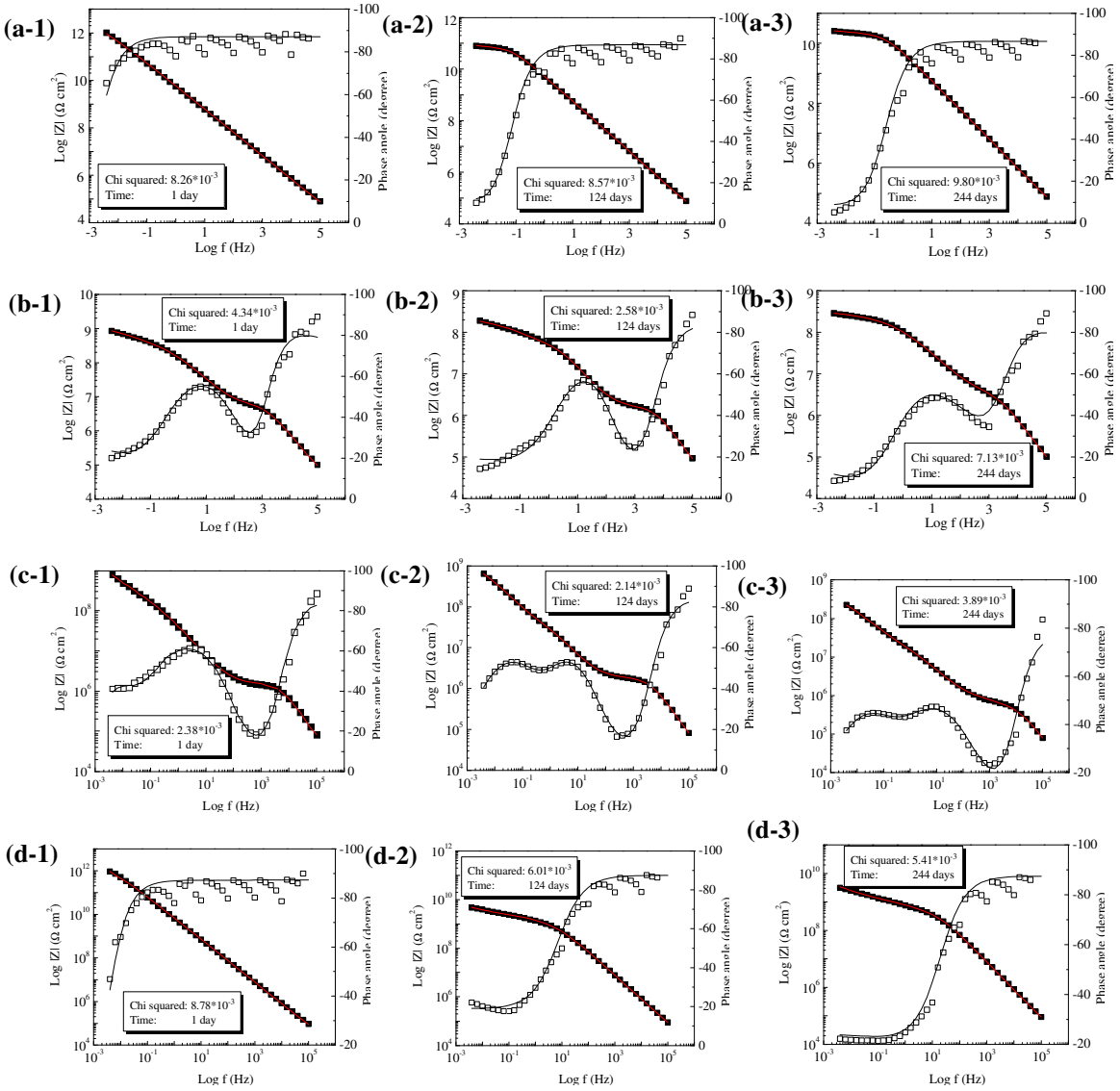

Figure 8.15 Measured versus simulated Bode plots of mortar cylinders with FBE coated steel bars for (a) w/c=0.40 and continuous immersion in 3.5 wt.% NaCl solution, (b) w/c=0.40 and bi-weekly wet-dry cycles, (c) w/c=0.55 and continuous immersion in 3.5 wt.% NaCl solution, and (d) w/c=0.55 and bi-weekly wet-dry cycles at (1) 1 day, (2) 124 days, and (3) 244 days test.

Table 8.2 Mortar cylinders with uncoated steel bars

Time (day)	R_m ($k\Omega$ cm^2)	n_m	Y_m (nF cm^{-2} $s^{-(1-n_m)}$)	R_f ($k\Omega$ cm^2)	n_f	Y_f (μF cm^{-2} $s^{-(1-n_f)}$)	R_{ct} ($k\Omega$ cm^2)	n_{dl}	Y_{dl} (μF cm^{-2} $s^{-(1-n_{dl})}$)	Y_W (mF cm^{-2} $s^{-0.5}$)	EEC	Chi Squared ($\times 10^{-4}$)
w/c=0.40, in 3.5 wt.% NaCl solution												
1	3.56	0.96	0.12	1.79	0.47	54	677	0.74	47	-	a-I	1.27
29	3.76	0.88	0.34	1.44	0.50	30	230	0.68	59	-	a-I	1.05
61	4.29	0.84	0.53	1.84	0.51	23	269	0.69	57	-	a-I	2.59
94	4.77	0.79	0.94	1.81	0.56	13	264	0.60	67	-	a-I	3.46
124	4.71	0.98	0.09	3.11	0.41	30	264	0.60	83	-	a-I	1.17
154	4.48	1.00	0.06	4.72	0.30	60	220	0.59	106	-	a-I	0.89
182	4.63	1.00	0.06	6.06	0.28	68	224	0.60	109	-	a-I	0.74
213	4.67	1.00	0.07	6.42	0.28	68	229	0.60	107	-	a-I	0.81
244	4.82	0.97	0.11	6.37	0.27	75	255	0.61	106	-	a-I	0.86
w/c=0.40, bi-weekly wet-dry cycles												
1	2.81	0.57	27.2	5.06	0.45	20	208	0.75	166	-	a-I	1.44
29	2.91	1.00	0.08	0.50	0.55	15	132	0.46	155	-	a-I	0.83
61	2.94	1.00	0.08	1.44	0.35	275	6	0.55	270	0.32	a-II	0.13
94	2.85	1.00	0.09	3.41	0.33	227	12	0.49	249	0.58	a-II	0.12
124	2.55	1.00	0.11	1.82	0.27	122	5	0.56	219	0.93	a-II	0.20
154	2.67	1.00	0.10	1.57	0.31	84	3	0.57	239	0.96	a-II	0.14
182	2.52	1.00	0.11	2.67	0.17	197	7	0.61	255	0.04	a-II	0.31
213	2.30	1.00	0.13	3.88	0.15	175	10	0.56	276	0.05	a-II	0.44
244	2.75	1.00	0.12	2.15	0.27	106	3	0.55	321	1.42	a-II	0.23
w/c=0.55, in 3.5 wt.% NaCl solution												
1	2.85	0.99	0.08	2.16	0.38	119	527	0.77	55	-	a-I	0.63
29	3.56	0.98	0.09	2.12	0.41	43	185	0.66	102	-	a-I	1.13
61	3.45	1.00	0.07	3.57	0.31	77	199	0.63	143	-	a-I	0.43
94	3.24	1.00	0.08	4.61	0.28	95	237	0.61	163	-	a-I	0.33
124	3.46	1.00	0.08	5.43	0.27	105	302	0.59	182	-	a-I	0.27
154	3.04	1.00	0.08	4.52	0.20	207	361	0.64	386	-	a-I	0.33
182	3.05	1.00	0.09	3.52	0.21	193	413	0.66	461	-	a-I	0.44
213	3.00	1.00	0.09	1.46	0.22	191	466	0.67	524	-	a-I	0.48
244	2.93	1.00	0.10	1.67	0.22	197	402	0.67	504	-	a-I	0.46
w/c=0.55, bi-weekly wet-dry cycles												
1	2.19	1.00	0.10	0.45	0.48	66	60	0.60	140	-	a-I	1.53
29	2.68	0.91	0.31	1.06	0.48	32	53	0.60	126	-	a-I	1.48
61	2.37	1.00	0.10	2.19	0.32	100	8	0.57	455	0.27	a-II	0.25
94	3.14	1.00	0.08	3.23	0.30	89	7	0.64	231	0.74	a-II	0.17
124	2.12	1.00	0.13	0.72	0.34	100	6	0.35	339	2.81	a-II	0.21
154	1.86	1.00	0.13	0.78	0.36	177	7	0.21	291	5.13	a-II	0.17
182	1.94	0.91	0.48	0.81	0.37	228	7	0.21	765	4.23	a-II	0.12
213	2.33	0.93	0.32	-	-	-	4	0.27	189	3.88	a-III	0.07
244	2.16	1.00	0.14	-	-	-	3	0.28	179	4.87	a-III	0.18

Table 8.3 Mortar cylinders with pure enamel coated steel bars

Time (day)	R_m (kΩ cm^2)	n_m	Y_m (nF cm^{-2} s$^{-(1-n_m)}$)	R_f (kΩ cm^2)	n_f	Y_f (μF cm^{-2} s$^{-(1-n_f)}$)	R_{ct} (MΩ cm^2)	n_{dl}	Y_{dl} (μF cm^{-2} s$^{-(1-n_{dl})}$)	Y_d (μF cm^{-2} s$^{-(1-n_d)}$)	n_d	EEC	Chi Squared ($\times 10^{-4}$)
w/c=0.40, in 3.5 wt.% NaCl solution													
1	5.85	0.89	0.51	26.8	0.36	6.37	18.8	0.60	1.40	-	-	b-I	3.64
29	5.47	0.99	0.13	22.4	0.29	8.85	16.6	0.59	1.70	-	-	b-I	1.95
61	6.07	1.00	0.12	17.7	0.31	6.53	17.4	0.55	2.31	-	-	b-I	0.68
94	8.12	0.88	0.55	39.2	0.28	8.93	40.3	0.54	2.76	-	-	b-I	0.96
124	9.47	0.78	1.86	30.1	0.31	8.85	67.1	0.52	3.03	-	-	b-I	0.35
154	9.99	0.81	1.30	31.4	0.34	8.32	64.5	0.50	3.64	-	-	b-I	1.90
182	10.6	0.81	1.15	30.4	0.35	7.32	54.8	0.50	3.48	-	-	b-I	2.06
213	8.45	0.84	1.59	17.1	0.41	5.28	65.5	0.49	3.43	-	-	b-I	1.61
244	8.55	0.86	0.72	36.4	0.28	11.3	29.8	0.50	3.48	-	-	b-I	1.32
w/c=0.40, bi-weekly wet-dry cycles													
1	5.81	0.85	1.49	352	0.31	4.45	858	0.68	1.11	-	-	b-I	0.20
29	5.98	0.83	1.98	298	0.27	6.47	833	0.66	1.08	-	-	b-I	2.57
61	6.40	0.94	0.31	23.3	0.35	2.92	50.0	0.56	1.60	-	-	b-I	1.15
94	9.03	0.72	4.62	-	-	-	0.38	0.37	3.50	17.4	0.76	b-II	3.15
124	7.90	0.80	1.67	-	-	-	0.23	0.35	4.12	39.3	0.76	b-II	1.52
154	7.77	0.74	4.16	-	-	-	0.33	0.34	4.54	36.9	0.87	b-II	2.55
182	8.04	0.78	2.50	-	-	-	0.53	0.36	3.24	55.9	0.76	b-II	2.03
213	6.58	0.85	1.10	-	-	-	0.29	0.33	4.79	44.0	0.65	b-II	1.64
244	6.51	0.87	0.82	-	-	-	0.29	0.33	4.67	66.3	0.68	b-II	1.47
w/c=0.55, in 3.5 wt.% NaCl solution													
1	6.46	0.83	1.61	121	0.41	2.29	28.1	0.72	1.03	-	-	b-I	3.64
29	10.8	0.79	2.56	19.7	0.37	3.41	27.2	0.57	0.67	-	-	b-I	1.67
61	12.0	0.77	3.39	18.6	0.23	2.03	11.6	0.51	0.93	-	-	b-I	6.33
94	7.62	0.96	0.27	10.6	0.42	6.87	10.0	0.50	0.96	-	-	b-I	2.17
124	8.72	0.91	0.47	18.8	0.45	5.95	10.3	0.48	1.06	-	-	b-I	1.69
154	11.6	0.83	1.36	14.9	0.34	1.88	10.9	0.48	1.17	-	-	b-I	1.40
182	15.3	0.73	5.04	22.4	0.44	1.54	11.1	0.60	4.26	-	-	b-I	2.35
213	13.1	0.74	4.67	15.6	0.45	1.76	15.2	0.54	4.32	-	-	b-I	2.57
244	15.4	0.73	5.17	25.1	0.42	5.81	18.3	0.49	1.41	-	-	b-I	2.84
w/c=0.55, bi-weekly wet-dry cycles													
1	8.26	0.61	26.5	195	0.45	2.58	46.0	0.60	1.02	-	-	b-I	1.12
29	9.33	0.52	92.7	154	0.44	5.99	61.2	0.57	0.86	-	-	b-I	1.90
61	6.70	0.64	19.2	-	-	-	0.82	0.48	1.43	16.2	0.74	b-II	4.97
94	5.14	0.71	19.4	-	-	-	0.59	0.49	1.60	6.82	0.49	b-II	3.88
124	5.28	0.89	0.53	-	-	-	0.33	0.55	2.15	4.27	0.38	b-II	2.07
154	6.10	0.86	0.80	-	-	-	0.31	0.59	1.79	4.51	0.37	b-II	1.91
182	5.58	0.85	0.86	-	-	-	0.38	0.60	1.74	4.44	0.38	b-II	2.37
213	11.3	0.64	19.3	-	-	-	1.19	0.51	1.11	7.10	0.46	b-II	6.62
244	9.97	0.64	20.4	-	-	-	0.97	0.50	1.21	7.20	0.43	b-II	6.42

Table 8.4 Mortar cylinders with mixed enamel coated steel bars

Time (day)	R_m (kΩ cm^2)	n_m	Y_m (nF cm^{-2} s$^{-(1-n_m)}$)	R_f (kΩ cm^2)	n_f	Y_f (μF cm^{-2} s$^{-(1-n_f)}$)	R_{ct} (kΩ cm^2)	n_{dl}	Y_{dl} (μF cm^{-2} s$^{-(1-n_{dl})}$)	EEC	Chi Squared ($\times 10^{-4}$)
w/c=0.40, in 3.5 wt.% NaCl solution											
1	2.59	0.96	0.14	2.49	0.43	176	487	0.79	630	a-I	1.77
29	3.53	1.00	0.08	2.33	0.32	89	571	0.74	740	a-I	0.67
61	3.57	1.00	0.09	3.41	0.18	145	631	0.77	2310	a-I	1.37
94	3.84	1.00	0.09	3.79	0.21	112	84	0.78	1520	a-I	2.37
124	3.34	1.00	0.11	4.73	0.19	159	76	0.78	1670	a-I	1.99
154	3.12	0.99	0.13	5.03	0.18	178	59	0.79	1820	a-I	2.28
182	3.00	1.00	0.12	4.34	0.20	199	55	0.79	1500	a-I	4.12
213	3.36	1.00	0.17	3.51	0.26	178	52	0.77	1400	a-I	6.45
244	3.24	0.98	0.19	3.47	0.24	221	50	0.77	1460	a-I	5.79
w/c=0.40, bi-weekly wet-dry cycles											
1	6.37	0.88	0.33	2.83	0.28	87	864	0.74	260	a-I	1.50
29	6.89	0.98	0.24	2.57	0.22	76	887	0.83	430	a-I	1.04
61	4.07	1.00	0.07	1.55	0.35	60	884	0.73	810	a-I	0.62
94	4.09	1.00	0.08	2.13	0.31	81	77	0.74	1460	a-I	2.15
124	4.42	1.00	0.32	2.76	0.27	77	71	0.74	2570	a-I	2.18
154	4.97	1.00	0.07	3.05	0.26	70	81	0.64	1440	a-I	1.62
182	3.19	1.00	0.11	2.19	0.31	86	71	0.63	2150	a-I	1.17
213	6.24	1.00	0.06	4.42	0.25	59	42	0.68	1080	a-I	1.06
244	4.72	1.00	0.08	3.36	0.26	86	49	0.58	2690	a-I	0.70
w/c=0.55, in 3.5 wt.% NaCl solution											
1	3.55	0.98	0.12	2.23	0.30	167	243	0.80	410	a-I	1.39
29	4.26	0.97	0.14	4.54	0.20	87	444	0.85	470	a-I	0.66
61	3.96	0.95	0.10	4.24	0.30	73	85	0.81	1260	a-I	5.77
94	3.47	1.00	0.12	6.90	0.21	46	92	0.78	850	a-I	5.51
124	4.28	0.83	1.26	7.95	0.21	86	79	0.81	1080	a-I	3.75
154	4.17	0.84	1.13	9.40	0.22	99	54	0.86	1330	a-I	5.43
182	4.43	0.84	1.04	14.9	0.20	103	57	0.86	1500	a-I	3.61
213	4.60	0.84	1.26	17.8	0.23	96	54	0.87	1550	a-I	4.40
244	4.13	0.86	0.97	15.7	0.25	104	67	0.80	1250	a-I	3.29
w/c=0.55, bi-weekly wet-dry cycles											
1	3.75	1.00	0.08	1.45	0.33	171	459	0.84	370	a-I	0.85
29	4.07	1.00	0.07	1.77	0.31	83	160	0.76	510	a-I	0.88
61	3.64	1.00	0.09	2.52	0.26	91	72	0.64	1410	a-I	1.13
94	3.91	0.99	0.11	3.83	0.23	92	77	0.65	1200	a-I	1.49
124	3.11	1.00	0.12	3.81	0.20	97	64	0.64	1760	a-I	0.93
154	7.40	1.00	0.12	3.10	0.39	48	46	0.47	490	a-I	2.73
182	2.64	1.00	0.12	2.27	0.30	87	32	0.47	1880	a-I	1.40
213	4.78	1.00	0.08	2.69	0.33	47	33	0.42	440	a-I	1.68
244	3.66	1.00	0.10	5.04	0.22	13	24	0.54	1720	a-I	0.99

Table 8.5 Mortar cylinders with double enamel coated steel bars

Time (days)	R_m (kΩ cm^2)	n_m	Y_m (nF cm^{-2} s$^{-(1-n_m)}$)	R_f (kΩ cm^2)	n_f	Y_f (μF cm^{-2} s$^{-(1-n_f)}$)	R_{ct} (MΩ cm^2)	n_{dl}	Y_{dl} (μF cm^{-2} s$^{-(1-n_{dl})}$)	Y_d (mF cm^{-2} s$^{-(1-n_d)}$)	n_d	EEC	Chi Squared ($\times 10^{-4}$)
w/c=0.40, in 3.5 wt.% NaCl solution													
1	6.61	0.72	2.56	83	0.86	3.16	3.87	0.64	5.8	-	-	b-I	6.27
29	9.68	0.67	4.76	115	0.90	3.43	0.62	0.61	7.2	-	-	b-I	8.40
61	9.95	0.61	11.4	133	0.88	3.64	1.35	0.58	8.5	-	-	b-I	9.93
94	11.3	0.40	180	214	0.83	3.54	0.78	0.58	11.2	-	-	b-I	6.77
124	11.0	0.39	236	262	0.79	3.97	1.30	0.61	12.3	-	-	b-I	6.71
154	10.7	0.39	245	296	0.79	4.03	1.35	0.62	11.4	-	-	b-I	5.97
182	10.5	0.59	15.1	173	0.85	6.05	1.25	0.62	7.2	-	-	b-I	12.6
213	10.3	0.60	12.9	221	0.85	6.88	1.50	0.60	8.4	-	-	b-I	12.8
244	9.94	0.65	7.49	198	0.84	7.72	1.53	0.60	9.1	-	-	b-I	13.4
w/c=0.40, bi-weekly wet-dry cycles													
1	10.4	0.82	0.48	108	0.88	7.52	4.38	0.65	2.99	-	-	b-I	3.78
29	7.41	0.77	1.55	39	0.66	9.17	0.29	0.46	20.7	-	-	b-I	2.10
61	8.93	0.72	2.23	-	-	-	0.07	0.60	5.43	0.02	0.34	b-II	5.36
94	10.7	0.70	2.76	-	-	-	0.06	0.58	5.98	0.04	0.37	b-II	6.35
124	8.83	0.98	0.06	-	-	-	0.02	0.75	7.86	0.04	0.27	b-II	1.54
154	9.79	0.56	21.3	-	-	-	0.03	0.56	8.91	0.11	0.39	b-II	1.91
182	6.74	0.55	31.5	-	-	-	0.02	0.50	1.47	0.22	0.40	b-II	1.42
213	15.0	0.61	9.29	-	-	-	0.06	0.53	7.19	0.21	0.54	b-II	2.77
244	13.7	0.61	11.4	-	-	-	0.03	0.53	8.51	0.29	0.49	b-II	3.04
w/c=0.55, in 3.5 wt.% NaCl solution													
1	4.36	1.00	0.19	63	0.88	5.47	93.7	0.60	4.07	-	-	b-I	17.8
29	10.4	0.71	2.45	49	0.94	3.95	12.5	0.64	4.77	-	-	b-I	7.51
61	10.6	0.68	4.24	89	0.87	4.23	0.68	0.54	9.37	-	-	b-I	9.16
94	8.96	0.72	2.77	91	0.82	5.00	0.64	0.47	14.4	-	-	b-I	9.04
124	8.71	0.68	4.83	117	0.81	4.65	0.82	0.50	13.6	-	-	b-I	9.66
154	7.99	0.65	7.87	116	0.80	5.25	0.68	0.52	13.4	-	-	b-I	9.16
182	8.87	0.68	5.05	124	0.81	5.27	0.74	0.53	11.8	-	-	b-I	10.4
213	8.82	0.70	3.56	131	0.81	5.58	0.82	0.55	10.4	-	-	b-I	10.8
244	8.99	0.71	3.22	150	0.80	5.53	0.89	0.57	9.91	-	-	b-I	12.3
w/c=0.55, bi-weekly wet-dry cycles													
1	9.12	0.81	0.58	298	0.71	4.97	6.25	0.69	6.84	-	-	b-I	4.42
29	8.50	0.79	0.96	54	0.76	8.01	0.44	0.55	12.7	-	-	b-I	5.42
61	8.24	0.80	0.89	35	0.77	8.38	0.25	0.42	21.6	-	-	b-I	4.23
94	6.70	0.76	1.58	-	-	-	0.03	0.69	8.49	0.06	0.29	b-II	1.48
124	4.64	0.49	90.2	-	-	-	0.01	0.54	16.0	0.21	0.39	b-II	1.85
154	4.70	0.84	0.63	-	-	-	0.02	0.71	9.50	0.08	0.26	b-II	0.85
182	3.78	0.59	26.0	-	-	-	0.02	0.48	20.5	0.56	0.50	b-II	2.11
213	6.67	0.73	3.10	-	-	-	0.06	0.55	8.77	0.25	0.50	b-II	7.18
244	7.23	0.51	64.2	-	-	-	0.03	0.60	7.20	0.06	0.21	b-II	3.10

Table 8.6 Mortar cylinders with FBE coated steel bars

Time (days)	R_m ($M\Omega$ cm^2)	n_m	Y_m ($nF\ cm^{-2}\ s^{-(1-n_m)}$)	R_f ($M\Omega$ cm^2)	n_f	Y_f ($nF\ cm^{-2}\ s^{-(1-n_f)}$)	R_{ct} ($G\Omega$ cm^2)	n_{dl}	Y_{dl} ($nF\ cm^{-2}\ s^{-(1-n_{dl})}$)	Y_d ($nF\ cm^{-2}\ s^{-(1-n_d)}$)	n_d	EEC	Chi Squared ($\times 10^{-3}$)
w/c=0.40, in 3.5 wt.% NaCl solution													
1	-	-	-	-	-	-	2210	0.97	0.03	-	-	c-I	8.26
29	-	-	-	-	-	-	528	0.97	0.03	-	-	c-I	8.30
61	-	-	-	-	-	-	256	0.96	0.03	-	-	c-I	6.76
94	-	-	-	-	-	-	190	0.96	0.03	-	-	c-I	8.33
124	-	-	-	-	-	-	75	0.96	0.03	-	-	c-I	8.57
154	-	-	-	-	-	-	49	0.96	0.03	-	-	c-I	8.70
182	-	-	-	-	-	-	30	0.96	0.04	-	-	c-I	9.00
213	-	-	-	-	-	-	26	0.96	0.03	-	-	c-I	9.72
244	-	-	-	-	-	-	23	0.96	0.04	-	-	c-I	9.80
w/c=0.40, bi-weekly wet-dry cycles													
1	4.44	1.00	0.03	327	0.73	1.76	0.80	0.72	11.6	-	-	c-III	4.34
29	4.52	1.00	0.03	148	0.73	1.40	0.39	0.68	18.0	-	-	c-III	6.64
61	4.12	1.00	0.03	76.8	0.73	1.38	0.31	0.64	25.4	-	-	c-III	7.88
94	6.23	1.00	0.04	92.6	0.78	0.78	0.19	0.70	10.5	-	-	c-III	9.52
124	1.36	0.98	0.03	50.0	0.81	3.01	0.16	0.64	20.8	-	-	c-III	2.58
154	8.31	0.96	0.04	76.4	0.78	0.79	0.19	0.69	9.6	-	-	c-III	8.95
182	7.21	0.98	0.03	40.9	0.84	5.31	0.09	0.67	26.7	-	-	c-III	1.71
213	3.15	0.97	0.04	72.5	0.73	1.72	0.14	0.71	8.2	-	-	c-III	7.05
244	2.69	0.97	0.04	105	0.72	1.90	0.19	0.70	8.2	-	-	c-III	7.13
w/c=0.55, in 3.5 wt.% NaCl solution													
1	1.39	0.97	0.03	171	0.75	9.44	1.89	0.73	18.2	-	-	c-III	2.38
29	1.53	0.96	0.03	177	0.79	8.83	3.22	0.71	18.9	-	-	c-III	2.25
61	1.66	0.96	0.03	84.6	0.81	10.4	2.56	0.69	15.2	-	-	c-III	1.96
94	1.70	0.99	0.02	43.5	0.74	10.6	1.54	0.77	18.0	-	-	c-III	4.30
124	1.68	0.96	0.04	17.4	0.79	14.5	1.54	0.70	15.9	-	-	c-III	2.14
154	0.75	0.90	0.08	16.0	0.78	27.3	1.12	0.69	23.3	-	-	c-III	4.31
182	0.74	1.00	0.02	10.2	0.65	58.0	1.20	0.64	25.9	-	-	c-III	2.57
213	0.88	0.98	0.03	13.0	0.69	32.2	0.87	0.60	31.6	-	-	c-III	2.60
244	0.55	0.93	0.06	11.7	0.62	34.0	0.65	0.62	34.2	-	-	c-III	3.89
w/c=0.55,bi-weekly wet-dry cycles													
1	-	-	-	-	-	-	1330	0.97	0.03	-	-	c-I	8.78
29	-	-	-	-	-	-	5.70	0.97	0.03	-	-	c-II	4.91
61	-	-	-	-	-	-	0.29	0.97	0.03	2.93	0.36	c-II	5.15
94	-	-	-	-	-	-	0.11	0.97	0.03	0.52	0.23	c-II	6.23
124	-	-	-	-	-	-	0.09	0.97	0.03	0.48	0.21	c-II	6.01
154	-	-	-	-	-	-	0.08	0.97	0.03	0.42	0.20	c-II	5.84
182	-	-	-	-	-	-	0.09	0.97	0.03	0.50	0.22	c-II	5.99
213	-	-	-	-	-	-	0.13	0.97	0.03	1.47	0.27	c-II	4.97
244	-	-	-	-	-	-	0.17	0.97	0.03	0.93	0.28	c-II	5.41

For the specimens with ME-coated steel bars, no general trend was observed either over time or under different exposure conditions. The average bulk matrix resistance for all specimens over time as presented in Table 8.4 is 4.12±1.10 kΩ cm^2, which is higher than what was determined for specimens with uncoated steel bars (3.15±0.87 kΩ cm^2). The overall average bulk matrix resistance for specimens with PE-coated steel bars is 8.48±2.69 kΩ cm^2 as shown in Table 8.3, and 8.85±2.40 kΩ cm^2 for specimens with DE-coated bars as shown in Table 8.5. The greater resistances for the three sets of enamel coated specimens, compared with the uncoated specimens, is related to the different dielectric properties of the ME coating, compared with the mortar paste, and the superior barrier properties of the PE and DE coatings. Therefore, the effects of the water-cement ratio and exposure condition were less obvious in comparison to the dominant effect of the coatings, particularly the PE and DE coatings.

Table 8.6 lists the bulk matrix resistances of the specimens with FBE coated bars. It can be seen from Table 8.6 that the specimens with FBE-coated bars and with w/c=0.40 subjected to bi-weekly wet-dry cycles have an average bulk matrix resistance of 4.67±2.28 MΩ cm^2, about 1000 times higher than those with uncoated and ME-coated steel bars and 500 times higher than those with PE- and DE-coated bars. This is because the bulk matrix resistance is significantly influenced by the outstanding barrier properties of the FBE coating.

The capacitive parameters Y_m and n_m of the combined mortar cover and coating, obtained by fitting EEC models to the EIS test results, were less useful because of the frequency range used in this study. Specifically, the semicircle in the test frequency up to 100 kHz was incomplete as other authors suggested that tests ought to be done up to the MHz range to get accurate values of Y_m and n_m [203-205]. Therefore, comparison of these parameters between different specimens would be less meaningful.

8.3.6.2 Intermediate frequency region (passive film). The intermediate frequency region reflects the properties of the passive film that is formed around the connected channels in the porous mill scale on the uncoated samples and in the ME coatings, or around the damaged areas of the PE, DE, and FBE coatings. As presented in Table 8.2 for specimens with uncoated steel bars, the passive film resistances (R_f) range

from 0.45 to 6.42 kΩ cm^2, and the capacitances range from 13 to 275 μF cm^{-2} $s^{-(1-n_f)}$; these values are similar to those observed in other studies [215]. As shown in Table 8.4, the passive film formed on the ME coating has similar dielectric properties to that formed on the uncoated specimens. The resistances and capacitances are in the range of 1.45~17.8 kΩ cm^2 and 13~221 μF cm^{-2} $s^{-(1-n_f)}$, respectively. Influences of both water-cement ratio and exposure condition on the properties of the passive film formed on the uncoated and the ME coated samples were not observed even after the formation of corrosion products. This is probably because the passive film and corrosion products have similar properties.

As shown in Tables 8.3 and 8.5, the passive film resistances of the PE- and DE-coated bars are in the range of 14.9~121 kΩ cm^2 and 49~296 kΩ cm^2, respectively, when immersed in the 3.5 wt.% NaCl solution. Their corresponding passive film capacitances are in the range of 1.54~11.3 μF cm^{-2} $s^{-(1-n_f)}$ and 3.16~7.72 μF cm^{-2} $s^{-(1-n_f)}$, respectively. The higher passive film resistance and lower passive film capacitance formed on the PE- and DE-coated specimens, compared to those formed on the uncoated and the ME coated samples, are attributed to the small coating damage areas compared to the connected channels in the mill scale and ME coatings. When normalized by the total surface area of the steel bar, these differences are amplified. For specimens subjected to bi-weekly wet-dry cycles, their impedance spectra representing the passive film disappeared after two or three months, indicating the initiation of corrosion. This is because, prior to the initiation of corrosion, a passive film was formed on the exposed steel surface around any damaged coating area, the EIS measurement circuit was distributed around the entire steel bar surface, and the dielectric properties of mortar cover, enamel coating, and enamel-steel interface were then reflected in the impedance spectra. After breakdown of the passive film around the damaged coating area, the flow of charge was concentrated around the small damaged area, which is significantly affected by the buildup of corrosion products.

The passive film resistance and capacitance of FBE-coated steel bars can only be observed in two specimens with moderate surface damage. The passive film resistances are in the range of 10.2~327 MΩ cm^2, which are 100~1000 times higher than those for the PE- and DE-coated bars, and 10,000 times higher than those for the uncoated and ME-coated samples. The passive film capacitances are in the range of 0.78~58 nF cm^{-2} $s^{-(1-n_f)}$, which is significantly lower than the capacitances associated with the other samples

and likely reflects the much smaller damage areas on the FBE-coated samples, as shown in Figure 8.4.

8.3.6.3 Low frequency region (coating-steel interface). The low frequency region reflects properties of the electrolyte-steel interface at active sites: charge transfer resistance R_{ct} and double layer capacitance Y_{dl}. Charge transfer resistance represents the difficulty of charges across the interface of steel where corrosion occurs and is inversely proportional to the rate of corrosion. Double layer capacitance represents the separation of charge at the steel-electrolyte interface [19]. For specimens with uncoated steel bars immersed in salt solution, R_{ct} evolution over time is not as obvious as for specimens subjected to bi-weekly wet-dry cycles (Table 8.2). After one month on test, specimens immersed in salt solution reached relatively stable values of R_{ct} of 244±21 kΩ cm^2 with w/c=0.40, and 321±106 kΩ cm^2 with w/c=0.55, respectively. However, for specimens subjected to bi-weekly wet-dry cycles, R_{ct} decreased significantly after two months on test, from 208 to 6 kΩ cm^2 with w/c=0.40 and from 60 to 8 kΩ cm^2 with w/c=0.55. The decrease of R_{ct} indicated the penetration of chloride ions to the steel interface and initiation of pitting corrosion. The double layer capacitance Y_{dl} increased over time for all specimens, although there is no obvious trend. For example, Y_{dl} increased from 47 to 106 μF cm^{-2} s$^{-(1-n_{dl})}$ with w/c=0.40 and from 55 to 504 μF cm^{-2} s$^{-(1-n_{dl})}$ with w/c=0.55 for samples continuously immersed in solution. The increase in double layer capacitance probably reflects the change of steel surface due to the arrival of chloride. The R_{ct} values for the uncoated steel bars in this study are in good agreement with values reported in the literature [214-216].

For ME-coated bars as shown in Table 8.4, R_{ct} significantly decreased for all testing after two or three months on test. The significant decrease is attributed to the breakdown of the passive film due to the arrival of chlorides and the initiating steel bar corrosion. Accompanying the decrease in R_{ct} was an increase in the double layer capacitance, Y_{dl}, for all samples tested. After the breakdown of the passive film and onset of corrosion, the average charge transfer resistance and the double layer capacitance for all samples remained stable, with values of 62±18 kΩ cm^2 and 1480±512 μF cm^{-2} s$^{-(1-n_{dl})}$, respectively.

For the PE-coated bars immersed in salt solution, as shown in Table 8.3, R_{ct} remained stable over time and had values of 42±22 MΩ cm^2 with w/c=0.40 and 16±7 MΩ cm^2 with w/c=0.55, which is approximately 100 times higher than those with the uncoated steel bars. For specimens subjected to weekly wetting-drying cycles, after two or three months of test, R_{ct} decreased significantly, from 858 to 0.38 MΩ cm^2, with w/c=0.40 and from 46 to 0.82 MΩ cm^2 with w/c=0.55. This decrease indicated the initiation of pitting corrosion due to breakdown of passive film on damaged PE coating area. After the decrease, R_{ct} remained stable and had an average value of 0.51±0.30 MΩ cm^2 for specimen both with w/c=0.40 and with w/c=0.55. The double layer capacitance $Y_{dl,}$ remained constant for all specimens, with a value of 2.29±1.32 μF cm^{-2} s$^{-(1-n_{dl})}$, which is lower than the uncoated and ME-coated steel bars. The higher R_{ct} and lower Y_{dl} values demonstrated that the PE coating outperformed the uncoated and the ME coating in terms of corrosion resistance.

For the DE-coated steel bars in salt solution, as shown in Table 8.5, R_{ct} decreased significantly after one or two months on test for all specimens, reflecting a transition from corrosion passivity to activity. After the decrease, R_{ct} remained stable and had values of 1.21±0.33 MΩ cm^2 for specimens with w/c=0.40 continuously immersion in salt solution, 0.04±0.02 MΩ cm^2 for specimens with w/c=0.40 subjected to bi-weekly wet-dry cycles, 0.75±0.10 MΩ cm^2 for specimens with w/c=0.55 continuous immersion in salt solution, and 0.03±0.02 MΩ cm^2 for specimens with w/c=0.55 subjected to bi-weekly wet-dry cycles. The Y_{dl} average value of all specimens in both exposure conditions is 9.82±4.65 μF cm^{-2} s$^{-(1-n_{dl})}$, significantly lower than those for the specimens with uncoated and ME-coated steel bars, indicating that the DE coating provided a better corrosion protection. Compared with the PE coating, however, the DE coating was less protective.

For specimens (a, d) with FBE-coated steel bars, R_{ct} decreased gradually from 2210 to 23 GΩ cm^2 with w/c=0.40 when immersed in salt solution, and from 1330 to 0.17 GΩ cm^2 with w/c=0.55 when subjected to bi-weekly wet-dry cycles. However, Y_{dl} remained stable and had values of 0.03±0.003 nF cm^{-2} s$^{-(1-n_{dl})}$ in both situations. The greater reduction in charge transfer resistance over time with w/c=0.55 is attributed to the continuous penetration of chloride between wetting and drying cycles, resulting in

increased corrosion activity of these samples. In addition, an average R_{ct} of 0.95±0.91 GΩ cm^2 and Y_{dl} of 18.9±7.8 nF cm^{-2} $s^{-(1-n_{dl})}$ was obtained for specimens (b, c) with w/c=0.40 when subjected to weekly wet-dry cycles and with w/c=0.55 when immersed in salt solution. The lower charge transfer resistance and the higher double layer capacitance for specimens (b) and (c) indicated that these samples experienced more severe damage than specimens (a) and (d).

8.3.6.4 Diffusion behavior. In this study, diffusion behavior was observed with samples of uncoated bars, PE- and DE-coated bars, and FBE-coated bars. As described previously, the diffusion behavior of the uncoated and coated bar surfaces can be simulated using the Warburg impedance W and the CPE_D. The diffusion behavior observed from the impedance spectra reflects the transport of charged ions, electrons and dissolved oxygen through the corrosion products formed at connected channels and around coating defect areas, and depends on both the size of the defects and the porosity of corrosion products [14].

The diffusion admittances are in the range of 0.04 ~ 5.13 mF cm^{-2} $s^{-0.5}$ for specimens with uncoated steel bars, 4.27 ~ 66.3 μF cm^{-2} $s^{-(1-n_d)}$ with PE-coated steel bars, and 0.02 ~ 0.56 mF cm^{-2} $s^{-(1-n_d)}$ with DE-coated steel bars, and 0.42 ~ 2.93 nF cm^{-2} $s^{-(1-n_d)}$ with FBE-coated steel bars. If similar corrosion products form on each sample, the difference in diffusion admittance then mainly depends on the size of coating damage, and so the coatings, FBE-coated samples are the least damaged, followed by the PE-coated samples, then the DE-coated samples.

8.3.6.5 Non-homogeneities of mortar-coating-steel system. The non-homogeneity of materials is reflected by the CPE coefficient n as discussed in [115]. Due to incomplete tests in terms of mortar cover effect, the following discussion will be focused on the passive film and electrolyte-steel interface where corrosion occurs.

The passive film parameter n_f indicates the overall non-homogeneity of a passive film that is randomly formed over the entire surface of a test specimen, and is affected by the microstructure of the coating layer. The n_f values are 0.34±0.11 for the passive film formed within the mill scale on the uncoated samples, 0.26±0.06 within the connected channels of ME coating, 0.36±0.07 on the damaged area of the PE coatings, 0.83±0.05 on the damaged area of the DE coatings, and 0.75±0.06 on the damaged area of the FBE

coatings. The lower n_f values of the passive films formed on the uncoated and ME-coated specimens are attributed to the significant randomness of the large connected channels leading to the steel as a result of large variations in the microstructure of the mill scale and ME coating, respectively. The greater n_f values of passive films formed on the DE and FBE-coated specimens are due to less coating damage and the relatively homogeneous microstructures of these coatings.

The average n_{dl} values of electrolyte-steel surface are 0.57±0.14 for the active corrosion areas of the uncoated specimens, 0.52±0.10 in the damaged areas of the PE-coatings, 0.73±0.12 for the connected open channels of the ME coatings, and 0.58±0.07 in the damaged areas of the DE-coatings. These values are all significantly less than the average value of 0.97±0.01 for the FBE-coated specimens with w/c=0.40 immersed in salt solution and w/c=0.55 subjected to weekly wet-dry cycles. This is because FBE coating has less active corrosion area compared with uncoated, ME-, PE- and DE-coated steel rebar specimens. However, the n_{dl} values of the other two FBE-coated specimens with w/c=0.40 when subjected to weekly wet-dry cycles and w/c=0.55 when immersed in salt solution are 0.68±0.04. This is because the coatings of specimens both with w/c=0.40 when in salt solution and w/c=0.55 when subjected to weekly wet-dry cycles are less severely damaged than the other two specimens as pointed out in Section 8.3.3

8.3.7 Deterioration Mechanism and Rate over Time.

8.3.7.1 Deterioration mechanism. The deterioration process, over time, of the uncoated steel bars is illustrated in Figure 8.16(a). Three stages of corrosion, corresponding to the three equivalent circuits in Figure 8.10a, were observed: (I) initial protection by the passive film; (II) occurrence of pitting corrosion after the partial breakdown of the passive film due to chloride attack; (III) buildup of the corrosion products through the increase of the active area due to continuous penetration of chloride. In Stage I, corrosion kinetics is controlled by charge transfer across the passive film [30]. In Stage II, the spatial randomness of connected pores and chloride concentration controls the rate at which the passive film breaks down locally, leading to pitting corrosion. Diffusion impedance due to the formation of corrosion products appears in this stage. In Stage III, substantial concentrations of chloride ions have penetrated to the surface of the steel, extending the active corrosion area over time. When the active area

exceeds the passive area, the electrochemical behavior of the passive film disappears and the diffusion process through the corrosion products (rust film) becomes dominant. The diffusion component has been suggested to be related to oxygen transport across the interface [207], and this is probably why the diffusion impedance is associated with active corrosion [140, 208].

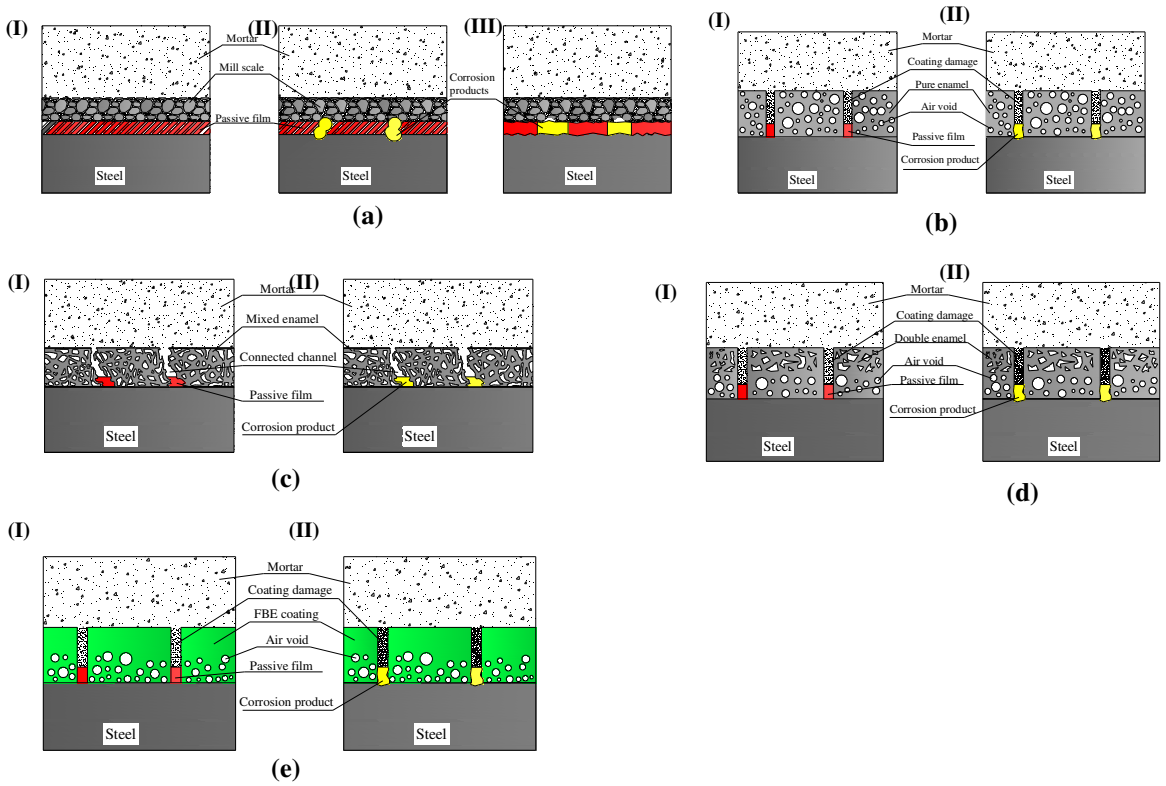

Figure 8.16 Schemes of deterioration processes of mortar with: (a) uncoated, (b) pure enamel, (c) mixed enamel, and (d) double enamel, and (e) FBE coated steel bar.

For specimens with ME-coated steel bars, two stages as illustrated in Figure 8.16(c) were observed, corresponding to the two equivalent circuits in Figure 8.10. In Stage I, the steel bars were protected by the passive film formed inside the connected channels due to the penetration of pore solution during cement hydration. In Stage II, the chloride concentrations in the connected channels reached threshold values so that the passive film broke down and then corrosion initiated. Unlike the uncoated steel bars, the

ME-coated bars have large cavities inside the ME coating, which functioned as reservoirs, accumulated and redistributed chloride and oxygen around the steel surface, and broke down the passive film through the connected pores, as indicated by a sudden drop of impedance magnitude as shown in Figure 8.13.

The PE- and DE-coated bars followed similar deterioration patterns, as indicated in Figures 8.16(b) and 8.16(d). Both coatings served as effective physical barriers to the penetration of aggressive ions. Therefore, the corrosion processes of PE- and DE-coated bars were mainly controlled by the extent of coating damage prior to testing. Two stages corresponding to the two equivalent circuits in Figure 8.10(b) were identified. In Stage I, small damage areas were protected by the passive film that initially formed due to the hydration of cement, and the electrochemical system was controlled by the charge transfer through the small passive film and PE or DE coating. In Stage II, corrosion initiated and corrosion products formed as the chloride content was increased and exceeded the critical threshold.

Figure 8.16(e) illustrates the corrosion mechanism of the FBE-coated steel bars. Despite a large variation in the extent of the coating damage, the corrosion behavior can be grouped into a passive state (stage I) and active state (stage II). In Stage I, steel rebar was protected by both the FBE coating and the passive film that formed around the damaged coating area. In Stage II, the passive film around the entire steel surface broke down, and active corrosion initiated.

8.3.7.2 Deterioration rates. The deterioration rate of the samples is inversely related to the charge transfer resistance. Figure 8.17 shows the evolution of charge transfer resistance over time for all samples with different coatings, water-cement ratios, and exposure conditions. After two or three months, each sample experienced a transition from passive (Stage I) to active corrosion (Stage II), as indicated by the shaded area in Figure 8.17. The enamel coatings did not substantially delay this transition (extend stage I to stage I', Figure 1) since the coatings used in this study were not pristine, due to defect and damage as pointed out previously.

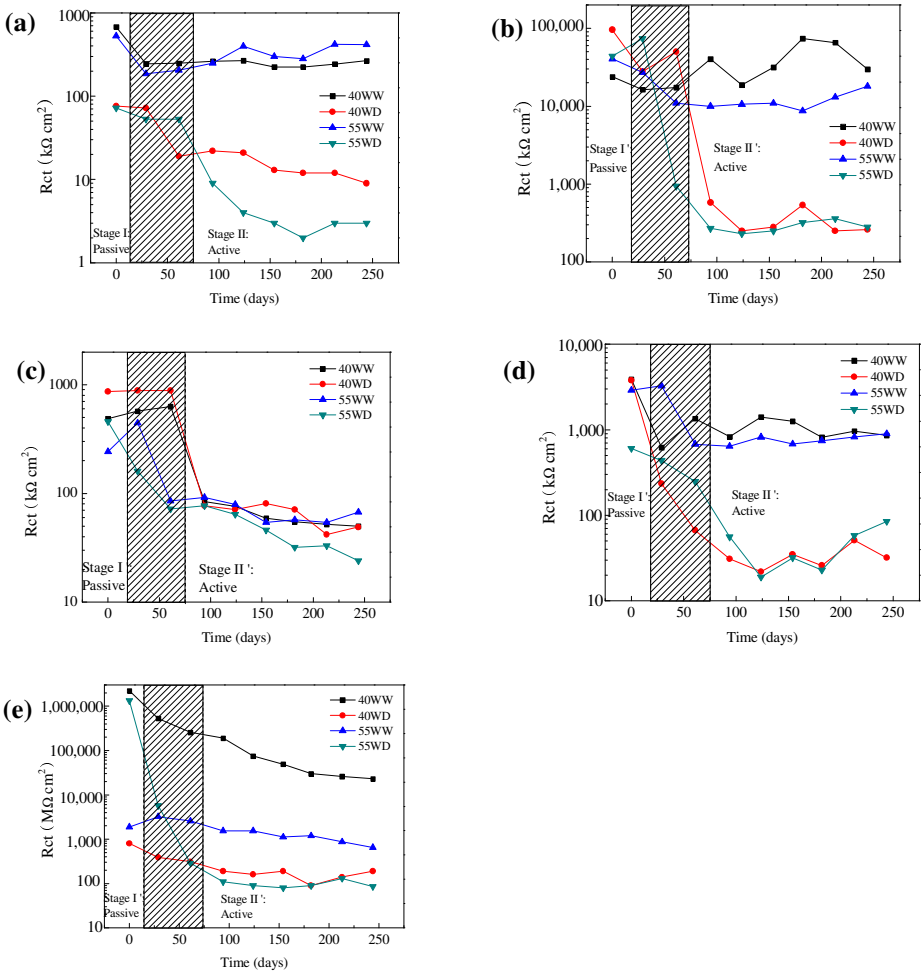

Figure 8.17 Evolution of charge transfer resistance of mortar with: (a) uncoated, (b) pure enamel coated, (c) mixed enamel coated, (d) double enamel, and (e) FBE coated steel bar. (Note: 40WW--- w/c=0.40, in 3.5 wt.% NaCl solution; 40WD--- w/c=0.40, weekly wet-dry cycles; 55WW--- w/c=0.55, in 3.5 wt.% NaCl solution; 55WD--- w/c=0.55, weekly wet-dry cycles.)

Table 8.7 shows the deterioration rates of the three enamel- and three FBE-coated steel bars, normalized by the deterioration rates of the uncoated steel bars under the same respective conditions. Among all coatings, the FBE- and PE-coated specimens have the lowest deterioration rates and the ME-and DE-coated specimens have greater deterioration rates. The ME-coated bars continuously immersed in salt solution have a greater deterioration rate than the uncoated bars. Table 8.8 shows the deterioration rates of specimens under different exposure conditions, normalized by the rates of the

respective samples with w/c=0.40 and continuously immersed in salt solution. The effect of exposure conditions on the deterioration rate is more significant than that of water-cement ratio for all but the ME-coated samples. When subjected to weekly wet-dry cycles, all specimens deteriorated more rapidly than when those samples were immersed continuously in salt solution. This is probably due to the slower diffusion rates of oxygen through the pore networks of the mortar cover under the latter conditions. When samples are subjected to the weekly wet-dry cycles, the dissolved oxygen in salt solution can be rapidly transported by capillary suction and the oxygen contained in the pore networks significantly contributed to the specimen deterioration in the drying process. For ME-coated specimens, no significant differences of deterioration rate were observed for all four exposure conditions.

Table 8.7 Normalized average deterioration rates in stage II according to coating type

Exposure conditions	Uncoated	PE-coated	ME-coated	DE-coated	FBE-coated
w/c=0.40 Continuously in solution	1	4.5×10^{-3}	3.85	0.20	5.9×10^{-6}
w/c=0.40 Bi-weekly wet-dry cycles	1	1.9×10^{-2}	0.10	0.09	4.2×10^{-5}
w/c=0.55 Continuously in solution	1	2.5×10^{-2}	4.55	0.43	2.7×10^{-4}
w/c=0.55 Bi-weekly wet-dry cycles	1	8.5×10^{-3}	0.12	0.20	5.9×10^{-5}

Table 8.8 Normalized average deterioration rates in stage II according to corrosion conditions

Exposure conditions	Uncoated	PE-coated	ME-coated	DE-coated	FBE-coated
w/c=0.40 Continuously in solution	1	1	1	1	1
w/c=0.40 Bi-weekly wet-dry cycles	37	159	1	17	256
w/c=0.55 Continuously in solution	1	4	1	1	34
w/c=0.55 Bi-weekly wet-dry cycles	41	77	1	40	410

8.4. SUMMARY

Based on the test results and discussion in this study, the following conclusions can be drawn on the equivalent circuit representation, deterioration mechanism and deterioration rate of mortar-coating-steel systems with uncoated, enamel-coated, and FBE-coated steel bars, either continuously immersed in 3.5% NaCl solution or subjected to bi-weekly wetting-drying cycles:

(1). A mortar-coating-steel system can be modeled by an equivalent electrical circuit (EEC) that consists of a series of components representing the behavior of various material layers in different frequency ranges. Each EEC component included a parallel pair of CPE and resistor. The CPE accounted for the non-homogeneity of the mortar, coating, and electrolyte-steel interfaces. The EEC representation of the mortar-coating-steel system depended on the thickness and porosity of the mortar (concrete) cover, barrier and dielectric property as well as the damage extent of the coating layer and the state of the steel surface.

(2). The diffusion behavior can be generally modeled with a Warburg element for uncoated steel bar but must be represented by a CPE for steel bars with PE-, DE-, and FBE-coating since the diffusion process is affected by the characteristics of the corrosion products.

(3). Three stages of deterioration were observed for uncoated steel bars: protection by dense passive film prior to the accumulation of chloride ions to the threshold value, local breakdown of the passive film and appearance of pitting corrosion, and significant breakdown of the passive film and buildup of corrosion products.

(4). Two stages of deterioration were observed for ME-coated steel bars: protection by passive film formed during cement hydration due to the penetration of high pH pore solution, and dramatic damage of the passive film and buildup of corrosion products. The passive film damaged suddenly and significantly since the thick porous ME coating accelerated the transport of chloride to the steel.

(5). Two stages of deterioration were observed for PE- and DE-coated steel bars: stage I for protection by enamel coating and passive film in small damage areas, and stage II for breakdown of the passive film, initiation of corrosion, and buildup of

corrosion products. Buildup of corrosion products prevented the diffusion of oxygen, thus decelerating the corrosion process over time.

(6). No coatings tested in this study delayed the initiation of deterioration associated with the breakdown of passive film. However, once deterioration initiated, FBE and PE coatings can significantly reduce the deterioration rate of steel bars; DE coatings had little effect on deterioration rates, and ME coatings may increase the deterioration rate for samples continuously immersed in salt solution. Bi-weekly wet-dry cycles accelerated the deterioration rates of almost all samples since oxygen transport was enhanced by capillary suction. The effect of different water-cement ratios on the deterioration rates was not as significant as that of the different exposure conditions.

9. CONCLUSIONS AND FUTURE WORK

9.1 MAIN FINDINGS FROM THE OVERALL DISSERTATION WORK

In this dissertation, the corrosion-induced deterioration of steel reinforced concrete (RC) structures and the corrosion performance of various enamel coatings applied to structural steel and reinforcement steel were investigated to lay down a solid foundation for the long-term durability and life-cycle performance assessment of RC structures. Three main components affecting RC structural deterioration were studied, including concrete cracking, steel property degradation, and steel-concrete bond loss. To combat the structural deterioration due to steel corrosion, porcelain enamel coating as a barrier to aggressive chloride ions was developed and evaluated for corrosion resistance improvement. Specifically, three types of enamel coating (pure enamel, mixed enamel, and double enamel) were investigated with four types of specimens (steel plates, deformed steel bar, smooth steel bar and deformed steel bar embedded in mortar cylinder) tested in 3.5 wt.% NaCl and saturated $Ca(OH)_2$ solutions. Their corrosion resistances and mechanisms were also compared with fusion-bonded epoxy coating. The effects of coating thickness, thickness variation, potential damage, mortar cover, corrosion environment, and coating microstructures were investigated.

9.1.1 Corrosion-induced RC Structural Deterioration. Based on the test data and analysis on corrosion-induced RC structural deterioration, several main conclusions can be drawn:

(1) Concrete cover cracking due to reinforcement steel corrosion can be divided into four stages: I from the completion of new construction to the initiation of cracking, II from the initiation of cracking to a critical crack width that defines a transition from steady to decelerating crack propagation as corrosion of steel bars continues, III that transits from II to IV in which cracks in concrete cover stop growing even though steel bars continue to be corroded. Stage II represents the strongest correlation between the crack width and corrosion level in all times.

(2) Corrosion changes the cross section of steel bars but not their mechanical properties such as yield stress and ultimate stress. Both yielding and ultimate loads

depend upon the minimum cross section of corroded steel bars while the elongation of steel bars depends on the distribution of cross sections along the length of steel bars. As such, the minimum and average cross section areas are recommended to evaluate the mechanical strengths and elongation, respectively.

(3) Corrosion of a deformed steel bar reduces the bond stress between the bar and its surrounding concrete. The reduced bond stress depends on both the corrosion level and the spatial distribution of corrosion pits. If the steel bar is subjected to light corrosion, in comparison with a corresponding uncorroded steel bar, the bond stress increases slightly when corrosion pits are located along the lugs between two adjacent ribs and decreases when corrosion pits are located at the ribs. If the steel bar is subjected to severe corrosion, all the ribs corrode and become flattened, thus resulting in different bond-slip behaviors from the uncorroded and lightly corroded steel bars.

9.1.2 Corrosion Performance of Three Types of Enamel-coated Steel. Based on extensive corrosion tests, the following conclusions can be drawn:

(4) Three types of enamel coating can all improve the corrosion resistance of structural steel plate, deformed steel rebar, smooth steel rebar and deformed steel bar in mortar cylinder. Since the air bubbles generated during high temperature firing are isolated in pure and double enamel coatings and interconnected in mixed enamel coating, the pure and double enamel coatings are generally more effective barriers to aggressive chloride ions.

(5) The corrosion behaviors of three types of enamel coating are similar whether enamel-coated steel are immersed in 3.5 wt% NaCl or saturated $Ca(OH)_2$ solution. This is because enamel coating includes a ZrO_2 compound that makes it highly alkaline resistant.

(6) The thickness of pure and double enamel coatings significantly affects the corrosion resistance of coated steel bars. A thicker enamel layer can better prevent the penetration and diffusion of electrolytes in a corrosive environment. Similarly, the mortar cover on steel bars also helps protect the steel from corrosion.

(7) Coating damage and thickness variation are two main causes for the low corrosion resistance of deformed steel bars compared to steel plates and smooth steel bars.

(8) The pure and double enamel coatings can protect the substrate steel from corrosion over a long period of time. The double enamel coating also performs more consistently than the pure enamel coating. Therefore, it is recommended that double enamel coating be used for the design of RC structures in corrosion-sensitive environments.

(9) In short term, the enamel coatings presented in this dissertation are less corrosion resistant than intact fusion-bonded epoxy coating. However, once damaged, epoxy coating deteriorates over time much more rapidly than the enamel coating due to the weak bond between the epoxy coating and the substrate steel. As a result, the so-called under-film corrosion has been clearly observed in the damaged epoxy-coated bar. On the contrary, the corrosion of enamel-coated bar is limited to a local damaged area. For the long-term durability of RC structures, enamel coating is thus a viable alternative to the commonly-used epoxy coating for steel bars after more implementation studies with enamel coating technology have been carried out on real-world structures.

9.2 FUTURE WORK

The corrosion-induced structural deterioration and the corrosion performance of enamel coatings on structural steel and steel reinforcement have been comprehensively studied in individual entireties. However, their integration is necessary for the structural safety evaluation of RC structures with enamel-coated reinforcement. Specifically, future works should be directed to address the following topics:

9.2.1 Effect of Enamel Coating on Concrete Cover Cracking, Steel Bar Corrosion, and Steel-Concrete Bond. In space, the probability distribution of crack width depends on the distribution of corrosion products, concrete cover thickness, coarse aggregates, void and cement paste in concrete along the length of steel bars. Over time, crack width propagation is nonlinearly related to the corrosion-induced mass loss with their correlation gradually weakened as cracks are widened due to the diffusion of corrosion products and concrete softening. Enamel coating can alter the crack width distribution both spatially and temporally since the chemical bond between the coating, even damaged, and the surrounding concrete/steel can prevent the spreading of corrosion

products away from the damage location. Therefore, enamel coating will affect the cracking behavior in concrete cover in space and over time.

The mechanical strengths and elongation of enamel-coated steel bars quite differ from those of uncoated bars prior to and after corrosion. Damage spots of an enamel-coated steel bar will be the potential locations of pitting corrosion. The small damaged areas will probably produce a local macro-cell corrosion that potentially accelerates further corrosion in comparison with a corresponding uncoated steel bar.

The bond behavior of an enamel-coated steel bar is expected to be quite different from the uncoated bar both before and after corrosion. The bond behavior of mixed enamel-coated steel bars in concrete has been studied already. It was concluded that the mixed enamel coating significantly increased the bond strength with surrounding concrete. The effects of pure and double enamel on the bond behavior, particularly after corrosion, are yet to be investigated. The distribution of potential corrosion pits would be concentrated on the damaged coating area of enamel-coated steel bars, thus changing the bond behavior.

9.2.2 Development of a Reliability-based Durability and Life-Cycle Performance Evaluation Framework. To apply the research results in this dissertation into the condition assessment of RC structures, a system-level assessment framework and its specific design equations must be developed. For example, an empirical or analytical equation is needed to integrate the effect of concrete cover cracking, steel section reduction, and steel-concrete bond loss into a probabilistic evaluation of structural behaviors. Currently, there is no equation in the ACI design code to consider these effects. In the development of design equations, two limit states must be considered. One is the serviceability limit state that can be defined as a specified concrete cover crack width that can be evaluated using the probability density function of concrete crack width developed in this dissertation. The other is the ultimate limit state that can be defined as the reduction of structural capacity such as flexural and shear. The capacity reduction is directly related to the corrosion-induced area loss that can be modeled with the probability density function of cross sectional area developed in this dissertation.

Enamel coating can be applied to decelerate the deterioration process of RC structures associated with reinforcement steel corrosion. Application of enamel coating

can not only change the spatial distribution of potential active corrosion sites, but also moderate the corrosion rate over time. Therefore, the system performance improvement of RC structures with enamel coating technology must be evaluated in order to promote the use of enamel coating in various applications.

BIBLIOGRAPHY

[1] G.H. Koch, M.P.H. Brongers, N.G. Thompson, Y.P. Virmani, and J.H. Payer, "Corrosion Costs and Preventive Strategies in the United States," Publication No. FHWA-RD-01-156, *NACE International*, Houston TX, USA (2002).

[2] Report Card for American Infrastructure, 2009. "Report Card 2009 Grades," American Society of Civil Engineers website https://apps.asce.org/reportcard/2009/grades.cfm.

[3] U.S. Government Accountability Office, 2012. "Defense Management: The Department of Defense's Annual Corrosion Budget Report Does Not Include Some Required Information," GAO-12-823R, Website https://www.gao.gov/products/GAO-12-823R.

[4] M. Liao, T. Okazaki, R. Ballarini, A.E. Schultz, and T.V. Galambos, "Analysis of Critical Gusset Plates in the Collapsed I-35W Bridge," *Structure Congress 2009*, Pp. 1-10, Austin, TX, USA (2009).

[5] H. Song, and V. Saraswathy, "Corrosion Monitoring of Reinforced Concrete Structures-A Review," *International Journal of Electrochemical Science,* Vol. 2, Pp. 1-28, (2007).

[6] ASTM C876 (1999). Standard Test Method for Half-cell Potentials of Uncoated Reinforcing Steel in Concrete, *American Society of Testing and Materials*, West Conshohocken, PA.

[7] P. Gu, and J.J. Beaudoin, "Obtaining Effective Half-cell Potential Measurements in Reinforced Concrete Structures," Construction Technology Update No. 18, Institute for Research in Construction, National Research Council of Canada (1998).

[8] C. Page, K. Treadway, and P. Bamforth, (1990). *Corrosion of Reinforcement in Concrete*. Elservier Applied Science, London-New York. P.314.

[9] J.P. Broomfield, (2007). *Corrosion of Steel in Concrete: Understanding, Investigation and Repair.* Taylor & Francis: (Second Edition).

[10] J. Bennet, and T. Mitchell, (1992). "Reference Electrodes for Use with Reinforced Concrete Structures," Paper No. 191, Corrosion 92, NACE International, Houston.

[11] G. Grimaldi, P. Brevet, G. Pannier, and A. Raharinaivo, "Factors Influencing Electrode Potential of Steel in Concrete," *British Corrosion Journal*, Vol. 21, Pp. 55-62, (1986).

[12] M. Stern, and A.L. Geary, "Electrochemical Polarization I. A Theoretical Analysis of the Shape of Polarization Curves," *Journal of the Electrochemical Society,* Vol. 104, No. 1, Pp. 56-63, (1957).

[13] C. Andrade, M.C. Alonso, and J.A. Gonzalez, (1990). "An Initial Effort to Use Corrosion Rate Measurements for Estimating Rebar Durability Corrosion Rates of Steel in Concrete." ASTM STP 1065, Berke, N. S. et al. Editors, ASTM, Philadelphia, Pp. 29-37.

[14] A.A. Sagues, S.C. Kranc, and E.I. Moreno, "Evaluation of Electrochemical Impedance with Constant Phase Angle Components from the Galvanostatic Step Response of Steel in Concrete," *Electrochimica Acta*, Vol. 41, No. 78, Pp. 1239-1243, (1996).

[15] A.A. Sagues, S.C. Kranc, and E.I. Moreno, "The Time-domain Response of a Corroding System with Constant Phase Angle Interfacial Component: Application to Steel in Concrete," *Corrosion Science*, Vol. 37, No. 7, Pp. 1097-1113, (1995).

[16] V. Feliu, J.A. Gonzalez, and S. Feliu, "Corrosion Estimates from the Transient Response to a Potential Step," *Corrosion Science*, Vol. 49, No. 8, Pp. 3241-3255, (2007).

[17] V. Feliu, J.A. Gonzalez, and S. Feliu, "Modelling of the Steel-Concrete Interface to Obtain Information on Reinforcement Bar Corrosion," *Journal of Applied Electrochemistry*, Vol. 35, No. 5, Pp. 429-436, (2005).

[18] S. Feliu, J.A. Gonzalez, C. Andrade, and V. Feliu, "The Determination of the Corrosion Rate of Steel in Concrete by a Non-stationary Method," *Corrosion Science*, Vol. 26, No. 11, Pp. 961-965, (1986).

[19] V. Feliu, J.A. Gonzalez, C. Andrade, and S. Feliu, "Equivalent Circuit for Modeling the Steel-Concrete Interface. I. Experimental Evidence and Theoretical Predictions," *Corrosion Science*, Vol. 40, No. 6, Pp. 975-993, (1998).

[20] V. Feliu, J.A. Gonzalez, C. Andrade, and S. Feliu, "Equivalent Circuit for Modeling the Steel-Concrete Interface. II. Complications in Applying the Stern-geary Equation to Corrosion Rate Determinations," *Corrosion Science*, Vol. 40, No. 6, Pp. 995-1006, (1998).

[21] S.J. Ford, J.D. Shane, and T.O. Mason, "Assignment of Features in Impedance Spectra of the Cement Paste/Steel System," *Cement and Concrete Research*, Vol. 28, No. 12, Pp. 1737-1751, (1998).

[22] J.T.S. Irvine, D.C. Sinclair, and A.R. West, "Electroceramics: Characterization by Impedance Spectroscopy," *Advanced Materials*, Vol. 2, No. 3, Pp. 132-138, (1990).

[23] F. Tang, G. Chen, R.K. Brow, J.S. Volz, and M.L. Koenigstein, "Cement-modified Enamel Coating for Enhanced Corrosion Resistance," *Cement and Concrete Composites,* Vol. 35, No. 1, Pp. 171-180, (2013).

[24] G. Trabanelli, C. Monticelli, V. Grassi, and A. Frignani, "Electrochemical Study on Inhibitors of Rebar Corrosion in Carbonated Concrete," *Cement and Concrete Research*, Vol. 35, No. 9, Pp. 1804-1813, (2005).

[25] J.L. Kepler, D. Darwin, and C.E. Locke, (2000). "Evaluation of Corrosion Protection Methods for Reinforced Concrete Highway Structures." Structural Engineering and Engineering Materials SM Report No. 58. University of Kansas Center for Research. Inc., Lawrence, Kansas.

[26] H. Castro, C. Rodriguez, F.J. Belzunce, and A.F. Canteli, "Mechanical Properties and Corrosion Behaviour of Stainless Steel Reinforcing Bars," *Journal of Materials Processing Technology*, Vol. 143-144, Pp. 134-137, (2003).

[27] M.C. Garcia-Alonso, J.A. Gonzalez, J. Miranda, and M.L. Escudero, "Corrosion Behavior of Innovative Stainless Steels in Mortar." *Cement and Concrete Research,* Vol. 37, No. 11, Pp. 1562-1569, (2007).

[28] R.D. Moser. P.M. Singh, L.F. Kahn, and K.E. Kuitis, "Chloride-induced Corrosion Resistance of High-strength Stainless Steels in Simulated Alkaline and Carbonated Concrete Pore Solutions," *Corrosion Science*, Vol. 57, Pp. 241-253, (2012).

[29] D. Darwin, C.E. Locke, B.J. Jr., and J.T. Kahrs, (1999). Evaluation of Stainless Steel Clad Reinforcing Bars. SL Report No. 99-3, The University of Kansas Center for Research, Inc., Lawrence, Kansas.

[30] Y.P. Virmani, K.C. Clear, and T.J. Pasko, Jr. (1983). Time to Corrosion of Reinforcing Steel in Concrete Slabs. Vol. 5-Calcium Nitrite Admixture or Epoxy Coated Reinforcing Bars as Corrosion Protection Systems. Report No. FHWA-RD-83-012, Federal Highway Administration, Washington, D.C.

[31] D.B. McDonald, Y.P. Virmani, and D.F. Pfeifer, "Testing the Performance of Copper-Clad Reinforcing Bars," *Concrete International*, Vol. 18, No. 11, Pp. 39-43, (1996).

[32] M.K. Agony, Y. Kawamoto, H. Sakai, and K. Yagi, (1992). "Application of a Tendon Made of CFRP Rods to a Post-tensioned Prestressed Concrete Bridges,"

Advance Composite Materials in Bridges and Structures, Canadian Society for Civil Engineering.

[33] D.G. Manning, "Corrosion Performance of Epoxy-coated Reinforcing Steel: North American Experience," *Construction and Building Materials*, Vol. 10, No. 5, Pp. 349-365, (1996).

[34] A.A. Sagues, R.G. Powers, and R. Kessler, (2001). "Corrosion Performance of Epoxy-coated Rebar in Florida Keys Bridges," *Corrosion01*, NACE International, Houston.

[35] A.A. Sagues, K. Lau, R.G. Powers, and R.J. Kessler, "Corrosion of Epoxy-coated Rebar in Marine Bridges-Part I: a 30 Years Perspective," *NACE Corrosion*, Vol. 66, No. 6, Pp. 1-13, (2010).

[36] ACI 318-08 (2008). Building Code Requirement for Structural Concrete and Commentary. Farmington Hills, MI.

[37] L. McCrum, and C.J. Arnold, (1993). "Evaluation of Simulated Bridge Deck Slabs Using Uncoated, Galvanized, and Epoxy-coated Reinforcing Steel," Research Report No. R-1320, Michigan Department of Transportation, Lansing, MI.

[38] Z.Q. Tan, and C.M. Hansson, "Effect of Surface Condition on the Initial Corrosion of Galvanized Reinforcing Steel Embedded in Concrete," *Corrosion Science,* Vol. 50, No. 9, Pp. 2512-2522, (2008).

[39] T.A. Soylev, and M.G. Richardson, "Corrosion Inhibitors for Steel in Concrete: State-of-the-art Report," *Construction and Building Materials*, Vol. 22, No. 4, Pp. 609-622, (2008).

[40] L. Dhouibi, E. Triki, and A. Raharinaivo, (1998), "Laboratory Experiments for Assessing the Effectiveness of Inhibitors against Steel Corrosion in Concrete," In: *Proceedings of the Sixth International Symposium on Advances in Electrochemical Science and Technology*, Chennai, India.

[41] L. Dhouibi, E. Triki, M. Salta, P. Rodrigues, and A. Raharinaivo, "Studies on Corrosion Inhibitor of Steel Reinforcement by Phosphate and Nitrite," *Materials and Structures,* Vol. 36, No. 8, Pp. 530-540, (2003).

[42] K. Soeda, and T. Ichimura, "Present State of Corrosion Inhibitors in Japan," *Cement and Concrete Composites*, Vol. 25, No. 1, Pp. 117-122, (2003).

[43] L. Bertolini, F. Bolzoni, A. Cigada, T. Pastore, and P. Pedeferri, "Cathodic Protection of New and Old Reinforced Concrete Structures," *Corrosion Science,* Vol. 35, No. 5-8, Pp. 1633-1639, (1993).

[44] M. Mckenza, (1991). Cathodic Protection of Reinforced Concrete, Research Report 328, Transport and Road Research Laboratory, Department of Transport, Crowthorne, Berkshire, UK.

[45] P.J. Jurach, (1982). An Evaluation of the Effectiveness of Cathodic Protection of Seven Bridge Decks. Report No. FHWA-DP34-2, California Department of Transportation.

[46] J. Leggedoor, and G.E. Schuten, (1998). In: Proceedings of the Conference on Solution to Corrosion Problems, EUROCORR 98, Event #221, Bidthoven, Netherlands, 191.

[47] J.A. Apostolos, D.M. Parks, and R.A. Carello, "Cathodic Protection of Reinforced Concrete Using Metalized Zinc." Paper No. 137, *Corrosion 87*, NACE, Houston, TX (1987).

[48] M. Funahashi, and W.T. Young, (1998). Field Evaluation of New Aluminum Alloy Sacrificial Anode for Steel Embedded in Concrete. FHWA Publication, FHWA RD 98058.

[49] K.A.T. Vu, M.G. Stewart, and J. Mullard, "Corrosion-induced Cracking: Experimental Data and Predictive Models," *ACI Structural Journal*, Vol. 102, No. 5, Pp. 719-726, (2005).

[50] M.G. Stewart, and J.A. Mullard, "Spatial Time-dependent Reliability Analysis of Corrosion Damage and the Timing of First Repair for RC Structures," *Engineering Structures,* Vol. 29, No. 7, Pp. 1457-1464, (2007).

[51] A. Jamali, U. Angst, B. Adey, and B. Elsener, "Modeling of Corrosion-induced Concrete Cracking: a Critical Analysis," *Construction and Building Materials*, Vol. 42, Pp. 225-237, (2013).

[52] C. Andrade, C. Alonso, and F.J. Molina, "Cover Cracking as a Function of Rebar Corrosion: Part I-Experimental Test," *Materials and Structures*, Vol. 26, No. 8, Pp. 453-464, (1993).

[53] M.P. Webster, (2000). *The Assessment of Corrosion-damaged Concrete Structures,* Birmingham: The University of Birmingham.

[54] Z.P. Bazant, "Physical Model for Steel Corrosion in Sea Concrete Structures Applications." *ASCE Journal of the Structural Division*, Vol. 105, No. 6, Pp. 1155-1166, (1979).

[55] K. Yokozeki, K. Motohashi, K. Okada, and T. Tsutsumi, (1997). A Rational Model to Predict the Service Life of RC structures in Marie Environment. In: Malhotra V. Editor. Durability of Concrete, Detroit: ACI SP 170-40, Pp. 777-799.

[56] S.J. Pantazopoulou, and K.D. Papoulia, "Modeling Cover-cracking Due to Reinforcement Corrosion in RC Structures," *ASCE Journal of Engineering Mechanics*, Vol. 127, No. 4, Pp. 342-351, (2001).

[57] A.A. Almusallam, "Effect of Degree of Corrosion on the Properties of Reinforcing Steel Bars," *Construction and Building Materials*, Vol. 15, No. 8, Pp. 361-368, (2001).

[58] C.A. Apostolopoulos, and V.G. Papadakis, "Consequences of Steel Corrosion on the Ductility Properties of Reinforcement Bar," *Construction and Building Materials*, Vol. 22, No. 12, Pp. 2316-2324, (2008).

[59] J. Cairns, G.A. Plizzari, Y. Du, D.W. Law, and C. Franzoni, "Mechanical Properties of Corrosion-damaged Reinforcement," *ACI Materials Journal,* Vol. 102, No. 4, Pp. 256-264, (2005).

[60] Y.G. Du, L.A. Clark, and A.H.C. Chan, "Residual Capacity of Corroded Reinforcing Bars," *Magazine of Concrete Research*, Vol. 57, No. 3, Pp. 135-147, (2005).

[61] C.A. Apostolopoulos, S. Demis, and V.G. Papadakis, "Chloride-induced Corrosion of Steel Reinforcement-Mechanical Performance and Pit Depth Analysis," *Construction and Building Materials*, Vol. 38, Pp. 139-146, (2013).

[62] X. Wang, W. Zhang, X. Gu, and H. Dai, "Determination of Residual Cross-sectional Areas of Corroded Bars in Reinforced Concrete Structures Using Easy-to-measure Variables," *Construction and Building Materials*, Vol. 38, Pp. 846-853, (2013).

[63] C. Fang, K. Lundgren, L. Chen, and C. Zhu, "Corrosion Influence on Bond in Reinforced Concrete," *Cement and Concrete Research*, Vol. 34, No. 11, Pp. 2159-2167, (2004).

[64] C. Fang, K. Lundgren, M. Plos, and K. Gylltoft, "Bond Behaviour of Corroded Reinforcing Steel Bars in Concrete," *Cement and Concrete Research*, Vol. 36, No. 10, Pp. 1931-1938, (2006).

[65] F. Li, and Y. Yuan, "Effect of Corrosion on Bond Behavior Between Steel Strand and Concrete," *Construction and Building Materials,* Vol. 38, Pp. 413-422, (2013).

[66] D. Tang, T.K.C. Molyneaux, D.W. Law, and R. Gravina, "Influence of Surface Crack Width on Bond Strength of Reinforced Concrete," *ACI Materials Journal*, Vol. 108, No. 1, Pp. 29-37, (2011).

[67] H. Yalciner, O. Eren, and S. Sensoy, "An Experimental Study on the Bond Strength between Reinforcement Bars and Concrete as a Function of Concrete Cover, Strength and Corrosion Level," *Cement and Concrete Research*, Vol. 42, No. 5, Pp. 643-655, (2012).

[68] A. Steffens, D. Dinkler, and H. Ahrens, "Modeling Carbonation for Corrosion Risk Prediction of Concrete Structures," *Cement and Concrete Research*, Vol. 32, No. 6, Pp. 935-941, (2002).

[69] Y. Du, M. Cullen, and C. Li, "Structural Effects of Simultaneous Loading and Reinforcement Corrosion on Performance of Concrete Beams," *Construction and Building Materials*, Vol. 39, Pp. 148-152, (2013).

[70] M.K. Kassir, and M. Ghosn, "Chloride-induced Corrosion of Reinforced Concrete Bridge Decks," *Cement and Concrete Research*, Vol. 32, No. 1, Pp. 139-143, (2002).

[71] C. Li, and S.T. Yang, "Prediction of Concrete Crack Width under Combined Reinforcement Corrosion and Applied Load," *ASCE Journal of Structural Engineering,* Vol. 137, No. 11, Pp. 722-731, (2011).

[72] C. Li, "Life Cycle Modeling of Corrosion-affected Concrete Structures-Propagation," *ASCE Journal of Structural Engineering*, Vol. 129, No. 6, Pp. 753-761, (2003).

[73] L. Chernin, D.V. Val, and K.Y. Volokh, "Analytical Modeling of Concrete Cover Cracking Caused by Corrosion of Reinforcement," *Materials and Structures,* Vol. 43, No. 4, Pp. 543-556, (2010).

[74] X. Wang, and X. Liu, "Modeling Effects of Corrosion on Cover Cracking and Bond in Reinforced Concrete," *Magazine of Concrete Research*, Vol. 56, No. 4, Pp. 191-199, (2004).

[75] P. Grassl, and T. Davies, "Lattice Modeling of Corrosion Induced Cracking and Bond in Reinforced Concrete," *Cement and Concrete Composites*, Vol. 33, No. 9, Pp. 918-924, (2011).

[76] L. Chernin, and D.V. Val, "Prediction of Corrosion-induced Cover Cracking in Reinforced Concrete Structures," *Construction and Building Materials*, Vol. 25, No. 4, Pp. 1854-1869, (2011).

[77] S. Guzman, J.C. Galvez, and J.M. Sancho, "Modelling of Corrosion-induced Cover Cracking in Reinforced Concrete by an Embedded Cohesive Crack Finite Element," *Engineering Fracture Mechanics*, Vol. 93, Pp. 92-107, (2012).

[78] K. Bhargava, A.K. Ghosh, Y. Mori, and S. Ramanujam, "Modeling of Time to Corrosion-induced Cover Cracking in Reinforced Concrete Structures," *Cement and Concrete Research*, Vol. 35, No. 1, Pp. 2203-2218, (2005).

[79] J. Rodriguez, L.M. Ortega, J. Casal, and J.M. Diez, "Corrosion of Reinforcement and Service Life of Concrete Structures," *Durability of Building Materials and Components*, Vol. 7, No. 1, Pp. 117-126, (1996).

[80] C. Alonso, C. Andrade, J. Rodriguez, and J.M. Diez, "Factors Controlling Cracking of Concrete Affected by Reinforcement Corrosion," *Materials and Structures*, Vol. 31, No. 7, Pp. 435-441, (1998).

[81] T. Vidal, A. Castel, and R. Francois, "Analyzing Crack Width to Predict Corrosion in Reinforced Concrete," *Cement and Concrete Research*, Vol. 34, No. 1, Pp. 165-174, (2004).

[82] P. Ghods, O.B. Isgor, G. McRae, and T. Miller, "The Effect of Concrete Pore Solution Composition on the Quality of Passive Oxide Films on Black Steel Reinforcement," *Cement and Concrete Composites*, Vol. 31, No. 1, Pp. 2-11, (2009).

[83] X. Feng, Y. Zuo, Y. Tang, X. Zhao, and X. Lu, "The Degradation of Passive Film on Carbon Steel in Concrete Pore Solution under Compressive and Tensile Stresses," *Electrochimica Acta*, Vol. 58, Pp. 258-263, (2011).

[84] H. Yu, K.T.K. Chiang, and L. Yang, "Threshold Chloride Level and Characteristics of Reinforcement Corrosion Initiation in Simulated Concrete Pore Solutions," *Construction Building Materials*, Vol. 26, No. 1, Pp. 723-729, (2012).

[85] H. Bohni, (2005). *Corrosion in Reinforced Concrete Structures*. Woodhead Publishing, Cambridge, UK.

[86] C.A. Juarez, B. Guevara, G. Fajardo, and P. Castro-Borges, "Ultimate and Nominal Shear Strength in Reinforced Concrete Beams Deteriorated by Corrosion," *Engineering Structures*, Vol. 33, Pp. 3189-3196, (2011).

[87] J. Xia, W. Jin, and L. Li, "Shear Performance of Reinforced Concrete Beams with Corroded Stirrups in Chloride Environment," *Corrosion Science*, Vol. 53, Pp. 1794-1805, (2011).

[88] M. Dekoster, F. Buyle-Bodin, O. Maurel, and Y. Delmas, "Modelling of the Flexural Behaviour of RC Beams Subjected to Localized and Uniform Corrosion," *Engineering Structures*, Vol. 25, Pp. 1333-1341, (2003).

[89] W. Zhang, X. Song, X. Gu, and S. Li, "Tensile and Fatigue Behavior of Corroded Rebars," *Construction and Building Materials*, Vol. 34, Pp. 409-417, (2012).

[90] R. Francois, I. Khan, and V.H. Dang, "Impact of Corrosion on Mechanical Properties of Steel Embedded in 27-year-old Corroded Reinforced Concrete Dam," *Materials and Structures*, Vol. 46, Pp. 899-910, (2013).

[91] W. Yi, S.K. Kunnath, X. Sun, C. Shi, and F. Tang, "Fatigue Behavior of Reinforced Concrete Beams with Corroded Steel Reinforcement," *ACI Structural Journal,* Vol. 107, Pp. 526-533, (2010).

[92] A.A. Torres-Acosta, and P. Castro-Borges, "Corrosion-induced Cracking of Concrete Elements Exposed to a Natural Marine Environment for Five Years," *Corrosion*, Vol. 69, No. 11, Pp. 1122-1131, (2013).

[93] R. Zhang, A. Castel, and R. Francois, "Concrete Cover Cracking with Reinforcement Corrosion of RC Beam During Chloride-induced Corrosion Process," *Cement and Concrete Research*, Vol. 40, No. 3, Pp. 415-425, (2010).

[94] G. Malumbela, M. Alexander, and P. Moyo, "Variation of Steel Loss and Its Effect on the Ultimate Flexural Capacity of RC Beams Corroded and Repaired Under Load," *Construction and Building Materials*, Vol. 24, No. 6, Pp. 1051-1059, (2010).

[95] W. Zhu, R. Francois, D. Coronelli, and D. Cleland, "Effect of Corrosion of Reinforcement on the Mechanical Behavior of Highly Corroded RC Beams," *Engineering Structures*, Vol. 56, Pp. 544-554, (2013).

[96] J.A. Gonzalez, C. Andrade, C. Alonso, and S. Feliu, "Comparison of Rates of General Corrosion and Maximum Pitting Penetration on Concrete Embedded Steel Reinforcement," *Cement and Concrete Research*, Vol. 25, No. 2, Pp. 257-264, (1995).

[97] A.A. Torres-Acosta, and M. Martinez-Madrid, "Residual Life of Corroding Reinforced Concrete Structures in Marine Environment," *ASCE Journal of Materials in Civil Engineering,* Vol. 15, No. 4, Pp. 344-353, (2003).

[98] M.G. Stewart, "Spatial Variability of Pitting Corrosion and Its Influence on Structural Fragility and Reliability of RC Beams in Flexure," *Structural Safety*, Vol. 26, No. 4, Pp. 453-470, (2004).

[99] M.G. Stewart, and A. Al-Harthy, "Pitting Corrosion and Structural Reliability of Corroding RC Structures: Experimental Data and Probabilistic Analysis," *Reliability Engineering and System Safety*, Vol. 93, No. 3, Pp. 373-382, (2008).

[100] W. Zhang, B. Zhou, X. Gu, and H. Dai, "Probability Distribution Model for Cross-sectional Area of Corroded Reinforcing Steel Bars." *ASCE Journal of Materials in Civil Engineering*, http://dx.doi.org/10.1061/(ASCE)MT.1943-5533.0000888

[101] D.A. Koleva, J. Hu, A.L.A. Fraaij, P. Stroeven, N. Boshkov, and J.H.W. De Wit, "Quantitative Characterization of Steel/Cement Paste Interface Microstructure and Corrosion Phenomena in Mortars Suffering from Chloride Attack," *Corrosion Science,* Vol. 48, Pp. 4001-4019, (2006).

[102] Y. Zhao, Y. Wu, and W. Jin. "Distribution of Millscale on Corroded Steel Bars and Penetration of Steel Corrosion Products in Concrete," *Corrosion Science*, Vol. 66, Pp. 160-168, (2013).

[103] S. Guzman, J.C. Galvez, and J.M. Sancho, "Cover Cracking of Reinforced Concrete Due to Rebar Corrosion Induced by Chloride Penetration," *Cement and Concrete Research*, Vol. 41, No. 8, Pp. 893-902, (2011).

[104] L. Chung, J.H.J. Kim, and S.T. Yi, "Bond Strength Prediction for Reinforced Concrete Members with Highly Corroded Reinforcing Bars," *Cement & Concrete composites*, Vol. 30, No. 7, Pp. 603-611, (2008).

[105] G.J. Al-Sulainmani, M. Kaleemullah, I.A. Basunbul, and Rasheeduzzafar, "Influence of Corrosion and Cracking on Bond Behaviour and Strength of Reinforced Concrete Members," *ACI Structural Journal*, Vol. 87, No. 2, Pp. 220-231, (1990).

[106] K. Stanish, R.D. Hooton, and S.J. Pantazonpoulou, "Corrosion Effects on Bond Strength in Reinforced Concrete," *ACI Structural Journal*, Vol. 96, No. 6, Pp. 915-921, (1999).

[107] L. Chung, S.H. Cho, J.H.J. Kim, and S.T. Yi, "Correction Factor Suggestion for ACI Development Length Provisions Based on Flexural Testing of RC Slabs with Various Levels of Corroded Reinforcing Bars," *Engineering Structure*, Vol. 26, No. 8, Pp. 1013-1026, (2004).

[108] T.P. Tassios, "Properties of Bond between Concrete and Steel under Load Cycles Idealizing Seismic Actions," In: *Proceedings of the AICAP-CEB Symposium*, Rome, CEB, Bulletin No. 131, Pp. 67-122, (1979).

[109] Porcelain Enamel, 502-Mechanical, http://www.porcelainenamel.com/technical_information/502_mechanical.aspx. November 2013.

[110] G.H. Spencer-Strong, (1953). Porcelain Enamel Institute Conference Proceedings.

[111] K. Barcova, M. Mashlan, R. Zboril, J. Filip, J. Podjuklova, K. Hrabovska, and P. Schaaf, "Phase Composition of Steel-enamel Interfaces: Effects of Chemical Pre-treatment," *Surface and Coatings Technology*, Vol. 201, No. 3-4, Pp. 1836-1844, (2006).

[112] D.A. Jones, (1996). *Principles and Prevention of Corrosion*, 2nd ed., Prentice-Hall, Upper Saddle River, NJ.

[113] L. Samiee, H. Sarpoolaky, and A. Mirhabibi, "Microstructure and Adherence of Cobalt Contained and Cobalt Free Enamels to Low Carbon Steel," *Materials Science and Engineering: A,* Vol. 458, No. 1-2, Pp. 88-95, (2007).

[114] D. Wang, "Effect of Crystallization on the Property of Hard Enamel Coating on Steel Substrate," *Applied Surface Science*, Vol. 255, No. 8, Pp. 4640-4645, (2009).

[115] F. Tang, G. Chen, R.K. Brow. J.S. Volz, and M.L. Koenigstein, "Corrosion Resistance and Mechanism of Steel Rebar Coated with Three Types of Enamel," *Corrosion Science*, Vol. 59, Pp. 157-168, (2012).

[116] D. Yan, S. Reis, X. Tao, G. Chen, R.K. Brow, and M.L. Koenigstein, "Effect of Chemically Reactive Enamel Coating on Bonding Strength at Steel/Mortar Interface," *Construction and Building Materials*, Vol. 28, No. 1, Pp. 512-518, (2012).

[117] C. Wu, G. Chen, J.S. Volz, R.K. Brow, and M.L. Koenigstein, "Local Bond Strength of Vitreous Enamel Coated Rebar to Concrete," *Construction and Building Materials*, Vol. 35, Pp. 428-439, (2012).

[118] S. Mindess, J.F. Young, and D. Darwin, (1996). *Concrete*. 2nd ed., Pearson Education, Inc. Upper Saddle River, NJ.

[119] W. Chen, R. Du, C. Ye, Y. Zhu, and C. Lin, "Study on the Corrosion Behavior of Reinforcing Steel in Simulated Concrete Pore Solutions using In Situ Raman Spectroscopy Assisted by Electrochemical Techniques," *Electrochimica Acta,* Vol. 55, No. 20, Pp. 5677-5682, (2010).

[120] H. Xu, Y. Liu, W. Chen, R. Du, and C. Lin, "Corrosion Behavior of Reinforcing Steel in Simulated Concrete Pore Solution: A Scanning Micro-reference Electrode Study," *Electrochimica Acta*, Vol. 54, No. 16, Pp. 4067-4072, (2009).

[121] M. Sanchez, J. Gregori, C. Alonso, J.J. Garcia-Jareno, H. Takenouti, and F. Vicente, "Electrochemical Impedance Spectroscopy for Studying Passive Layers on Steel Rebars Immersed in Alkaline Solutions Simulated Concrete Pores," *Electrochimica Acta*, Vol. 52, No. 27, Pp. 7634-7641, (2007).

[122] NRC (1927). International Critical Tables, Vol. 2, National Research Council, McGraw-Hill, Washington, D.C.

[123] ASTM C150-07 (2007). Standard Specification for Portland Cement. *American Society of Testing and Materials*, West Conshohocken, PA.

[124] W. Aperador, R. Mejia de Gutierrez, and D.M. Bastidas, "Steel Corrosion Behaviour in Caronated Alkali-activated Slag Concrete," *Corrosion Science,* Vol. 51, No. 9, Pp. 2027-2033, (2009).

[125] X. Yang, A. Jha, R. Brydson, and R.C. Cochrane, "An Analysis of the Microstructure and Interfacial Chemistry of Steel-enamel Interface," *Thin Solid Films,* Vol. 443, No. 1-2, Pp. 33-45, (2003).

[126] X. Yang, A. Jha, R. Brydson, and R.C. Cochrane, "The Effects of a Nickel Oxide Precoat on the Gas Bubble Structures and Fish-scaling Resistance in Vitreous Enamels," *Materials Science and Engineering A*, Vol. 366, No. 2, Pp. 254-261, (2004).

[127] F.S. Shieu, K.C. Lin, and J.C. Wong, "Microstructure and Adherence of Porcelain Enamel to Low Carbon Steel," *Ceramics International*, Vol. 25, No. 1, Pp. 27-34, (1999).

[128] G. Ling, and J. He, "The Influence of Nano-Al_2O_3 Additives on the Adhesion between Enamel and Steel Substrate," *Materials Science and Engineering A,* Vol. 379, No. 1-2, Pp. 432-436, (2004).

[129] A. Zhang, Z. Jiang, S. Jiao, and D. Wei, "Microstructure and Adherence of Vitreous Enamel to Low Carbon Steel," *International Journal of Surface Science and Engineering*, Vol. 5, No. 5-6, Pp. 369-380, (2011).

[130] K.Y. Ann, and H.W. Song, "Chloride Threshold Level for Corrosion of Steel in Concrete." *Corrosion Science*, Vol. 49, No. 11, Pp. 4113-4133, (2007).

[131] M. Saremi, and E. Mahallati, "A Study on Chloride-induced Depassivation of Mild Steel in Simulated Concrete Pore Solution," *Cement and Concrete Research*, Vol. 32, No. 12, Pp. 1915-1921, (2002).

[132] R. Akid, M. Gobara, and H. Wang, "Corrosion Protection Performance of Novel Hybrid Polyaniline/sol-gel Coatings on an Aluminium 2024 Alloy in Neutral,

Alkaline and Acidic Solutions," *Electrochimica Acta*, Vol. 56, No. 5, Pp. 2483-2492, (2011).

[133] J. Liu, G. Gong, and C. Yan, "EIS Study of Corrosion Behaviour of Organic Coating/Dacromet Composite Systems," *Electrochimica Acta*, Vol. 50, No. 16-17, Pp. 3320-3332, (2005).

[134] V. Karpakam, K. Kamaraj, S. Sathiyanaranyanan, G. Venkatachari, and S. Ramu, "Electrosynthesis of Polyaniline-Molybdate Coating on Steel and Its Corrosion Protection Performance," *Electrochimica Acta,* Vol. 56, No. 5, Pp. 2165-2173, (2011).

[135] H. Luo, C. Dong, X. Li, and K. Xiao, "The Electrochemical Behaviour of 2205 Duplex Stainless Steel in Alkaline Solutions with Different pH in the Presence of Chloride," *Electrochimica Acta*, Vol. 64, Pp. 211-220, (2012).

[136] L. Wu, J. Zhang, J. Hu, and J. Zhang, "Improved Corrosion Performance of Electrophoretic Coatings by Silane Addition," *Corrosion Science*, Vol. 56, Pp. 58-66, (2012).

[137] L. Freire, M.J. Carmezim, M.G.S. Ferreira, and M. Montemor, "The Electrochemical Behaviour of Stainless Steel AISI 304 in Alkaline Solutions with Different pH in the Presence of Chloride," *Electrochimica Acta*, Vol. 56, No. 14, Pp. 5280-5289, (2011).

[138] B. Del Amo, R. Romagnoli, C. Deya, and J.A. Gonzalez, "High Performance Water-based Paints with Non-toxic Anticorrosive Pigments," *Progress in Organic Coatings*, Vol. 45, No. 4, Pp. 389-397, (2002).

[139] V. Barranco, S. Feliu, Jr. and S. Feliu, "EIS Study of the Corrosion Behaviour of Zinc-based Coatings on Steel in Quiesceent 3% NaCl solution. Part 2: Coating Covered with an Inhibitor-containing Lacquer," *Corrosion Science*, Vol. 46, No. 9, Pp. 2221-2240, (2004).

[140] C. Christodoulou, C.J. Goodier, S.A. Austin, J. Webb, and G. Glass, "On-site Transient Analysis for the Corrosion Assessment of Reinforced Concrete," *Corrosion Science,* Vol. 62, Pp. 176-183, (2012).

[141] C. Zhu, R. Xie, J. Xue, and L. Song, "Studies of the Impedance Models and Water Transport Behaviors of Cathodically Polarized Coating," *Electrochimica Acta,* Vol. 56, No. 16, Pp. 5828-5835, (2011).

[142] Z. Yao, Z. Jiang, and F. Wang, "Study on Corrosion Resistance and Roughness of Micro-plasma Oxidation Ceramic Coatings on Ti Alloy by EIS Technique," *Electrochimica Acta*, Vol. 52, No. 13, Pp. 4539-4546, (2007).

[143] F.B. Growcock, and J.H. Jasinski, "Time-Resolved Impedance Spectroscopy of Mild Steel in Concentrated Hydrochloric Acid," *Journal of the Electrochemical Society,* Vol. 136, No. 8, Pp. 2310-2314, (1989).

[144] A. Igual Munoz, J. Garcia Anton, J.L. Guinon, and V. Perez Herranz, "The Effect of Chromate in the Corrosion Behavior of Duplex Stainless Steel in LiBr Solutions," *Corrosion Science,* Vol. 48, No. 12, Pp. 4127-4151, (2006).

[145] M.G. Maitra, M. Sinha, A.K. Mukhopadhyay, T.R. Middya, U. De, and S. Tarafdar, "Ion-conductivity and Young's Modulus of the Polymer Electrolyte PEO-ammonium Perchlorate," *Solid State Ionics*, Vol. 178, No. 3-4, Pp. 167-171, (2007).

[146] B. Hirschorn, M.E. Orazem, B. Tribollet, V. Vivier, I. Frateur, and M. Musiani, "Determination of Effective Capacitance and Film Thickness from Constant-Phase-Element Parameters," *Electrochimica Acta,* Vol. 55, No. 21, Pp. 6218-6227, (2010).

[147] P. Cordoba-Torres, T.J. Mesquita, O. Devos, B. Tribollet, V. Roche, and R.P. Nogueira, "On the Intrinsic Coupling between Constant-phase Element Parameters α and Q in Electrochemical Impedance Spectroscopy," *Eletrochimica Acta*, Vol. 72, Pp. 172-178, (2012).

[148] J. Hernandez-Ferrer, A. Anson-Casaos, and M. Teresa Martinez, "Electrochemical Synthesis and Characterization of Single-walled Carbon Nanotubes/polypyrrole Films on Transparent Substrate," *Electrochimica Acta*, Vol. 64, Pp. 1-9, (2012).

[149] H.H. Hassan, E. Abdelghani, and M.A. Amin, "Inhibition of Mild Steel Corrosion in Hydrochloric Acid Solution by Triazole Derivatives: Part I. Polarization and EIS Studies," *Electrochimica Acta*, Vol. 52, No. 22, Pp. 6359-6366, (2007).

[150] C. Ye, R. Hu, S. Dong, X. Zhang, R. Hou, R. Du, C. Lin, and J. Pan, "EIS Analysis of Chloride-induced Corrosion Behavior of Reinforcement Steel in Simulated Carbonated Concrete Pore Solutions," *Journal of Electroanalytical Chemistry*, Vol. 688, Pp. 275-281, (2013).

[151] M.J. Shannag, and S.A. Al-Ateek, "Flexural Behavior of Strengthened Concrete Beams with Corroding Reinforcement," *Construction and Building Materials,* Vol. 20, No. 9, Pp. 834-840, (2006).

[152] O.S.B. Al-Amoudi, M. Maslehuddin, A.N. Lashari, and A.A. Almusallam, "Effectiveness of Corrosion Inhibitors in Contaminated Concrete," *Cement and Concrete Composites*, Vol. 25, No. 4-5, Pp. 439-449, (2003).

[153] L. Dhouibi, E. Triki, and A. Raharinaivo, "The Application of Electrochemical Impedance Spectroscopy to Determine the Long-term Effectiveness of Corrosion Inhibitors for Steel in Concrete," *Cement and Concrete Composites*, Vol. 24, No. 1, Pp. 35-43, (2002).

[154] M. Ormellese, M. Berra, F. Bolzoni, and T. Pastore, "Corrosion Inhibitors for Chlorides Induced Corrosion in Reinforced Concrete Structures," *Cement and Concrete Research*, Vol. 36, No. 3, Pp. 536-547, (2006).

[155] W. Sun, Y. Zhang, S. Liu, and Y. Zhang, "The Influence of Mineral Admixtures on Resistance to Corrosion of Steel Bars in Green High-performance Concrete," *Cement and Concrete Research*, Vol. 34, No. 10, Pp. 1781-1785, (2004).

[156] O. Kayali, and B. Zhu, "Corrosion Performance of Medium-strength and Silica Fume High-strength Reinforced Concrete in a Chloride Solution," *Cement and Concrete Composites*, Vol. 27, No. 1, Pp. 117-124, (2005).

[157] C. Shi, "Corrosion Resistance of Alkali-activated Slag Cement." *Advanced Cement Research*, Vol. 15, No. 2, Pp. 77-81, (2003).

[158] T. Bellezze, M. Malavolta, A. Quaranta, N. Ruffini, and G. Roventi, "Corrosion Behavior in Concrete of Three Differently Galvanized Steel Bars," *Cement and Concrete Composites,* Vol. 28, No. 3, Pp. 246-255, (2006).

[159] A.A. Almusallam, F.M. Khan, S.U. Dulaijan, and O.S.B. Al-Amoudi, "Effectiveness of Surface Coatings in Improving Concrete Durability," *Cement and Concrete Composites*, Vol. 25, No. 4-5, Pp. 473-481, (2003).

[160] A.B. Darwin, and J.D. Scantlebury, "Retarding of Corrosion Processes on Reinforcement Bar in Concrete with an FBE Coating," *Cement and Concrete Composites,* Vol. 24, No. 1, Pp. 73-78, (2002).

[161] M.A. Arenas, C. Casado, V. Nobel-Pujol, and J. Damborenea, "Influence of the Conversion Coating on the Corrosion of Galvanized Reinforcing Steel," *Cement and Concrete Composites*, Vol. 28, No. 3, Pp. 267-275, (2006).

[162] M. Criado, D.M. Bastidas, S. Fajardo, A. Fernandez-Jimenez, and J.M. Bastidas, "Corrosion Behavior of a New Low-nickel Stainless Steel Embedded in Activated Fly Ash Mortars," *Cement and Concrete Composites*, Vol. 33, No.6, Pp. 644-652, (2011).

[163] M.C. Garcia-Alonso, M.L. Escudero, J.M. Miranda, M.I. Vega, F. Capilla, M.J. Correia, M. Salta, A. Bennani, and J.A. Gonzalez, (2007). "Corrosion Behavior of New Stainless Steels Reinforcing Bars Embedded in Concrete," *Cement and Concrete Research,* Vol. 37, No. 10, Pp. 1463-1471, (2007).

[164] P.M. Chess, (1998). *Cathodic Protection of Steel in Concrete*. New York: Taylor & Francis.

[165] A.M. Hassanein, G.K. Glass, and N.R. Buenfeld, "Protection Current Distribution in Reinforced Concrete Cathodic Protection Systems," *Cement and Concrete Composites*, Vol. 24, No. 1, Pp. 159-167, (2002).

[166] F. Tang, G. Chen, J.S. Volz, R.K. Brow, and M.L. Koenigstein, "Microstructure and Corrosion Resistance of Enamel Coatings Applied to Smooth Reinforcing Steel," *Construction and Building Materials*, Vol. 35, Pp. 376-384, (2012).

[167] P. Ghods, O.B. Isgor, F. Bensebaa, and D. Kingston, "Angle-resolved XPS Study of Carbon Steel Passivity and Chloride-induced Depassivation in Simulated Concrete Pore Solution," *Corrosion Science*, Vol. 58, Pp. 159-167, (2012).

[168] H. Bruno, V.L. Hostis, F. Miserque, and H. Idrissi, "Electrochemical Behavior of Mild Steel in Concrete: Influence of pH and Carbonate Content of Concrete Pore Solution," *Electrochimica Acta*, Vol. 51, No. 1, Pp. 172-180, (2005).

[169] P.K. Mehta, (1977). Effect of Cement Composition on Corrosion of Reinforcing Steel in Concrete. *Chloride Corrosion of Steel in Concrete*. Philadelphia, ASTM STP 629, 12-19.

[170] K.K. Sagoe-crentsil, F.P. Glasser, and J.T. Irvine, "Electrochemical Characteristics of Reinforced Concrete Corrosion as Determined by Impedance Spectroscopy," *British Corrosion Journal,* Vol. 27, No.2, Pp. 113-118, (1992).

[171] Princeton Applied Research, ZSimpWin, Website http://www.princetonappliedresearch.com/Our-Products/Electrochemical-Software/ZSimpWin.aspx. November 2013.

[172] X. Liu, J. Xiong, Y. Lv, and Y. Zuo, "Study on Corrosion Electrochemical Behavior of Several Different Coating Systems by EIS," *Progress in Organic Coatings,* Vol. 64, No. 4, Pp. 497-503, (2009).

[173] A. Conde, and J.J. De Damborenea, "Electrochemical Impedance Spectroscopy for Studying the Degradation of Enamel Coatings," *Corrosion Science*, Vol. 44, No. 7, Pp. 1555-1567, (2002).

[174] A. Conde, and J.J. De Damborenea, "Monitoring of Vitreous Enamel Degradation by Electrochemical Noise," *Surface and Coatings Technology*, Vol. 150, No. 2-3, Pp. 212-217, (2002).

[175] V.F. Hock, S.W. Morefield, D.C. Day, C.A. Weiss, Jr. and P.G. Malone, (2008). "The Use of Vitreous Enamel Coatings to Improve Bonding and Reduce

Corrosion in Concrete Reinforcing Steel," *CORROSION 2008*, Paper No. 08220, NACE International, New Orleans LA.

[176] C.L. Hackler, C.A. Weiss, and P.G. Malone, "Reactive Porcelain Enamel Coatings for Reinforcing Steel to Enhance the Bond to Concrete and Reduce Corrosion," *XXI International Enamellers Congress*, Pp.11-18, Shanghai, China (2008).

[177] V.F. Hock, S.W. Morefield, C.A. Weiss, Jr. and P.G. Malone, (2009). "The Use of Vitreous Enamel Coatings to Improve Bonding and Reducing Corrosion in Concrete Reinforcing Steel and Stay-in-place Forms at Army Installations," Department of Defense Corrosion Conference, Gaylord National, Washington DC.

[178] K.M. Fyles, and P. Shorrock, (1982). Alkali Resistant Glass Fibers for Cement Reinforcement. U.S. Patent 4,345,037, Pilkington Brothers Ltd (GB).

[179] ASTM G 14-04 (2010). Standard Test Method for Impact Resistance of Pipeline Coatings (Falling Weight Test). *American Society of Testing and Materials*, West Conshohocken, PA.

[180] T.D. Marcotte, (2001). *Characterization of Chloride-induced Corrosion Products that Form in Steel-reinforced Cementitious Materials*. Ph.D. Dissertation, University of Waterloo, Canada.

[181] P.A. Schweitzer, (1989). *Corrosion and Corrosion Protection Handbook*. 2nd edition, CRC Press, New York.

[182] J.K. Singh, and D.D.N. Singh, "The Nature of Rusts and Corrosion Characteristics of Low Alloy and Plain Carbon Steel in Three Kinds of Concrete Pore Solution with Salinity and Different Ph," *Corrosion Science*, Vol. 56, Pp. 129-142, (2012).

[183] Y. Zhao, H. Ren, H. Dai, and W. Jin, "Composition and Expansion Coefficient of Rust Based on X-ray Diffraction and Thermal Analysis," *Corrosion Science,* Vol. 53, No. 5, Pp. 1646-1658, (2011).

[184] Y. Ma, Y. Li, and F. Wang, "Corrosion of Low Carbon Steel in Atmospheric Environments of Different Chloride Content," *Corrosion Science*, Vol. 51, No. 5, Pp. 997-1006, (2009).

[185] C.G. Oliveira and M.G.S. Ferreira, "Ranking High-quality Paint Systems Using EIS. Part I: Intact Coatings," *Corrosion Science*, Vol. 45, No. 1, Pp. 123-138, (2003).

[186] C.G. Oliveira, and M.G.S. Ferreira, "Ranking High-quality Paint Systems Using EIS. Part II: Defective Coatings." *Corrosion Science*, Vol. 45, No. 1, Pp. 139-147, (2003).

[187] X. Shi, T.A. Nguyen, Z. Suo, Y. Liu, and R. Avci, "Effect of Nanoparticles on the Anticorrosion and Mechanical Properties of Epoxy Coating," *Surface and Coatings Technology*, Vol. 204, No. 3, Pp. 237-245, (2009).

[188] Y. Huang, H. Shi, H. Huang, J. Daugherty, S. Wu, S. Ramanathan, C. Chang, and F. Mansfeld, "Evaluation of the Corrosion Resistance of Anodized Aluminum 6061 Using Electrochemical Impedance Spectroscopy (EIS)," *Corrosion Science*, Vol. 50, No. 12, Pp. 3569-3575, (2008).

[189] Y.S. Choi, J.G. Kim, and K.M. Lee, "Corrosion Behavior of Steel Rebar Embedded in Fly Ash Concrete," *Corrosion Science*, Vol. 48, No. 7, Pp. 1733-1745, (2006).

[190] Y. Zhang, Y. Huang, and L. Wang, "Study of EVOH Based Single Ion Polymer Electrolyte: Composition and Microstructure Effects on the Proton Conductivity," *Solid State Ionics*, Vol. 177, No. 1-2, Pp. 65-71, (2006).

[191] M.J. Rodiguez Presa, R.I. Tucceri, M.I. Florit, and D. Posada, "Constant Phase Element Behavior in the Poly (o-toluidine) Impedance Response," *Journal of Electroanalytical Chemistry,* Vol. 502, No. 1-2, Pp. 82-90, (2001).

[192] M. Mahdavian, and R. Naderi, "Corrosion Inhibition of Mild Steel in Sodium Chloride Solution by Some Zinc Complexes," *Corrosion Science*, Vol. 53, No. 4, Pp. 1194-1200, (2011).

[193] C.R. Werner, (2010). *Corrosion Resistance of Enamel-coated Steel Reinforcement for Concrete*, MS Thesis, Missouri University of Science and Technology, USA.

[194] Y. Zhang, Y. Shao, T. Zhang, G. Meng, and F. Wang, "The Effect of Epoxy Coating Containing Emeraldine Base and Hydrofluoric Acid Doped Polyaniline on the Corrosion Protection of AZ91D Magnesium Alloy," *Corrosion Science*, Vol. 53, Pp. 3747-3755, (2011).

[195] A. Zayed, A. Sagues, and R. Powers, (1989). "Corrosion of Epoxy-coated Reinforcing Steel." Paper No. 379, *NACE International*, Houston TX, USA.

[196] L.L. Smith, R.J. Kessler, and R.G. Powers, (1993). Corrosion of Epoxy-coated Rebar in a Marine Environment. Transportation Research Circular: Epoxy-Coated Reinforcement in Highway Structures, Report No. 403, Pp.36-45, National Research Council. Transportation Research Board, Washington.

[197] G.K. Glass, and N.R. Buenfeld, "The Influence of Chloride Binding on the Chloride Induced Corrosion Risk in Reinforced Concrete," *Corrosion Science*, Vol. 42, No. 2, Pp. 329-344, (2000).

[198] K.Y. Ann, J.H. Ahn, and J.S. Ryou, "The Importance of Chloride Content at the Concrete Surface in Assessing the Time to Corrosion of Steel in Concrete Structures," *Construction and Building Materials*, Vol. 23, No. 1, Pp. 239-245, (2009).

[199] J. Zhang, and Z. Lounis, "Sensitivity Analysis of Simplified Diffusion-based Corrosion Initiation Model of Concrete Structures Exposed to Chlorides," *Cement and Concrete Research,* Vol. 36, No. 7, Pp. 1312-1323, (2006).

[200] C. Lu, W. Jin, and R. Liu, "Reinforcement Corrosion-induced Cover Cracking and Its Time Prediction for Reinforced Concrete Structures," *Corrosion Science*, Vol. 53, No. 4, Pp. 1337-1347, (2011).

[201] C.J. Newton, and J.M. Sykes, "A Galvanostatic Pulse Technique for Investigation of Steel Corrosion in Concrete," *Corrosion Science*, Vol. 28, No. 11, Pp. 1051-1074, (1998).

[202] K.V. Subramaniam, and M. Bi, "Investigation of the Local Response of the Steel-concrete Interface for Corrosion Measurement," *Corrosion Science*, Vol. 51, No. 9, Pp. 1976-1984, (2009).

[203] L. Tang, L. Nilsson, and P.A.M Basheer, (2012). *Resistance of Concrete to Chloride Ingress: Testing and Modeling*. Taylor & Francis, New York.

[204] Mindness, S., Young, J. F. and Darwin, D. (2002). *Concrete*. 2nd ed., Prentice Hall, New Jersey.

[205] K. Li, C. Li, and Z. Chen, "Influential Depth of Moisture Transport in Concrete Subject to Drying-wetting Cycles," *Cement and Concrete Composites*, Vol. 31, No. 10, Pp. 693-698, (2009).

[206] C.M. Hansson, A. Poursaee, and A. Laurent, "Macrocell and Microcell Corrosion of Steel in Ordinary Portland Cement and High Performance Concretes," *Cement and Concrete Research*, Vol. 36, No. 11, Pp. 2098-2102, (2006).

[207] N. Birbilis, K.M. Nairn, and M. Forsyth, "On the Electrochemical Response and Interfacial Properties of Steel-$Ca(OH)_2$ and the Steel-concrete System Measured Using Galvanostatic Pulses," *Electrochimica Acta*, Vol. 49, No. 25, Pp. 4331-4339, (2004).

[208] G.K. Glass, A.M. Hassanein, and N.R. Buenfeld, "Obtaining Impedance Information on the Steel-concrete Interface," *Corrosion*, Vol. 54, No. 11, Pp. 887-897, (1998).

[209] L. Hachani, C. Fiaud, E. Triki, and A. Raharinaivo, "Characterization of Steel/concrete Interface by Electrochemical Impedance Spectroscopy," *British Corrosion Journal,* Vol. 29, No. 2, Pp. 122-127, (1994).

[210] C. Andrade, M. Keddam, C.R. Novoa, M.C. Perez, C.M. Rangel, and H. Takenouti, "Electrochemical Behavior of Steel Rebars in Concrete: Influence of Environmental Factors and Cement Chemistry," *Electrochimica Acta*, Vol. 46, No. 24-25, Pp. 3905-3912, (2001).

[211] F. Mansfeld, "Discussion: Electrochemical Techniques for Studying Corrosion of Reinforcing Steel: limitations and Advantages," *Corrosion*, Vol. 61, No. 8, Pp. 739-742, (2005).

[212] J.A. Gonzalez, J.M. Miranda, N. Birbilis, and S. Feliu, "Electrochemical Techniques for Studying Corrosion of Reinforcing Steel: Limitations and Advantages," *Corrosion*, Vol. 61, No. 1, Pp. 37-50, (2005).

[213] J. Zhang, J. Hu, J. Zhang, and C. Cao, "Studies of Water Transport Behavior and Impedance Models of Epoxy-coated Metals in NaCl Solution by EIS," *Progress in Organic Coatings*, Vol. 51, No. 2, Pp. 145-151, (2004).

[214] J. Zhang, J. Hu, J. Zhang, and C. Cao, "Studies of Impedance Models and Water Transport Behaviors of Polypropylene Coated Metals in NaCl Solution," *Progress in Organic Coatings*, Vol. 49, No. 4, Pp. 293-301, (2004).

[215] J. Hu, J. Zhang, and C. Cao, "Determination of Water Uptake and Diffusion of Cl Ion in Epoxy Primer on Aluminum Alloys in NaCl Solution by Electrochemical Impedance Spectroscopy," *Progress in Organic Coatings*, Vol. 46, No. 4, Pp. 273-279, (2003).

[216] P. Gu, and J.J. Beaudoin, "Estimation of Steel Corrosion Rate in Reinforced Concrete by Means of Equivalent Circuit Fittings of Impedance Spectra," *Advances in Cement Research*, Vol. 10, No. 2, Pp. 43-56, (1998).

[217] R. Vedalakshmi, V. Saraswathy, H. Song, and N. Palaniswamy, "Determination of Diffusion Coefficient of Chloride in Concrete Using Warburg Diffusion Coefficient," *Corrosion Science*, Vol. 51, No. 6, Pp. 1299-1307, (2009).

VITA

Fujian Tang was born on July 5, 1981 in the City of Qufu, Shandong, China. After graduation from the high school affiliated with the Qufu Normal University in 2000, Fujian pursued a B.S. degree in civil engineering at the University of South China located in the City of Hengyang, Hunan, China. Upon graduation in 2004, he was directly admitted into Ph.D. Program in Civil Engineering at Hunan University under the supervision of Professor Weijian Yi due to his excellent academic performance. Four years later, he discontinued his PhD study in Hunan University and came to the U.S. In 2008, Fujian was admitted into PhD Program in Civil Engineering at Missouri University of Science and Technology under the supervision of Professor Genda Chen. In 2012, he decided to pursue a second graduate degree at the same time, M.S. Program in Materials Science and Engineering, under the supervision of Professor Richard K. Brow and Professor Genda Chen at Missouri University of Science and Technology. During his many years of graduate study both in China and in the U.S., he published 7 papers in international journals. In addition, two more are under review and five more are in preparation for potential publication. In December 2013, he received his Ph.D. degree in Civil Engineering from Missouri University of Science and Technology, Rolla, Missouri.